Simulation and Comparison of Operational Modes in Simulated Moving Bed Chromatography and Gas-Phase Adsorptive Separation

Yueying Yu

Dissertation submitted to the faculty of the Virginia Polytechnic Institute and State University in partial fulfillment of the requirements for the degree of

Doctor of Philosophy
In
Chemical Engineering

Y. A. Liu (Chair)
Donald G. Baird
Richey M. Davis
Preston L. Durrill

December 02, 2015
Blacksburg, VA

Keywords: simulated moving bed chromatography, operational modes, adsorption, simulation, optimization, chiral separation.

Simulation and Comparison of Operational Modes in Simulated Moving Bed (SMB) Chromatography and Gas-Phase Adsorptive Separation

Yueying Yu

ABSTRACT

This dissertation describes the simulation and optimization of adsorptive and chromatographic separation processes. The first part focus on the simulation and comparison of operational modes in simulated moving bed (SMB) chromatography for separation and purification in bioprocesses. The second part includes the simulation of gas-phase adsorptive processes by pressure swing adsorption and temperature swing adsorption technologies.

The applications of SMB chromatography are popular in separating and purifying enantiomers, petrochemicals, pharmaceuticals and biochemicals with higher yield and lower solvent consumption. We simulate and compare several operational modes of simulated moving bed (SMB) for a binary and a ternary bioprocess using Aspen Chromatography. These operational modes are able to improve the separation efficiency of the basic SMB process by our simulation and optimization. We compare their separation performances and identify heuristics that will guide the selection of operational modes across a variety of systems.

Pressure swing adsorption (PSA) and temperature swing adsorption (TSA) are two of the main technologies for gas-phase adsorption separation processes. We simulate and demonstrate a PSA model for air separation system and a TSA model for CO2 capture system in Aspen Adsorption. We present their separation performance plots to provide the physical insights of these two systems.

Acknowledgement

We thank Aspen Technology, China Petroleum and Chemical Corporation (SINOPEC), BAE Systems, Marathon Petroleum, Universal Fibers, and Mid-Atlantic Technology, Research and Innovation Center for supporting our educational programs in computer-aided design and process system engineering at Virginia Tech.

I sincerely thank my advisor Dr. Y.A. Liu, for his guidance and encouragement through this research. His intelligence, enthusiasm and professionalism have always inspired me.

I would like to thank my committee members, Professors Donald G. Baird, Richey M. Davis and Preston L. Durrill for their valuable comments and kindness.

I am very lucky to work in a pleasant environment with my lab group. I specially want to thank my lab mate Kevin Wood, who offered me a lot of useful ideas and suggestions. I thank other group members, Stuart Higgins, Wei Shan Chin and Wei-Jun Wang for providing help to me whenever I need it.

Table of Contents

A List of Figures

A List of Tables

1. Introduction to the Dissertation

1.1. Scope and Organization of the Dissertation

This dissertation studies the simulation, optimization and comparison of the chromatographic and adsorptive separation processes. The first six chapters discuss in detail the simulation and comparison of operational modes in simulated moving bed (SMB) chromatography for two separation systems. In the interests of simplifying the design of SMB separation systems, we seek to identify heuristics that will guide the selection of operational modes across a variety of systems.

In this chapter, we give an outline of this dissertation, and discuss our motivation and significance of the research.

Chapter 2 describes the SMB adsorptive separation processes and various types of SMBs in both academic research and industrial applications. The chapter also presents a literature review of the SMB chromatography.

In Chapter 3, we apply the SMB column to both binary and ternary separations. We present the modeling equations, and analyze their separation performance based on our simulation results using Aspen Chromatography.

Chapter 4 discusses the details of the optimization methods we apply to the basic SMB and its operational modes in the following chapters.

Chapter 5 introduces the SMB operational modes we investigated. It considers:

(1) Varicol—switching the inlet and outlet ports asynchronously
(2) PowerFeed or Partial Feeding—varying feed flow rates
(3) ModiCon—varying feed concentrations
(4) Combinations of the previous three operational modes

Chapter 6 compares the simulation and optimization results of all the operational modes for both binary and ternary separations. Specifically, we aim to accomplish three key objectives. First, we identify trends in the optimization of each operational mode's variables. We compare the sensitivity

of purity and recovery to operational mode variables between the binary and ternary separations. Second, we quantify and compare the complete separation regions and the Pareto optimum plots for the operational mode variables found in the first step. Third, we apply the Powell optimization method to extend the investigation to more separation systems with different separation factors.

Chapters 7 to 9 cover the study of gas-phase adsorptive separation processes. Chapter 7 gives an overview of the gas-phase adsorptive separation by pressure swing adsorption and temperature swing adsorption technologies. Chapter 8 demonstrates a modeling application of the pressure swing adsorption process for the air separation using Aspen Adsorption. Chapter 9 introduces a temperature swing adsorption model for CO_2 capture from a mixture of CO_2/N_2 using Aspen Adsorption.

1.2. Motivation of the Research

Our research focuses on the simulation and optimization of gas and liquid adsorptive separation processes. Modeling incorporates key engineering fundamentals, including physical properties, kinetics, mass transfer, mass and energy balances, process dynamics and computer-aided design. Simulation models are important tools used in the development and operation of chemical process systems. Accurate, predictive models can help a plant minimize cost and maximize profit. Optimization aims at improving the process performance based on the current modeling and providing general guideline or trends for the separation systems.

Simulated moving bed (SMB) chromatography[1,2,3,4,5] has attracted growing research interests and industrial applications in separating and purifying enantiomers, petrochemicals, pharmaceuticals and biochemicals with higher yield and lower solvent consumption. The success of SMB applications has led to the development of new methods[2,4] for operating SMB units to further improve the separation efficiency. Our goal is to improve the separation performance of the SMB column by applying a variety of operational modes and their combinations. In our work, we focus particularly from a practical point of view on several operational modes applied to the existing SMB units by switching ports or adjusting control valves. We aim to analyze and compare their separation performance through our simulation and optimization to give physical insights of why a given operational mode performs better or worse than the basic SMB. Our purpose is to provide

quantitative guidelines for optimizing the performance of various operational modes, and present a general guide for the selection of operational modes across a variety of systems.

To that end, we analyze two separation systems to find common recommendations between them: a binary chiral separation and a ternary amino acid separation. The reason we choose these two systems is because SMB technology is commonly used in chiral separation in drug and protein production[1,3]. The SMB unit is originally applied for petrochemicals. Figure 1.1 (International Strategic Directions, Los Angeles, USA)[9] shows its applications have largely extended the pharmaceutical (35%) and bioproduct industry (25%), especially for the separation of chiral drugs and racemic mixtures. Chiral separation is very important in the pharmaceutical field. For example, one of thalidomide enantiomers is prescribed as a sedative drug, but the other causes really serious birth defects[6]. Their enantiomer formula are displayed in Figure 1.2.

In our study, the goal is to reach 99% for both product purity and recovery through modeling and optimization in a chiral separation process by applying various SMB operational modes. We also apply the simulation and optimization methods to a ternary amino acid separation system.

SMB chromatographic separation only involves the liquid adsorptive separation, and we would like to cover the gas-phase adsorptive processes as well in the dissertation. There are mainly two types of gas-phase adsorption processes according to different adsorbent regeneration methods: by changing the pressure called pressure swing adsorption (PSA)[7], or by varying the temperature called temperature swing adsorption[8]. We present two practical case studies using Aspen Adsorption: one is the modeling demonstration for building a pressure swing adsorption process; another is a hands-on workshop for a temperature swing adsorption process.

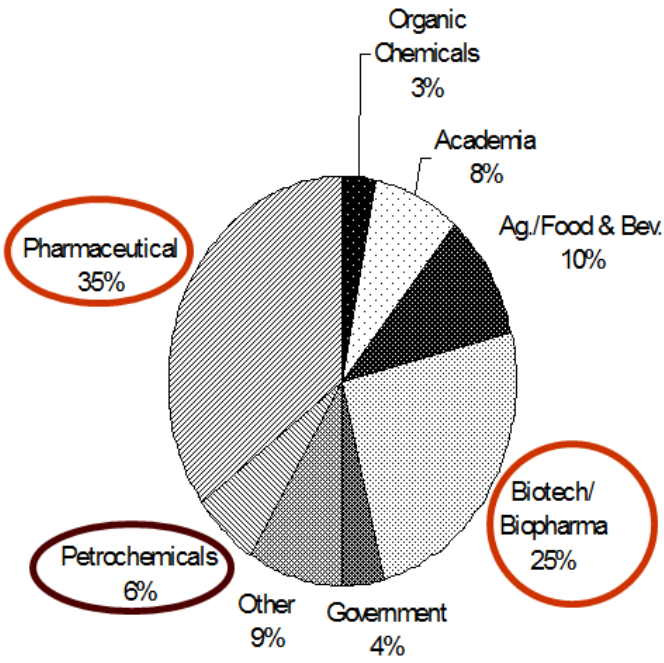

FIGURE 1.1 FRACTION OF CURRENT INSTALLED SMB UNITS.

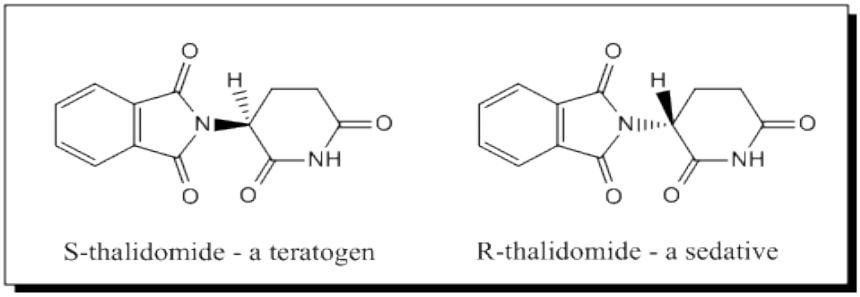

FIGURE 1.2 FORMULA OF THALIDOMIDE ENANTIOMERS.

1.3. Significance and Contributions of the research

For the SMB chromatography section, our work builds on the previous studies of operational modes and contributes the following:

(1) Investigate two separation systems to seek heuristic guidelines for improving the performance of the SMB operational modes and their combinations;

(2) Combine two or three operational modes (Varicol, PowerFeed and ModiCon);

(3) Present time-dependent column concentration profiles to give dynamic insights on the difference of the basic SMB with PowerFeed and with ModiCon;

(4) Evaluate the product purity and recovery results through rigorous simulations to show not only the improved separation regions for ranges of product purity and recovery, but also the robustness of the operational modes to changing flow rate ratios, i.e. m values;

(5) Analyze and compare the purity and productivity performance in the Pareto plot across all the operational modes;

(6) Investigate the validity of our recommendations on operational modes with different separation factors through rigorous simulation and optimization.

For the gas-phase adsorption section, our study includes:

(1) Demonstrate the simulations of pressure swing adsorption processes for air separation and temperature swing adsorption for CO_2 capture by Aspen Adsorption;

(2) Present the detailed modeling steps and performance results for both adsorptive separation processes.

Part I. Simulation and Comparison of Operational Modes in Simulated Moving Bed (SMB) Chromatography

2. Introduction to SMB

2.1. SMB Chromatographic Separation

Adsorptive and chromatographic processes are widely used in the chemical, pharmaceutical, and bioprocessing in industries for separation, purification and recovery purposes[10]. References 11 to 14 review the chromatographic techniques in the field of engineering applications. Chromatography is used to separate the components of a mixture carried by a mobile phase that flows through a stationary phase packed in a column. The separation is based on different partitioning of species between the mobile and the stationary phases.

Simulated moving bed (SMB) technology[1,2,3,4,5] is a powerful and promising chromatographic separation, and is a commercially popular for both small-scale bioseparations and for large-scale petrochemical applications. In 1961, Broughton and Gerhold[15] pioneered the concept of the SMB, and the initial applications invloved the petrochemical and sugar industries. Recently, it is getting an increasing attention by the research community, and finds commercial applications in separating and purifying enantiomers, pharmaceuticals, biochemicals, and chiral compounds with higher yield, lower solvent consumption, and lower operating cost[1]. The SMB process system has a major impact on the pharmaceutical and bioprocessing industries. The SMB technology allows for the continuous injection and separation for chiral drugs and racemic mixtures in the pharmaceutical area. The simulated countercurrent contact between the solid and liquid phases maximizes the mass-transfer driving force, leading to a significant reduction in mobile and stationary phase consumption compared with other chromatographic technologies, such as elution chromatography. This techniques leads to higher productivity and less diluted product streams. We discuss more about the SMB chromatography technology in the following sections.

2.2. *Introduction to SMBs*

2.2.1. True Moving Bed (TMB)

In a true moving bed (TMB)[16], the liquid and solid phases continuously flow in the opposite direction. Figure 2.1 illustrates a TMB for adsorptive separations and it has two inlet streams (feed and desorbent), and two outlet streams (extract and raffinate). The TMB allows for the attainment for high-purity products even when using a low-selectivity adsorbent. This is different when compared to the batch chromatography, in which high selectivity is critical to attain high-purity products. However, from an engineering point of view, the use of this type of equipment with the actual movement of the stationary phase is not practical for industrial implementation. This complex solid handling may lead to some technical problems, namely, equipment abrasion, mechanical erosion of adsorbent, and difficulties in maintaining plug flow for the solid (especially in beds with large diameters). These drawbacks motivate the development of the simulated moving bed (SMB) unit which represents an improvement of a true moving bed (TMB)[15,17].

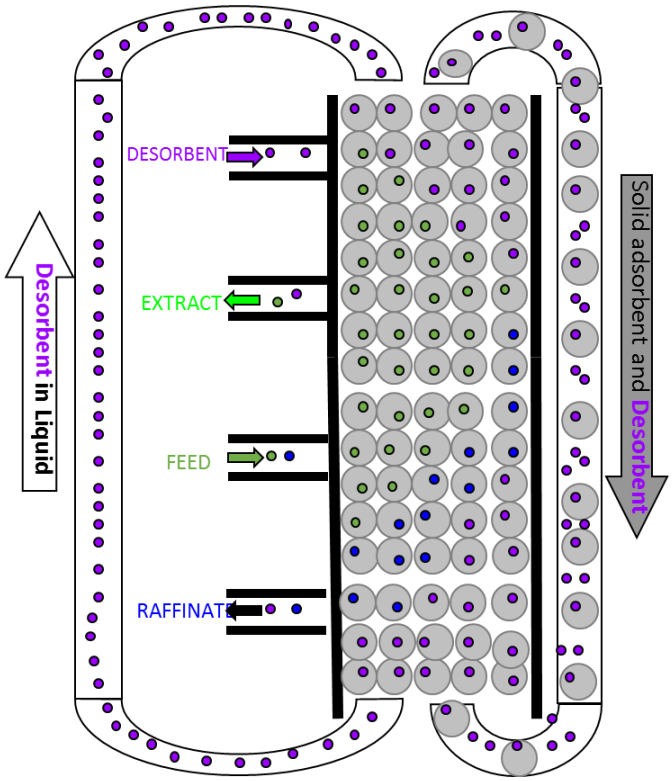

FIGURE 2.1. ILLUSTRATION OF A TMB FOR ADSORPTIVE SEPARATIONS.

2.2.2. The Classical Four-Zone SMB

The SMB unit[18] introduces a flow scheme to simulate the continuous counter-current flow of the solid adsorbent relative to the fluid, instead of actually moving it. This scheme holds the adsorbent as a stationary fixed bed, while periodically moving the inlet and outlet ports synchronously past one bed at a time. A SMB column consists of interconnected fixed beds with packed adsorbents. Figure 2.2 illustrates the concept of a 4-Zone SMB unit for adsorptive separation. The SMB column is divided into four zones by two incoming streams, feed (F) and desorbent (D), and by two outgoing streams, raffinate (R) and extract (E). It is possible to inject or remove the process streams between these beds through inlet and outlet ports.

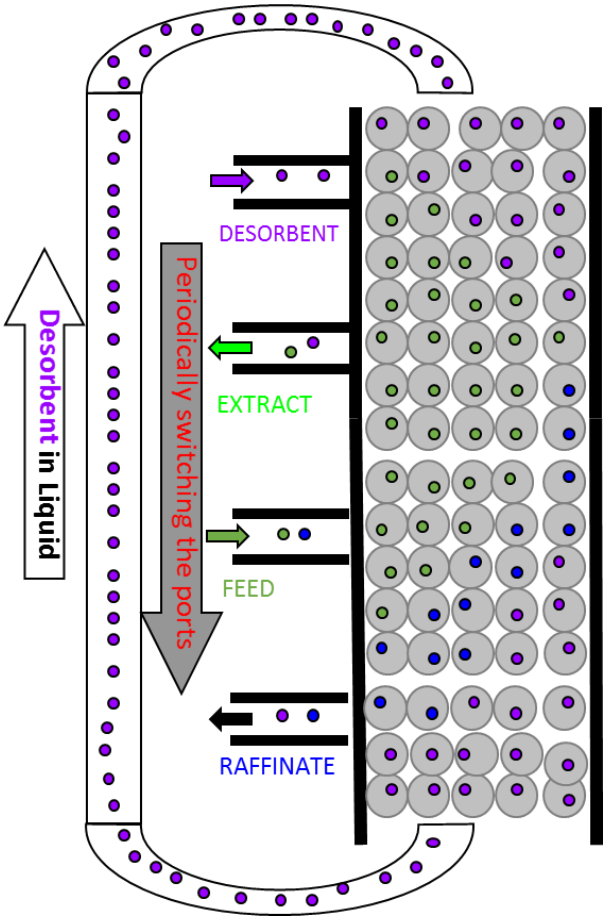

FIGURE 2.2. ILLUSTRATION OF A SMB FOR ADSORPTIVE SEPARATIONS.

These streams divide the SMB unit into four different zones, of which each zone in the process performs a different and specific role, as shown in Figure 2.3. Let us consider the adsorptive

separation of two components, the most-adsorbed component A and the least-adsorbed component B. An adsorption zone, zone 3, adsorbs component A and prevents it from reaching the raffinate port. Zone 2 is a purification zone that desorbs component B and prevents component B from reaching the extract port. Desorption zone in Zone 1 desorbs component A into the extract stream and regenerate the solid adsorbent in the column. Zone 4 is a buffer zone, which adsorbs component B to clean the desorbent, and blocks off zones 1 and 3. The right part of Figure 2.3 shows a typical concentration profile of components A and B within the TMB column after steady state.

Figure 2.4 illustrates the zone flow rate balances in the basic 4-zone SMB[19]. In the figure, Q_1, Q_2, Q_3, Q_4 are the internal flow rates in zone 1, 2, 3 and 4, respectively; Q_F, Q_R, Q_D, Q_E are the feed, raffinate, desorbent and extract flow rates, respectively; and $C_{i,j}^{in}$ and $C_{i,j}^{out}$ are the concentrations of component i at the inlet and outlet of zone j, respectively. In this 4-zone separation system, we fix the external flow rates Q_F, Q_D and Q_R, the internal recycle flow rate Q_4, and the feed and desorbent concentrations. The relationships among the flow rates in each zone of the SMB are:

$$Q_1 = Q_D + Q_{Recycle} \tag{2.1}$$

$$Q_2 = Q_1 - Q_E \tag{2.2}$$

$$Q_3 = Q_2 + Q_F \tag{2.3}$$

$$Q_4 = Q_3 - Q_R \tag{2.4}$$

Summing the previous relations and taking into account that $Q_4 = Q_{Recycle}$, we obtain the mass balance equation:

$$Q_F + Q_D = Q_R + Q_E \tag{2.5}$$

The role of each zone is guaranteed by setting the appropriate liquid flow rate in each zone as shown in Figure 2.4.

In order to simulate the countercurrent movement of the solid phase relative to the liquid phase, we switch the inlet and outlet ports simultaneously in the direction of fluid flow at a prespecified switching time t_{sw}. Figure 2.5 shows a schematic diagram of column configuration of four zones with six beds, which is denoted by χ = (1-2-2-1) in terms of the bed numbers in each zone. One complete cycle consists of six switches. In running a SMB process, we fix the switching time t_{sw} and column configuration χ throughout the entire operation.

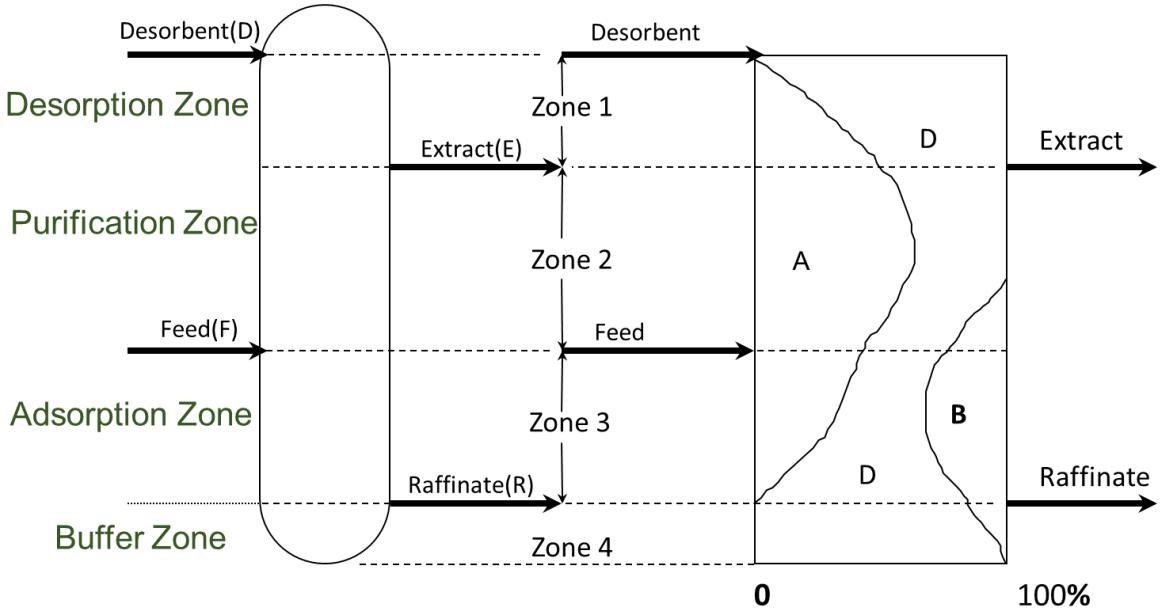

FIGURE 2.3. CONCEPT AND ZONE DISTRIBUTION OF A SMB FOR ADSORPTIVE SEPARATIONS.

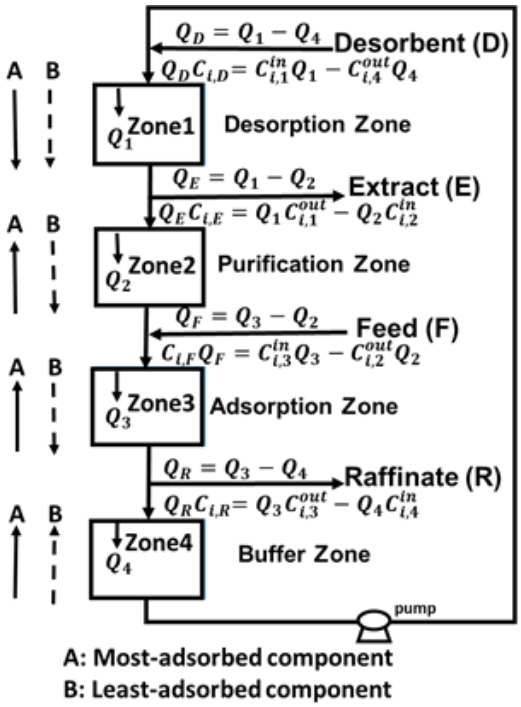

FIGURE 2.4. AN ILLUSTRATION OF ZONE FLOW RATE BALANCES IN THE BASIC 4-ZONE SMB.

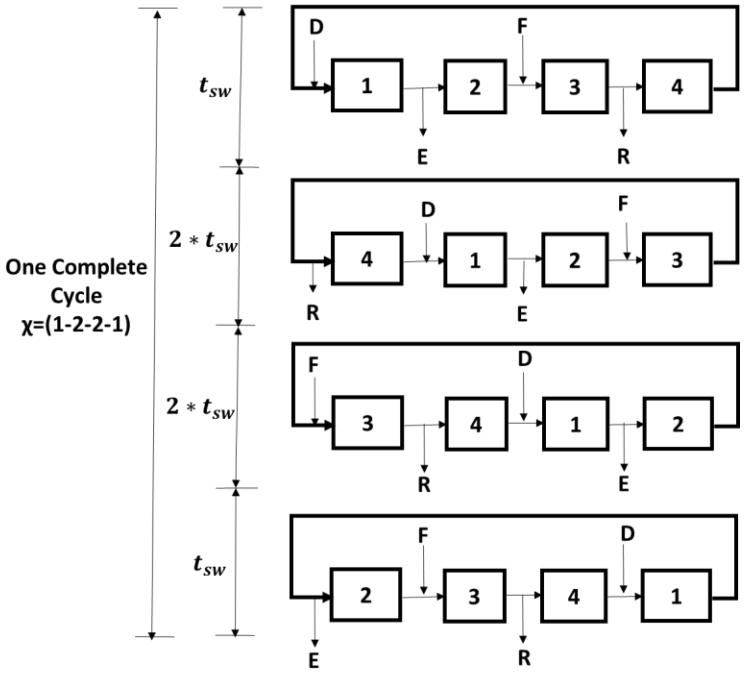

FIGURE 2.5. A SCHEMATIC DIAGRAM OF A FOUR-ZONE SMB WITH COLUMN CONFIGURATION X=(1-2-2-1).

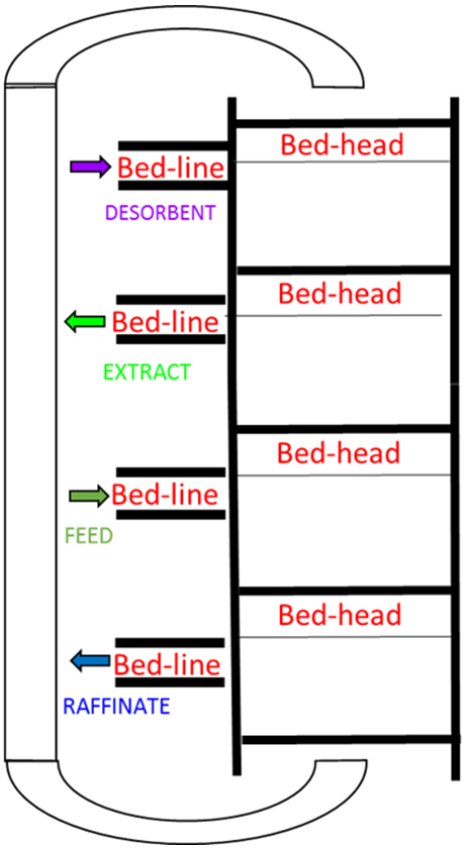

FIGURE 2.6. AN ILLUSTRATION OF EXTRA-COLUMN DEAD VOLUMES IN A SMB SYSTEM.

Figure 2.6 illustrates the extra-column dead volume which can impact the separation performance[20]. The dead volume consists of bed-head dead volumes and bed-line dead volumes. The bed-head dead volumes represent the dead parts connecting two consecutive chromatographic beds; the bed-line dead volumes are the ones in the inlet and outlet pipes, as shown in Figure 2.6. We approximate the dead volume by using an effective dead volume with an assumed and effective pipe diameter and pipe length in our SMB models.

2.2.3. The Classical Five-Zone SMB

If we want to separate an intermediate-adsorbed component or wish to obtain each pure component from a ternary mixture, a single 4-zone SMB will not suffice; we need additional separation zones to handle the added separations. There are a large number of ways to introduce the extra zones, such as cascading systems[21,22,23], hybrid SMB/Chromatography systems[24,25], or adding additional zones directly into a 4-zone SMB[26,27,28,29]. For our separation system, we want to investigate a 5-zone

configuration because it has received some attention recently[19,26,28,29], and the 5-zone is a simple extension of the 4-zone concept. We can implement all the operational modes investigated for 4 zones in 5 zones in nearly the same way. In general, tandem SMB systems are preferred for separation systems with low separation factors[21,23]; the amino acid system we select has large separation factors, making it a good candidate for the 5-zone configuration.

Figure 2.7 displays a 5-zone SMB unit for ternary separation[26]. In a 5-zone SMB unit, we divide the SMB unit into five zones by five inlet and outlet ports, namely, desorbent, extract1, extract2, feed and raffinate. The figure shows that the unit has three product ports: extract1 outlet stream produces the most-adsorbed component A; raffinate outlet stream contains the least adsorbed component B; extract2, upstream from the feed port for the desorption and separation of the intermediate-adsorbed component I. Just like the 4-zone diagram in Figure 2.4, arrows in Figure 2.8 show the flow directions of all the components A, I and B. Components A and I are both carried backwards relative to the liquid flow, which is illustrated by the upward arrows next to zones 3 and 4. The downward arrows near zones 1 and 2 indicate where desorption of A and I occurs. Component B moves with the liquid through zone 4 and out the raffinate stream. Any component B that is not removed in the raffinate stream is adsorbed in zone 5 and recycled back into zone 4 where it is released from the solid phase.

Figure 2.8 depicts the flow balances for a 5-zone system[19]; we see the parallels to the 4-zone system illustrated in Figure 2.4. Just like the 4-zone diagram, arrows in Figure 2.8 indicate the flow directions of components A, B and C. Components B and C are both adsorbed onto the solid phase, and are carried backwards relative to the liquid flow. This is indicated by the upward arrows next to zones 3 and 4. The downward arrows near zones 1 and 2 show the desorption of B and C. Component A, on the other hand, moves with the liquid through zone 4 and out the raffinate stream. Any component A that is not removed in the raffinate stream is adsorbed in zone 5 and recycled back into zone 4 by the solid phase. Any component A that is adsorbed in zone 4 is removed in zone 3, indicated by the downward arrow.

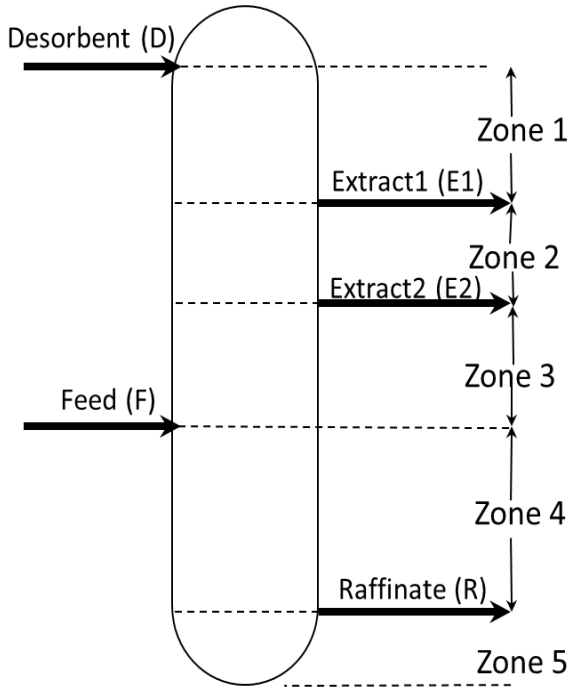

FIGURE 2.7. A FIVE-ZONE SMB UNIT FOR TERNARY SEPARATION.

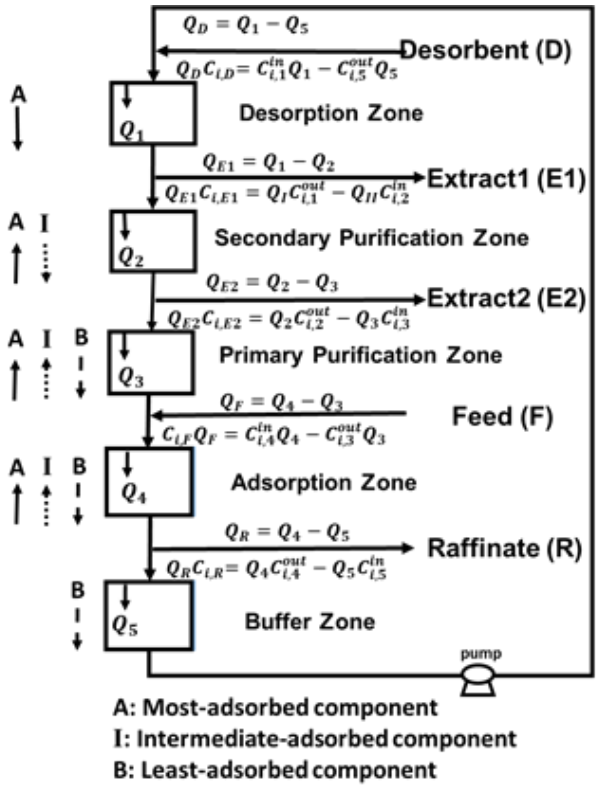

FIGURE 2.8. AN ILLUSTRATION OF ZONE FLOW RATE BALANCES IN A 5-ZONE SMB.

2.3. Literature Review of SMB Applications

As described in Section 2.1, Broughton and Gerhold introduced the SMB concept, as a practical improvement of a TMB unit[15] in 1961. The first commercial application was Molex process[30] for the removal of linear paraffins from the branched-chain and cyclic isomers. Later, UOP commercialized the Parex process[31], which produces high purity p-xylene from C8 aromatics.

Another important application is the separation of sugars. The separation of fructose and glucose is one of the largest applications of chromatography. Following the pioneering work of Barker and Critcher[32], there are a number of reported studies for sugar applications[33-36]. UOP developed the Sarex process[37] to separate fructose from sucrose and other sugars. Industries also apply SMBs to separate other sugars, such as monosaccharides like xylose or arabinose and disaccharides[38].

The applications of SMB later expanded to the pharmaceutical and fine chemical industries. In the early 1990s, Negawa and Shoji first applied system to enantiomer separations[39,40]. Since then, the SMB technology finds growing applications to the separation of chiral drugs and racemic mixtures[41-46].

Within five years of the first chiral separation demonstrations, UCB Pharma, in 1997, installed a multi-ton SMB unit for large-scale manufacturing[47]. Further in 2002, Lundbeck's single enantiomer drug Lexapro became the first drug approved by the US Food and Drug Administration's to be manufactured using SMB technology[48]. Since up to early 1990s, the pharmaceutical industrials starts to apply the SMB technology in chiral separation. It needs for rapid design methodologies, and fundamental understanding of the process. From early 1990s to around 2000, the first industrial example of enantiomer separations was installed for large-scale manufacturing in UCB Pharma[47, 49]. From 2000 till present, major pharma companies started using the SMB units for chiral separation[3, 48, 50], and it needs for optimization tools and robust control algorithms.

2.4. Literature Review of SMB Operational Modes

The successful applications of SMB extensively inspire the interest on the development of new theories, modeling methodologies and new operation modes in the industrial and research community. The latest review[4] details the most recent SMB operational modes, applications and developments. The literature contains a number of proposed modifications to SMB operations, which we refer to as operational modes.

In our work, we focus particularly from a practical point of view on several operational modes applied to the existing SMB units by switching ports or adjusting control valves. Specifically, this study considers:

(1) Varicol—switching the inlet and outlet ports asynchronously[51-57]
(2) PowerFeed or Partial Feeding—varying feed flow rates[51,58-62]
(3) ModiCon—varying feed concentrations[51,63]
(4) Combinations of the previous three operational modes[51,64,65]

Table 2.1 summarizes the relevant literature and compares the scopes of previous studies with the present work. We will discuss these operational modes in chapters 3 to 6 in details. In additionally, there are we many other relevant SMB operational modes we did not investigated in our study, such as the ones of variable external streams, namely, Partial-Feed[61,62], Partial-Discard[66], Partial-port-closing[67] and Outlet Swing Stream-SMB[68].

Table 2.1. A summary of the relevant literature and comparison of **THE SCOPES OF PREVIOUS STUDIES WITH THE PRESENT WORK.**

Reference	***Sep. system***	***Comp.***	***Operational mode***	***Experimental or Modeling***	***SMB Design Method***	***Opt. Method***	***Program***	***Isotherm form***
Zhang, et al[56]	Enantio-separation of racemic pindolol	Binary	Varicol	Both	Included in opt.	Non-dominated sorting genetic algorithm with jumping genes	rigorous model	Bi-Langmuir
Schramm, et al[63,64]	Cyclopentanone & Cycloheptanone	Binary	PowerFeed, ModiCon	Both	--	Control algorithm	DIVA	Langmuir
Zang and Wankat[65]	Dextran T6&Raffinose	Binary	Variable flow rate operation	Modeling	Triangle Theory	Two-layer Nelder-Mead	Aspen Chromatography	Langmuir
	Enantiomers							Dual-site Langmuir
Zhang, et al[51]	Chiral separation	Binary	Varicol, PowerFeed, ModiCon	Modeling	Included in opt.	Multi-objective Genetic Algotithm	--	Langmuir
Pedeferri, et al[69]	Tröger's base	Binary	An open-loop SMB	Experimental	Triangle Theory	--	--	Langmuir
Katsuo and Mazzotti[70-72]	Tröger's base	Binary	Intermittent-SMB	Experimental	Triangle Theory	--	--	Linear and Bi-Langmuir
Amanullah and Mazzotti[73]	Tröger's base	Binary	Chromatography-crystallization	Modeling	Triangle Theory	Multi-objective NSGA	--	Bi-Langmuir
		Binary	3-zone, I-SMB & Outlet	Both		Simultaneous optimization-	AMPL	Linear

Sreedhar and Kawajiri[74]	Glucose and fructose		stream swing-partial feed hybrid operation		Included in opt	model correction	+IPOPT	
Wu and Wang, et al[75]	Amino Acid (tryptophan and phenylalanine)	Binary	SMB	Both	Standing Wave Design (SWD)	Column configuration via exhaustive search	VERSE	Linear
N-H Linda Wang, et al[23]	Insulin Purification	Ternary	Tandem SMB	Both	SWD	Multi-loop iterative search	VERSE	Linear
Chin and Wang[76]	Sugar Isolation from Impurities	Multi-Comp.	5-zone SMB	Both	SWD	Iterative methods	VERSE	Linear
H. Khan, et al[26]	Amino Acid	Ternary	5-zone SMB	Modeling	Triangle Theory & Safety margin	--	Aspen Chromatography	Linear
Jo, et al [19]	Amino Acid	Ternary	5-zone & 2-zone SMB	Modeling	Safety margin	Genetic Algorithm	Aspen Chromatography	Linear
This work	Tröger's base	Binary	Varicol, PowerFeed, ModiCon & Combinations	Modeling	Triangle Theory	Multi-objective & Grid searching	Aspen Chromatography	Bi-Langmuir
	Amino Acid	Ternary						Linear

3. SMB Modeling for Two Separation Processes

3.1. Theoretical and Mathematical Method for the Modeling of SMB Units

3.1.1. Flow Rates Constraints of the Design

The design problem of a SMB consists in setting the flow rate in each section to obtain the desired separation. Some constraints have to be met if one wants to recover the less-adsorbed component B in the raffinate and the most-adsorbed component A in the extract. These constraints are expressed in terms of the net fluxes of components in each zone (ratio of molar flow rates of a species transported by the liquid phase and by the solid phase). As illustrated in Figure2.4, in zone 1, both species must move upward; in sections 2 and 3 the light species must move upward. The net flux of the most-adsorbed component must be downward: in zone 4, the net flux of both species has to be downward[18], that is,

$$\frac{Q_1 C_{A,1}}{Q_S q_{A,1}} > 1 \tag{3.1}$$

$$\frac{Q_2 C_{A,2}}{Q_S q_{A,2}} > 1 \quad \text{and} \quad \frac{Q_2 C_{B,2}}{Q_S q_{B,2}} > 1 \tag{3.2}$$

$$\frac{Q_3 C_{A,3}}{Q_S q_{A,3}} > 1 \quad \text{and} \quad \frac{Q_3 C_{B,3}}{Q_S q_{B,3}} > 1 \tag{3.3}$$

$$\frac{Q_1 C_{A,1}}{Q_S q_{A,1}} > 1 \tag{3.4}$$

3.1.2. Mass Transfer and Differential Equations

In simulating a 4-zone SMB model in Aspen Chromatography, we use a countercurrent model, in which solid particles flow counter-currently to the direction of the fluid flow along the column. We assume the linear driving force (LDF) model[77], where the axial dispersion flow for the bulk fluid phase is considered and the mass transfer rate in solid phase is taken as proportional to the concentration difference from the equilibrium. The mass balance equation and mass transfer equation are as follows:

Mass balance equation:

$$\frac{\partial C_i}{\partial t} + \frac{(1-\varepsilon^*)}{\varepsilon^*}\frac{\partial q_i}{\partial t} + u\frac{\partial C_i}{\partial z} = D_L\frac{\partial^2 C_i}{\partial z^2} \quad \textbf{(3.5)}$$

Mass transfer equation:

$$\frac{\partial q_i}{\partial t} = k_i(q_i^* - q_i) \quad \textbf{(3.6)}$$

where $C_i$and q_i are solute concentrations of the liquid and solid phases, respectively, u the superficial velocity of the fluid, ε^* the overall bed voidage , $D_L$the axial dispersion coefficient , k_f the linear lumped mass transfer coefficient and q_i^* represents the adsorbed phase concentration at equilibrium with the liquid phase.

We add the following boundary and initial conditions:

$$\text{At t} = 0\text{: } 0 \le \text{z} \le \text{L}, C_i = 0 \quad \textbf{(3.7)}$$

$$\text{At t} > 0 \text{ and } z = 0\text{: } \varepsilon^* u(C - C_0) = D_L\frac{\partial C_i}{\partial z} \quad \textbf{(3.8)}$$

$$\text{At z} = \text{L: } \frac{\partial C_i}{\partial z} = 0 \quad \textbf{(3.9)}$$

3.1.3. Core Assumptions and Design Equations

Using Aspen Chromatography, we model a SMB process by applying the dynamic models of the single chromatographic columns while considering the periodic port switching. We specify the operating conditions through the use of the m-parameters defined in the triangle theory[77,78,]. These parameters define the relationship between the net flow rate of liquid and the net "flow" of solid adsorbent in a bed. The ratio of net liquid to solid flow in each zone j (j=1 to 4 or 5) is:

$$m_j = \frac{\text{the net flow rate of liquid}}{\text{the flow rate of adsorbent}} = \frac{Q_j t_{sw} - V_{bed}\mathcal{E} - V_j^D}{V_{bed}(1-\varepsilon)} \quad (3.10)$$

The liquid flow through zone j with liquid flow rate Q_j over a switching time interval t_{sw} is $Q_j t_{sw}$. However, since the zone shifts by one bed per switching interval, we need to subtract the liquid holdup in the bed that was left behind from the total liquid flow. The holdup is $V_{bed}\mathcal{E} +$

V_j^D where V_{bed} is the adsorbent bed volume, ε is the bed voidage, and the dead volume is V_j^D so the *net liquid flow* is $Q_j t_{sw} - V_{bed}\varepsilon - V_j^D$.

The solid "flow" is simply the volume of solid in each bed, specifically, $V_{bed}(1-\varepsilon)$. This is because in each switching interval, the ports move past one bed worth of adsorbent.

The net mass flow rate ratios m_j are the key design variables for the SMB and any operational modes. This is because a key to determining the chromatographic separation performance is the volume of liquid which contacts a given volume of the adsorbent; m-value represents this important design variable as a multiple of the solid flow rate. In addition, for a given SMB system, the switching time is constant, which means that the difference between consecutive m-values is proportional to the inlet or outlet flow between the zones. For example, $m_3 - m_2 = Q_F\left(\frac{t_{sw}}{V_{bed}(1-\varepsilon)}\right)$, represents the handling capacity of Q_F the unit could afford. We want to enlarge m_3 value but reduce m_2 value in our study .This means that by specifying all four m values (along with a maximum pressure drop), we have set all the flow rates in the system. We will evaluate m_2 and m_3 values for each operational mode, which lead to complete separation region plots. In the process, m_4 refers to $Q_{recycle}$; m_1 is related to $Q_{recycle} + Q_D$.

We cannot neglect the dead volume of the SMB column, because the column volume is rather small in our selected separation system and the dead volume is of the same order of magnitude. We consider the effect of the dead volume in our binary separation in order to evaluate the separation performance more accurately. We do not include dead volume in the ternary separation.

A set of flow rate ratios for each zone is sufficient to calculate the operating conditions[70,71] for the SMB unit given eqs (3.11) to (3.13) as well as the mass balance equations in Figure 2.4. Eq 3.11 is a simple rearrangement of eq 3.10, while eq 3.12 relates the pressure drop to the flow rates in the column. Eq 3.13 ensures that the system will be operating at the maximum pressure drop; this gives a consistent basis for comparison between different operating conditions.

$$Q_j = \frac{V_{bed}(1-\varepsilon) * m_j + V_{bed}\varepsilon + V_j^D}{t_{sw}} \quad \textbf{(3.11)}$$

$$\frac{\Delta P_j}{L} = \frac{-150\mu(1-\varepsilon)^2}{(2r_p\psi)^2\varepsilon^3}\frac{Q_j}{S} \quad \textbf{(3.12)}$$

$$t_{sw} \geq \frac{\phi L^2}{\Delta P_{max}} \sum_{j=1}^{j=4} n_j(m_j(1-\varepsilon)+\varepsilon) \quad \textbf{(3.13)}$$

In the equations, ΔP_j =pressure drop in each zone; n_j=bed number in each zone; l=length of each bed; ΔP_{max}= maximum pressure drop through the column; ϕ = pressure drop coefficient; S = cross-sectional area of the bed; ε = overall bed voidage; μ = fluid viscosity; r_p = particle radius; $and\ \psi$ = particle shape factor. For turbulent flows, the Ergun equation is a better correlation for pressure drop; in this case, the difference in pressure drop estimates by the Carman Kozeny and Ergun equations is very small (less than 0.5%). Therefore, we employ the simpler of the two.

We use the convection with dispersion based on Peclet number as a material balance assumption. This assumption evaluates the axial dispersion coefficient as a function of the Peclet number based on the column length:

$$D_L = \frac{uL}{Pe\ \varepsilon_i} \quad (3.14)$$

where D_L= axial dispersion coefficient, u=superficial velocity of the fluid, L=column length, Pe=particle Peclet number, ε_i =interparticle voidage.

3.1.4. Isotherm Approach

We use the bi-Langmuir adsorption isotherm [71,72] at 23°C:

$$C_i^* = \frac{a_{i,1}C_i}{1+\sum b_{i,1}C_i} + \frac{a_{i,2}C_i}{1+\sum b_{i,2}C_i}\ (i = A, B) \quad \textbf{(3.15)}$$

$$H_A = a_{A,1} + a_{A,2} \quad \textbf{(3.16)}$$

$$H_B = a_{B,1} + a_{B,2} \quad \textbf{(3.17)}$$

In the equations, C_i^* is the adsorbed phase concentration of component i in equilibrium with the mobile phase. H_A and H_B are the Henry's constants of two components. $a_{i,1}, a_{i,2}, b_{i,1}, b_{i,2}$ are the bi-Langmuir isotherm parameters for component i.

3.2. SMB Modeling for Binary Separation of Tröger's Base

This study investigates the performance of different SMB operational modes for the binary separation of chiral enantiomers of Tröger's base[70-73]. We model a six-bed SMB column as a basic four-zone SMB model specified in section 2.2.2. We refer to the binary components (±)-2, 8-dimethyl-6H, 12H-5, 11-methanodibenzo [b,f] [1,5] diazocine (TB+ and TB-) as components A and B in all the equations and models. We use a feed concentration of 0.5 g/l for each component in the basic SMB model, and the feed contains 50% component A and 50% component B by weight. This process uses ChiralPak AD as the chiral stationary phase and ethanol as the mobile phase. Table 3.1 lists the column and isotherm parameters for this binary separation process[70-72].

We apply the extra dead volume values from Mazzotti's paper[71] as Figure 2.6 shows. In our model, we consider that all dead volumes, including the bed-head and bed-line dead volumes, are identical tubing volumes. We give a name of the total dead volume as V_j^D. We assume an effective dead volume with fixed pipe diameter and pipe length. Through our modeling experience, changing pipe diameters and lengths does not affect the performances much as long as the total dead volume between beds is fixed in this system

TABLE 3.1. COLUMN AND ISOTHERM PARAMETERS FOR TRÖGER'S BASE SEPARATION.

Column Configuration		1-2-2-1 (Figure 2.5)	
Column Length (L)	cm	15	
Column Diameter (Dia)	cm	0.46	
Bed volume per column (V_{bed})	cm^3	2.493	
Bed voidage Ɛ	m^3 void /m^3	0.68	
Adsorbent particle diameter	micron	10	
Particle Shape factor ψ	--	0.1475	
Dead Volume per Zone	ml	0.23	
Pressure Drop Coefficient ϕ	bar min/cm^2	0.1	
Bi-Langmuir isotherm	Dual-Site	A (TB+)	B (TB-)
a_{i1}	--	3.99	1.56
b_{i1}	L/g	0.0107	0.0132
a_{i2}	--	0.986	0.304
b_{i2}	L/g	0.601	0.136
k_i	1/s	1.81	2.96
Henry's constant	--	4.976	1.864
Peclet number	--	500	500
Feed concentration	g/L	0.5	0.5
Axial dispersion coefficient	cm^2/min	Chung and Wen[79]	

Table 3.1 shows the resulting operating conditions relating to the flow rates in the basic SMB model. We simulate the basic SMB model and several operational modes using Aspen Chromatography. For the basic SMB model, the starting point is based on the experimental data from Mazzotti's paper[71]. We validate this basic SMB model with their experimental results, and list our results in column 3 of Table 3.5. This basic SMB model is the starting point and comparison basis for all the investigated operational modes. We use the quadratic upwind differencing scheme (QUDS) with 40 element nodes as a discretization method. QUDS is a linear finite element scheme that gives a good fit of model predictions to experimental results[71]. For this binary separation, QUDS method has very good accuracy and little numerical dispersion, and is well suited to time integration. We integrate the resulting ordinary differential equations using Gear method with a variable time step size (0.1 min initial step size, 0.1 to 0.5

min step size range and 0.5 step reduction factor) and the integration error tolerance set to the value of 10^{-4} in Aspen Chromatography.

TABLE 3.2. OPERATING CONDITIONS RELATING TO FLOW RATES IN THE BASIC 4-ZONE SMB MODEL FOR BINARY TRÖGER'S BASE SEPARATION.

Flow rate ratio	--	m_I	6.54
		m_{II}	1.75
		m_{III}	4.785
		m_{IV}	1.35
Zone flow rates	ml/min	Q_I	1.12
		Q_{II}	0.52
		Q_{III}	0.9
		Q_{IV}	0.47
Inlet and outlet flow rates	ml/min	Q_D	0.65
		Q_E	0.6
		Q_F	0.38
		Q_R	0.43
Recycle flow rate	ml/min	$Q_{Recycle}$	0.47
Switching time	min	t_{sw}	6.38

3.3. SMB Modeling for Ternary Separation of Amino Acid Mixture

We investigate the ternary separation of phenylalanine (the most-adsorbed component A), tryptophan (the intermediate-adsorbed component I) and methionine (the least-adsorbed component B)[25,26,28]. This process uses poly-4 vinyl pyridine (PVP) resin as the adsorbent. In this system, we implement a basic 5-zone SMB with an eight-bed column with configuration χ = (1-2-1-2-2) in Aspen Chromatography. We use the biased upwind differencing scheme (BUDS) with 40 element nodes as a discretization method. BUDS is a linear finite element scheme, which gives model predictions that fit with the literature results[26] well. For this ternary separation, BUDS gives good accuracy for small node counts, and good stability with no oscillations. Tables 3.3 and 3.4 include column configuration and operating conditions for the ternary separation[26]. We choose feasible operating conditions but without considering dead volume in the model based on Khan and Younas[26].

TABLE 3.3. COLUMN CONFIGURATION AND ISOTHERM PARAMETERS FOR TERNARY SEPARATION.

Column Configuration		1-2-1-2-2		
Column Length (L)	cm	25		
Column Diameter	cm	2.5		
Bed volume per	cm^3	122.73		
Internal bed voidage	m^3 void	0.346		
External bed voidage	m^3 void	0.55		
Adsorbent particle	cm	0.0362		
Mobile phase density	g/cm^3	0.996		
Mobile phase viscosity	cp	0.89		
Amino Acids		Methionine (B)	Phenylalanine(A)	Tryptophan (I)
Feed concentration	g/L	0.5	0.5	0.5
Mass transfer	cm/min	0.0518	0.0171	0.0157
Linear isotherm	L/L	0.3537	11.771	1.6015
Axial dispersion	cm^2/min	Chung and Wen[79]		

TABLE 3.4. OPERATING CONDITIONS IN THE BASIC 5-ZONE SMB MODEL FOR TERNARY SEPARATION.

Flow rate ratio	--	$\boldsymbol{m_I}$	18.83
		m_{II}	2.56
		m_{III}	0.56
		m_{IV}	1.001
		m_V	0.22
Zone flow rates	cm^3/min	Q_I	48.742
		Q_{II}	11.384
		Q_{III}	6.792
		Q_{IV}	7.804
		Q_V	6.011
Inlet and outlet flow rates	cm^3/min	Q_D	42.731
		Q_{E1}	37.358
		Q_{E2}	4.592
		Q_F	1.013
		Q_R	1.793
Recycle flow rate	cm^3/min	$Q_{Recycle}$	6.011
Switching time	min	t_{sw}	15.73

3.4. Performance Evaluation

3.4.1. Performance Indices

Since we consider the dynamic state in all the models, the results are recorded once the system reaches a cyclic steady state. We determine the steady state by finding the time at which the average of the performance indices over one step becomes constant. The steady state is attained after 10 cycles (each cycle contains 6 switching time rounds). Our simulation time is therefore 382.8 min.

We define a number of performance indices for both binary and ternary separations in our SMB chromatography columns[71]. For the binary separation, we have the extract outlet stream containing the most-adsorbed component A, and the raffinate outlet stream containing the least-adsorbed component B. For the ternary separation, we have the extract1 product containing the most-adsorbed component A, the raffinate product containing the least-adsorbed component B, and we obtain mostly the intermediate-adsorbed component I in the extract2 stream. For simplicity, we define the performance index equations in terms of the binary separation.

Purity ($\overline{Pur}$) and recovery ($\overline{Rec}$) of component A in the extract (E) stream and of component B in the raffinate (R) stream through one complete cycle time after achieving the steady state. $\bar{C}_A^E, \bar{C}_B^E, \bar{C}_A^R$ and $\bar{C}_B^R$ represent the average concentrations of components A and B in the extract and raffinate during one switching interval.

$$\overline{Pur}_A = \overline{Pur}_A^E = \frac{\bar{C}_A^E}{\bar{C}_A^E + \bar{C}_B^E} \tag{3.18}$$

$$\overline{Rec}_A = \overline{Rec}_A^E = \frac{Q_E \bar{C}_A^E}{Q_F \bar{C}_A^F} \tag{3.19}$$

$$\overline{Pur}_B = \overline{Pur}_B^R = \frac{\bar{C}_B^R}{\bar{C}_A^R + \bar{C}_B^R} \tag{3.20}$$

$$\overline{Rec}_B = \overline{Rec}_B^R = \frac{Q_R \bar{C}_B^R}{Q_F \bar{C}_B^F} \tag{3.21}$$

Productivity ($\overline{Pro}$) of both components A and B through one switching interval after steady state, which represents the total amount of recovered products per unit volume per unit time. In eq 3.22, n is the bed number through the column, and V_{bed} is the adsorbent bed volume.

$$\overline{Pro} = \frac{Q_E C_A^E + Q_R C_B^R}{n V_{bed}} \tag{3.22}$$

Desorbent consumption ($\overline{DC}$) represents the amounts of desorbent needed per unit of pure product A and B received from extract and raffinate:

$$\overline{DC} = \frac{Q_D (C_A^F + C_B^F)}{Q_F (\overline{Rec}_A C_A^F + \overline{Rec}_B C_B^F)} \tag{3.23}$$

3.4.2. Simulation Results with Fixed m Values for Binary and Ternary Separations

Column 3 of Table 3.5 and of Table 3.6 summarizes the simulation results of the 4-zone SMB for the binary separation and the 5-zone SMB for the ternary separation, including all the performance indices defined in equations 3.18 through 3.23. We note that the purity of component B and the recovery of component A in the basic SMB models for the binary separation (the purity of component I and the recovery of component A for the ternary separation) are relatively low, so our goal is to improve these two performance indices, while keeping the other purity and recovery results above acceptable levels (larger than 99%).

Columns 4 to 8 of Tables 3.5 and 3.6 include the corresponding performance results for several operational modes applied to the binary and ternary separations that we will discuss in the subsequent sections. For both binary and ternary separations, all of the investigated operational modes improve the product purity, recovery, total productivity, and solvent consumption over the basic SMB cases.

TABLE 3.5. A COMPARISON OF THE PERFORMANCE OF THE BASIC 4-ZONE SMB AND SEVERAL OPERATIONAL MODES FOR THE BINARY SEPARATION OF TRÖGER'S BASE ENANTIOMERS.

1. Performance Parameter	2. Unit	3. Basic SMB	4. Varicol	5. PowerFeed (PF)	6. ModiCon (MC)	7. PF&MC	8. V&PF&MC
$\overline{Pur}_A$	%	99.97	97.29	99.99	99.96	99.98	100
$\overline{Pur}_B$	%	**92.74**	99.60	96.66	98.84	99.30	99.28
$\overline{Rec}_A$	%	**89.23**	98.54	90.38	97.59	98.43	98.68
$\overline{Rec}_B$	%	99.99	93.57	100	100	99.88	99.74
$\overline{Pro}$	g/l/h	1.442	1.464	1.453	1.506	1.512	1.512
$\overline{SC}$	l/g	2.864	2.822	2.844	2.743	2.734	2.732

TABLE 3.6. A COMPARISON OF THE PERFORMANCE OF THE BASIC 5-ZONE SMB AND SEVERAL OPERATIONAL MODES FOR THE TERNARY SEPARATION OF AMINO ACID MIXTURES.

1. Performance Parameter	2. Unit	3. Basic SMB	4. Varicol	5. PowerFeed (PF)	6. ModiCon (MC)	7. PF&MC	8. V&PF&MC
$\overline{Pur}_A$	%	99.95	98.17	99.97	99.97	99.98	97.89
$\overline{Pur}_I$	%	92.57	91.65	93.04	93.08	93.45	93.05
$\overline{Pur}_B$	%	99.79	100	99.93	99.88	99.98	100
$\overline{Rec}_A$	%	80.54	85.28	89.68	88.72	91.12	91.42
$\overline{Rec}_I$	%	100	99.85	99.54	99.98	99.76	99.45
$\overline{Rec}_B$	%	100	100	98.76	99.23	99.18	100
$\overline{Pro}$	g/l/hr	0.086	0.0882	0.0891	0.0891	0.0898	0.090
$\overline{SC}$	ml/g	4.620	4.545	4.500	4.501	4.468	4.456

3.4.3. Column Concentration Profiles

We record the dynamic concentration profile for each simulation run after its steady state. The red and green curves represent the concentrations of component A and B through the column. We use the SMB concentration profile to compare with other SMB operational modes. Basically, we use these left and right axial gaps between two components, and the overlapped area in the shadow, as shown in Figure 3.1, in conjunction with product purity and recovery to describe how complete the separation is.

Figure 3.1 also displays the inlet and outlet ports switching in the basic SMB model. At t=0, all the inlet and outlet ports are in their original position, and at t=t_{sw}, all of them (Desorbent, Extract, Feed and Raffinate) move to the next bed at the same time.

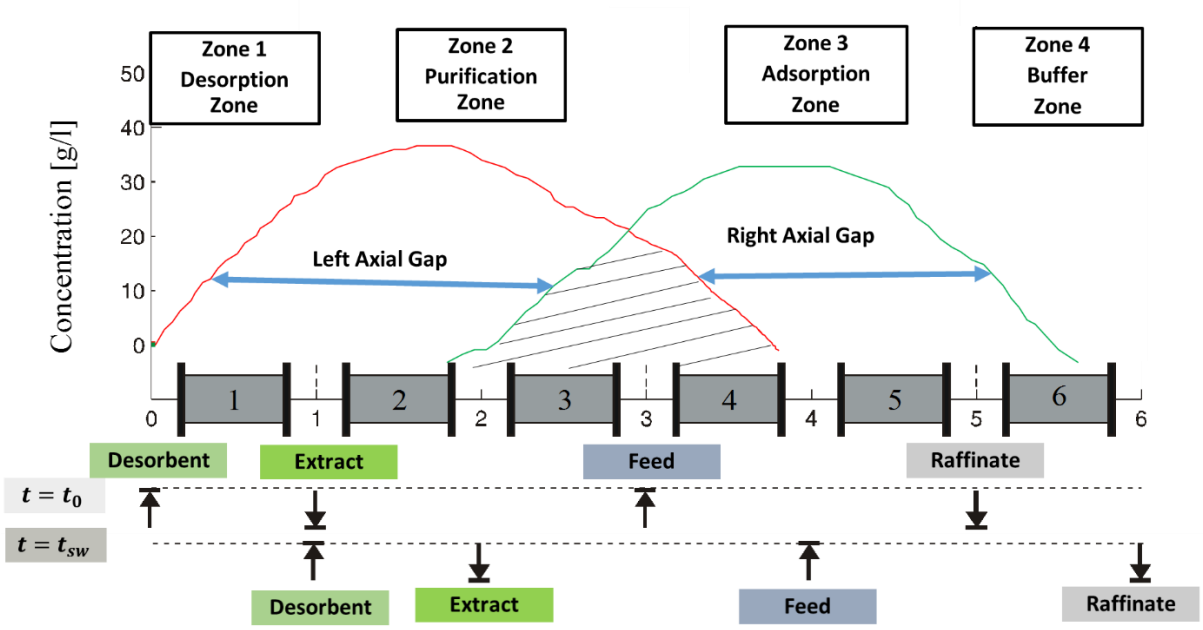

FIGURE 3.1. THE DYNAMIC COLUMN CONCENTRATION PROFILE IN THE BASIC SMB COLUMN.

3.5. Separation Region and Pareto Plots for Varied m Values Systems

3.5.1. Separation Region Plots

There are two families of analytical design methods: triangle theory and standing wave design (SWD), for predicting the operating conditions of the SMB units. The triangle theory[77,78] predicts

a region of complete separation based on the ratios of net liquid to solid flow in various separation zones for an ideal true moving bed (TMB) separation unit under certain assumptions, for example, without mass-transfer limitations. Another design method, standing wave design[21,23,75] (SWD), takes the mass transfer limitations into account, but retains the TMB assumptions. However, once the TMB assumption is violated as in the case of our operational modes, neither design method is capable of defining the separation region with analytic functions of the system variables. Since the separation regions of the operational modes (as shown in Figure 5.18), especially the ModiCon and the combined operational modes, differ significantly from the base case, the operational mode performance is not captured entirely by m-values, which are the primary output of the SWD and triangle theory. Therefore, we must rely on a grid of detailed simulation results to describe the separation region, as we shall show below in Figures 5.18 and 5.28.

To construct the separation region plots, we run simulations in a grid pattern over a region in the vicinity of the optimum operating conditions. These plots clearly demonstrate the effect of the operational modes on the region of complete separation, as well as the optimum operating point. Based on the previous studies, such as Mazzotti[71], we have extended the approach in the following ways:

(1) Consider both product purity and recovery results in the separation region plots.
(2) Include multiple separation performance regions to allow some visualization of robustness.
(3) Provide a clear picture of the region around the optimum point of their separation performance by applying different SMB operational modes.

Figure 3.2a demonstrates how to identify the optimum operating region on a m_2-m_3 plot. The inner blue rectangle represents the region spanned by our grid of simulation results. The optimum operating conditions correspond to complete separation with the maximum feed flow rate and minimum desorbent consumption. Because the difference between m_2 and m_3 is precisely the feed flow rate, we want to find the point where this difference is greatest, i.e. is farthest from the $m_2=m_3$ diagonal.

Figure 3.2b illustrates the separation region plot for the basic SMB model in terms of their product purity and recovery results. We divide the simulated purity and recovery into four different value regions. These include: (1) both product purities and product recoveries are larger than 99% in the pink region; (2) product recovery values from 98% to 99% with A&B purities $\geq$ 99% are marked in blue; (3) both purity and recovery values larger than 98% but lower than 99% by gray region; and (4) all the values lower than 98% put in yellow region, as shown in this symbol box. The labeled point on the graph represents the m_2-m_3 pair with maximum productivity that still satisfies the high purity (99%) and high recovery (99%) constraints for the basic SMB model.

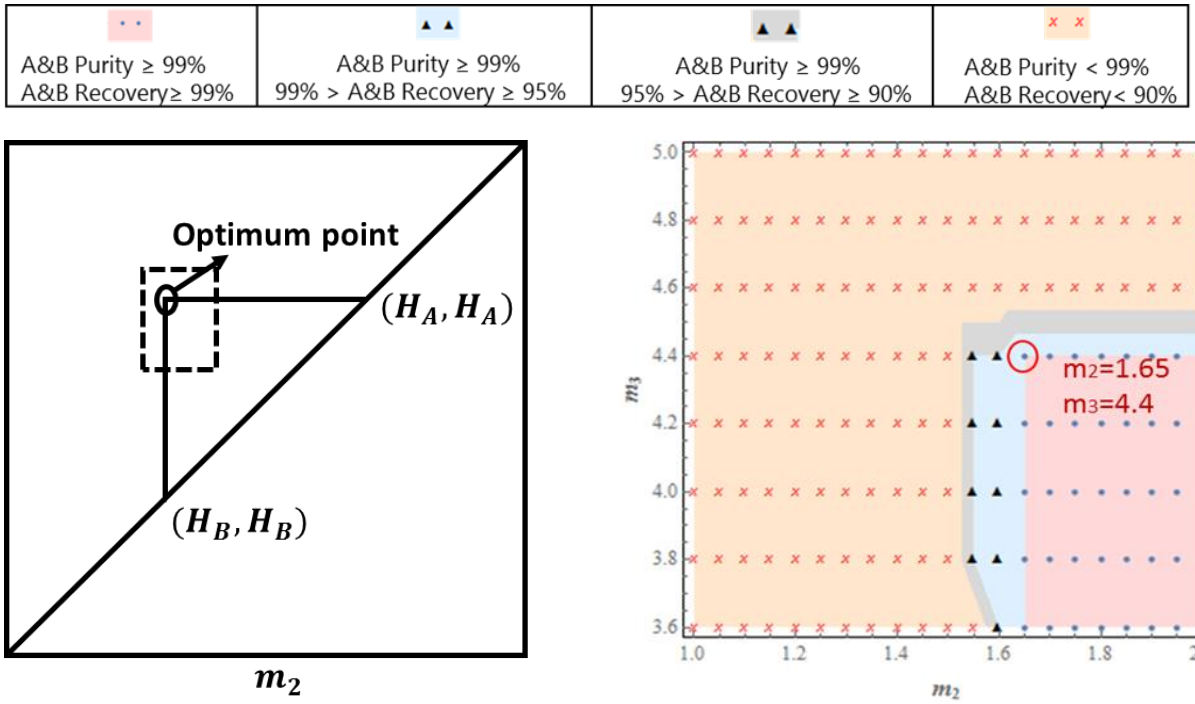

a. The separation region on an m_2-m_3 plot with the optimum point.

b. The exampled separation region plot for the basic SMB model.

FIGURE 3.2. AN ILLUSTRATION OF SEPARATION REGION ON AN M_2-M_3 PLOT.

3.5.2. Pareto Plots

The Pareto plot is a common tool for multiobjective optimization, which involves the search for tradeoffs between conflicting performance indices[51, 56, 58, 59, 73, 80, 81]. This means that we cannot improve one performance index without sacrificing the other. In order to simultaneously maximize these two indices (for example, B purity and productivity for the binary separation),

we generate a Pareto plot for all the operational modes and compare their results. Figures 3.3a and b demonstrate how to make a Pareto plot from a separation region plot. Purity and productivity are the two conflicting performance indices we try to maximize. Let us start with Figure 3.2a of the separation region on a m_2-m_3 plot. We divide the dashed inner rectangle box in Figure 3.2a into six different purity regions based on their product purity results, as we adjust the (m_2-m_3) sets. We label the maximum productivity values in the specified sub-regions as points A, B, C, D and E. Figure 3.3b is a converted Pareto plot for the optimization of two conflicting performance indices, purity and productivity, obtained by specifying threshold purities in Figure 3.3a over the $m_2 - m_3$ plot. We obtain Pro_A, Pro_B, Pro_C, Pro_D and Pro_E by optimizing the productivity at point A, B, C, D and E for the specified purity regions. In this way, we can combine the m_2-m_3 plot and the Pareto plots to see the robustness of the effect to the B purity and productivity from the m_2-m_3 sets.

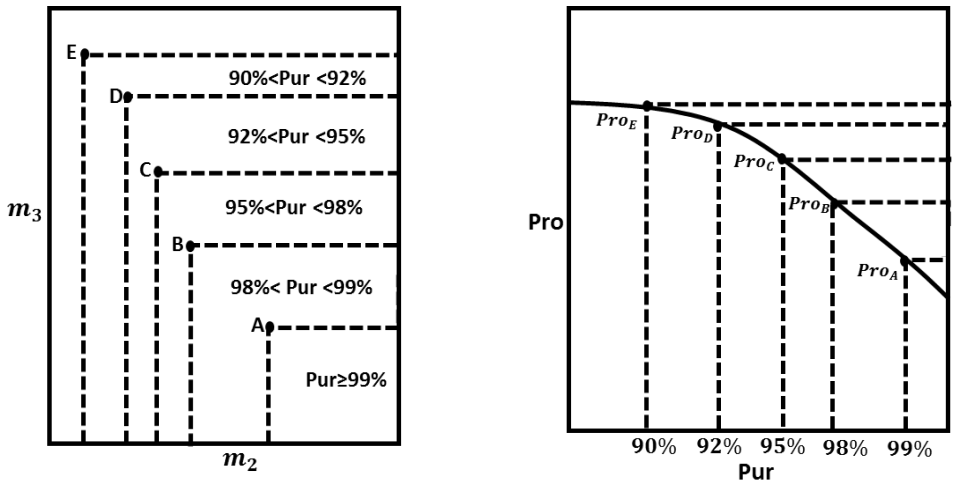

a. The m_2-m_3 plot with different purity regions.

b. The Pareto plot of two conflicting performance indices, purity and productivity.

FIGURE 3.3. THE DEMONSTRATION OF MAKING A PARETO PLOT FROM A SEPARATION REGION PLOT.

4. Introduction to SMB Operational Modes

4.1. VARICOL

The key difference between the Varicol operation[51-57] and the basic SMB is an asynchronous shift of the inlet/outlet ports in a multicolumn system. The zone lengths are varied in time, but the variation of the zone lengths is periodic so that the column recovers its initial position after a whole switching cycle. Thus, the operation is cyclic. The fact that the zone lengths vary over time means that the effective solid flow rate is not a meaningful concept. The change in the relative position of the ports suggests that we cannot say that each zone moves past one bed per switching time as in the case of the basic SMB.

Figure 4.1 illustrates the asynchronous shifting of inlet/outlet ports in a Varicol process within a 6-bed SMB column. We denote the initial column configuration by $\chi = (1\text{-}2\text{-}2\text{-}1)$, and define the asynchronous shifting ratio (AS) as a fraction of the switching time t_{sw} at which the inlet or outlet port moves to its next port position. Specifically, AS_D, AS_E, AS_F and AS_R with values between 0 and 1 represent, respectively, the asynchronous shifting ratios for the desorbent-in port, extract-out port, feed-in port and raffinate-out port. For example, $AS_F = AS_E = 0.5$, together with $AS_D = AS_R = 1$ mean that at $t = 0.5 * t_{sw}$, both feed-in port and extract-out port switch to the next bed, and the column configuration becomes $\chi = (2\text{-}2\text{-}1\text{-}1)$. Then, at $t=t_{sw}$, desorbent-in port and raffinate-out port move to their next beds. At $t=t_{sw}$, all four ports have switched to their next beds, and the column configuration returns to $\chi = (1\text{-}2\text{-}2\text{-}1)$.

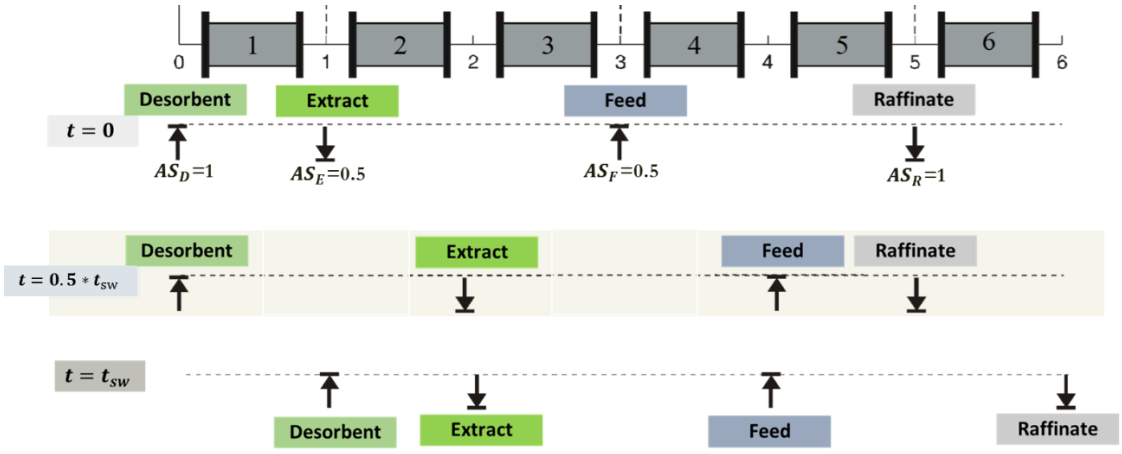

FIGURE 4.1. DIAGRAM OF THE ASYNCHRONOUS SHIFT OF INLET/OUTLET PORTS IN A VARICOL PROCESS.

The effective number of beds is a useful parameter for describing a specific Varicol configuration. This number describes the effect of the asynchronous switching ratios on the length of a given zone. Given in equation form, we calculate the effective numbers of beds, Z_1 to Z_4, for a 4-zone Varicol system by:

$$Z_1 = N_1 + AS_D - AS_E \quad \textbf{(4.1)}$$

$$Z_2 = N_2 + AS_E - AS_F \quad \textbf{(4.2)}$$

$$Z_3 = N_3 + AS_F - AS_R \quad \textbf{(4.3)}$$

$$Z_4 = N_4 + AS_R - AS_D \quad \textbf{(4.4)}$$

where N_1, N_2, N_3 and N_4 are the bed number in the four zones, and Z_1, Z_2, Z_3 and Z_4 are the effective zone lengths.

The derivation of the equation for zone 1 is provided in Figure 4.2 as an example.

The starting point is the base configuration N_1 i.e. the initial number of beds in the zone. When the desorbent port is switched at time AS_D, the length of the zone decreases by the number of beds that the desorbent port moves past. When the extract port is switched at time AS_E, the length of the zone increases by the number of beds that the extract port moves past. Our ports only move by one bed at a time, so the change in the number of beds is always exactly equal to 1. We therefore have two possible scenarios, either the extract port switches before the desorbent port (scenario 1 in Figure 4.2) or the desorbent port switches before the extract port (scenario 2 in Figure 4.2). When they switch at exactly the same time, the two scenarios are equivalent.

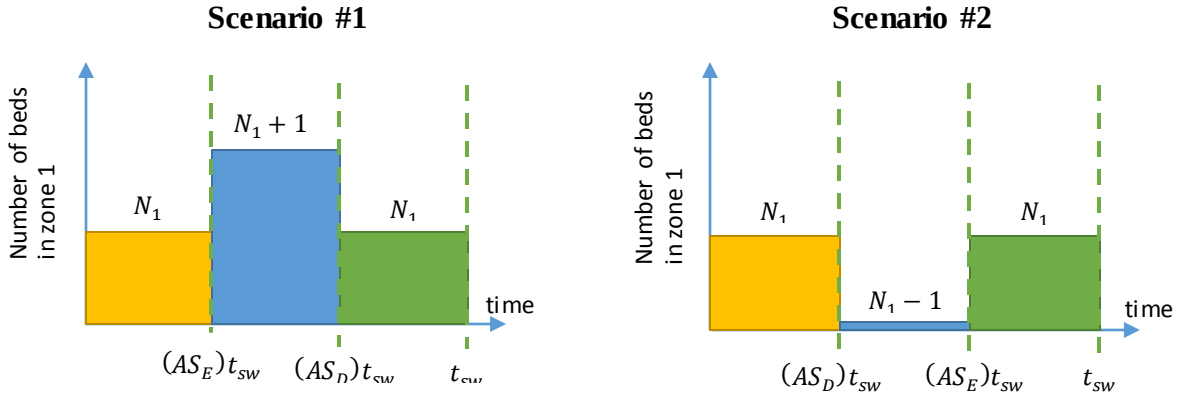

FIGURE 4.2. ILLUSTRATION OF THE EFFECTIVE NUMBER OF BEDS IN THE FIRST ZONE OF A VARICOL SYSTEM.

We find the average number of beds in zone 1 by averaging the number of beds over a switching interval. Since we have three rectangular regions, we can immediately write down the equation for the weighted average:

Scenario #1

$$Z_1 = \frac{N_1(AS_E)(t_{sw}) + (N_1+1)(AS_D - AS_E)(t_{sw}) + N_1(1-AS_D)(t_{sw})}{t_{sw}} \quad \textbf{(4.5)}$$

Scenario #2

$$Z_1 = \frac{N_1(AS_D)(t_{sw}) + (N_1-1)(AS_E - AS_D)(t_{sw}) + N_1(1-AS_E)(t_{sw})}{t_{sw}} \quad \textbf{(4.6)}$$

Simple algebra reveals that both equations reduce to the same expression:

$$Z_1 = N_1 + 1(AS_D) - 1(AS_E) \quad \textbf{(4.7)}$$

We simply name individual Varicol as (Z_1-Z_2- Z_3-Z_4) for the study. We can use these effective bed numbers to evaluate the effect on the product purity and recovery in the evaluation and optimization section for the Varicol.

4.2. PowerFeed and Partial Feeding

Our second operational mode is a modified PowerFeed process[51,58-62]. The difference between our work and the conventional PowerFeed is that we also adjust the recycle flow rates within the switching subintervals, not only the feed flow rates. This is because in some cases, changing the feed flow rates may cause the system to exceed the maximum pressure drop. In our modified PowerFeed operation, we divide the switching time t_{sw} into three subintervals, and vary the feed flow rates (F_1, F_2 and F_3) from one subinterval to the next. In order to satisfy the maximum pressure drop criterion, eq 3.12, we vary the recycled flow rates ($Recy_1$, $Recy_2$ and $Recy_3$) during each operation cycle, as illustrated in Figure 4.3a. Figure 4.3b compares the feed flow rate policies of a basic SMB and the PowerFeed operation in three switching subintervals. We keep the average feed flow rate the same as the feed flow rate in our basic SMB model. In this modified PowerFeed with three switching subintervals, $t = 0 \sim t_1$, $F = F_1$, $Recy = Recy_1$; $t = t_1 \sim t_2$, $F = F_2$, $Recy = Recy_2$; $t = t_2 \sim t_3$, $F = F_3$, $Recy = Recy_3$; $t = t_{sw}$, $F = F_1$, $Recy = Recy_1$.

We note that the Partial Feeding[56,61] is a special case of the PowerFeed operation when the feed stream and the raffinate stream are active only during certain subintervals within a switching time.

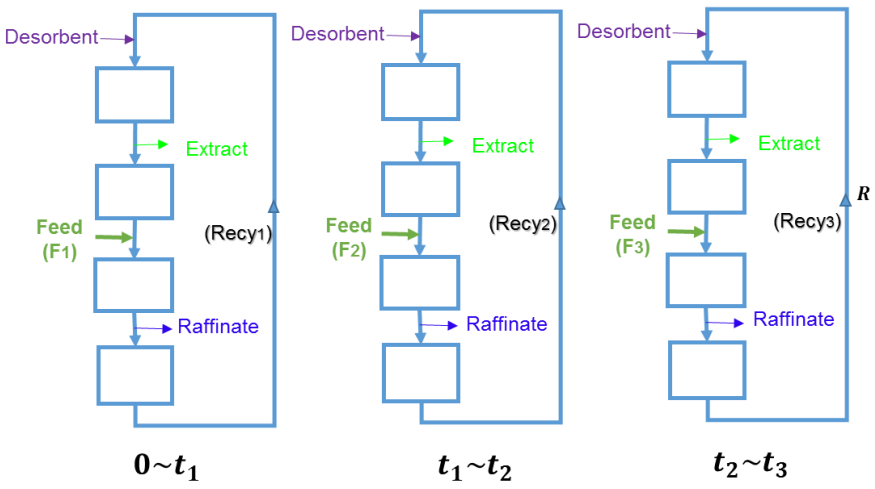

a. An illustration of variable feed and recycle flow rates within subintervals in the modified PowerFeed process.

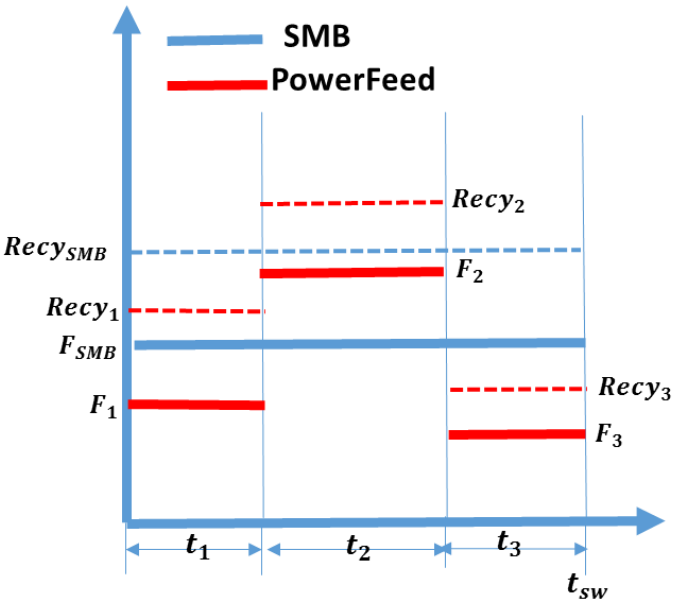

b. A comparison of feed and recycle flow rates policies of the basic SMB and PowerFeed in three switching subintervals.

FIGURE 4.3. THE BASIC PRINCIPLE OF THE POWERFEED IN THREE SWITCHING SUBINTERVALS.

4.3. *ModiCon*

ModiCon[63,64] varies the feed concentration (C_1, C_2, and C_3) of the SMB process within three switching subintervals, as illustrated in Figures 4.4a and b. It keeps the feed flow rate and the column configuration unchanged as the basic SMB model. In this ModiCon with three switching subintervals, $t = 0 \sim t_1$, $C = C_1$; $t = t_1 \sim t_2$, $C = C_2$; $t = t_2 \sim t_3$, $C = C_3$; $t = t_{sw}$, $C = C_1$.

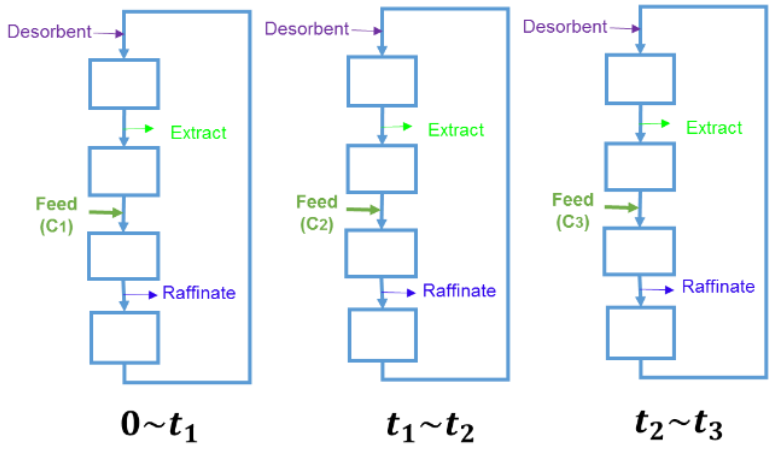

a. An illustration of variable feed concentrations within three subintervals in the ModiCon process.

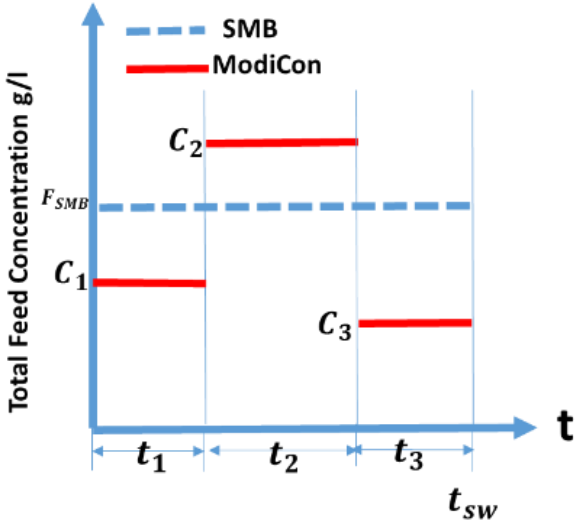

b. A comparison of feed concentration policies of the basic SMB and ModiCon within three switching subintervals.

FIGURE 4.4. THE BASIC PRINCIPLE OF THE MODICON IN THREE SWITCHING SUBINTERVALS.

5. Simulation and Comparison of Operational Modes in SMB Chromatography

This chapter involves the modeling, optimization and evaluation of two bioprocesses, a binary chiral separation of Tröger's base enantiomers and a ternary separation of amino acid mixture. We accomplish the binary separation in a 4-zone column, and the ternary separation in a 5-zone column. We simulate and compare both separation systems under several SMB operational modes including Varicol, PowerFeed and ModiCon, together with their combinations in the following sections 5.1 and 5.2. We compare the simulation results in terms of purities and recoveries of both extract and raffinate products, along with other performance indices. Concentration profiles within the column provide a basis for comparison between operational modes, and give physical insights that explain why a given operational mode performs better or worse than the basic SMB. Our goal is to improve the performance of the basic SMB cases and expand the feasible separation regions of these systems by applying different operational modes. We propose guidelines for improving the performance of the operational modes of the studied systems, and present the improved separation regions where certain purity and recovery thresholds are met for various operational modes.

5.1. Simulation and Optimization of SMB Operational Modes for Binary Separation

5.1.1. Varicol

For the Varicol modeling, all the process and operating conditions are the same as the basic SMB, except for the new asynchronous port switching. We have outlined an effective evaluation procedure using the rigorous models developed in Aspen Chromatography to demonstrate how the Varicol can achieve superior separation performance over the basic SMB. We want to maximize the purity and recovery of the process by changing the effective bed numbers Z_j for each zone. This means that we need to maximize the lengths of the separation regions (zones 2 and 3), while making the non-separating regions as small as possible without causing impurity contamination. Figure 5.1 shows the strategy for the Varicol evaluation.

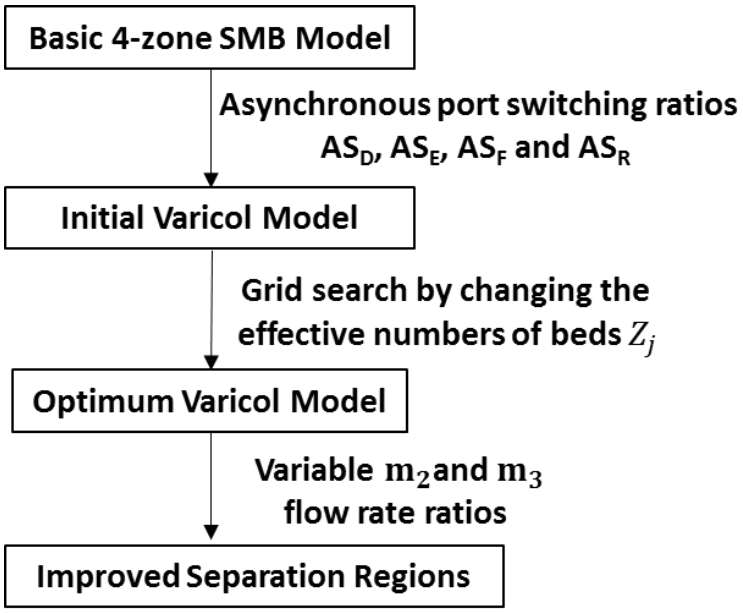

FIGURE 5.1. THE VARICOL EVALUATION AND IMPROVEMENT STEPS.

Figure 5.2 illustrates the general trends by looking at a contour plot of A and B purities in the (Z_1, Z_3) plane at Z_2=2.4. The figure shows that there is no overlap between the regions where both A and B purities exceed 99% or 99.9%. We find that if we improve A purity to 99.9%, then B purity will drop, and this is observed at all Z_2 values. Therefore, we can conclude that the Varicol operational mode is not able to achieve greater than 99% or 99.9% purity in both components at the optimization point. However, it is possible to improve on the base case in some of performance indices significantly, while only slightly sacrificing other separation performance indices.

We see a nice change in the concentration profiles between the Varicol and the basic SMB column in Figure 5.3. The concentration of B (the yellow curve) moves to right a little, so the regions containing components A and B overlap less, that means we are getting a better separation, although the improvement is not that much.

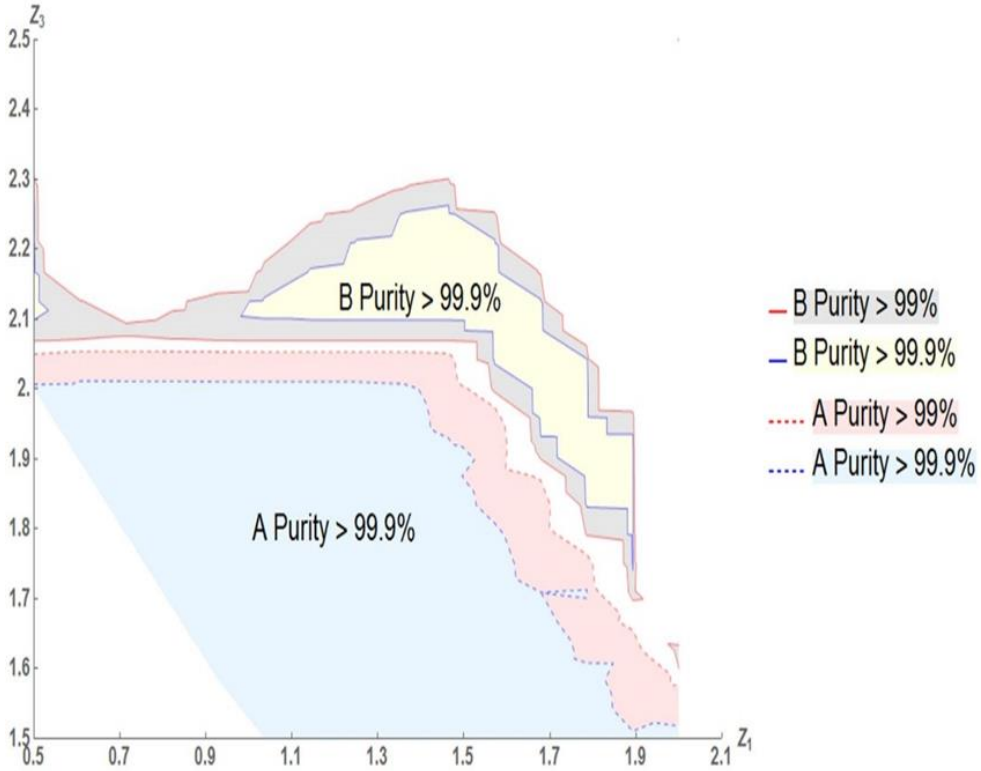

FIGURE 5.2. CONTOUR PLOT OF A AND B PURITIES IN THE (Z_1, Z_3) PLANE WITH Z_2 = 2.4.

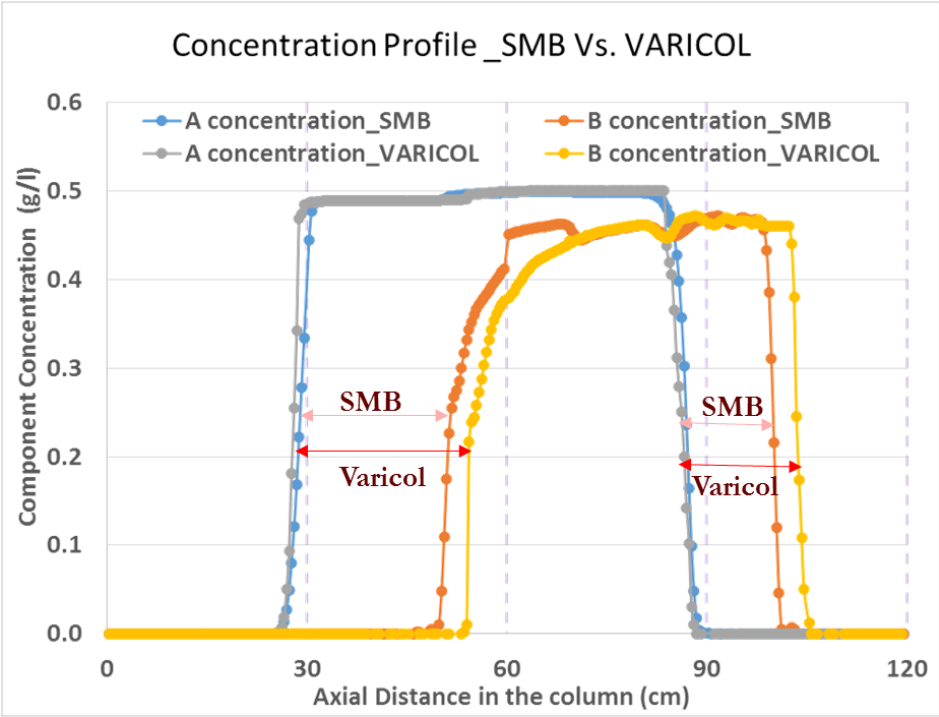

FIGURE 5.3. CONCENTRATION PROFILES BETWEEN SMB AND VARICOL.

We choose a Varicol model with column configuration (1-1.7-2.4-0.9) as our best model because it results in the highest product purity and recovery. Column 4 of Table 3.5 summarizes the resulting Varicol performance indices. In this Varicol process, the average product purity of both A and B increases by 2.17%, the average product recovery of both A and B increases by 1.45%, and solvent consumption decreases by 1.5%, compared to the basic SMB model. This increase results from our ability to effectively fine-tune the zone lengths, allowing us to choose configurations that are part-way between two SMB configurations. However, the resulting Varicol configuration is actually very close to the original SMB configuration. Because Z_1 and Z_4 for the Varicol are almost the same as those in the basic SMB, we conclude that a guideline to optimize this Varicol operation is to increase the length of zone 3, but decrease the length of zone 2. We also note from comparing columns 3 and 4 of Table 3.5 that increasing B purity lowers A purity, and increasing A recovery lowers B recovery. Therefore, applying the Varicol method in this case involves a tradeoff.

5.1.2. PowerFeed

For the binary separation, we start with the same basic 4-zone SMB. We choose the average m_i values under PowerFeed operation to be equal to those of the original SMB, and apply the analysis scheme shown in Figure 5.4 and the feed and recycle flow rate policies of Figure 5.5. We analyze the effects of this PowerFeed system on the product purity and recovery, and seek an improved PowerFeed model with two or three subintervals. We then adjust feasible m_2 and m_3 flow rate ratios to make the $(m_2 - m_3)$ separation plane for providing some useful guidelines of the PowerFeed.

In step 1, we evaluate the PowerFeed with two subintervals, as shown in Figure 5.5a. In order to see if a front feed loading (larger F_1) or a rear feed loading (Larger F_2) gives a better separation performance, we evaluate the performance by changing the subinterval feed flow rates, and find that rear loading is better than front loading.

From the step 2 of evaluating the PowerFeed with three subintervals in Figure 5.5b, we find that there is no benefit to the PowerFeed system with three subintervals.

In step 3, we evaluate the partial feeding[61,62] with two switching subintervals to find the best manipulated variables for PowerFeed. We identify the second subinterval feed flow rate F_2 as the most important manipulated variable. We consider the B purity as the most important performance index, because the A purity, and the recovery of the product A and B essentially do not change much when we increase the F2 value.

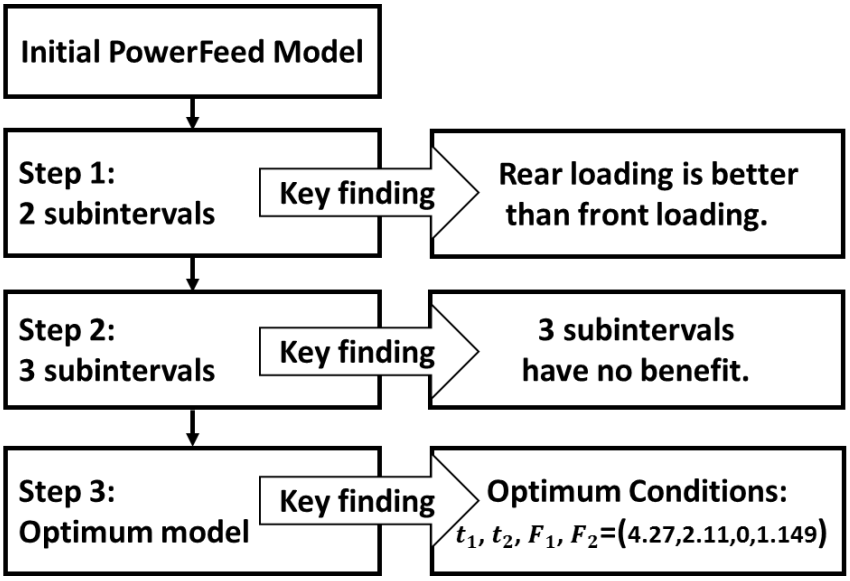

FIGURE 5.4. THE POWERFEED EVALUATION AND IMPROVEMENT STEPS.

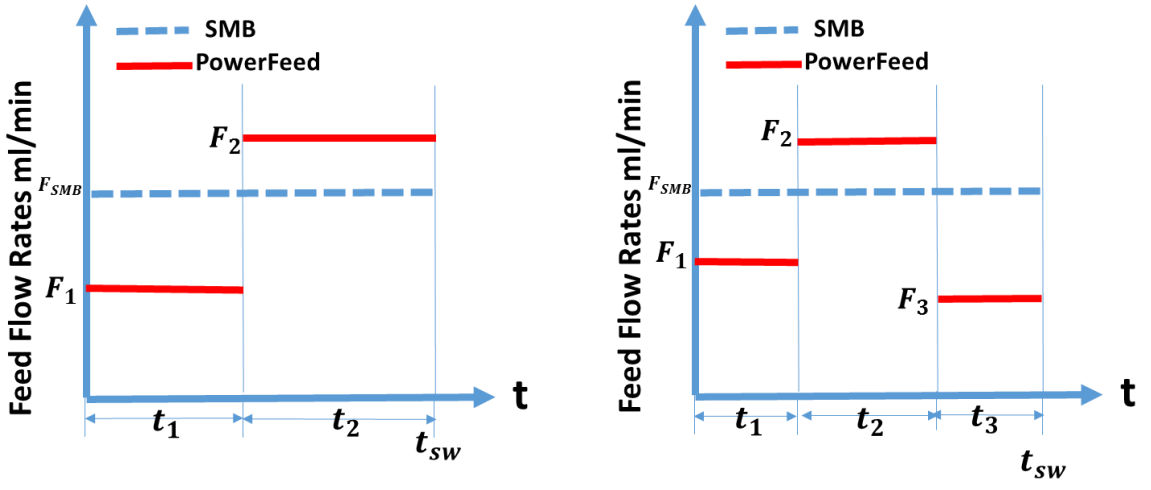

a.PowerFeed with two subintervals **b. PowerFeed with three subintervals**

FIGURE 5.5. FEED AND RECYCLE FLOW RATE POLICIES FOR SMB AND POWERFEED.

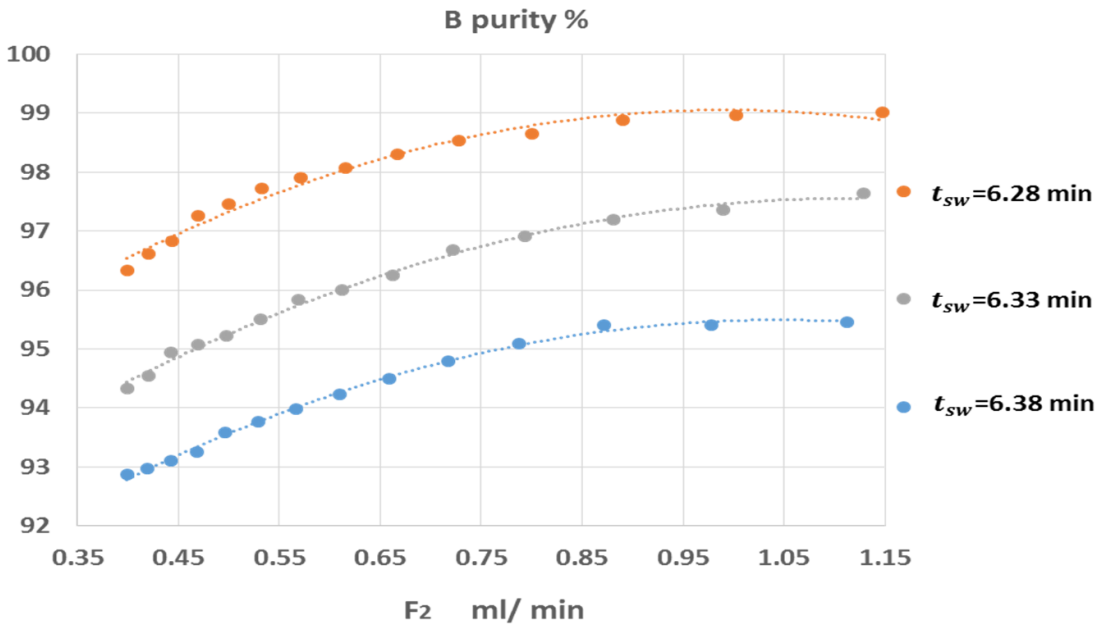

FIGURE 5.6. B PURITY SIMULATION RESULTS IN THE POWERFEED MODEL WITH TWO SUBINTERVALS.

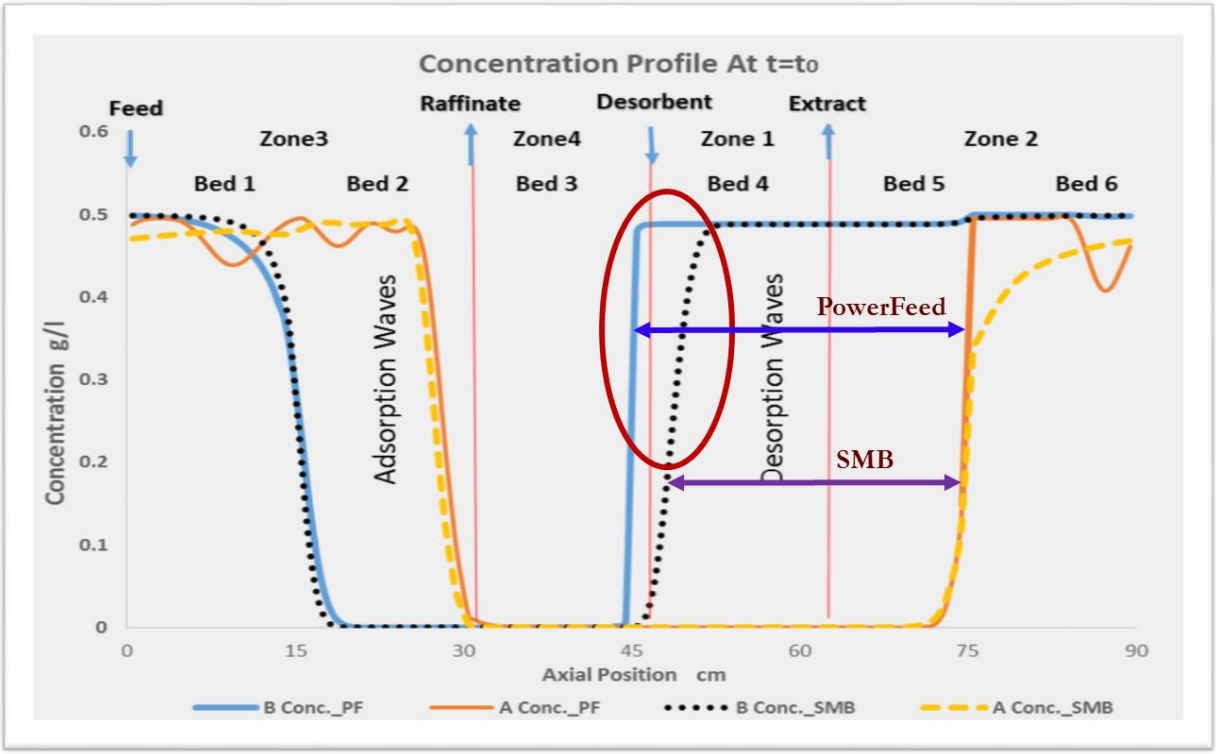

FIGURE 5.7. CONCENTRATION PROFILES FOR POWERFEED (PF) AND SMB.

Figure 5.6 shows the effect of increasing the second subinterval feed flow rate F_2 on B purity for three different switching times in the PowerFeed with two subintervals. Compared to the SMB results with 6.38 min switching time, A purity and both A and B recoveries do not change much throughout the simulations. Specifically, A recovery only slightly increases from 89.15% to 89.54%, B recovery almost stays at essentially 100%, A purity increases from 99.61% to 99.99%, while B purity improves more significantly from 92.76% to 95.46% as we increase F_2 from 0.386 ml/min to 1.149 ml/min. All the curves in Figure 5.6 show that the larger the subinterval with zero feeding, the higher is B purity. Therefore, the best PowerFeed model for these conditions corresponds to $F_1 = 0,\ F_2 = 1.149\ ml/min$ and $t_1 = 4.27\ min, t_2 = 2.11\ min$.

A comparison of the column concentration profiles of the PowerFeed model and the basic SMB model reveals the reasons for this trend. Figure 5.7 shows the steady-state concentration profiles for both PowerFeed and SMB. Solid curves represent concentration values from the PowerFeed model, while dashed curves refer to the SMB model. We find that the adsorption wave in zone 3 for component A in PowerFeed drops more quickly and earlier than the one in SMB, which results in more component B left in the flow coming into the raffinate stream. This explains the improved raffinate purity; the raffinate contains a high concentration of B for a longer period of time. The desorption waves in zones 1 and 2 are sharper in PowerFeed than those in the SMB model. In other words, the components are desorbed over a shorter distance in PowerFeed, which may improve the A recovery a little bit. The arrowed gap between two components in PowerFeed is wider than the one in SMB, suggesting that components separate better under PowerFeed operation.

5.1.3. ModiCon

ModiCon[63,64] varies the feed concentration (C_1, C_2 and C_3), instead of the feed flow rates, of the SMB process. It keeps the feed flow rate and the column configuration the same as the basic SMB model. Unlike PowerFeed, adding a third subinterval to ModiCon operation results in an improved performance. Figure 5.8 defines the three different ModiCon patterns within three switching subintervals: higher front, higher middle and higher later feed concentration.

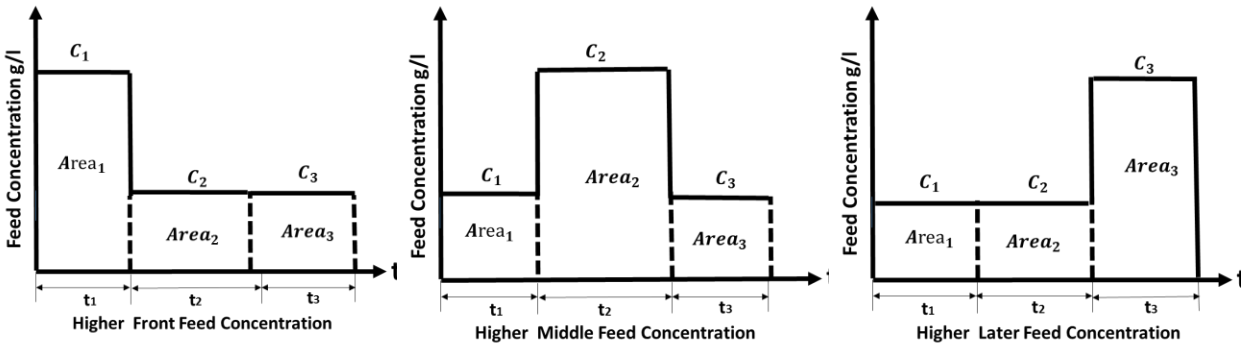

FIGURE 5.8. THE DEFINITION OF THREE MODICON PATTERNS.

We find that the one with greater middle area is the best, and the second subinterval feed concentration C_2 is the most effective manipulated variable in improving our system's performance. We simply assert that Area$_1$=Area$_3$, and evaluate the separation performance while varying C_2 from 0.1 g/L to 2.5 g/L.

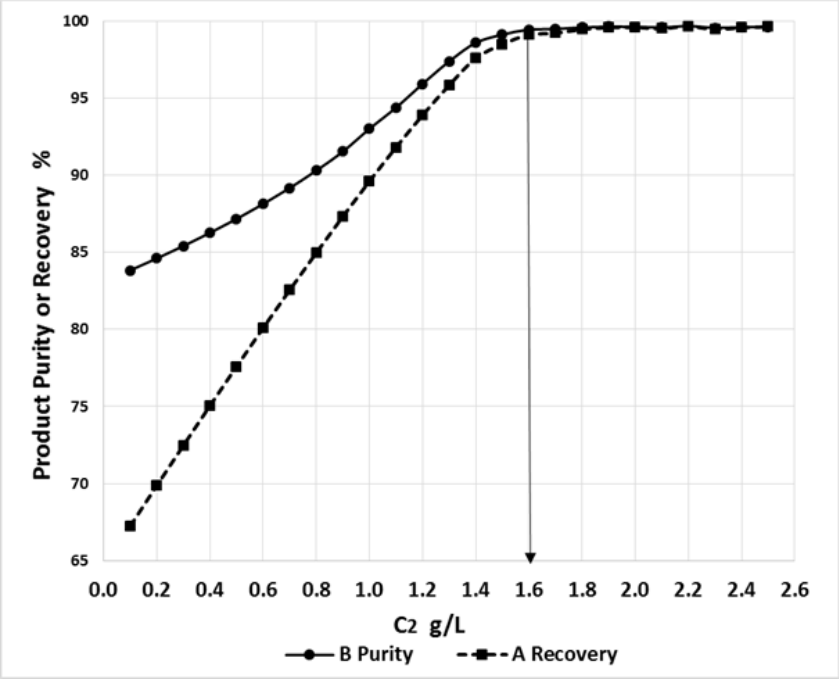

FIGURE 5.9. THE MODICON SIMULATION RESULTS FOR IMPROVED PURITY AND RECOVERY.

Figure 5.9 shows that the larger C_2 values give higher B purity and A recovery; both B purity and A recovery remain constant after 1.6 g/L total feed concentration. We observe diminishing returns as C_2 increases beyond 1.6 times the original concentration. Therefore, we select a C_2 value of 1.6 g/L as our improved model. ModiCon achieves an improved separation performance with t_1 =

t_3=1.3 min, t_2 =3.78 min, C_1 = C_3 = 0.166 g/L, C_2 = 1.6 g/L. The resulting B purity is 99.08%, which is 6.8% higher than that in the basic SMB process, and A recovery is 99.34%, an 11.3% increase from that in the basic SMB model.

Figures 5.10 and 5.11 explain why ModiCon performs better than the basic SMB for both B purity and A recovery. Figure 5.10 displays that the concentration of A in the raffinate for the ModiCon is lower and the average concentration of B is higher than those in the basic SMB, which increases B purity in the raffinate. Figure 5.11 shows the improved A concentration in the extract stream when component B concentrations are effectively zero in both SMB and ModiCon models, which increases A recovery in the extract.

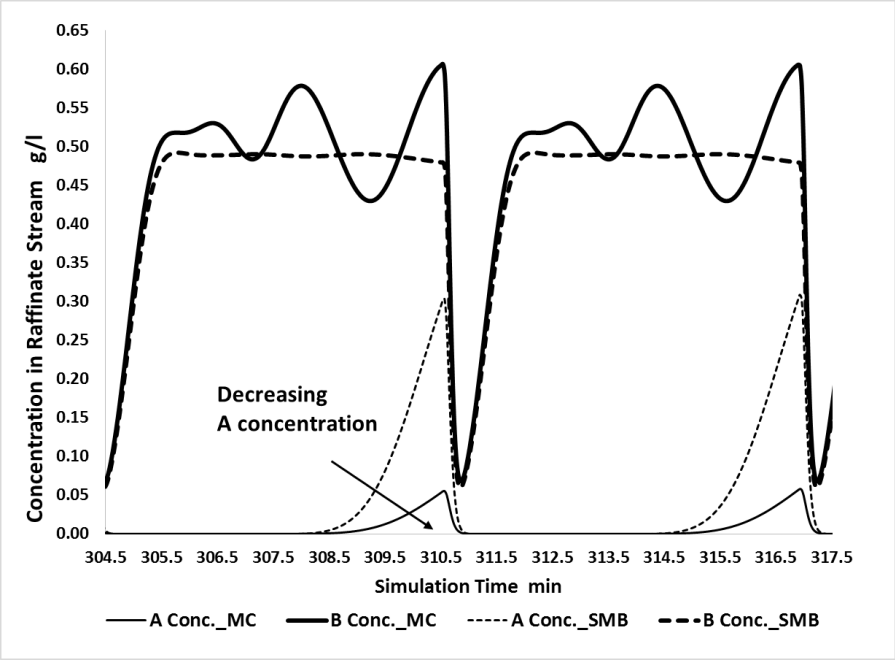

FIGURE 5.10. RAFFINATE CONCENTRATIONS OVER TIME IN SMB AND MODICON (MC).

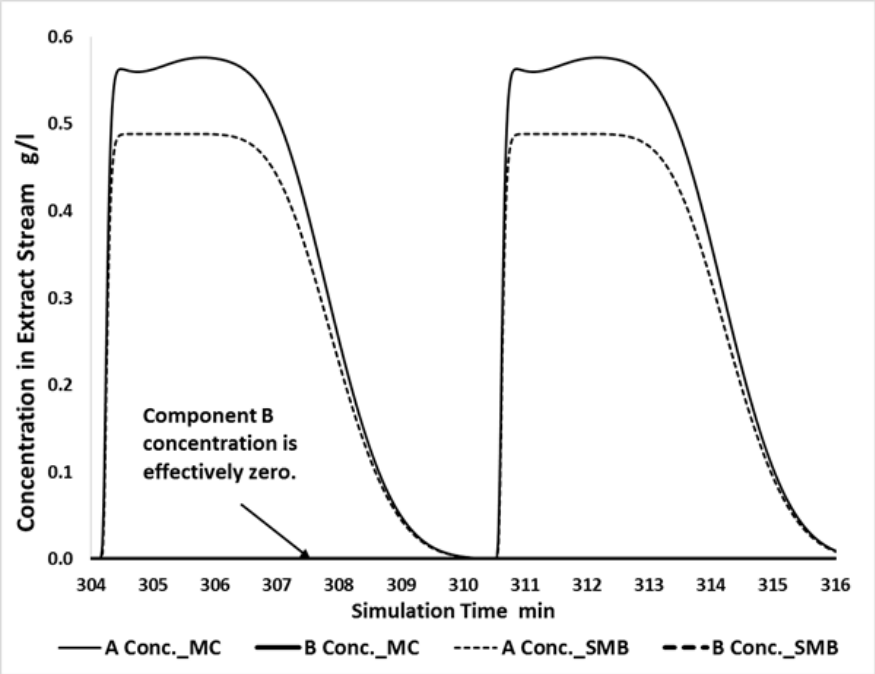

FIGURE 5.11 EXTRACT CONCENTRATIONS OVER TIME IN SMB AND MODICON (MC).

The column concentration profiles in Figures 5.12 show how modifying the subinterval feed concentrations in ModiCon achieves a better separation performance. The figure shows the steady-state concentration profiles at $t = t_1 + t_2$ within one switching time for both ModiCon and SMB. When the subinterval feed concentration in ModiCon increases, the adsorption wave of component B in zones 3 and 4 moves slowly through the column. As a result, more component B reaches the raffinate stream over the course of the switching time, which results in a higher concentration of B in the raffinate. We find that in Figure 5.12, the A concentration in zones 3 is much lower in the ModiCon model than in the SMB model, because the components are accumulating in zone 1 and 2, which is good for collecting component A in the extract stream. This explains the improved A recovery in the extract.

In order to study the system's oscillation tendency shown in Figure 5.12 further, we have validated our ModiCon simulations, showing that 40 and 80 grid points all give similar simulation results. We show the concentration profiles with 80 grid points after steady state in Figure 5.13, which displays a very similar oscillatory tendency. The oscillations are also observed in simulations with small Peclet numbers (Pe=50) and in simulations that employ an orthogonal collocation on finite elements (OCFE) in Figures 5.14 and 5.15. Therefore, we believe that the oscillations are actually a feature of the ModiCon operational mode; moreover,

the ModiCon study of Schramm et al[63,64] also shows similar oscillations in their concentration profiles (see Figure 3 in reference 63). The main reason for the concentration oscillation is the feed concentration switching in combination with the dead volumes.

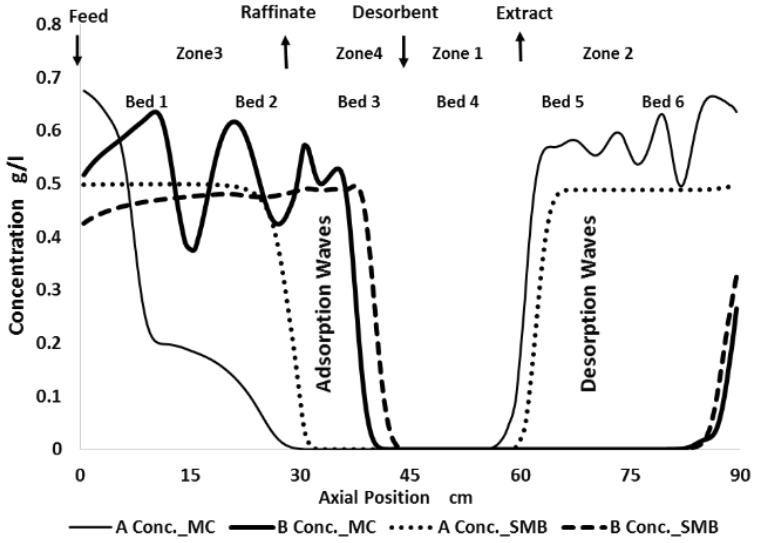

FIGURE 5.12. MODICON (MC) CONCENTRATION PROFILES WITH 40 GRID POINTS.

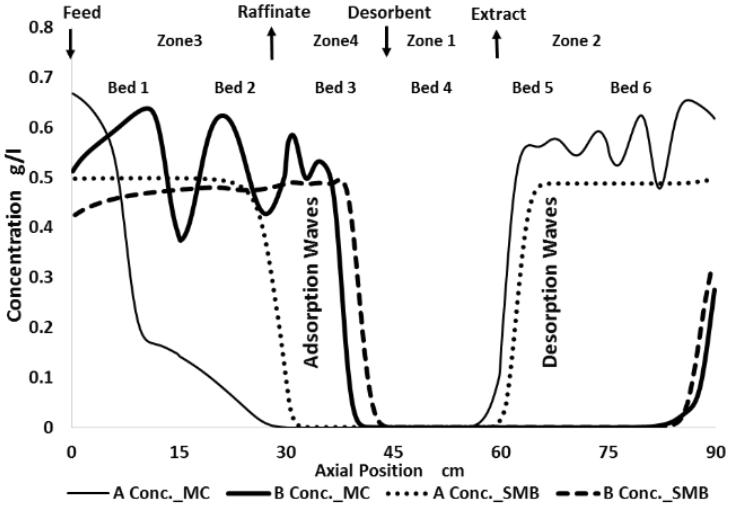

FIGURE 5.13. MODICON (MC) CONCENTRATION PROFILES WITH 80 GRID POINTS.

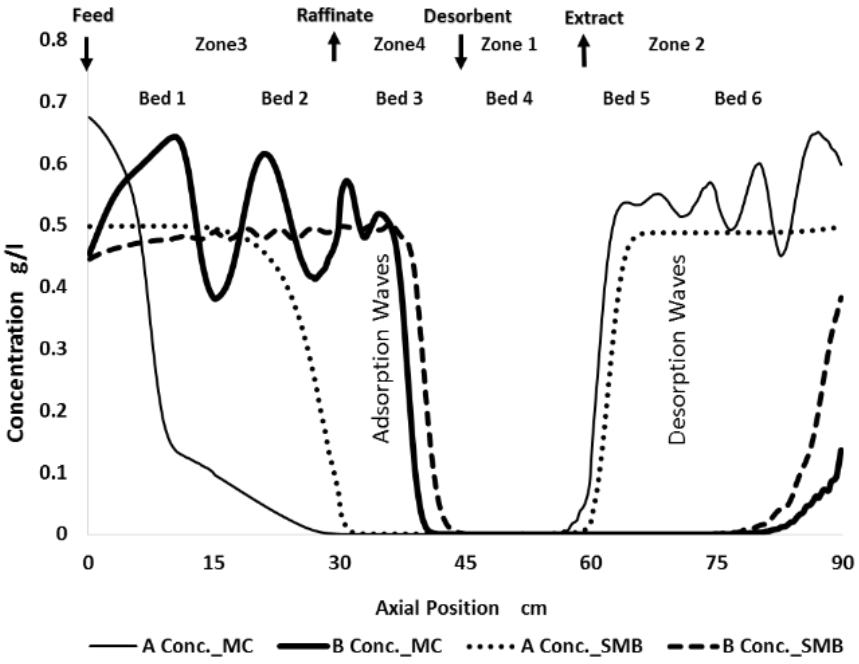

FIGURE 5.14. MODICON (MC) CONCENTRATION PROFILES WITH OCFE.

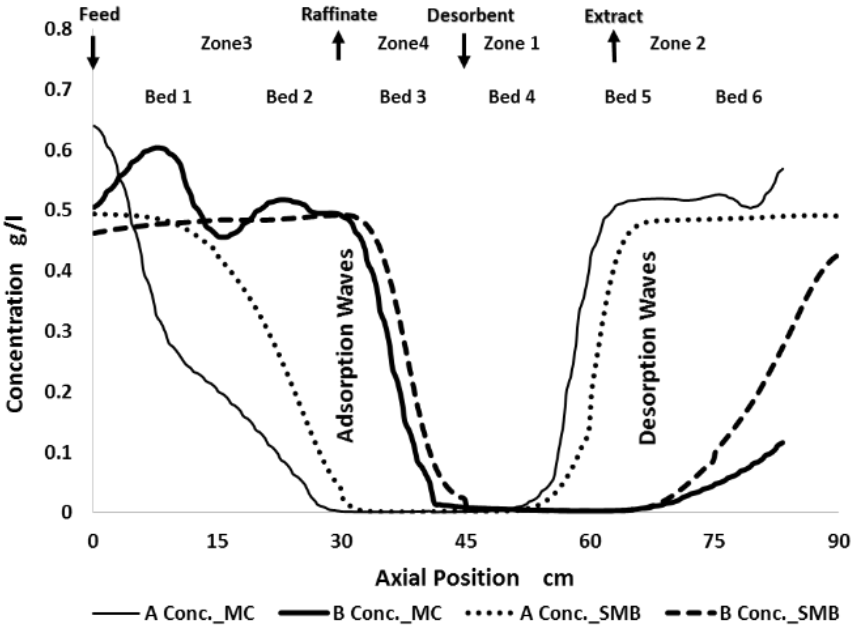

FIGURE 5.15. MODICON (MC) CONCENTRATION PROFILES WITH PECLET NUMBERS (PE = 50.)

5.1.4. Combined Operational Modes

Through sections 5.1.1 to 5.1.3, we find that each operational mode has unique advantages, and we want to explore whether combining these modes will provide a greater efficiency. For example, based on the previous results for PowerFeed and ModiCon, ModiCon increases the product purity and recovery compared to the basic SMB case, while decreasing the solvent consumption. PowerFeed, on the other hand, performs similarly to the basic SMB case, while being more flexible. Therefore, we combine these two or three processes to see if the integrated system will perform better than either one individually[51,64,65] .

We compare two operational modes, PowerFeed and ModiCon, and refer to it as PF&MC. We vary the feed flow rates (F_1, F_2 and F_3), recycle flow rates ($Recy_1$,$Recy_2$ and $Recy_3$) and feed concentrations (C_1, C_2 and C_3) within given switching subintervals. In order to select an initial model to generate the (m_2-m_3) separation plots, we follow the similar evaluation steps for PF&MC as for PowerFeed or ModiCon, as shown in Figure 5.16.

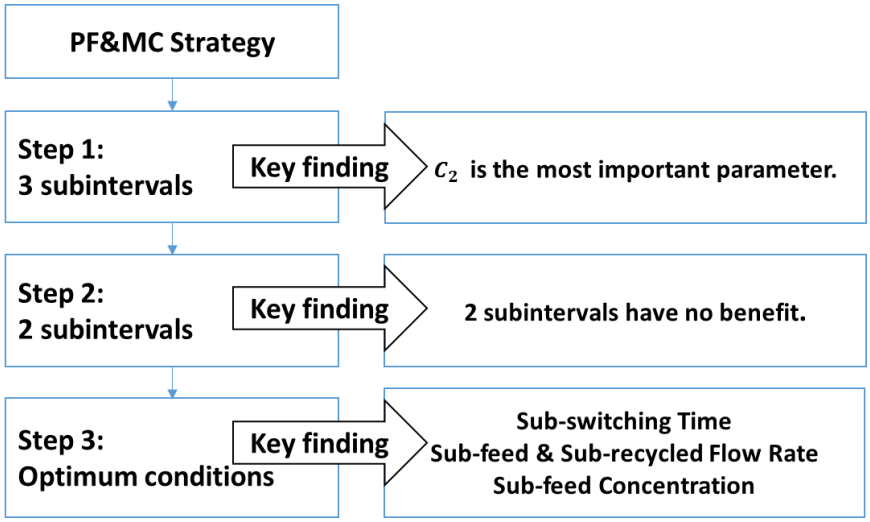

FIGURE 5.16. THE POWERFEED EVALUATION AND IMPROVEMENT STEPS.

We find that the improvement of the combined modes proceeds similarly to the improvement of ModiCon. Specifically, the operational mode performs best with a single peak of high concentration in the middle of the switching interval. Compared to the concentration changes, the effects of changes in the feed flow rate within the switching interval are modest. To

demonstrate the importance of the central concentration (C_2) peak, we set fixed values for subinterval switching times and subinterval flow rates and increase the C_2 value from 1.5 g/L to 2.1 g/L. The results, like the ModiCon results, are that B purity and A recovery increase with increasing C_2.

The design of the V&PF&MC mode starts from the improved PF&MC mode and uses the same improvement method as Varicol. It turns out that both combined modes are able to improve over the ModiCon mode, and adding Varicol to PF&MC offers benefit over the PF&MC operation as shown in Figure 5.17. However, it involves a balance for the selection of the combined operational modes because of the increasing complex of the process.

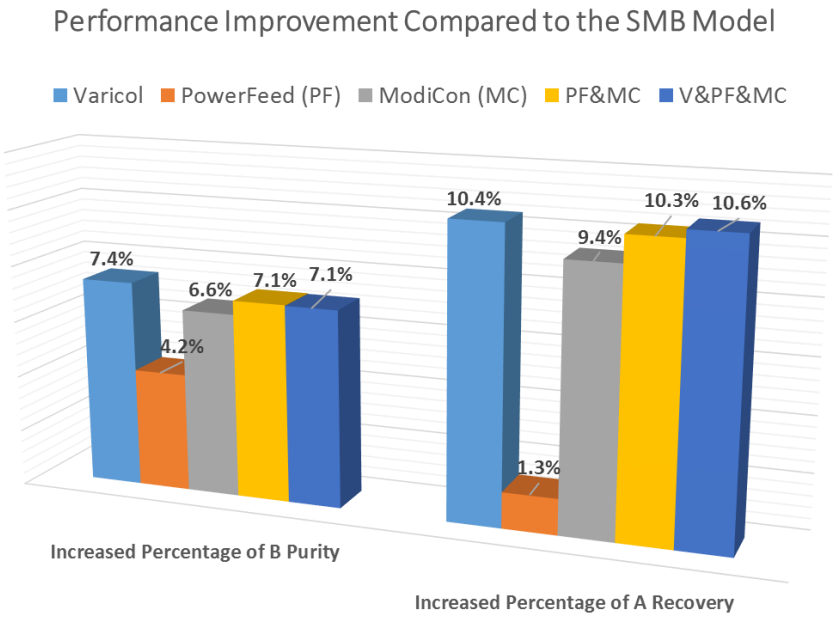

FIGURE 5.17. PERFORMANCE IMPROVEMENT FOR EACH OPERATIONAL MODE COMPARED TO THE BASIC 4-ZONE SMB MODEL.

5.1.5. Comparison of Improved Separation Regions of Operational Modes

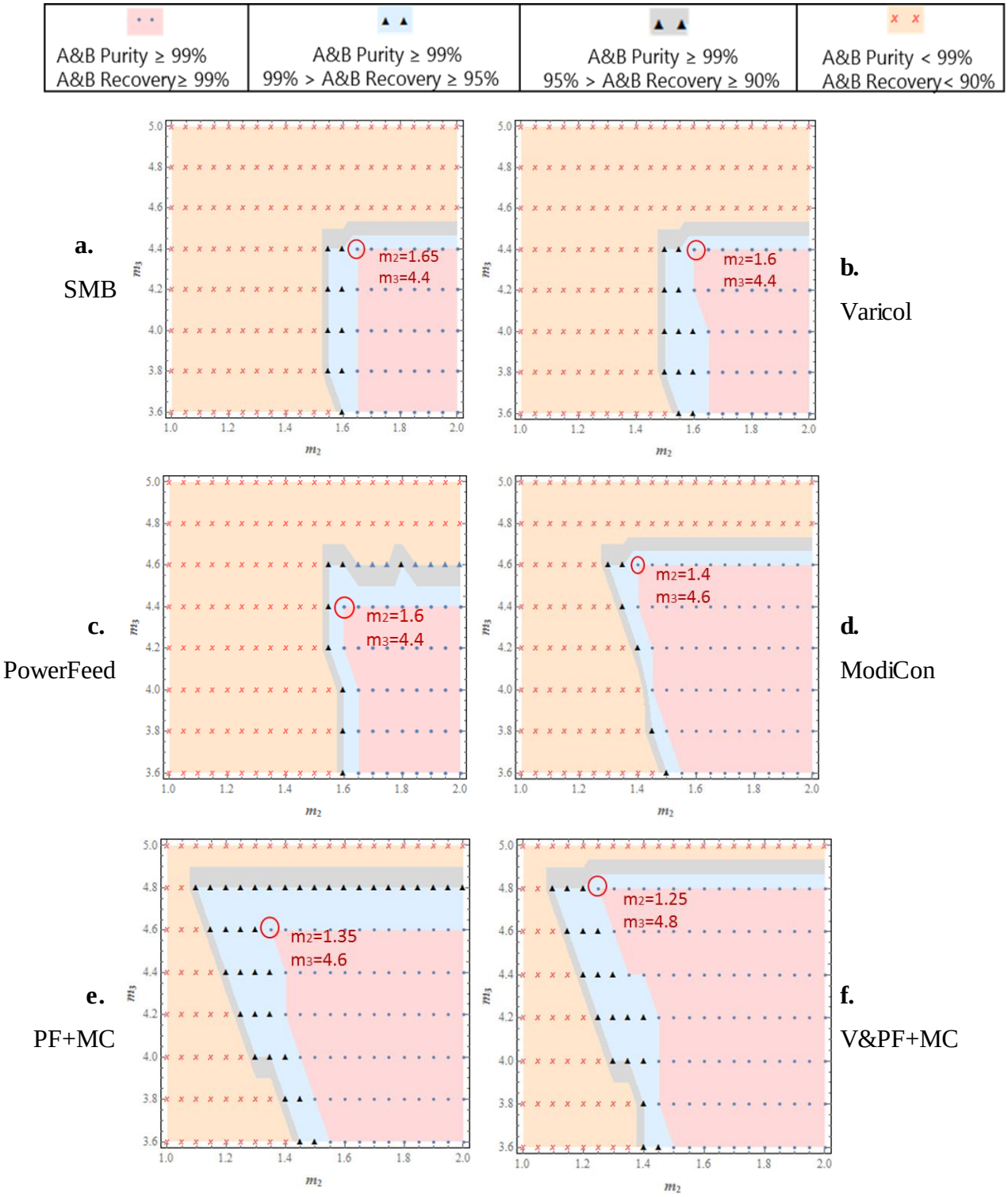

FIGURE 5.18. THE SEPARATION REGION PLOTS OF OPERATIONAL MODES FOR THE BINARY SEPARATION.

For completeness, we follow the instruction in section 3.5.1, and define these separation regions in terms of both product purity and recovery. Figure 5.18a represents the separation region with respect to product purity and recovery in the SMB basic model. The point of greatest productivity with the desired separation performance (A and B purity ≥99% and A and B recovery ≥99%) is marked at m_2=1.65 and m_3=4.4.

Figure 5.18b shows that the Varicol operational mode gives only small improvements over the base case for both the purity and recovery results. This result is consistent with previous work, which found that the benefit of the Varicol operational mode decreases as the number of beds increases[54]. While Varicol is promising in 4- and 5-bed systems, it struggles to improve upon 6-bed systems. We notice that in our system, the Varicol mode involves a tradeoff. It may be possible to improve the separation region more significantly if we abandon our goal of maximizing the purity and recovery of both components to maximize one component at the expense of the other. This finding is consistent with other work, which has found a similar tradeoff when performing optimizations of Varicol systems[54].

Figure 5.18c represents the separation region plots of the PowerFeed, which reveals the following trends in our separation system: (1) PowerFeed has very little benefit in the m_2 direction, similar to the Varicol operational mode. In this case, neither the Varicol nor PowerFeed improves the basic SMB operation. (2) PowerFeed operational mode is highly sensitive to the flow rate ratio m_2. Therefore, great care should be taken when operating a PowerFeed unit to keep the flow rate in zone 2 constant.

The separation region applying the ModiCon in Figure 5.18d enlarges both the m_2 and m_3 directions for both product purity and recovery performance. ModiCon expands the separation regions in the m_3 direction as effectively as PowerFeed; but unlike PowerFeed, it simultaneously improves the performance in the m_2 direction. If we choose to achieve high values of both purity and recovery of products, ModiCon is a better choice than Varicol and PowerFeed.

While the PF&MC results are very similar to ModiCon, the (m_2-m_3) separation plot in Figure 5.18e has enlarged the grey regions with purity and recovery greater than 99%. In other words,

the changes in feed flow rate, while small compared to the changes in concentration, do allow improvements over ModiCon alone.

Figure 5.18f shows a small improvement over the combined PF&MC operation. However, from our observation, we conclude that adding Varicol to PF&MC offers very little benefit over the PF&MC operation.

5.1.6. Calculation Example of the Optimum Point in ModiCon Operation

In this section, we give an application example to illustrate how to apply the separation region plots to calculate the conditions of the operational modes, that will help in guiding the experimental design and process operations.This example comes from Figure 5.18d of the ModiCon operation. In this ModiCon optimum separation plot, the optimum point for product purity is m_2=1.3, m_3=4.6, for product recovery is m_2=1.4, m_3=4.6. Therefore, for both purity and recovery, the optimum point is the one with m_2=1.4, m_3=4.6.

In this case, the net flow rate ratios are m_1=6.54, m_2=1.4, m_3=4.6, m_4=1.35.

According to Table 3.2 and eq 3.10, $Q_1 = 1.155\frac{ml}{min}, Q_2 = 0.492\frac{ml}{min}, Q_3 = 0.904\frac{ml}{min}, Q_4 = 0.485\frac{ml}{min}$.

Since $Q_{recycle} = Q_4, Q_D = Q_1 - Q_4, Q_E = Q_1 - Q_2, Q_F = Q_3 - Q_2, Q_R = Q_3 - Q_4,$

We get $Q_{recycle} = 0.4847\frac{ml}{min}, Q_D = 0.6703\frac{ml}{min}, Q_E = 0.6633\frac{ml}{min}, Q_F = 0.4126\frac{ml}{min}, Q_R = 0.4196\frac{ml}{min}$.

According to eq 3.13, we assume that

$$t_{sw} = \frac{\phi L^2}{\Delta P_{max}} \sum_{j=1}^{j=4} n_j (m_j(1-\varepsilon) + \varepsilon) \tag{5.1}$$

$$t_{sw} = \frac{0.1 * (15cm)^2}{40 \text{ bar}} [n_1(m_1(1-0.68)+0.68) + n_2(m_2(1-0.68)+0.68)$$

$$+n_3(m_3(1-0.68)+0.68)+n_4(m_4(1-0.68)+0.68)] \quad (5.2)$$

Because $(n_1, n_2, n_3, n_4) = (1,2,2,1)\ and\ (m_1, m_2, m_3, m_4) = (6.54, 1.4, 4.6, 1.35)$,

We get:

$$t_{sw} = \frac{0.1*(15cm)^2}{40\ \text{bar}}[1*(6.54*(1-0.68)+0.68)+2*(1.4*(1-0.68)+0.68)+2*$$
$$(4.6*(1-0.68)+0.68)+1*(1.35*(1-0.68)+0.68)]$$

$$t_{sw} = 6.187\ min \quad (5.3)$$

In this way, we reduce m_2 value from 1.75 to 1.4, and m_3 value from 4.785 to 4.4, which enlarge the feed handling capacity, while decreasing the desorbent consumption and even increasing the productivity, compared to the ModiCon with m_2=1.75,m_3=4.785.

Table 5.1 and 5.2 list all the operating conditions and the optimum operating points for the binary separation of Troger's base enantiomers.

TABLE 5.1. OPERATING CONDITIONS IN THE OPERATIONAL MODES FOR THE BINARY SEPARATION OF TRÖGER'S BASE ENANTIOMERS.

	Optimized Conditions for Operational Modes									
	Varicol		**PowerFeed**		**ModiCon**		**PF&MC**		**V&PF&MC**	
Optimum Operating Conditions	AS_D	1	t_1	4.25	t_1	1	t_1	1.117	C_1	0.1
	AS_F	0.6	t_2	2.13	t_2	4.38	t_2	4.147	C_2	1.751
	AS_E	1	F_1	0	t_3	1	t_3	1.117	C_3	0.1
	AS_R	0.9	F_2	1.14	C_1	0.1	F_1	0.494		
			$Recy_1$	0.344	C_2	1.5	F_2	0.319	AS_D	1
			$Recy_2$	0.724	C_3	0.1	F_3	0.494	AS_F	0.6
							$Recy_1$	0.508	AS_{E1}	1
							$Recy_2$	0.45	AS_R	0.9
							$Recy_3$	0.508		

TABLE 5.2. OPERATING CONDITIONS IN THE OPERATIONAL MODES WE INVESTIGATED.

		Optimized Points for Operational Modes									
		SMB	Varicol		PowerFeed		ModiC		PF&MC		V&PF&MC	
Flow rate ratio	m_I	6.54	6.54		6.54		6.54		6.54		6.54	
	m_{II}	1.65	1.6		1.6		1.4		1.35		1.25	
	m_{III}	4.4	4.4		4.4		4.6		4.6		4.8	
	m_{IV}	1.35	1.35		1.35		1.35		1.35		1.35	
Zone flow rates ml/min	Q_I	1.152	1.155		1.155		1.155		1.158		1.145	
	Q_{II}	0.522	0.517		0.517		0.492		0.487		0.481	
	Q_{III}	0.876	0.879		0.879		0.904		0.907		0.922	
	Q_{IV}	0.483	0.485		0.485		0.485		0.486		0.481	
Inlet and outlet flow rates	Q_D	0.668	0.670		0.670		0.670		0.672		0.665	
	Q_E	0.629	0.638		0.638		0.663		0.672		0.664	
	Q_F	0.354	0.361		0.361		0.413		0.420		0.441	
	Q_R	0.393	0.394		0.394		0.420		0.421		0.442	
Recycle flow rate	$Q_{Recycle}$	0.483	0.485		0.485		0.485		0.486		0.481	
Switching time min	t_{sw}	6.205	6.187		6.187		6.187		6.169		6.241	
Optimum Operating Conditions		--	AS_D	1	t_1	4.124	t_1	1.0	t_1	1.08	t_1	1.093
			AS_F	0.6	t_2	2.063	t_2	4.0	t_2	4.01	t_2	4.056
			AS_E	1	F_1	0	t_3	1.0	t_3	1.08	t_3	1.093
			AS_R	0.9	F_2	1.083	C_1	0.1	F_1	0.546	F_1	0.573
					Rec	0.364	C_2	1.4	F_2	0.352	F_2	0.370
					Rec	0.725	C_3	0.1	F_3	0.546	F_3	0.573
									C_1	0.1	C_1	0.1
									C_2	1.752	C_2	1.752
									C_3	0.1	C_3	0.1
											AS	1
											AS_F	0.6
											AS_E	1
											AS_R	0.9

5.1.7. Comparison of Sensitivities across All Operational Modes

To give some additional details to the comparisons among different operational modes, let us compare the sensitivity of the different operational modes side by side. Figure 5.19 through Figure 5.24 show how the different operational modes perform as m_2, m_3 and feed flow rate are varied. The change in feed flow rate is expressed as a deviation from the optimal feed flow rate. The optimum feed flow rate may be different for each operational mode.

Figures 5.19 and 5.20 show the performance order (Combined PF&MC/V&PF&MC > ModiCon > SMB/Varicol > PowerFeed) we find for A purity and B recovery results are same at varied m_2, but before m_2=1.6 and at fixed m_3 value of 4.4.

Figures 5.21 and 5.22 give B purity and A recovery results for all the operational modes at fixed m_2 and varied m_3. We see that after m_2= around 4.25, the performance of ModiCon, PF&MC and V&PF&MC drops steadily instead of increasing sharply like other operational modes.

Figures 5.23 and 5.24 show the effect of changing feed flow rate on both A and B purities. PowerFeed works the best in B purity but the worse in A purity as we change the feed flow rates, but the performance of ModiCon, PF&MC and V&PF&MC work steadily.

Thus, these plots show some interesting results. First, the PowerFeed operational mode is highly sensitive to the m_2 parameter, even more so than the basic SMB. Therefore, great care should be taken when operating a PowerFeed unit to keep the flow rate in zone 2 constant. The similarity of the Varicol to the SMB is expected because of the number of beds in the system, as discussed in section 5.1.1. Most importantly, however, is the low sensitivity of operational modes which involve ModiCon. All three scenarios involving ModiCon *not only* expand the operating region, *but also* show less sensitivity to m_2, m_3, and feed flow rate.

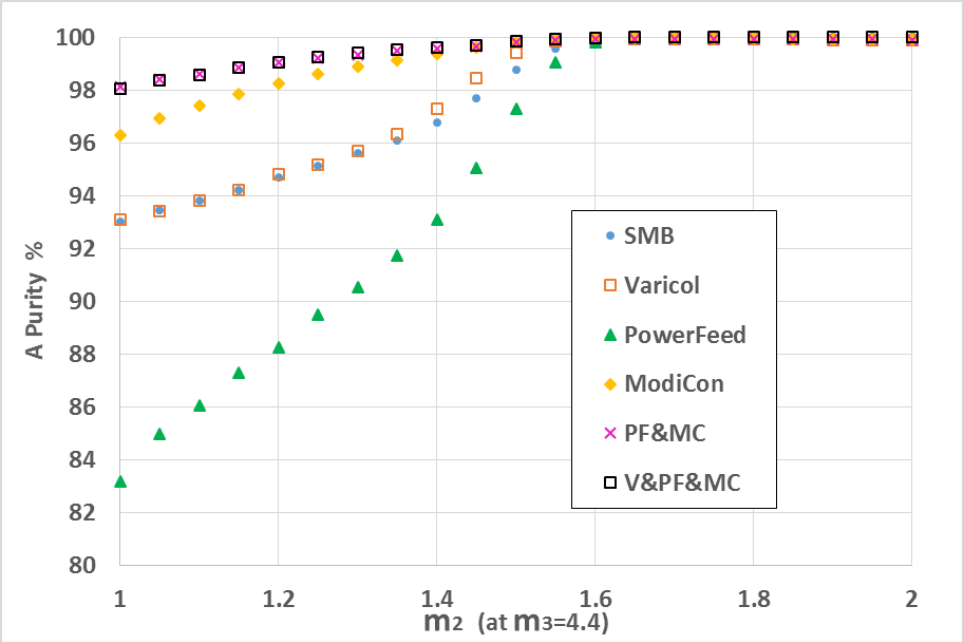

FIGURE 5.19. A PURITY EFFECT OF THE M_2 VALUE.

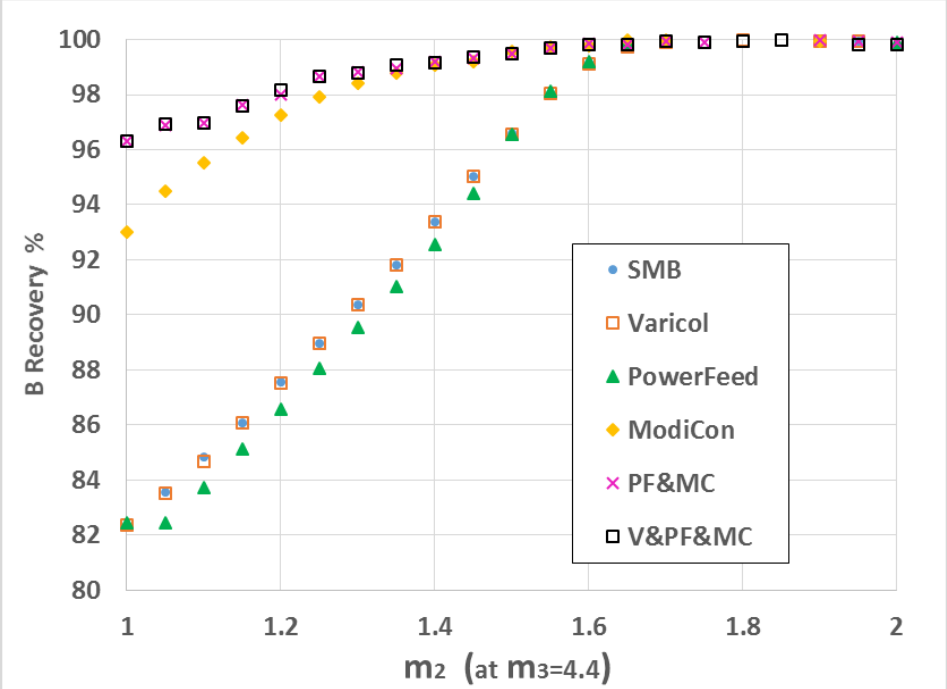

FIGURE 5.20. B RECOVERY EFFECT OF THE M_2 VALUE.

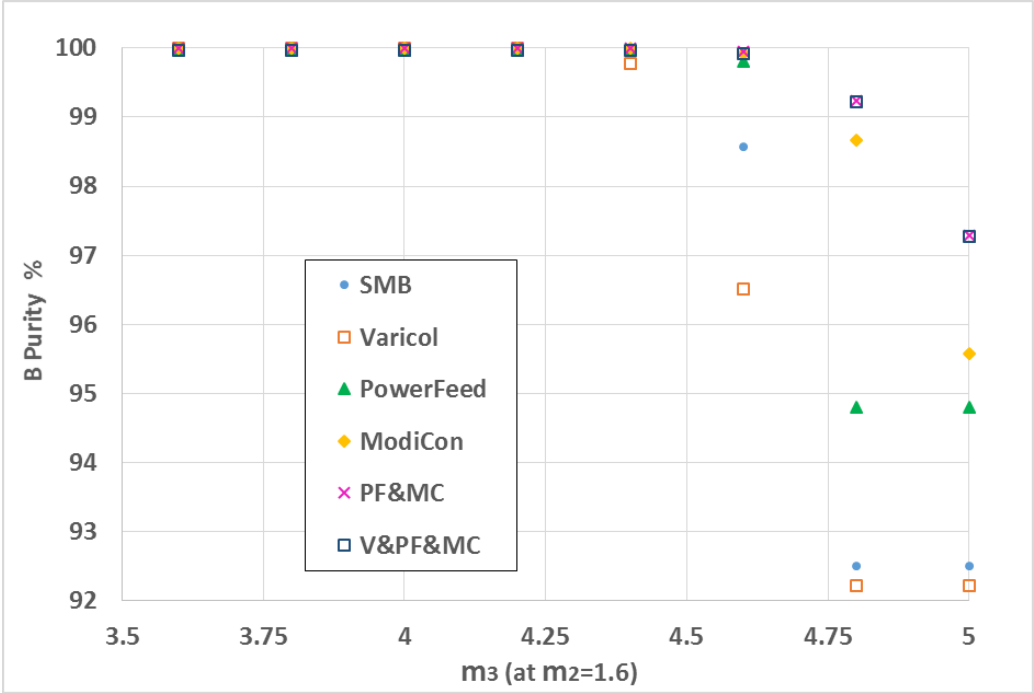

FIGURE 5.21. B PURITY EFFECT OF THE M_3 VALUE.

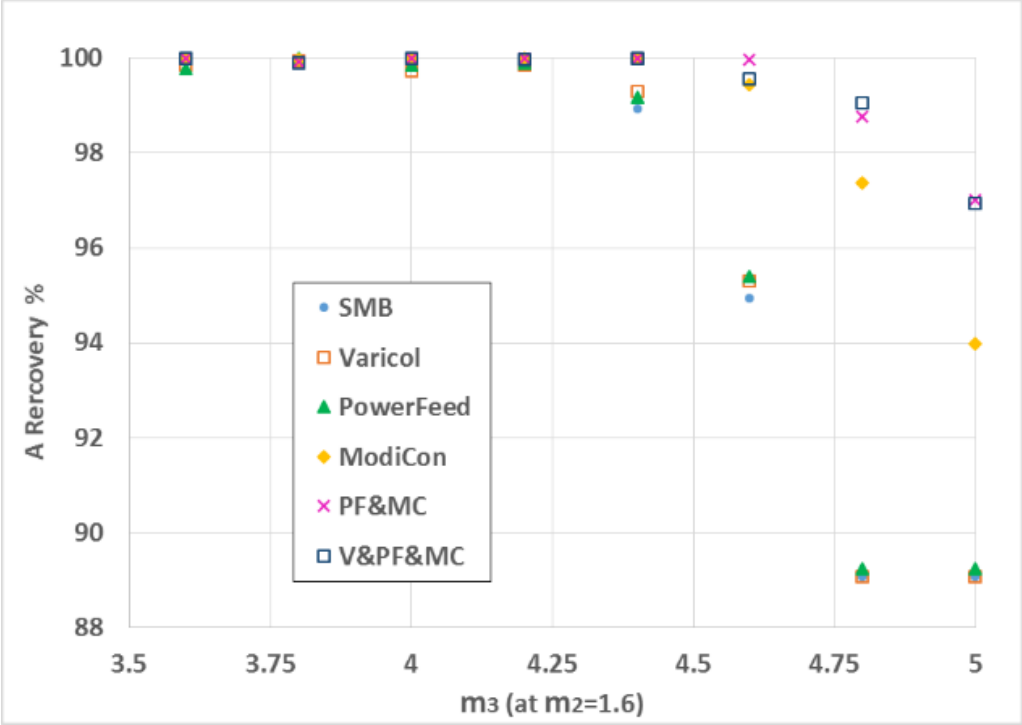

FIGURE 5.22. A RECOVERY EFFECT OF THE M_3 VALUE.

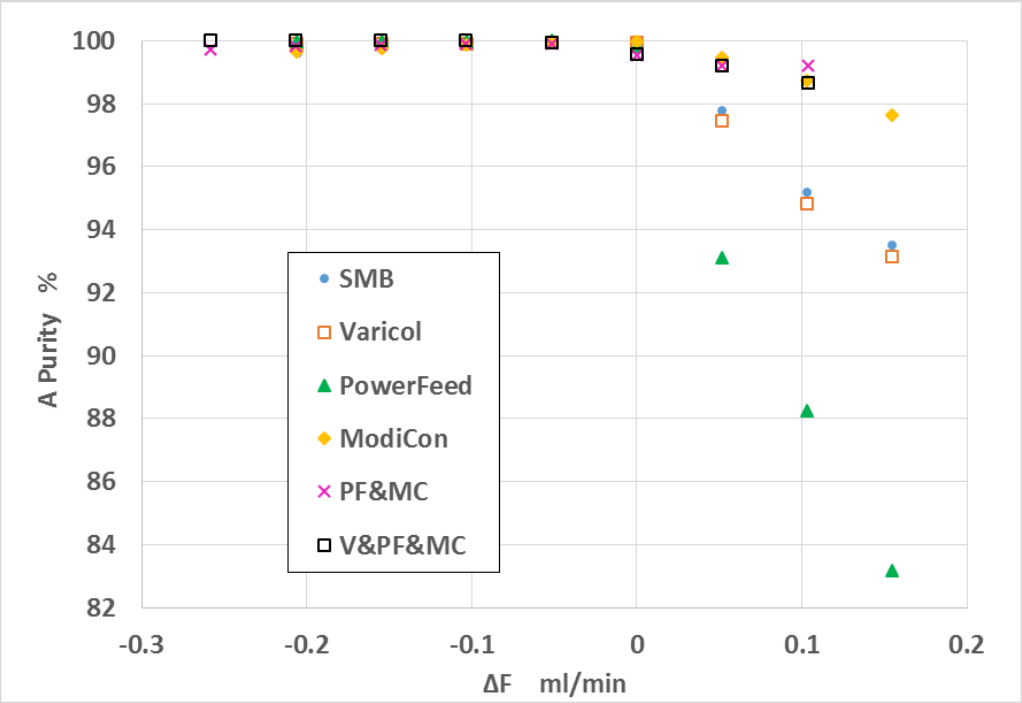

FIGURE 5.23. A PURITY EFFECT ON THE CHANGE OF FEED FLOW RATE.

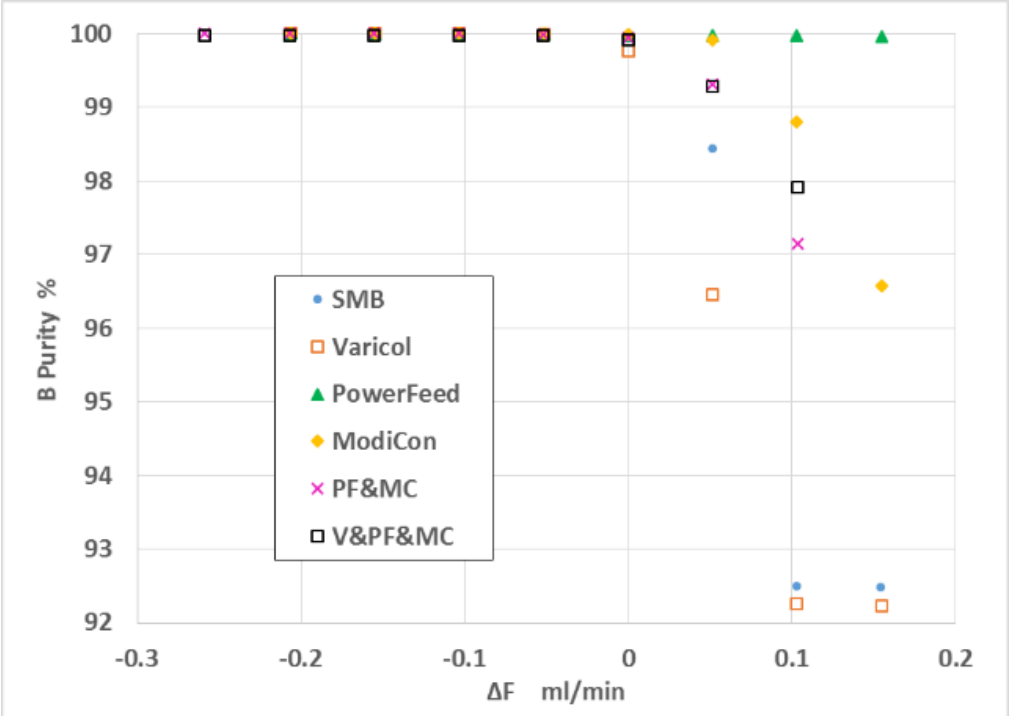

FIGURE 5.24. B PURITY EFFECT ON THE CHANGE OF FEED FLOW RATE.

5.1.8. Pareto Approach for All Operational Modes

As we discussed in section 3.5.2, the Pareto plot is a popular method for multiobjective optimization between conflicting performance indices. This means that we cannot improve one performance index without sacrificing the other. In order to simultaneously maximize these two indices (B purity and productivity), we generate a Pareto plot for all the operational modes and compare their results in Figure 5.25a. We combine the m_2-m_3 plot and the Pareto plots[51,56,58,59,73,80,81] to see the robustness of the effect of B purity on the productivity from the m_2-m_3 sets. We give an example on how to generate a Pareto plot for Varicol in Figure 5.25b, which shows some of the simulation points we evaluated from the m_2-m_3 sets. The dark circled points represent the Pareto points for Varicol optimum ones in Figure 5.25a.

The mathematical expressions for the optimization problem are as follows:

$$\text{Max } F_1 = Pur_B[m_2, m_3] \tag{5.4}$$

$$\text{Max } F_2 = Productivity[m_2, m_3] \tag{5.5}$$

$$m_2 \in [1.0\ , 2.0]; \tag{5.6}$$

$$m_3 \in [3.6\ , 5.0]; \tag{5.7}$$

$$\text{Subject to:} \quad Pur_B \geq 92\% \tag{5.8}$$

$$\text{and} \quad Productivity \geq 1.4 \frac{g}{L}/hr \tag{5.9}$$

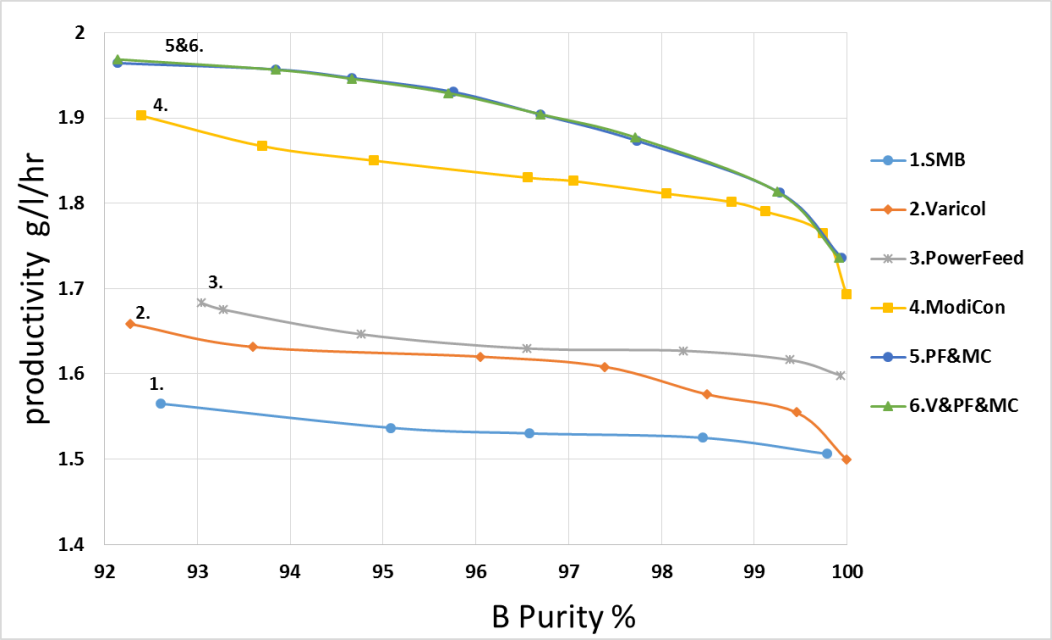

FIGURE 5.25A.PARETO PLOTS BETWEEN B PURITY AND PRODUCTIVITY ACROSS ALL THE OPERATIONAL MODES.

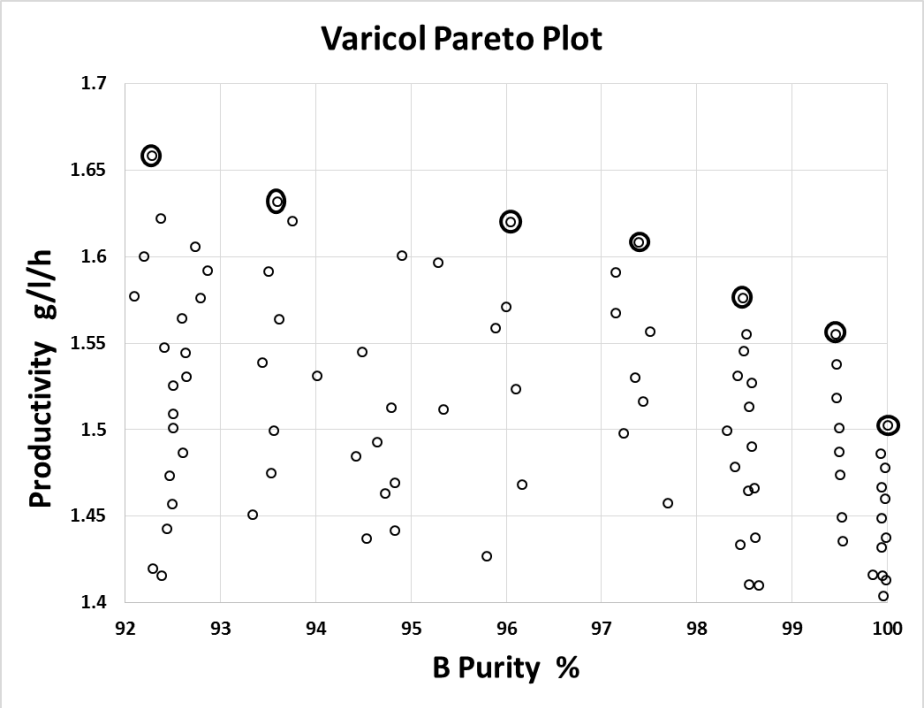

FIGURE 5.25B. AN EXAMPLE OF PARETO PLOT FOR VARICOL.

Figure 5.25a displays all the resulting Pareto plots for two conflicting performance indices, purity of component B and total productivity, across all the operational modes we have investigated. It reveals the following:

(1) All the operational modes give better Pareto optimum results compared to the basic SMB model.
(2) Varicol and PowerFeed have similar improved results, and both are not sensitive to productivity in terms of different B purity ranges.
(3) ModiCon has the largest improvement, and is more sensitive to the productivity, compared to other single operational modes.
(4) The two combined operational modes we have studied have essentially identical results in the Pareto plot, and they are the most sensitive to the productivity over different purity regions.

5.1.9. Powell Optimization for Different Separation Factors

Of the factors which describe the separation performance of a SMB column, the separation factor is the most commonly cited and easily understood. To improve the generalizability of our findings, we create additional separations based on the 4- and 5- zone systems in this study which differ only by their separation factors. We perform a simple Powell optimization[82] on the settings of these systems, and compare the improvements yielded by the operational mode in more difficult separations. The Powell optimization is an effcient method for finding the minimum of a function of several variables without calculating derivatives. The variation is such that when the procedure is applied to a quadratic form, it causes conjugate directions to be chosen, so the ultimate rate of convergence is fast when the method is used to minimize a general function. A further variation completes the method, and it ensures that the convergence rate from a bad approximation to a minimum is always efficient. Practical applications of the procedure have proved to be very satisfactory.

We find that the physical insights used to explain the ModiCon performance hold across the range of separation factors tested by our systems.

To create the new separations, we linearly scale the isotherm parameters ($a_{1,i}, b_{1,i}$ for bi-Langmuir, and Henry's constants for the linear system) while not changing the column's total capacity. For example, in the linear system, we let the separation factor be given as:

$$\alpha = \frac{H_A}{H_B} \tag{5.10}$$

where H_A and H_B are the Henry's constants. The column capacity is

$$capacity = H_A C_A^F + H_B C_B^F \tag{5.11}$$

where C_A^F and C_B^F are average concentration of components A and B in the feed.

We show the results in Figure 5.26. We define the percent improvement as

$$\%improvement = \frac{Productivity_{Modicon} - Productivity_{BaseCase}}{Productivity_{BaseCase}} \times 100\% \tag{5.12}$$

In the 4-zone system, we maintain the purity of A and B at above 95%; in the 5-zone system, we keep the purity above (95%, 90%, 95%) for (A,I,B).

The result of the Powell optimization of the separation systems shown in Figure 5.26 is consistent with our recommendations regarding ModiCon operation, although the systems with lower separation factors show a greater improvement in performance. In other words, the physical insights on which we base our recommendations are applicable across systems of different separation factors. There are still other system variables (e.g. degree of nonideality, nonlinearity) which may limit the applicability of these insights; we intend to address those in future research.

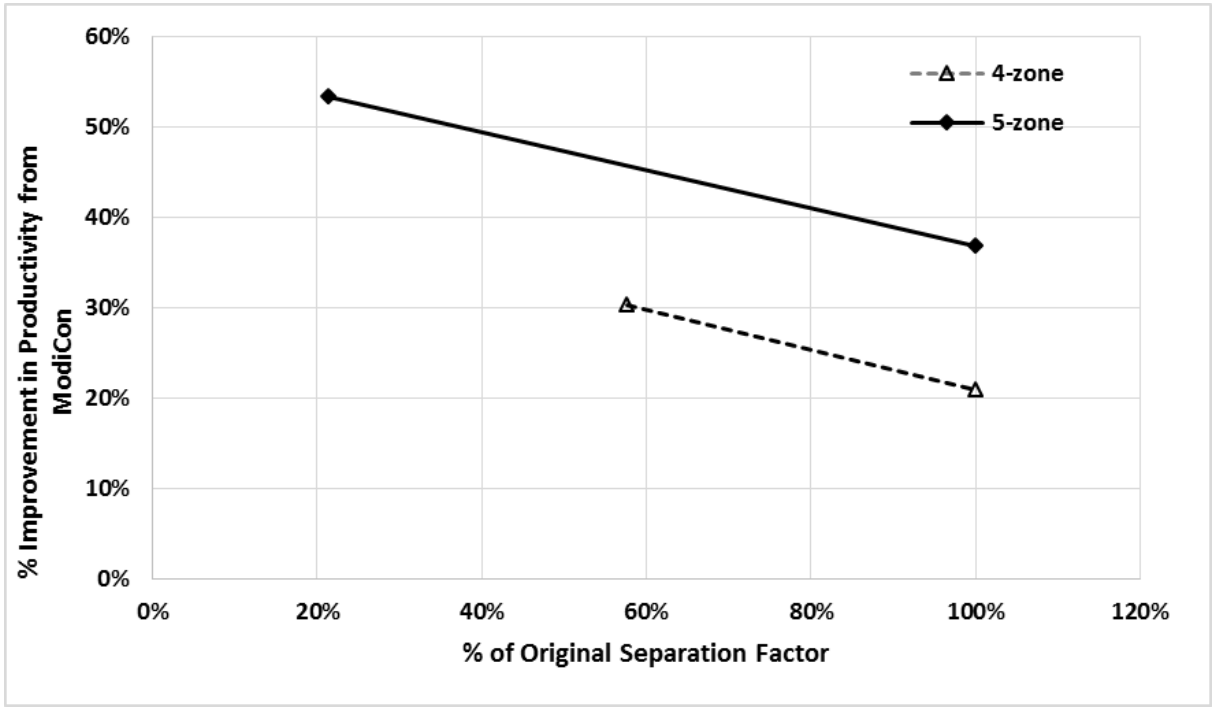

FIGURE 5.26. THE EFFECT OF SEPARATION FACTOR ON MODICON PERFORMANCE.

5.2. Five-Zone SMB and Operational Modes for Ternary Separation

5.2.1. Performance Results for the Ternary Separation with Fixed m Values

This section shows the performance results for the ternary separation of a mixture of amino acids. Basically, we follow all the steps as we have done for the 4-zone system. Table 3.6 summarizes and compares the simulation results for the basic 5-zone SMB model and the other operational modes. From the basic 5-zone SMB model, we find that the purity of the component I and the recovery of the component A in the column 3 of Table 3.6 are relatively low and need to be improved for this ternary separation system.

Figure 5.27 displays the performance improvement percentage by applying operational modes to the 5-zone SMB. First, we see from this figure that applying operational modes has very little benefit to the purity performance of the intermediate-affinity component I, but it could largely improve the A recovery performance index. Second, we find that 5-zone PowerFeed performs better than the 4-zone PowerFeed, even better than the 5-zone ModiCon. Third, combined operational modes still outperform others.

Therefore, through the design, evaluation and optimization for this ternary separation of amino acids, we have some conclusions for the 5-zone operational modes with fixed m-values. Varicol still works well on only improving one of the component purity, instead of improving the purity in both components at the optimization point. In the 5-zone system, PowerFeed performs quite well. ModiCon has very largely improvement for product purity and recovery in both cases we investigated. PF&MC is still the overall suggested choice with both highest product purity and recovery. Adding Varicol into PF&MC offers little benefit over the PF&MC operation for both cases. Therefore, it involves a balance for the selection of the combined operational modes because of the increasing complex of the process.

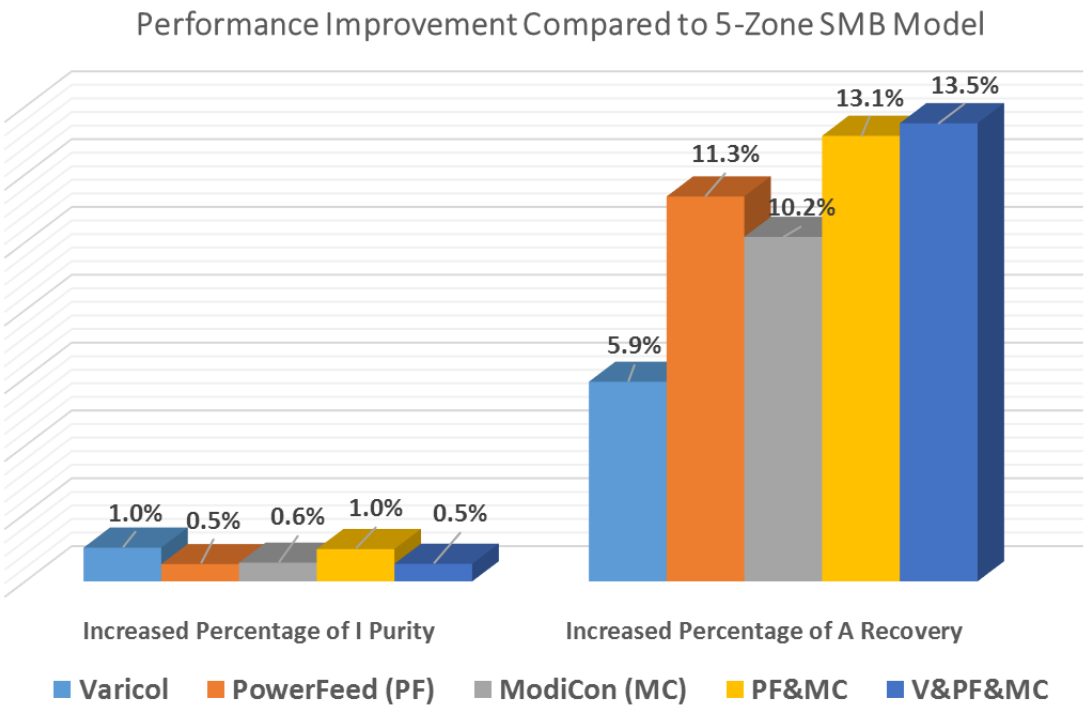

FIGURE 5.27. PERFORMANCE IMPROVEMENT FOR EACH OPERATIONAL MODE COMPARED TO THE BASIC 5-ZONE SMB MODEL.

5.2.2. Comparison of Improved Separation Regions for the Ternary Separation

We apply all the operational modes we have studied for the 4-zone process to a 5-zone process. We use the same evaluation methods to find the improved model for each operational mode: VARICOL, PowerFeed, ModiCon and combined operations. Afterward, we examine the flow rate ratios by creating the separation region plots to compare all the operational modes. In the 5-zone case, we plot the m_3-m_4 region, which is analogous to the m_2-m_3 region in a 4-zone system. The flow rate ratios m_j in a 5-zone system have precisely the same meaning as in the 4-zone system, and the difference between m_3 and m_4 values is proportional to the feed flow rate. Therefore, we find the best operating conditions by selecting the point in a complete separation region that is farthest from the $m_3 = m_4$ line (i.e. the point with the maximum feed capacity that satisfies our purity requirements.)

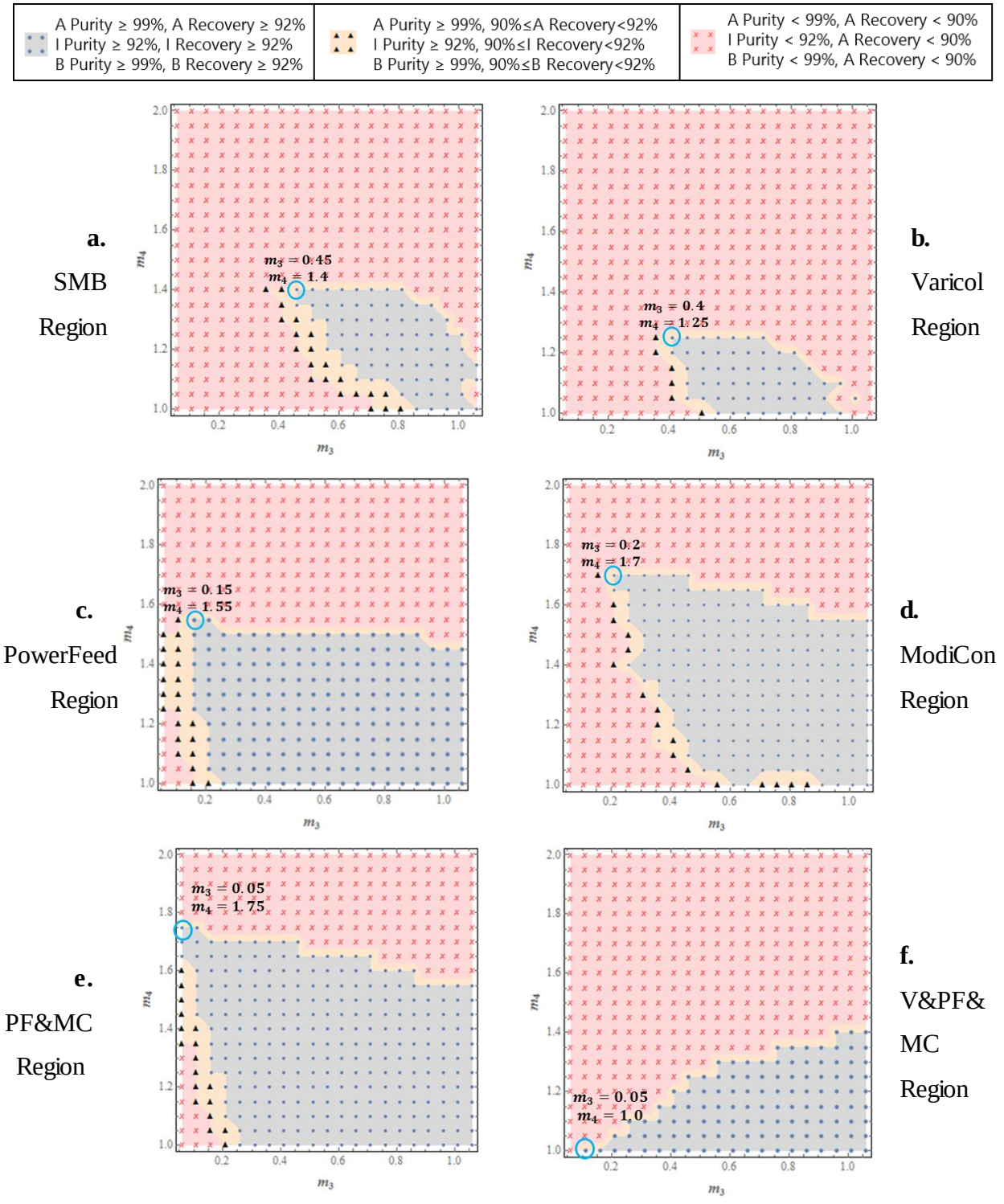

FIGURE 5.28. THE SEPARATION REGION PLOTS OF THE 5-ZONE OPERATIONAL MODES FOR THE TERNARY SEPARATION.

Figures 5.28 a to f show the complete separation regions for both purity and recovery results in the 5-zone base case and its operational modes. As in the 4-zone separation, we divide the simulations into three categories based on their separation performance indices. For product purity, the gray and yellow regions represent the purity criterion that both A&B purities are larger than 99%, and the purity of intermediate adsorbed component I is larger than 92%; but the pink region does not satisfy this purity criterion. For the recovery results, the gray region shows the region with all product recoveries larger than 92%, and the yellow area with all the recoveries larger than 90% but smaller than 92%, and the pink region is the one with all the recoveries lower than 90%, as shown in the symbol box in Figure 5.28. Each plot represents the simulation results of the specified operational mode. The labeled point on each graph represents the m_3-m_4 pair with maximum productivity that still satisfies the high purity (A&B $\geq$99%, I$\geq$92%) and given recovery (all recoveries $\geq$ 92%) constraints. We discuss each operational mode as follows.

(1) Varicol Model

In the 5-zone Varicol model, we observe similar trends of product purities concerning the effective numbers of beds as in the 4-zone system. In our 5-zone system, the most important manipulated variable is the effective bed number of zone 3, which means that this system is at least somewhat limited by its ability to desorb the intermediated-adsorbed component I from the solid fully. Figure 5.28b shows that, compared to the basic SMB separation region in Figure 5.28a, the Varicol by itself is unable to expand the separation region meaningfully.

(2) PowerFeed Model

Unlike the 4-zone system, PowerFeed performs quite well in the 5-zone system, as Figure 5.28c shows. It largely expands the separation region over the base case. The 5-zone PowerFeed still performs best with a rear-feeding scheme, just like in the 4-zone system.

(3) ModiCon Model

Figure 5.28d shows that ModiCon also gives a large improvement in the feasible separation region, as well as the PowerFeed did. This means that the PowerFeed or ModiCon column is able

to provide both the high productivity and low solvent consumption of the single operational modes for the 5-zone ternary process.

(4) Combinations

Figure 5.28e displays a small improvement over the PowerFeed or ModiCon. This result shows that like the 4-zone system, the combined PF&MC can extend the separation regions compared the single operational modes we studied. However, the differences between the combined operational modes and the single ModiCon mode are not significant enough to recommend one over the other, and the increased complexity needs to be considered in practice.

Figure 5.28f reveals that combining three operational modes does not expand the separation regions nearly as other modes did for the 5-zone system. This failure to outperform PF&MC or any other operational mode may be caused by an increased sensitivity to the m_3 and m_4 values, or the Varicol conditions we add into the PF&MC are not the optimum ones.

5.2.3. Pareto Approach for All Operational Modes

Figure 5.29a shows the Pareto plots for two conflicting performance indices, purity of the intermediate adsorbed component I and total productivity of the ternary separation for all the operational modes investigated. Each numbered curve represents the basic SMB or the operational mode's Pareto optimal results. Figure 5.29b shows an example of generating a basic SMB's Pareto plot with circled dark points. All the points represent the simulation runs with different sets of $(m_2 - m_3 - m_4)$. We distribute the product purity and recovery performance results in Figure 5.29b, and choose the Pareto points in terms of the following mathematical expressions for the optimization problem:

$$\text{Max } F_1 = Pur_I[m_2, m_3, m_4] \tag{5.13}$$

$$\text{Max } F_2 = Productivity[m_2, m_3, , m_4] \tag{5.14}$$

$$m_2 \in [2.0\ , 3.0]; \tag{5.15}$$

$$m_3 \in [0.06, 1.06]; \tag{5.16}$$

$$m_4 \in [1\ ,2]; \tag{5.17}$$

Subject to: $$Pur_I \geq 80\% \tag{5.18}$$

and $$Productivity \geq \frac{0.02\frac{g}{L}}{hr} \tag{5.19}$$

Through the simulations with changing m-values in the provided ranges, we make all the simulation points in one graph for each operational mode, and choose the optimal points for the Pareto plots. Figure 5.29a shows the improved separation performance by operational modes and the robustness of the effect to component I purity on the total productivity from the $m_2 - m_3 - m_4$ sets. Specifically, we find that:

(1) All operational modes for the 5-zone system give improve performance in the Pareto Plot over the basic 5-zone base case, just as is the case for the 4-zone system.

(2) Like 4-zone binary system, Varicol has similar trend and a small improvement over the basic SMB.

(3) 5-zone PowerFeed performs better than the 4-zone PowerFeed, compared to their own basic SMBs.

(4) Like 4-zone binary system, ModiCon outperforms other single operational modes. The 5-zone ModiCon in the Pareto plot shows better results than the combined operational modes.

(5) The combined PF&MC operational mode for 5-zone system has very similar results as the 5-zone ModiCon.

(6) Adding Varicol to the PF&MC has no benefit and is even worse than the combined PF&MC mode for the 5-zone. The separation region plots in Figure 5.28 also support this conclusion.

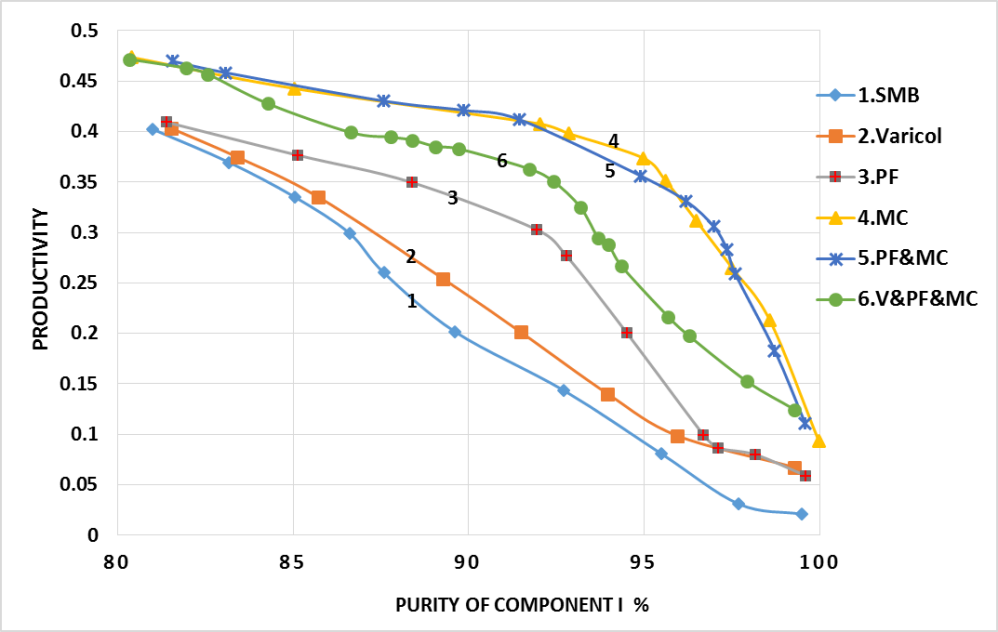

FIGURE 5.29A. PARETO APPROACH BETWEEN COMPONENT I PURITY AND PRODUCTIVITY FOR THE TERNARY SEPARATION FOR ALL THE OPERATIONAL MODES.

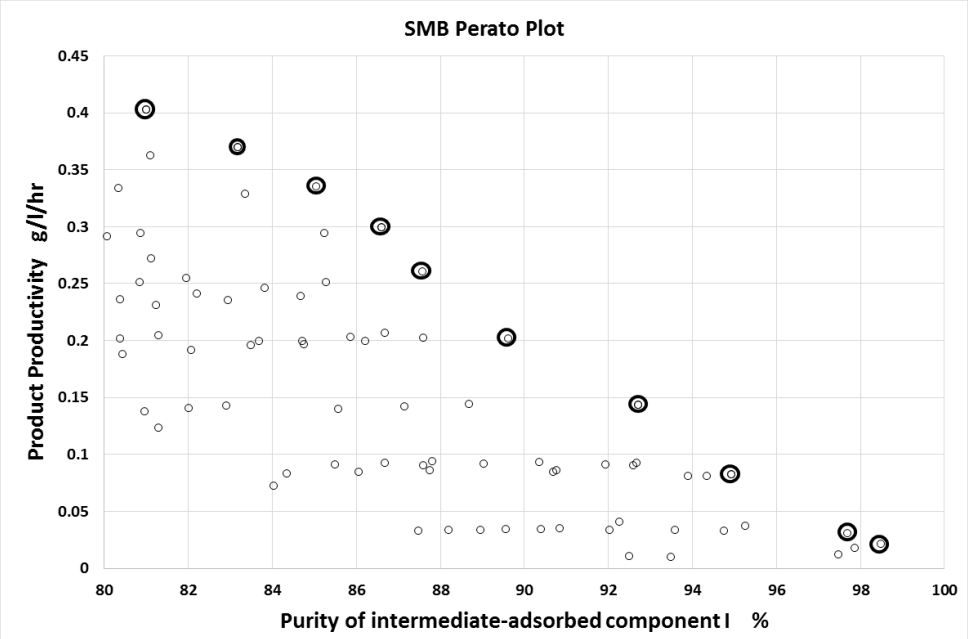

FIGURE 5.29B. AN EXAMPLE OF PARETO PLOT FOR THE BASIC SMB.

5.3. Key Findings and Conclusions for Both Separations

Our work outlines an approach for simulating and improving the performance of several operational modes in SMB systems in terms of product purity, recovery, concentration profiles, and other performance indices. Our approach is based on enumeration of different schemes, tuning the scheme's manipulated variables using heuristics, and evaluation of the robustness of the resulting variable set. Specifically, we consider the operational modes with the asynchronous shift of inlet/outlet ports ("Varicol"), variable feed flow rates ("PowerFeed" and "Partial feeding") and variable feed concentrations ("ModiCon") within the switching interval, together with their combinations. We perform this analysis on a binary enantiomer system and a ternary amino acid mixture. We compare the performance of the operational modes with the basic 4-zone SMB for the binary separation, and with the basic 5-zone SMB for the ternary separation. Separation regions on the plane of key ratios of net liquid flow rate through separation zone illustrate improved separation performances over the basic SMB cases. While we cannot guarantee our approach to find a global optimum, we are able to achieve notable improvements; some additional grid searches have confirmed that the operating points we find are close to the global optimum. We compare the separation performance in terms of different purity and recovery regions, and combine with the Pareto plots for the operational modes to provide the performance results for two conflicting indices.

Figures 30a and b summarize the results of the operational mode improvement with varying m-values in terms of productivity and recovery for both cases. These two figures reveal that the addition of the operational modes improves the productivity over that of the basic 4-zone or 5-zone SMB (1.38, 1.53 and 1.57 g/L/hr for the binary separation, and 0.08, 0.14 and 0.18 g/L/hr for the ternary separation at three recovery regions ≥99%, 95%-99% and 90%-95%). Each bar result represents the highest productivity result we can get in that specific average product recovery range. We can get higher productivity improvement if we drop the recovery criterion. We conclude from the separation region plots and the Pareto plots that applying operational modes does improve the performance much for the models with changing m-values, although it barely improves the basic SMB model with the chosen m-values. Therefore, it is possible to

improve the performance of both the basic 4-zone and 5-zone SMBs significantly by applying various operational modes and their combinations.

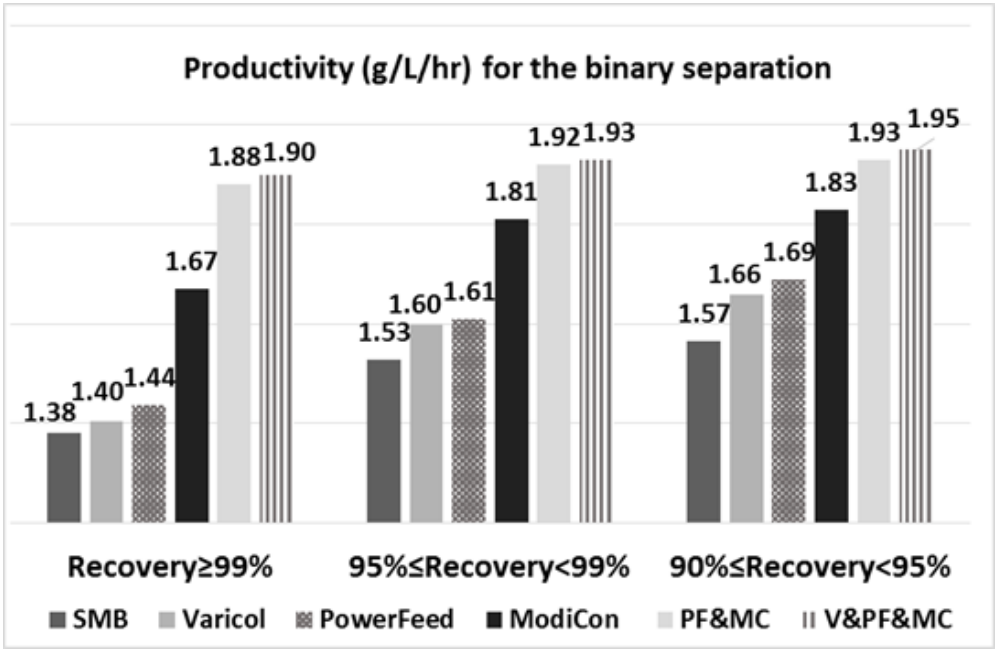

FIGURE 5.30A. PRODUCTIVITY RESULTS AT DIFFERENT PRODUCT RECOVERY RANGES FOR THE BINARY SEPARATION.

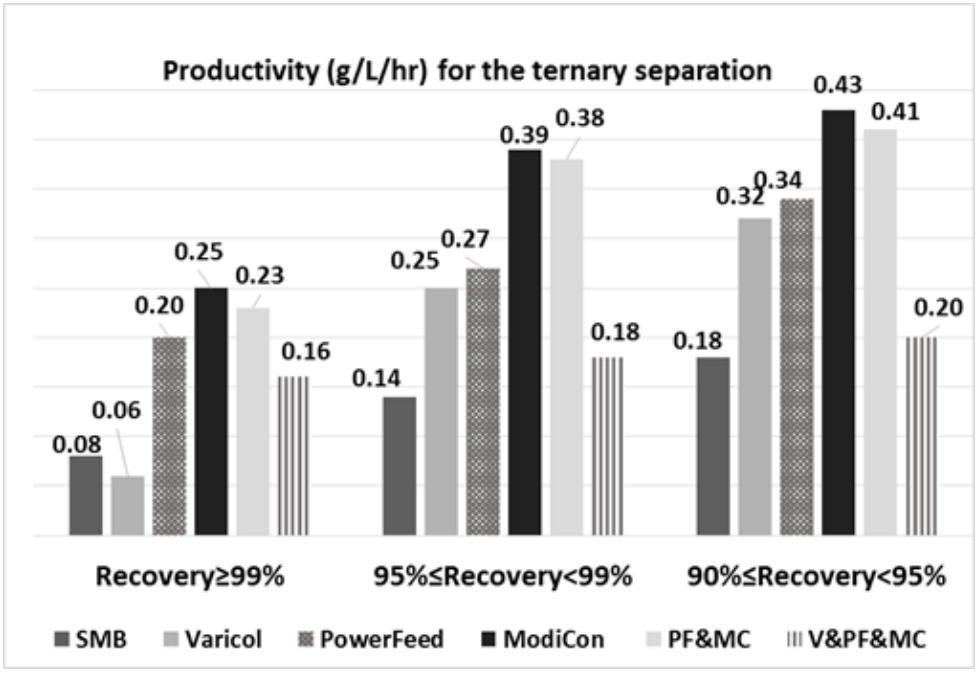

FIGURE 5.30B. PRODUCTIVITY RESULTS AT DIFFERENT PRODUCT RECOVERY RANGES FOR THE TERNARY SEPARATION.

Through the simulation and improvement, we find some similar trends between the two cases:

(1) Varicol provides only small improvements over the basic 4-zone or 5-zone SMB. Varicol is limited by its ability to fully improve all the component purities in both cases. However, it improves the base case in some of performance indices, while only slightly sacrificing other performance indices. We consider this operational mode when we need high purity in one component, but the other is considered as waste.
(2) PowerFeed in both systems performs better with a rear feed loading scheme. PowerFeed is highly sensitive to the m_2 ratio. We should be cautious when operating a PowerFeed unit to keep the flow rate in zone 2 constant.
(3) ModiCon is the best single operational mode for both product purity and recovery, and is the first choice for a single operational mode. ModiCon gives the largest improvement in the feasible separation region, and it is able to achieve both the highest productivity and lowest solvent consumption of the single operational modes we investigated.
(4) PF&MC expands the separation region over the ModiCon operation, and is the best choice of the combined operational modes we investigated for both cases.
(5) Significantly, the qualitative rankings of the different operational mode improvement mostly remains identical across the different performance indices between our heuristic improvement methods and Pareto optimization.

We also find some different trends between the binary and ternary cases.

(1) For the 4-zone SMB, PowerFeed gives only small improvement over the base case. However, PowerFeed performs quite well in the 5-zone system, nearly as well as ModiCon. In the future work, we need to study more separation systems to see whether PowerFeed works better for the systems with multi-components and multi-zones.
(2) For the 4-zone case, the combined operational mode V&PF&MC only has small improvement over the PF&MC. However, for the 5-zone case, adding Varicol to PF&MC has no benefit at all compared to other operational modes. It is not recommended over others because of its increased complexity.

6. Workshops for SMB Operational Modes

In this section, we include several workshops to demonstrate how to build models step by step using Aspen Chromatography[83] for both SMB and its operational modes, and analyze their separation performance through these simulations. We use the binary chiral separation of Tröger's base as an example for the following workshops. The purpose of this section is to guide the reader to build different SMB operational modes using Aspen Chromatography. It would help the reader understand the physical insights of the chromatographic processes better through these workshops. We give more details on the mode input for each operational mode. We also illustrate how to make plots and output the purity, recovery and concentration profile results from the SMB model and its operational modes in Aspen Chromatography.

6.1. Workshop 1: Using Aspen Chromatography to Model a 4-Zone SMB Unit

This workshop provides a step-by-step illustration to build a 4-zone basic SMB model for the binary chiral separation of the Tröger's base described in section 3.2.

Step 1: Start a new case in Aspen Chromatography, and save it as "4-zone basic SMB model".

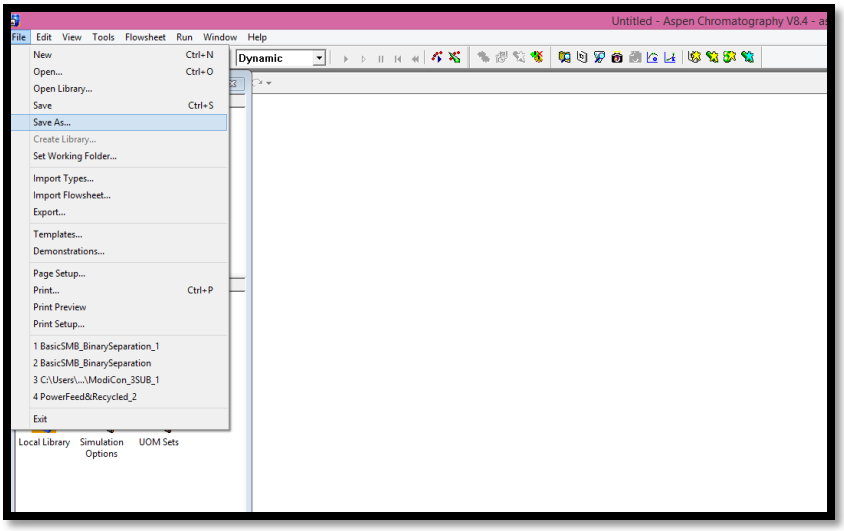

FIGURE 6.1. A NEW FILE NAMED 4-ZONE BASIC SMB MODEL.

Step 2: Go to "Model Library", then choose the blocks in Figure 6.2, and create the flowsheet for the basic SMB model. Select "Chromatography: Non-Reversible" ->"chrom_ccc_separator2" for the SMB column; select "Chromatography: Non-Reversible" ->"chrom_feed" for the DESORBENT and FEED blocks; select "Chromatography: Non-Reversible" ->"

chrom_product" for the EXTRACT and RAFFINATE blocks. Name the desorbent-in, extract-out, feed-in and raffinate-out streams as D, E, F and R.

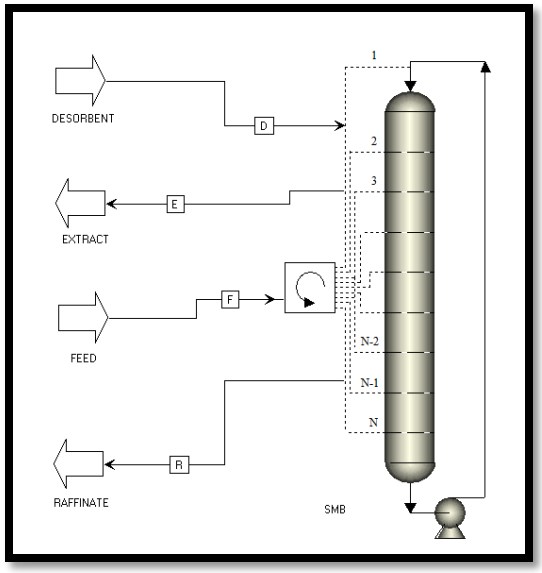

FIGURE 6.2. FLOWSHEET OF THE BASIC SMB MODEL IN ASPEN CHROMATOGRAPHY.

Step 3: Go to "Component Lists" in the Exploring window, double-click "Add Component List", and choose "Do not use Physical Properties (Set)" to add a new component set into the model. Name the components as TB+ (the most adsorbed component) and TB- (the least adsorbed component). See also the trace liquid assumption discussed in step 5 and illustrated in Figure 6.6.

FIGURE 6.3. BUILD A NEW COMPONENT SET AS DEFAULT.

Step 4: Go back to the flowsheet and double-click the SMB column block to edit the column configuration in the window of "Configure Block/Stream SMB", as shown in Figure 6.4. This figure shows the conditions of the separator:

1) We use a SMB unit with 6 beds in the column, which considers the solid adsorbent as a stationary phase packed in a fixed column.
2) All of the beds in this column have an identical cross-section with the same bed diameter and the same bed length.
3) We assume this column as a carousel internal configuration.
4) Since the column configuration for this 4-zone system is (1-2-2-1), the initial ports for D-In, F-In, E-Out and R-Out, respectively, are 1, 4, 2 and 6.
5) We apply the synchronous port switching control in the base case.
6) We use the sequential valves to deal with the port switching.
7) All the inlet and outlet ports would move to the next bed every 6.38 minutes as a switching time.
8) The closed recycle flow rate in this system is 0.47 ml/min.

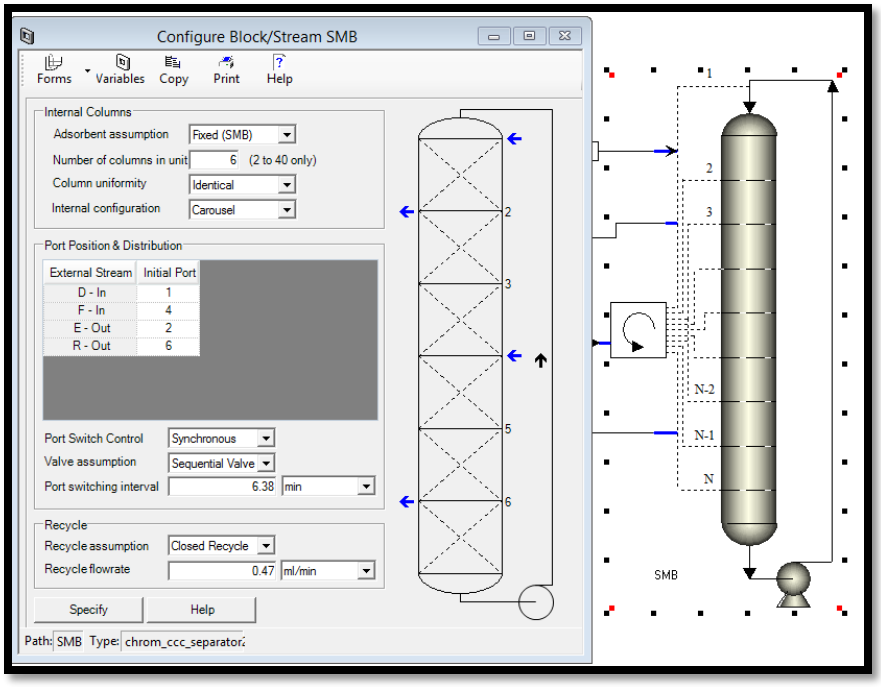

FIGURE 6.4. EDIT THE COLUMN CONFIGURATION IN THE SMB COLUMN BLOCK.

Step 5: Go to "Forms", and choose the option of "Column" to define the assumptions of the SMB column: General->PDE Discretization Method. We use the quadratic upwind differencing scheme

(QUDS; QDS in the software) with 40 element nodes as a discretization method. QUDS is a linear finite element scheme that gives a good fit of model predictions to experimental results. For this binary separation, QUDS method has very good accuracy and little numerical dispersion, and is well suited to time integration.

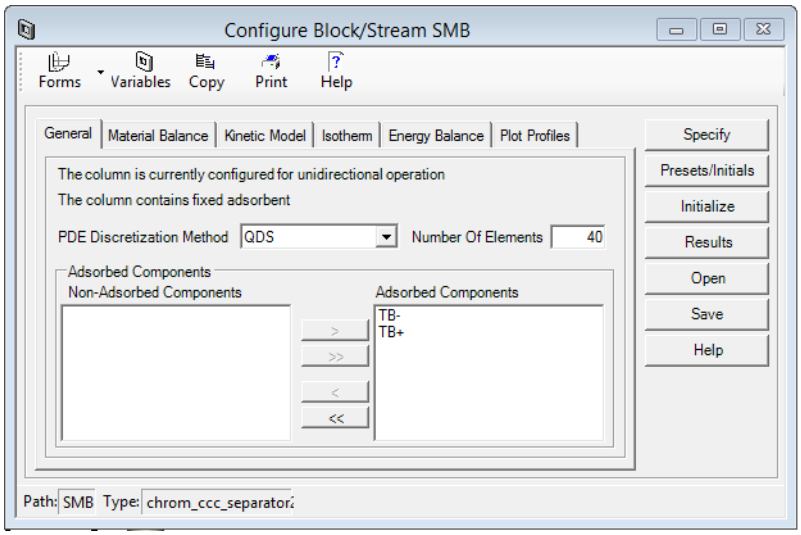

FIGURE 6.5. PARTIAL DIFFERENTIAL EQUATION DISCRETIZATION METHOD IN THE BASIC SMB MODEL.

Step 6: Material Balance -> Material Balance Assumption -> Convection with Dispersion Based on Peclet Number (Hb). We use the convection with dispersion based on Peclet number as a material balance assumption. This assumption evaluates the axial dispersion coefficient as a function of the Peclet number based on the column length:

$$D_L = \frac{uL}{Pe\,\varepsilon_i} \tag{6.1}$$

where D_L= axial dispersion coefficient, u=superficial velocity of the fluid, L=column length, Pe=particle Peclet number, ε_i =interparticle voidage.

We use the trace liquid assumption because the bulk density through the column is considered not significantly during operation. This is the typical case when modeling trace solute systems. In this way, we do not need to consider the solvent as a modeled component. Then, the mass balance equation is:

$$\frac{\partial C_i}{\partial t} + \frac{(1-\varepsilon)}{\varepsilon}\frac{\partial q_i}{\partial t} + u\frac{\partial C_i}{\partial z} = D_L\frac{\partial^2 C_i}{\partial z^2} \tag{6.2}$$

where C_i is the concentration for component i in the fluid phase, q_i is the concentration for component i in the solid phase, and ε represents the overall bed voidage, z is the axial distance through the column and D_L is the axial dispersion coefficient.

For this 4-zone SMB model, we simply choose the assumption of packing pressure drop in the column. It applies the Carman-Kozeny equation, which relates the pressure drop inside the chromatographic column to the superficial velocity:

$$\frac{\Delta P_j}{n_j * l} = \frac{-150\mu(1-\varepsilon)^2}{(2r_p\psi)^2\varepsilon^3}\frac{Q_j}{S} \qquad \textbf{(6.3)}$$

In the equations, ΔP_j =pressure drop in each zone; n_j=bed number in each zone; l=length of each bed; ΔP_{max}= maximum pressure drop through the column; ϕ = pressure drop coefficient; S = cross-sectional area of the bed; ε = overall bed voidage; μ = fluid viscosity; r_p = particle radius; $and\ \psi$ = particle shape factor.

The Carman-Kozeny equation is the only pressure drop correlation implemented in Aspen Chromatography, though this equation is valid only for laminar flow in packed beds. For the turbulent flows, the Ergun equation is a better correlation for pressure drop. However, the difference in pressure drop estimates by the Carman Kozeny and Ergun equations is very small (less than 0.5%). Therefore, we employ the Carman-Kozeny in this case.

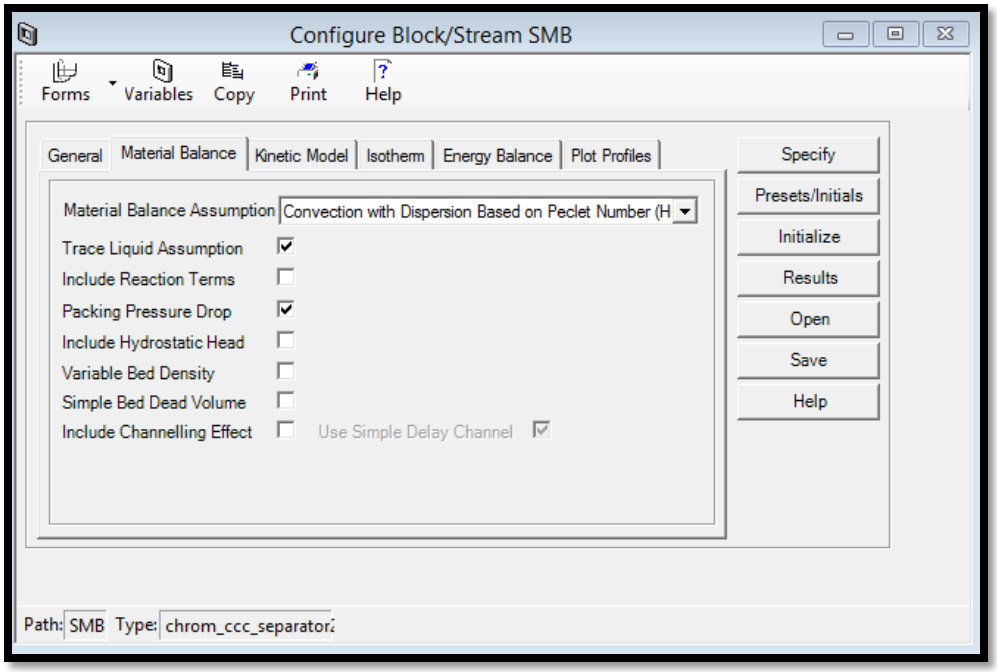

FIGURE 6.6. MATERIAL BALANCE METHOD IN THE BASIC SMB MODEL.

Step 7: Kinetic Model->Film Model Assumption and Mass Transfer Coefficients.

As we know, a species that is being adsorbed from the bulk liquid phase onto an active surface site of the adsorbent, usually encounters mass transfer resistances:

- Between the bulk liquid and the external adsorbents surface
- Exerted by the adsorbents pore structure

We select the linear lumped resistance in this model, where we lump together these resistances. The mass transfer driving force for component i is a linear function of the solid phase loading:

$$\frac{\partial q_i}{\partial t} = k_i(q_i^* - q_i) \tag{6.4}$$

where k_i is the linear lumped mass transfer coefficient, q_i is solute concentrations of the solid phase, and q_i^* represents the adsorbed phase concentration at equilibrium with the liquid phase.

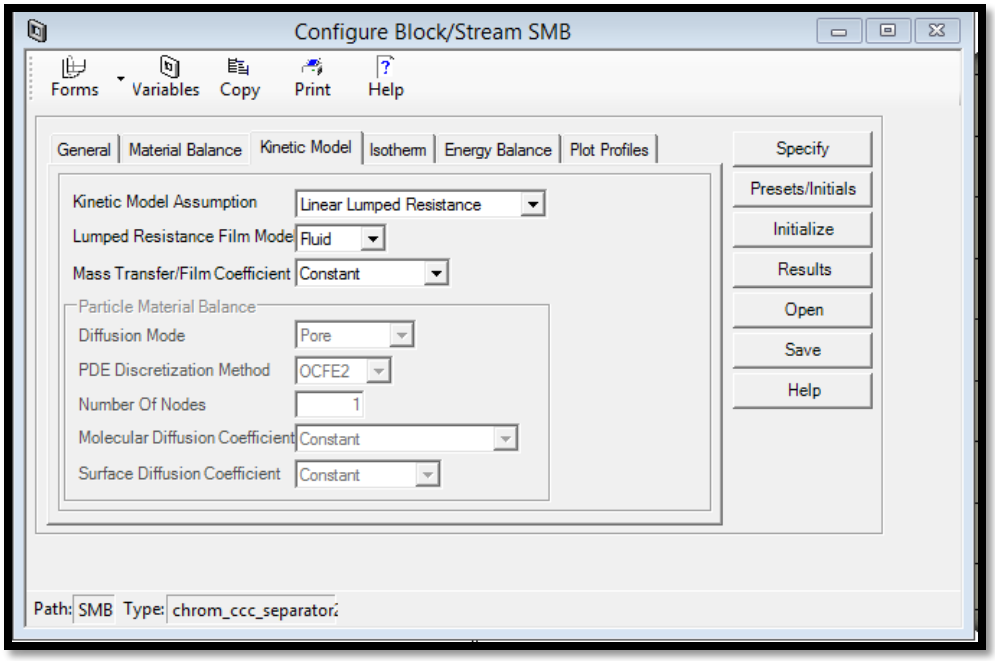

FIGURE 6.7. KINETIC METHOD IN THE BASIC SMB MODEL.

Step 8: Isotherm -> Langmuir Assumption -> Dual-Site Langmuir.

Adsorption isotherms are important data in the design of chromatographic systems, because the driving force behind all adsorptive liquid separation processes lies in the departure from adsorption equilibrium.

We assume the bi-Langmuir adsorption isotherm based on volume loading to predict the performance of the chromatographic column for the specified operating conditions. The bi-Langmuir adsorption isotherm equation is:

$$C_i^* = \frac{a_{i,1} C_i}{1 + \sum b_{i,1} C_i} + \frac{a_{i,2} C_i}{1 + \sum b_{i,2} C_i} \quad (i = A, B) \qquad \textbf{(6.5)}$$

In the equation, C_i^* is the adsorbed phase concentration of component i in equilibrium with the mobile phase. $a_{i,1}, a_{i,2}, b_{i,1}, b_{i,2}$ are the bi-Langmuir isotherm parameters for component i.

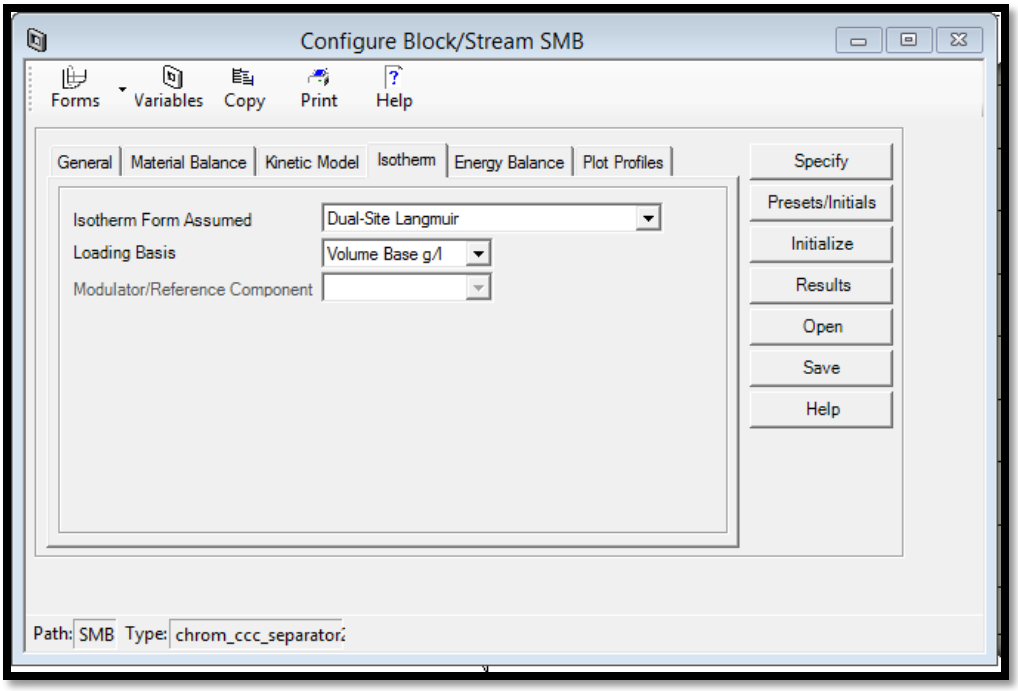

FIGURE 6.8. ISOTHERM METHOD IN THE BASIC SMB MODEL.

Step 9: Energy Balance->Isothermal Operation at 23 °C.

We select the isotherm operation at 23 °C, where the variables for fluid, solid and wall temperature would become inactive in this mode.

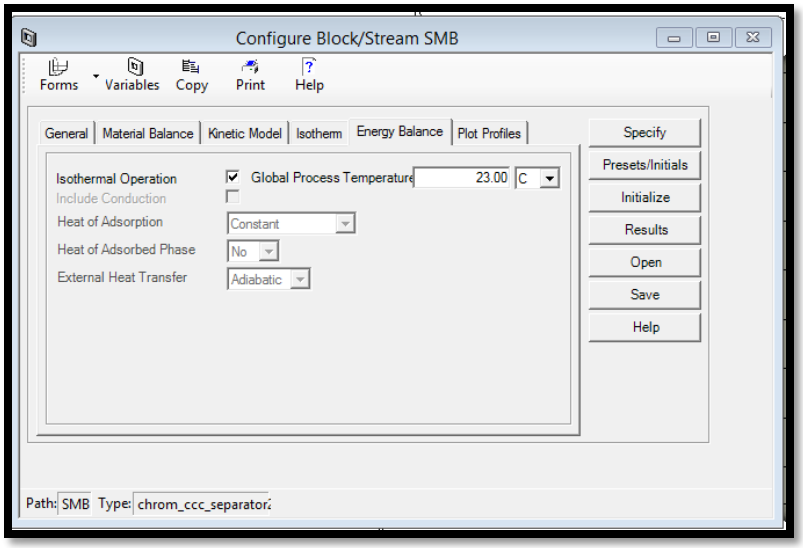

FIGURE 6.9. ENERGY BALANCE METHOD IN THE BASIC SMB MODEL.

Step 10: Plot Profiles->Available Plot Profiles.

Theses Plot Profiles tab in Figure 6.10 contains the most commonly used profile variables for the generation of profiles plots. We can simply copy and paste the variables when generating a Profile plot.

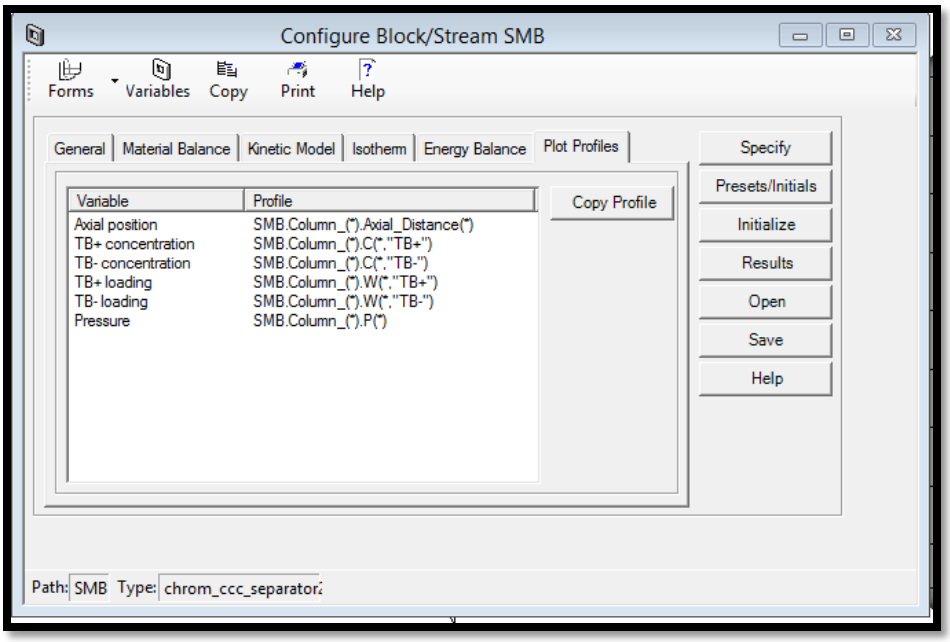

FIGURE 6.10. AVAILABLE PLOT PROFILES IN THE BASIC SMB MODEL.

Step 11: SMB Column -> Specify

Table 6.1 summarizes all the variable values assumed in steps 5 to 10 for the basic SMB column. Figure 6.11 shows the implementation. Since eq 6.5 is the bi-Langmuir adsorption isotherm, and the equation with IP1, IP2, IP3 and IP4 in Aspen Chromatography is given by:

$$C_i^* = \frac{IP_{1i}IP_{2i}C_i}{1+\sum IP_{2i}C_i} + \frac{IP_{3i}IP_{4i}C_i}{1+\sum IP_{4i}C_i} \quad (i = A, B) \qquad \textbf{(6.6)}$$

By comparing eqs 6.5 and 6.6, we get:

$IP_{2A} = b_{A,1} = 0.0107;$

$IP_{2B} = b_{B,1} = 0.0132;$

$IP_{4A} = b_{A,2} = 0.601;$

$IP_{4B} = b_{B,2} = 0.136;$

$$IP_{1A} = \frac{a_{A,1}}{IP_{2A}} = \frac{3.99}{0.0107} = 372.9;$$

$$IP_{1B} = \frac{a_{B,1}}{IP_{2B}} = \frac{1.56}{0.0132} = 118.18;$$

$$IP_{3A} = \frac{a_{A,2}}{IP_{4A}} = \frac{0.986}{0.601} = 1.64;$$

$$IP_{3B} = \frac{a_{B,2}}{IP_{4B}} = \frac{0.304}{0.136} = 2.235$$

TABLE 6.1. THE SPECIFICATION FOR ALL THE ASSUMPTIONS IN THE SMB COLUMN.

Column Length	Hb	15 cm
Column Diameter	Dia	0.46 cm
Inter-particle voidage	ε	0.68 m^3 void /m^3 bed
Adsorbent particle radius	r_p	10 micron
Particle shape factor	ψ	0.1475
Liquid (Ethanol) viscosity	MUI	1.07 Cp
Recycle Pressure	P_{recy}	15 bar
Dual-Site Bi-Langmuir isotherm	A (TB+)	B (TB-)
$a_{i,1}$	3.99	1.56
$b_{i,1}$ (L/g)	0.0107	0.0132
$a_{i,2}$	0.986	0.304
$b_{i,2}$ (L/g)	0.601	0.136
Mass transfer coefficient k_i (1/s)	1.81	2.96
Peclet number	500	500

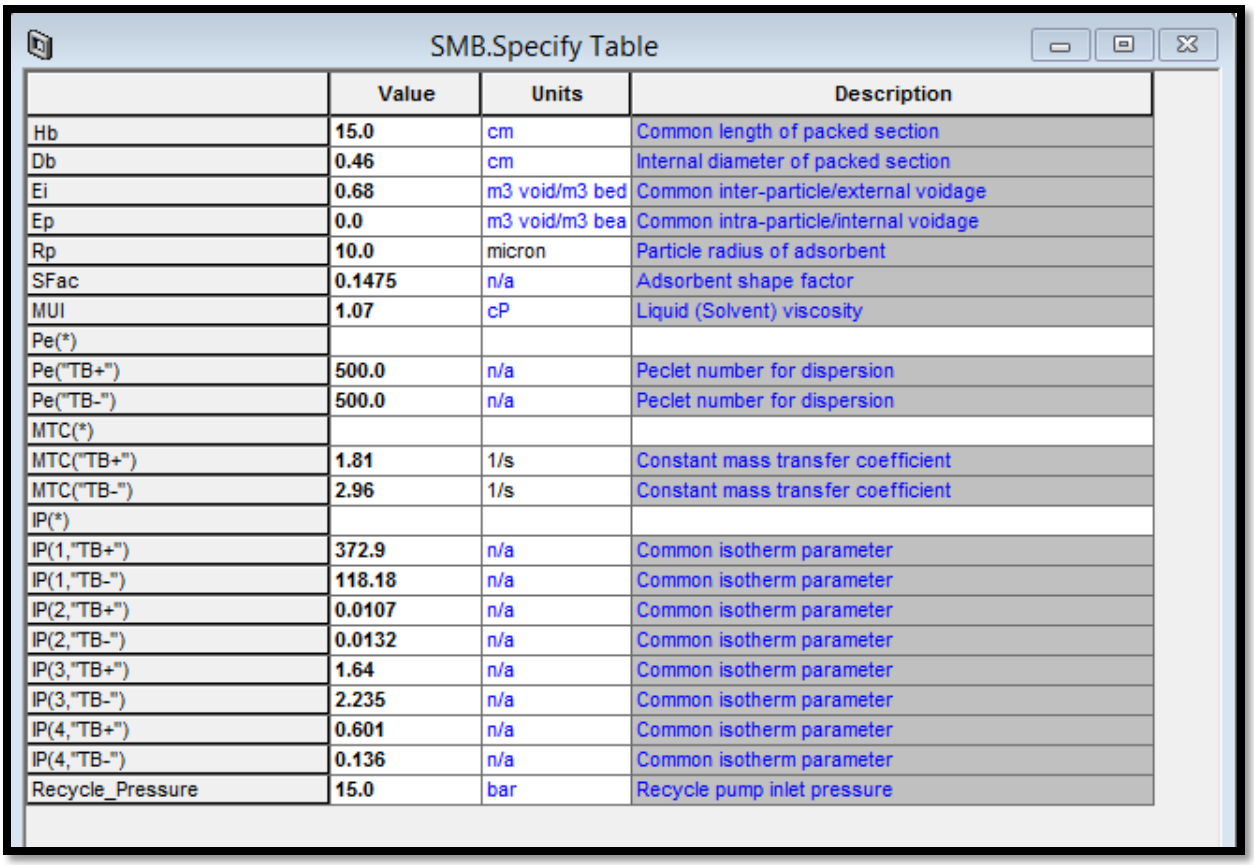

	Value	Units	Description
Hb	15.0	cm	Common length of packed section
Db	0.46	cm	Internal diameter of packed section
Ei	0.68	m3 void/m3 bed	Common inter-particle/external voidage
Ep	0.0	m3 void/m3 bea	Common intra-particle/internal voidage
Rp	10.0	micron	Particle radius of adsorbent
SFac	0.1475	n/a	Adsorbent shape factor
MUI	1.07	cP	Liquid (Solvent) viscosity
Pe(*)			
Pe("TB+")	500.0	n/a	Peclet number for dispersion
Pe("TB-")	500.0	n/a	Peclet number for dispersion
MTC(*)			
MTC("TB+")	1.81	1/s	Constant mass transfer coefficient
MTC("TB-")	2.96	1/s	Constant mass transfer coefficient
IP(*)			
IP(1,"TB+")	372.9	n/a	Common isotherm parameter
IP(1,"TB-")	118.18	n/a	Common isotherm parameter
IP(2,"TB+")	0.0107	n/a	Common isotherm parameter
IP(2,"TB-")	0.0132	n/a	Common isotherm parameter
IP(3,"TB+")	1.64	n/a	Common isotherm parameter
IP(3,"TB-")	2.235	n/a	Common isotherm parameter
IP(4,"TB+")	0.601	n/a	Common isotherm parameter
IP(4,"TB-")	0.136	n/a	Common isotherm parameter
Recycle_Pressure	15.0	bar	Recycle pump inlet pressure

FIGURE 6.11. ALL THE VARIABLE VALUES NEEDED FOR ALL THE ASSUMPTIONS.

Step 12: SMB Column -> Presets/Initials

We set all the initial variable values in Figure 6.11 as zero for the model, and then press the "Initialize" button to initialize the column, as illustrated in Figure 6.12.

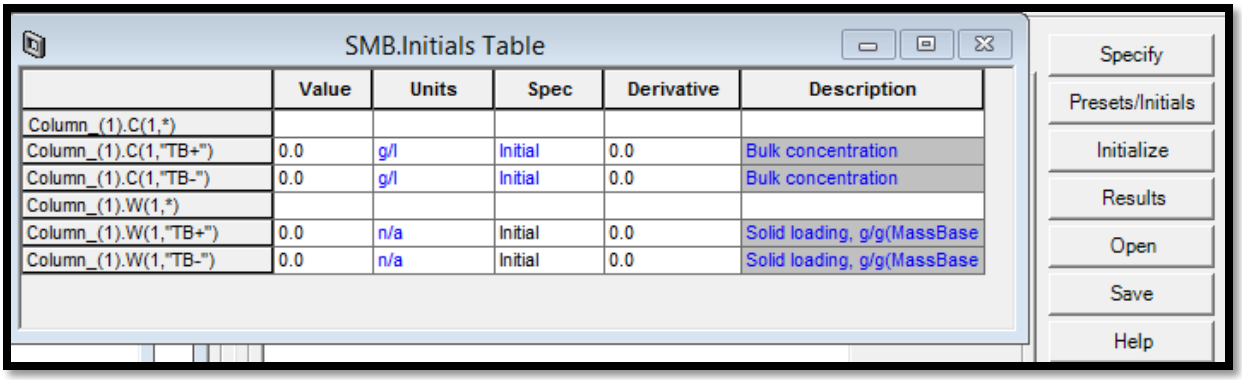

	Value	Units	Spec	Derivative	Description
Column_(1).C(1,*)					
Column_(1).C(1,"TB+")	0.0	g/l	Initial	0.0	Bulk concentration
Column_(1).C(1,"TB-")	0.0	g/l	Initial	0.0	Bulk concentration
Column_(1).W(1,*)					
Column_(1).W(1,"TB+")	0.0	n/a	Initial	0.0	Solid loading, g/g(MassBase
Column_(1).W(1,"TB-")	0.0	n/a	Initial	0.0	Solid loading, g/g(MassBase

FIGURE 6.12. ALL THE INITIAL VARIABLE VALUES NEEDED FOR THE MODEL.

Step 13: Feed block->Feed Specification.

In this process, the feed-in flow rate is 0.38 ml/min. We use a feed concentration of 0.5 g/l for each component, and the feed contains 50% component A and 50% component B by weight. We set the feed pressure as a free variable.

FEED.Specify Table

	Value	Units	Spec	Description
Flowrate	0.38	ml/min	Fixed	Feed flowrate
Overall_Concentration	1.0	g/l	Fixed	Total concentration of the feed
Material_Fraction(*)				
Material_Fraction("TB+")	50.0	%	Fixed	Mass fraction of the feed
Material_Fraction("TB-")	50.0	%	Fixed	Mass fraction of the feed
Pressure	35.2094	bar	Free	Feed pressure
Cref(*)				
Cref("TB+")	1.0	g/l	Fixed	Reference concentration
Cref("TB-")	1.0	g/l	Fixed	Reference concentration

FIGURE 6.13. FEED SPECIFICATION FOR THE MODEL.

Step 14: Desorbent block->Desorbent Specification.

In this process, the desorbent-in flow rate is 0.65 ml/min. Since the liquid desorbent does not contain the TB+ and TB-, we set both concentrations as zero in Figure 6.14. We set the pressure as a free variable.

DESORBENT.Specify Table

	Value	Units	Spec	Description
Flowrate	0.65	ml/min	Fixed	Feed flowrate
Component_Concentration(*)				
Component_Concentration("TB+")	0.0	g/l	Fixed	Component concentration of the
Component_Concentration("TB-")	0.0	g/l	Fixed	Component concentration of the
Pressure	54.4394	bar	Free	Feed pressure
Cref(*)				
Cref("TB+")	1.0	g/l	Fixed	Reference concentration
Cref("TB-")	1.0	g/l	Fixed	Reference concentration

FIGURE 6.14. DESORBENT SPECIFICATION FOR THE MODEL.

Step 15: Raffinate block-> Raffinate Specification.

The raffinate-out flow rate is 0.43 ml/min. We set the pressure as a free variable.

RAFFINATE.Specify Table

	Value	Units	Spec	Description
Flowrate	0.43	ml/min	Fixed	Sink flowrate
Pressure	19.1843	bar	Free	Sink pressure
Cref(*)				
Cref("TB+")	1.0	g/l	Fixed	Reference concentration
Cref("TB-")	1.0	g/l	Fixed	Reference concentration

FIGURE 6.15. RAFFINATE SPECIFICATION FOR THE MODEL.

Step 16: Extract block->Extract Specification.

In the Extract block, we set both extract flow rate and the pressure as free in Figure 6.16. Since all the other three (feed, desorbent, raffinate) flow rates as fixed, we can calculate the extract flow rate through the mass balance in the model.

EXTRACT.Specify Table

	Value	Units	Spec	Description
Flowrate	0.6	ml/min	Free	Sink flowrate
Pressure	44.4683	bar	Free	Sink pressure
Cref(*)				
Cref("TB+")	1.0	g/l	Fixed	Reference concentration
Cref("TB-")	1.0	g/l	Fixed	Reference concentration

FIGURE 6.16. EXTRACT SPECIFICATION FOR THE MODEL.

Step 17: Dead Volume Specification -> Pipe Volume in the inlet and outlet streams.

For all the inlet outlet streams Desorbent (D), Extract (E), Feed (F) and Raffinate (R), we set the same dead volume with the pipe length of 18 cm and pipe diameter as 0.075 cm.

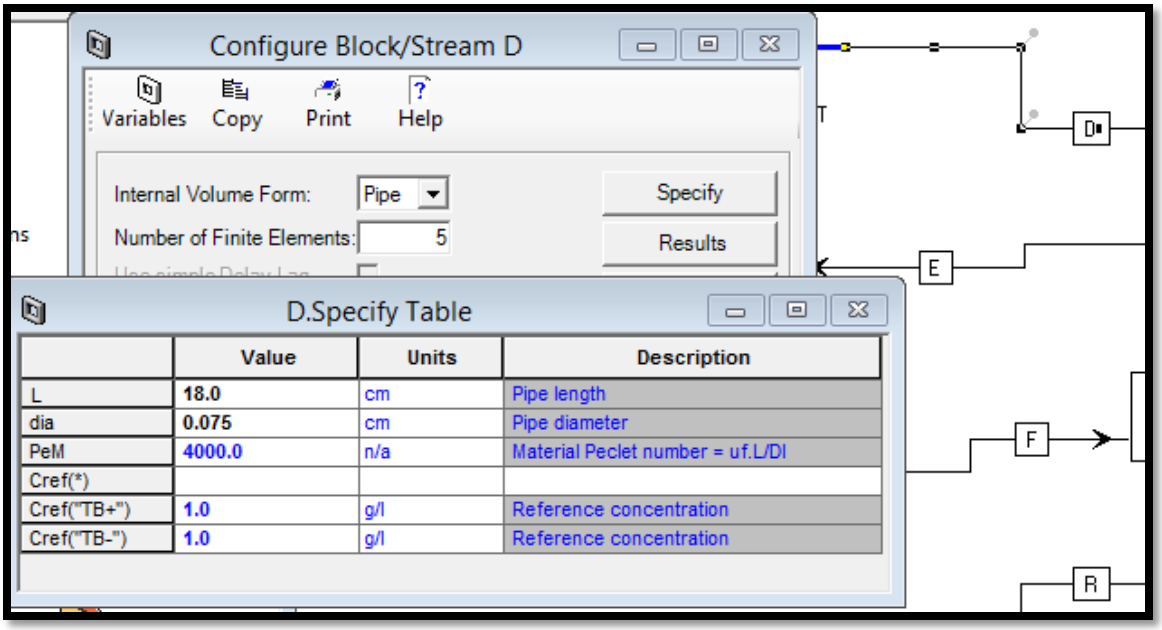

FIGURE 6.17. DEAD VOLUME SPECIFICATION IN ALL THE INLET AND OUTLET STEAMS.

Step 18: Dead Volume Specification in the column.

Go to the "Forms" in the "Configure Block/Stream SMB", select the streams and press the "Open".

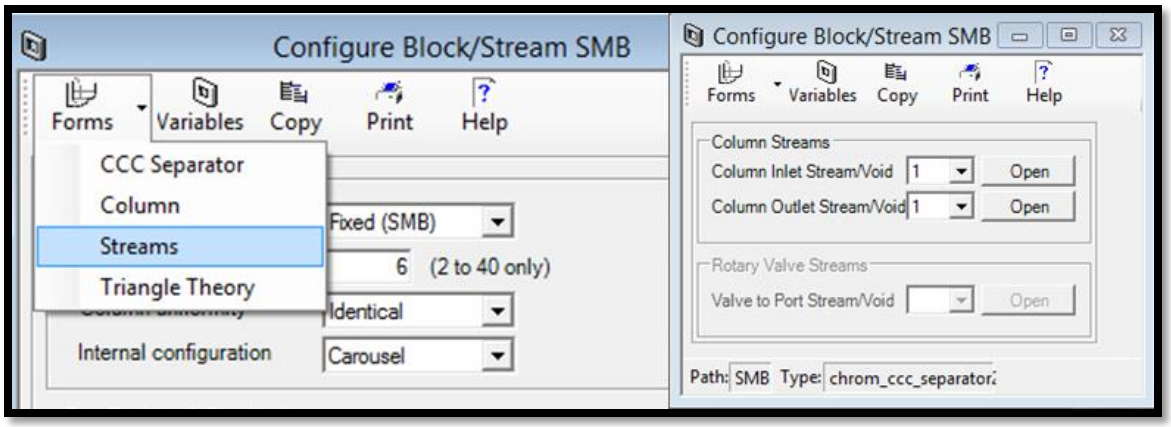

FIGURE 6.18. OPEN THE INLET/OUTLET STREAMS IN THE COLUMN.

We make sure that the total dead volume equals to 0.23 mL, and assume an effective dead volume with fixed pipe diameter and pipe length. For all the dead volumes in the column, we define the same dead volume with the pipe length of 20 cm and pipe diameter as 0.075 cm for each inlet and outlet void.

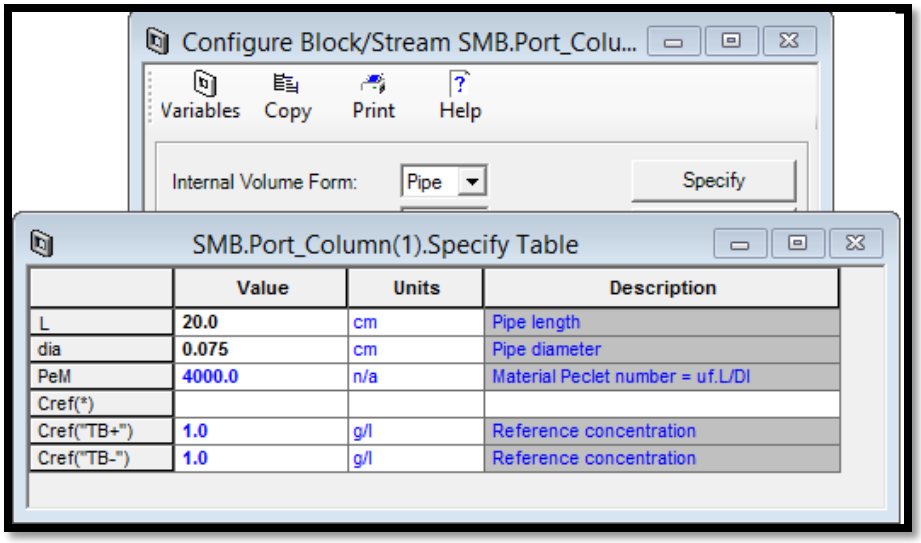

FIGURE 6.19. DEAD VOLUME SPECIFICATION IN THE COLUMN.

Step 19: Flowsheet Constraints-> the calculation of flow rates form m-values.

This step shows the detailed programming we put in the flowsheet constraints of the model to define the calculation of the flow rate ratios in eqs 6.7 to 6.10.

$$m_1 = \frac{Q_1 t_{sw} - V_{bed}\varepsilon - V_1^D}{V_{bed}(1-\varepsilon)} \quad \textbf{(6.7)}$$

$$m_2 = \frac{Q_2 t_{sw} - V_{bed}\varepsilon - V_2^D}{V_{bed}(1-\varepsilon)} \quad \textbf{(6.8)}$$

$$m_3 = \frac{Q_3 t_{sw} - V_{bed}\varepsilon - V_3^D}{V_{bed}(1-\varepsilon)} \quad \textbf{(6.9)}$$

$$m_4 = \frac{Q_4 t_{sw} - V_{bed}\varepsilon - V_4^D}{V_{bed}(1-\varepsilon)} \quad \textbf{(6.10)}$$

In the euqations, m_1, m_2, m_3 and m_4 represent the flow rate ratios in the zone1, zone2, zone3 and zone4, respectively; Q_1, Q_2, Q_3 and Q_4 represent the flow rates in the zone1, zone2, zone3 and zone4, respectively; V_1^D, V_2^D, V_3^D and V_4^D represent the dead volume in the zone1, zone2, zone3 and zone4, respectively; V_{bed}=the bed volume through the column; ε= the overall voidage.

First, we define m values as real variables at fixed values:

```
m1 as RealVariable(fixed);
m2 as RealVariable(fixed);
m3 as RealVariable(fixed);
m4 as RealVariable(fixed);
```

Second, we include all the definition of the volume we use in the equations, including the whole column volume (ColVol) and the dead volume in each zone (DeadVol):

```
ColVol as c_Volume(free);
DeadVol as c_Volume(free);
DeadVol = 0.23;
ColVol = SMB.Hb * 3.1415926 * (SMB.Db / 2) ^ 2;
```

Third, we follow equations 6.7 to 6.10 to define the flow rate ratio of each zone:

```
m1 * ColVol * (SMB.Ei - 1) = ColVol * SMB.Ei - SMB.Switch_Time * 1000 *
(DESORBENT.Flowrate + SMB.Recycle_Flowrate) + DeadVol;
m2 * ColVol * (SMB.Ei - 1) = ColVol * SMB.Ei - SMB.Switch_Time * 1000 *
(RAFFINATE.Flowrate - FEED.Flowrate + SMB.Recycle_Flowrate) + DeadVol;
m3 * ColVol * (SMB.Ei - 1) = ColVol * SMB.Ei - SMB.Switch_Time * 1000 *
(RAFFINATE.Flowrate + SMB.Recycle_Flowrate) + DeadVol;
m4 * ColVol * (SMB.Ei - 1) = ColVol * SMB.Ei - SMB.Switch_Time * 1000
*SMB.Recycle_Flowrate + DeadVol;
```

Step 20: Flowsheet Constraints-> the calculation of performance indices

This step shows the detailed programming in the flowsheet constraints of the model to define the calculation of performance indices in eqs 6.11 to 6.17.

First, we set the PurityA, PurityB, RecoveryA and RecoveryB as fraction variables in eqs 6.11 to 6.14.

$$\text{PurityA} = \overline{Pur_A} = \frac{\bar{C}_A^E}{\bar{C}_A^E + \bar{C}_B^E} \qquad \textbf{(6.11)}$$

$$\text{PurityB} = \overline{Pur}_B = \frac{\bar{C}_B^R}{\bar{C}_A^R + \bar{C}_B^R} \quad \textbf{(6.12)}$$

$$RecoveryA = \overline{Rec}_A = \frac{Q_E \bar{C}_A^E}{Q_F \bar{C}_A^F} \quad \textbf{(6.13)}$$

$$RecoveryB = \overline{Rec}_B = \frac{Q_R \bar{C}_B^R}{Q_F \bar{C}_B^F} \quad \textbf{(6.14)}$$

```
PurityA  as Fraction;
PurityA  = Min(E.Total_Component("TB+")  / Max(E.Total_Mass,0.0000001),1);

PurityB  as Fraction;
PurityB  = Min(R.Total_Component("TB-")  /  Max(R.Total_Mass,0.0000001),1);

RecoveryA  as Fraction;
RecoveryA=Min(1-
R.Total_Component("TB+")/Max(F.Total_Component("TB+"),0.0000001),1);

RecoveryB  as Fraction;
RecoveryB  = Min(1-E.Total_Component("TB-")/Max(F.Total_Component("TB"),  0.0000001),
1);
```

Second, we set the ProductivityA, ProductivityB and ProductivityTotal as mass flow variables in eqs 6.15 to 6.17. The unit of the productivity is gram per liter per hour.

$$\text{ProductivityA} = \frac{Q_E \bar{C}_A^E}{nV_{bed}} \quad \textbf{(6.15)}$$

$$\text{ProductivityB} = \frac{Q_R \bar{C}_B^R}{nV_{bed}} \quad \textbf{(6.16)}$$

$$\text{ProductivityTotal} = \text{ProductivityA} + \text{ProductivityB} = \frac{Q_E \bar{C}_A^E + Q_R \bar{C}_B^R}{nV_{bed}} \quad \textbf{(6.17)}$$

```
ProductivityA  as c_Flow_Mass;
ProductivityB  as c_Flow_Mass;
ProductivityTotal  as c_Flow_Mass;

ProductivityA  = (E.Total_Component("TB+")  / SMB.Switch_Time)*60*1000/ColVol  ;
ProductivityB  = (R.Total_Component("TB-")  / SMB.Switch_Time)*60*1000/ColVol;
ProductivityTotal  = ProductivityA  + ProductivityB;
```

Step 21: Add Form->Table->FlowSpecification.

We create Table 6.2 that displays all the flow specifications based on the flowsheet constraints in the previous step 19.

TABLE 6.2. THE FLOW SPECIFICATION DEFINED IN THE FLOWSHEET CONSTRAINTS.

FlowSpecification Table

	Value	Spec	Units
SMB.Recycle_Flowrate	0.47	Free	ml/min
SMB.Switch_Time	6.38	Free	min
DESORBENT.Flowrate	0.65	Free	ml/min
EXTRACT.Flowrate	0.6	Free	ml/min
FEED.Flowrate	0.38	Free	ml/min
RAFFINATE.Flowrate	0.43	Free	ml/min
SMB.Hb	**15.0**	Fixed	cm
SMB.Db	**0.46**	Fixed	cm
SMB.Ei	**0.68**	Fixed	m3 void/m3 bed
M1	**6.54**	Fixed	
M2	**1.75**	Fixed	
M3	**4.785**	Fixed	
M4	**1.35**	Fixed	
MaxPdrop	**40.0**	Fixed	bar
EffectVol	6000.0	Free	cm3
ColVol	2.49285	Free	cm3

We give the following calculations on how to get the flow rate ratios m values in Table 6.2 from the zone flow rate values in terms of eqs 6.7 to 6.10.

$$m_1 = \frac{Q_1 t_{sw} - V_c \varepsilon - V_1^D}{V_{bed}(1-\varepsilon)} = \frac{\frac{1.12\text{ml}}{\text{min}} * 6.38\ \text{min} - 2.493\text{cm}^3 * 0.68 - 0.23\text{ml}}{2.493\text{cm}^3 * (1-0.68)} = 6.54 \quad (6.18)$$

$$m_2 = \frac{Q_2 t_{sw} - V_c \varepsilon - V_2^D}{V_{bed}(1-\varepsilon)} = \frac{\frac{0.52\text{ml}}{\text{min}} * 6.38\ \text{min} - 2.493\text{cm}^3 * 0.68 - 0.23\text{ml}}{2.493\text{cm}^3 * (1-0.68)} = 1.75 \quad (6.19)$$

$$m_3 = \frac{Q_3 t_{sw} - V_c \varepsilon - V_3^D}{V_{bed}(1-\varepsilon)} = \frac{\frac{0.9\text{ml}}{\text{min}} * 6.38\ \text{min} - 2.493\text{cm}^3 * 0.68 - 0.23\text{ml}}{2.493\text{cm}^3 * (1-0.68)} = 4.785 \quad (6.20)$$

$$m_4 = \frac{Q_4 t_{sw} - V_c \varepsilon - V_4^D}{V_{bed}(1-\varepsilon)} = \frac{\frac{0.47\text{ml}}{\text{min}} * 6.38\ \text{min} - 2.493\text{cm}^3 * 0.68 - 0.23\text{ml}}{2.493\text{cm}^3 * (1-0.68)} = 1.35 \quad (6.21)$$

The criterion of the switching time is:

$$t_{sw} \geq \frac{\phi L^2}{\Delta P_{max}} \sum_{j=1}^{j=4} n_j \left[\left(m_j(1-\varepsilon) + \varepsilon \right) + \frac{V_j^D}{V} \right] \quad (6.22)$$

$\sum_{j=1}^{j=4} n_j(m_j(1-\varepsilon)+\varepsilon)$=1*(6.54*(1-0.68) + 0.68 + 0.23/2.493) +2*(1.75*(1-0.68) +0.68+0.23/2.493)+ 2*(4.785*(1-0.68) + 0.68+0.23/2.493)+ 1*(1.35*(1-0.68) +0.68+0.23/2.493)=2.8551+2.66452+4.60692+1.20426=11.3308

$$t_{sw} \geq \frac{0.1 * 15^2}{40} * 11.3308 = 6.38\, min \quad (6.23)$$

Step 22: Add Form->Table->Results.

We also create Table 6.3 to display all the performance indices defined in step 20. It shows all the results as zero before running, and will display the performance results after running.

TABLE 6.3. THE PERFORMANCE INDICES DEFINED IN THE FLOWSHEET CONSTRAINTS.

Results Table

	Value	Spec	Units
PurityA	0.0	Free	%
PurityB	0.0	Free	%
RecoveryA	0.0	Free	%
RecoveryB	0.0	Free	%
ProductivityA	0.0	Free	g/min
ProductivityB	0.0	Free	g/min
ProductivityTotal	0.0	Free	g/min

Step 23: Add Form->Plot ->Purity_Recovery.

In order to clearly see the changing of both product purity and recovery over the simulation time, we make a performance plot of the product purity and recovery results named as Purity_Recovery.

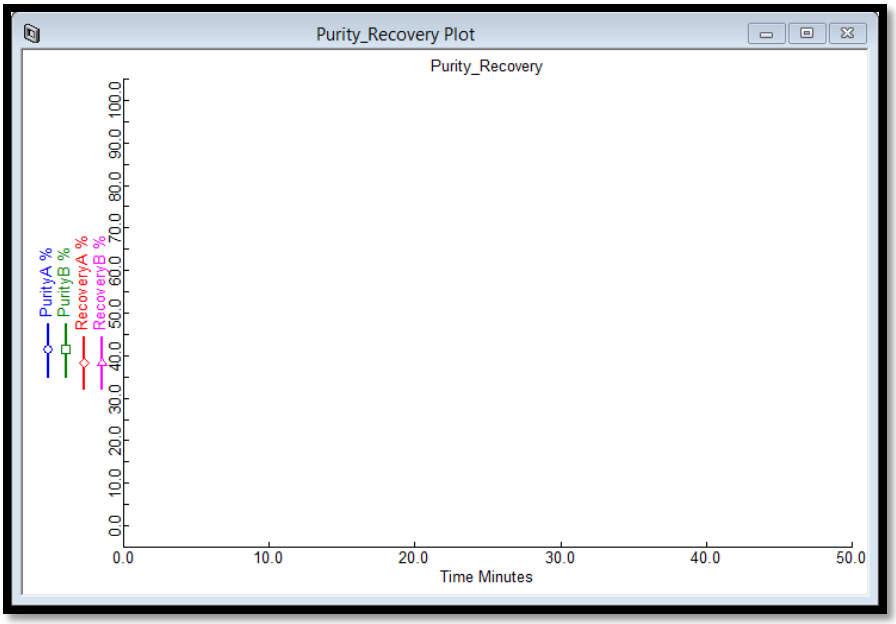

FIGURE 6.20. THE PERFORMANCE PLOT OF THE PRODUCT PURITY AND RECOVERY RESULTS.

Step 24: Add Form->Plot->Extract Plot.

The extract stream receives most of the component A, so we make a plot "Extract" to see the concentration and mole fraction for both components in the extract-out stream.

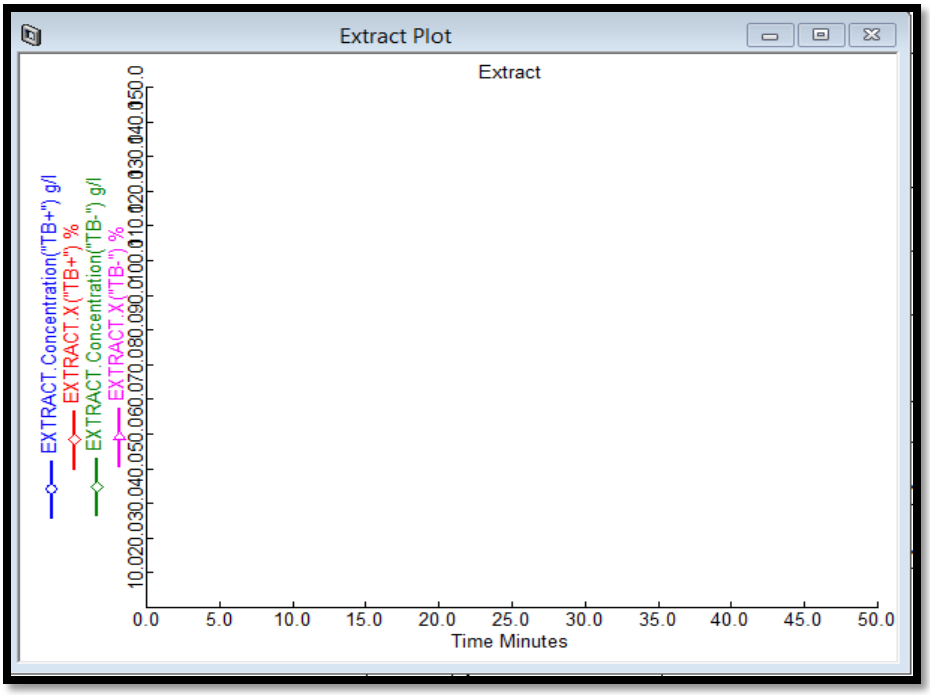

FIGURE 6.21.THE EXTRACT CONCENTRATION AND MOLE FRACTION RESULTS FOR BOTH COMPONENTS.

Step 25: Add Form->Plot->Raffinate Plot.

The raffinate stream receives most of component B, so we make a plot "Raffinate" to see the concentration and mole fraction for both components in the raffinate-out stream.

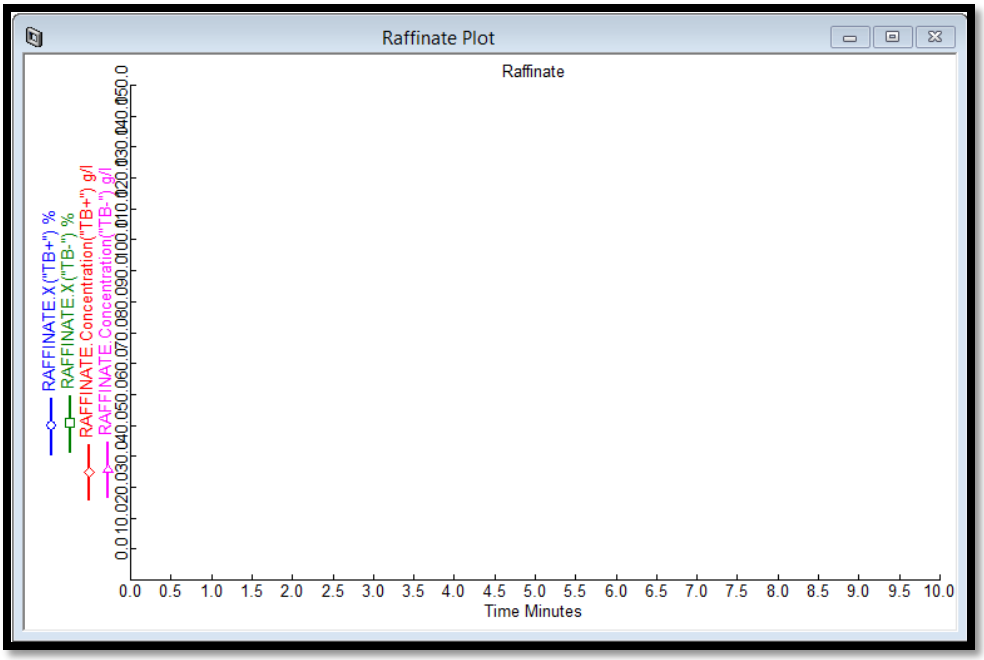

FIGURE 6.22.THE RAFFINATE CONCENTRATION AND MOLE FRACTION RESULTS FOR BOTH COMPONENTS.

Step 26: Add Form->Profile Plot->Concentration Profile Plot.

Our next goal is to make a concentration profile, which gives physical insights within the SMB column of their separation performance for both components. It reveals us how the concentrations change through the axial distance of the column over the time.

We define the axial position of the column by "SMB. Column_(*).Axial_Distance(*)"; TB+ Concentration by "SMB. Column_(*).C (*,"TB+")"; and TB- Concentration by "SMB. Column_(*). C (*,"TB-")", as shown in Figure 6.23.

After we press the "Apply", it will show the resulting column concentration profile for both TB+ and TB- at zero simulation time, as shown in Figure 6.24.

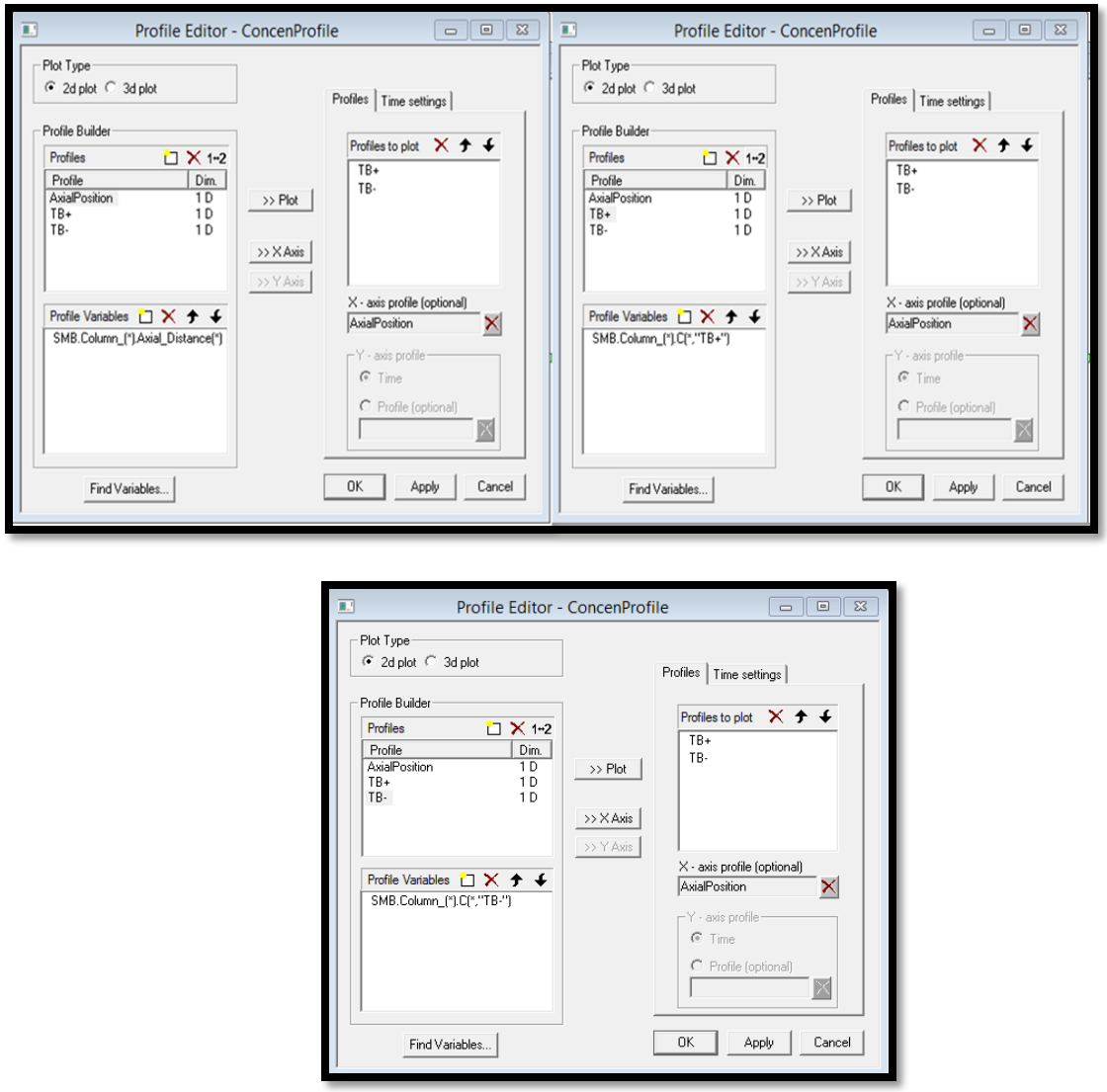

FIGURE 6.23.THE VARIABLE DEFINITION OF THE CONCENTRATION PROFILE WITHIN THE COLUMN.

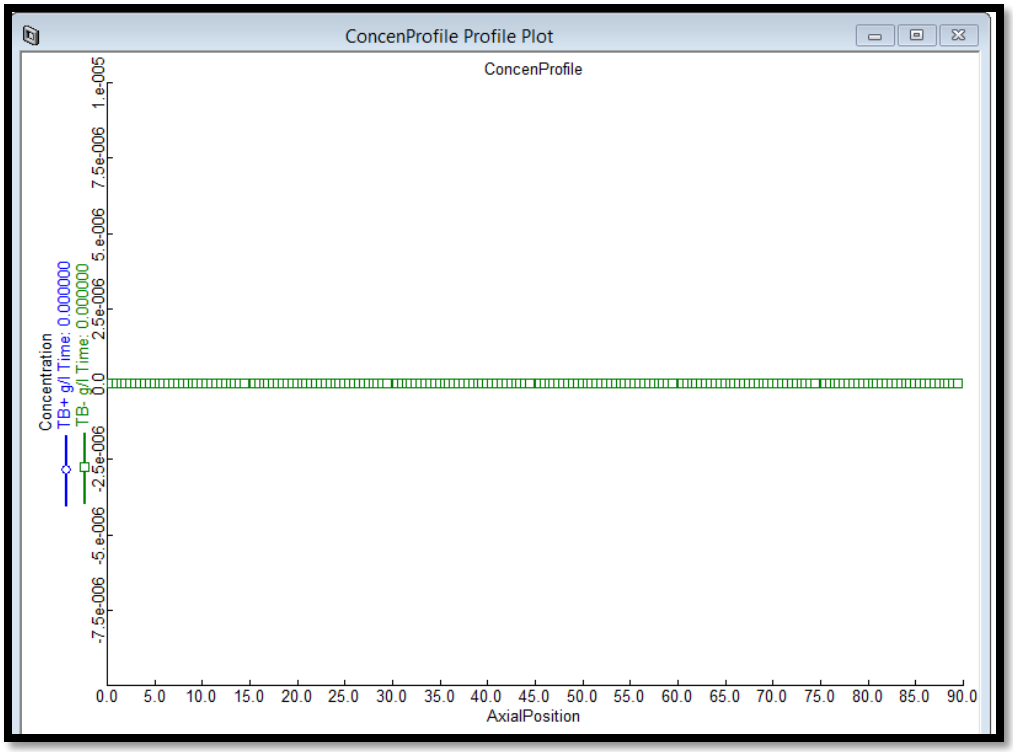

FIGURE 6.24. THE RESULTING CONCENTRATION PROFILE FOR BOTH TB+ AND TB- AT ZERO SIMULATION TIME.

Step 27: Run -> Solver Options->Integrator.

After we finish making all the previous plots and profile plots, we define the solver options. The Solver Options dialog box in Aspen Chromatography enables us to change the default settings for numerical algorithms used in your simulation. For example, we may change some of the algorithm properties to:

- Solve a difficult simulation or to improve the speed of a dynamic run.
- Get comprehensive diagnostic output from our simulation to determine why a simulation does not converge or runs more slowly than expected.

We integrate the resulting ordinary differential equations using Gear method with a variable time step size (0.1 min initial step size, 0.1 to 0.5 min step size range and 0.5 step reduction factor) and the integration error tolerance set to the value of 10^{-4} in Aspen Chromatography, as shown in Figure 6.25.

The Gear method is a variable-order, variable-step backward difference implicit method with high accuracy. The user can define the behavior of the method for model discontinuities and variable step changes.

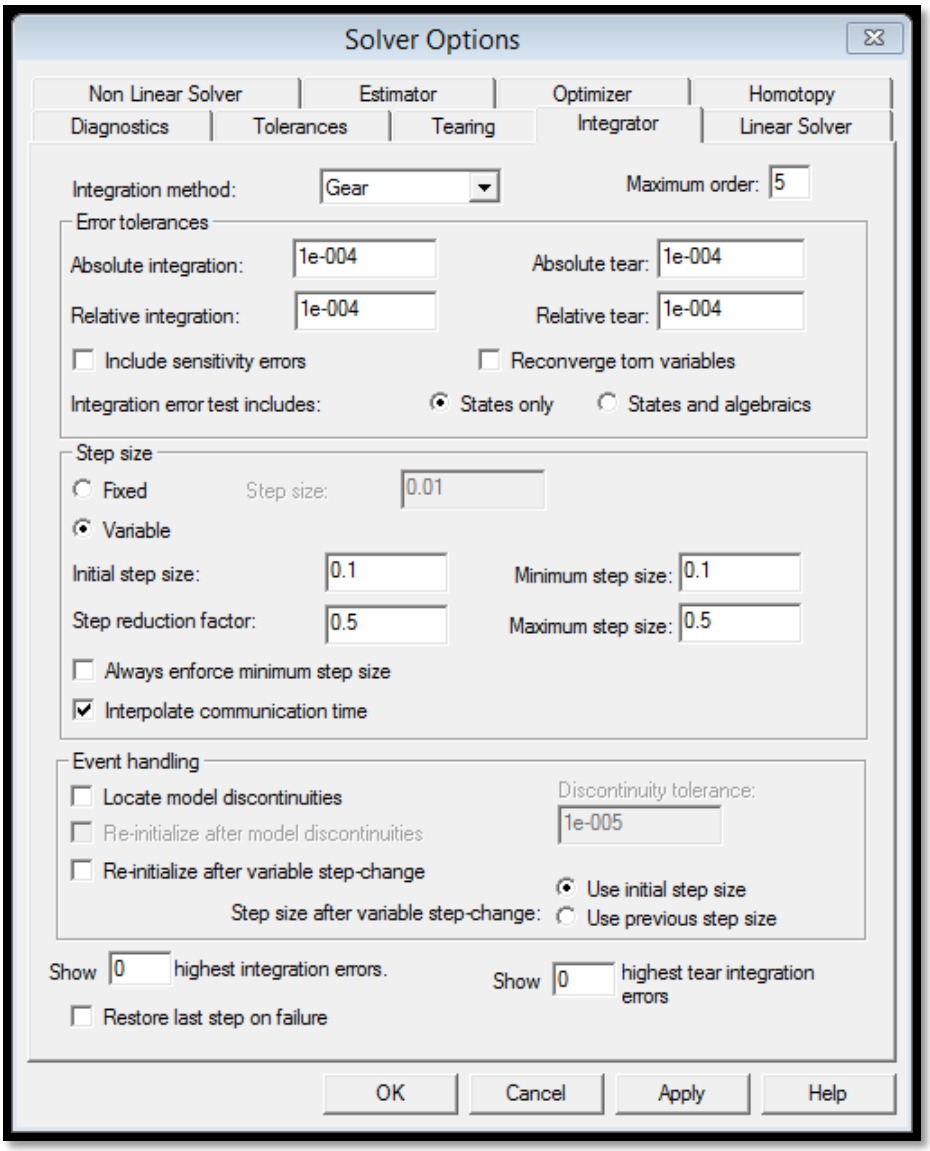

FIGURE 6.25. THE INTEGRATOR SETTINGS IN THE SOLVER OPTIONS OF THE MODEL.

Step 28: Run -> Solver Options->Tolerances.

We set the absolute and relative variable tolerances. The Tolerances tab in Aspen Chromatography enables us to change the options for controlling tolerances, and to control solver scaling and the elimination of equivalence equations.

We can change the value of the tolerances to affect the speed and accuracy of the solution under most solution methods available. Figure 6.26 shows our tolerance settings based on our simulation experiences.

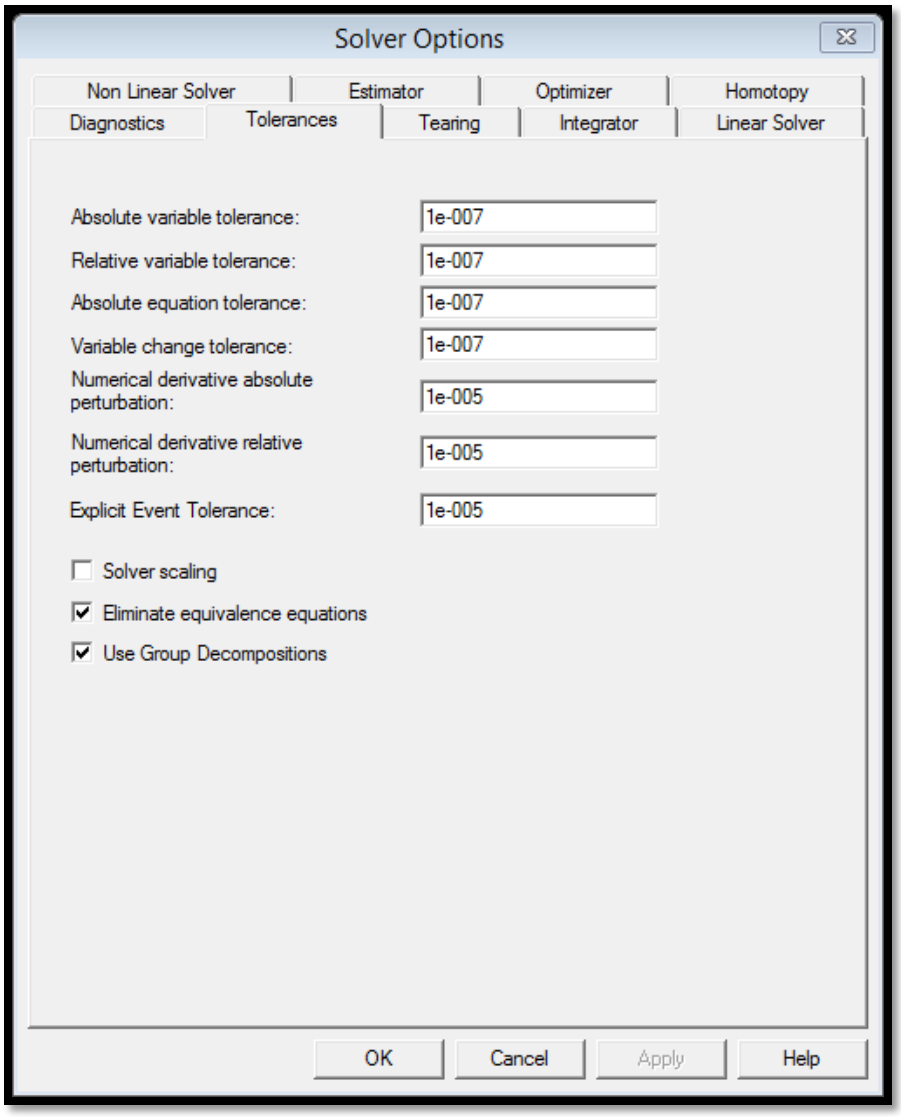

FIGURE 6.26. THE TOLERANCE SETTINGS IN THE SOLVER OPTIONS OF THE MODEL.

Step 29: Run Options->Initialization.

The model is ready to initialize.

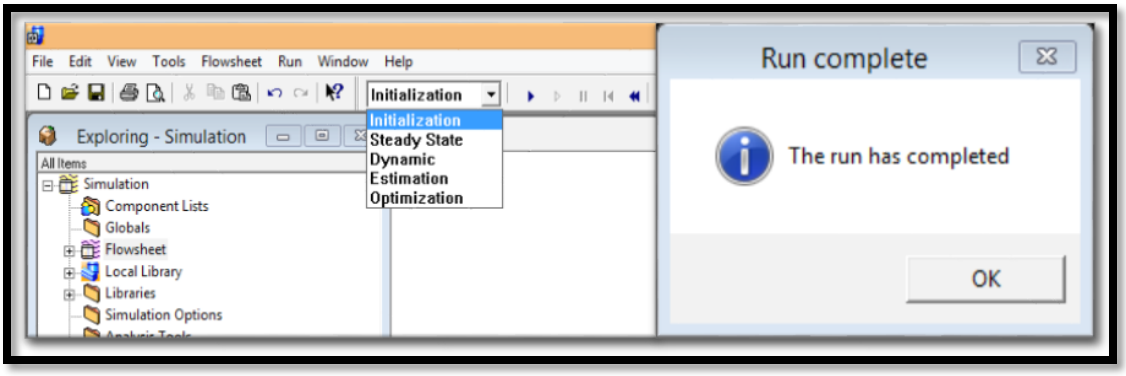

FIGURE 6.27.THE INITIALIZATION OF THE SMB MODEL.

Step 30: Run Options->Pause at 382.8 seconds.

Since we consider the dynamic state in all the models, the results are recorded once the system reaches a cyclic steady state. We determine the steady state by finding the time at which the average of the performance indices over one step becomes constant. The steady state is attained after 10 cycles (each cycle contains 6 switching time rounds). Thus, our simulation time is therefore 6.38*6*10=382.8 min.

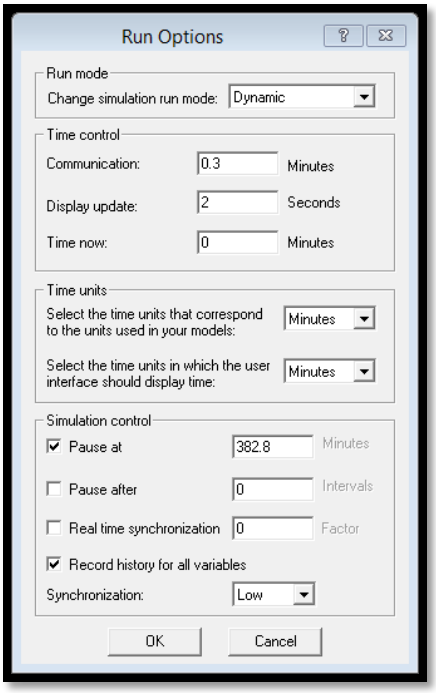

FIGURE 6.28. THE SIMULATION RUNNING TIME SETTING IN THE RUN OPTIONS OF THE MODEL.

Step 31: Run Options->Dynamic.

The model is ready for the dynamic run after reaching the pause time (382.8 min) we set.

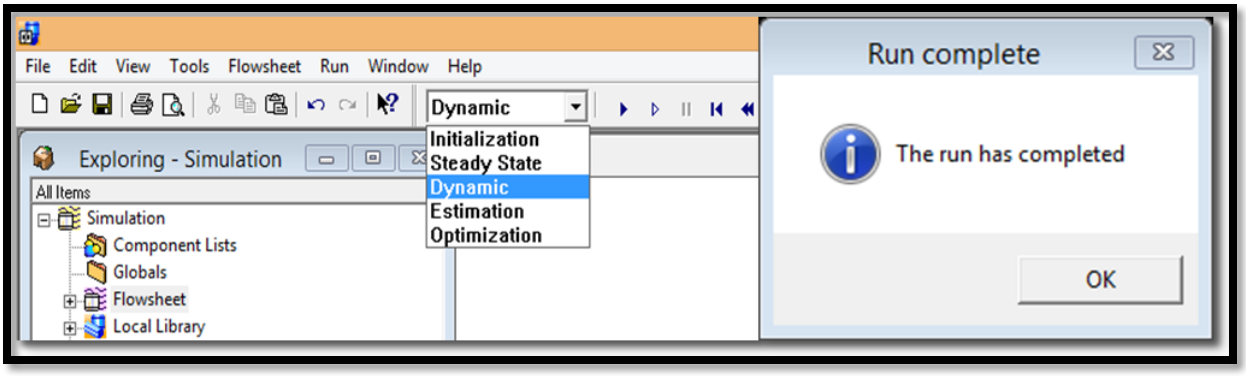

FIGURE 6.29.THE DYNAMIC RUN OF THE SMB MODEL.

Step 32: Results->Purity and Recovery Results.

After each simulation run, we would open the purity and recovery plot to either see the plot or to look at the detailed result history through the simulation times. Figure 6.30 illustrates the Purity_Recovery plot results for both product.

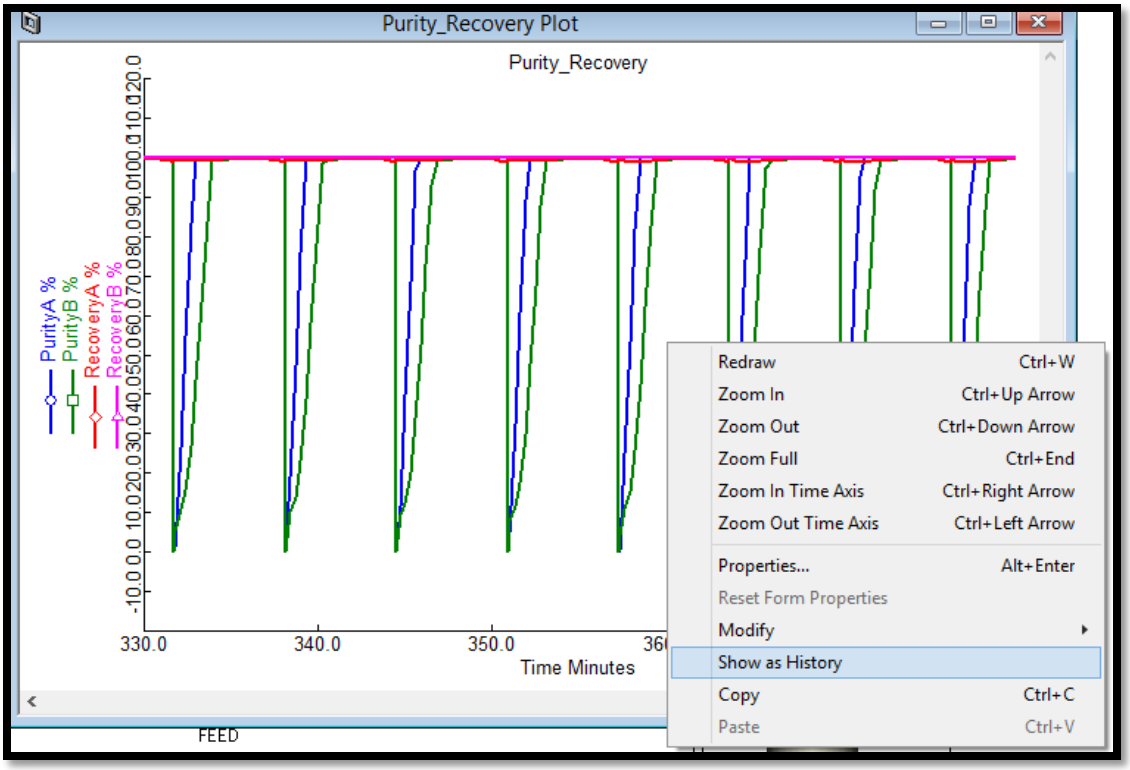

FIGURE 6.30.THE PURITY_RECOVERY PLOT RESULTS FOR BOTH PRODUCT.

If we want to look at the detailed values for both product purity and recovery, right-click the plot, and then choose the "Show as History" in Figure 6.30. We get the Purity_Recovery history table as shown in Figure 6.31. The blue highlighted region in the figure represents the purity and recovery results through one whole switching time. We can calculate the average purity and recovery based on these results.

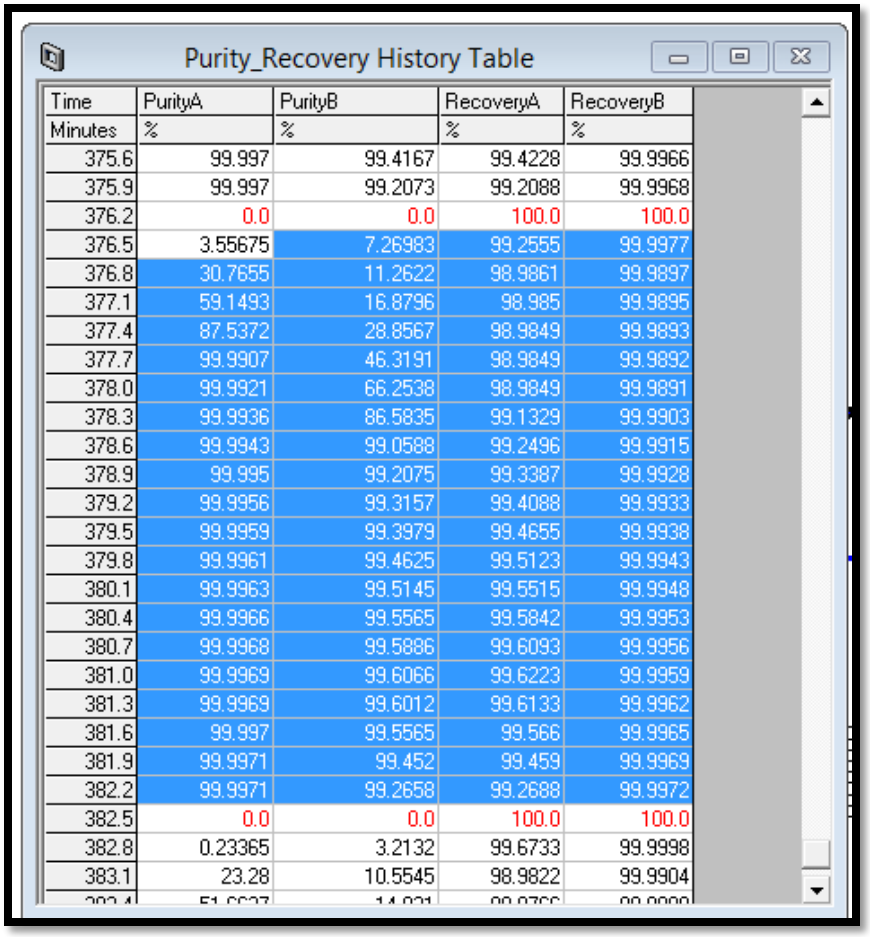

Purity_Recovery History Table

Time	PurityA	PurityB	RecoveryA	RecoveryB
Minutes	%	%	%	%
375.6	99.997	99.4167	99.4228	99.9966
375.9	99.997	99.2073	99.2088	99.9968
376.2	0.0	0.0	100.0	100.0
376.5	3.55675	7.26983	99.2555	99.9977
376.8	30.7655	11.2622	98.9861	99.9897
377.1	59.1493	16.8796	98.985	99.9895
377.4	87.5372	28.8567	98.9849	99.9893
377.7	99.9907	46.3191	98.9849	99.9892
378.0	99.9921	66.2538	98.9849	99.9891
378.3	99.9936	86.5835	99.1329	99.9903
378.6	99.9943	99.0588	99.2496	99.9915
378.9	99.995	99.2075	99.3387	99.9928
379.2	99.9956	99.3157	99.4088	99.9933
379.5	99.9959	99.3979	99.4655	99.9938
379.8	99.9961	99.4625	99.5123	99.9943
380.1	99.9963	99.5145	99.5515	99.9948
380.4	99.9966	99.5565	99.5842	99.9953
380.7	99.9968	99.5886	99.6093	99.9956
381.0	99.9969	99.6066	99.6223	99.9959
381.3	99.9969	99.6012	99.6133	99.9962
381.6	99.997	99.5565	99.566	99.9965
381.9	99.9971	99.452	99.459	99.9969
382.2	99.9971	99.2658	99.2688	99.9972
382.5	0.0	0.0	100.0	100.0
382.8	0.23365	3.2132	99.6733	99.9998
383.1	23.28	10.5545	98.9822	99.9904

FIGURE 6.31.THE PURITY_RECOVERY HISTORY TABLE.

Step 32: Results->Plots.

This step presents all the plots and profile plots we made in steps 23 to 26, including the extract concentions (Figure 6.32), raffinate concentrations (Figure 6.33), the column concentration profile (Figure 6.34) and the concentration profile table (Figure 6.35).

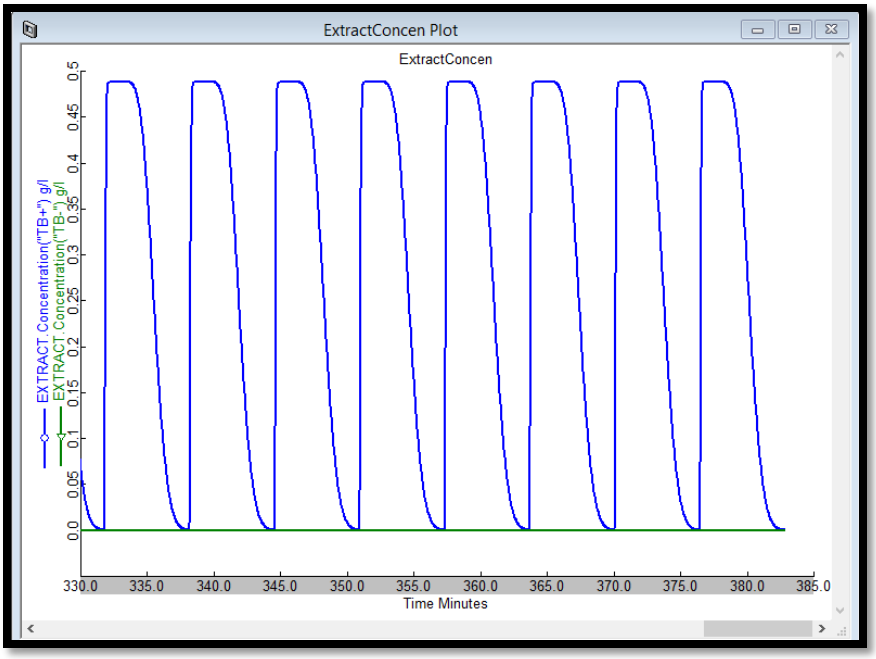

FIGURE 6.32.THE RESULTING EXTRACT CONCENTRATION RESULTS FOR BOTH COMPONENTS.

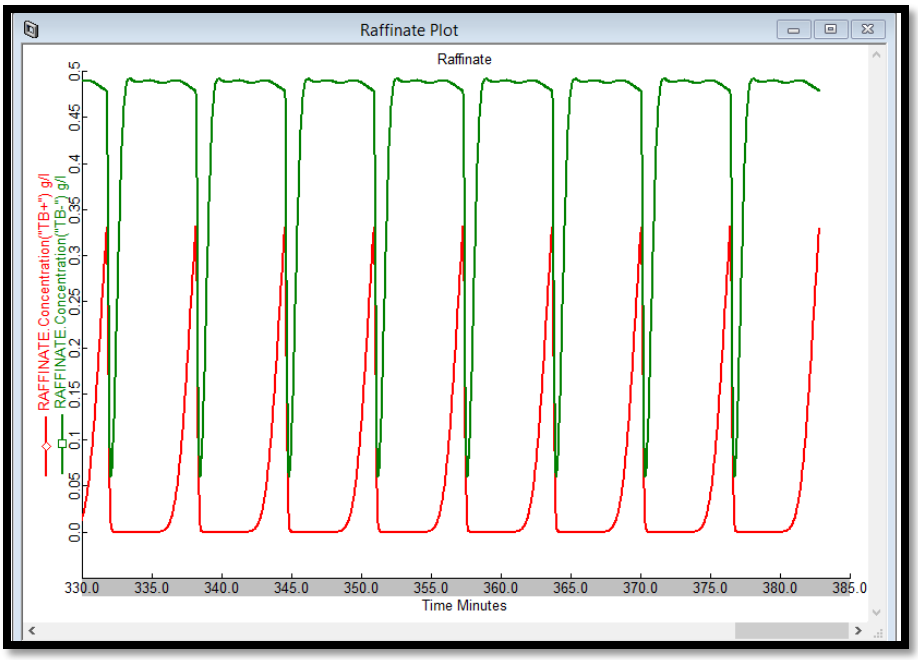

FIGURE 6.33.THE RESULTING RAFFINATE CONCENTRATION RESULTS FOR BOTH COMPONENTS.

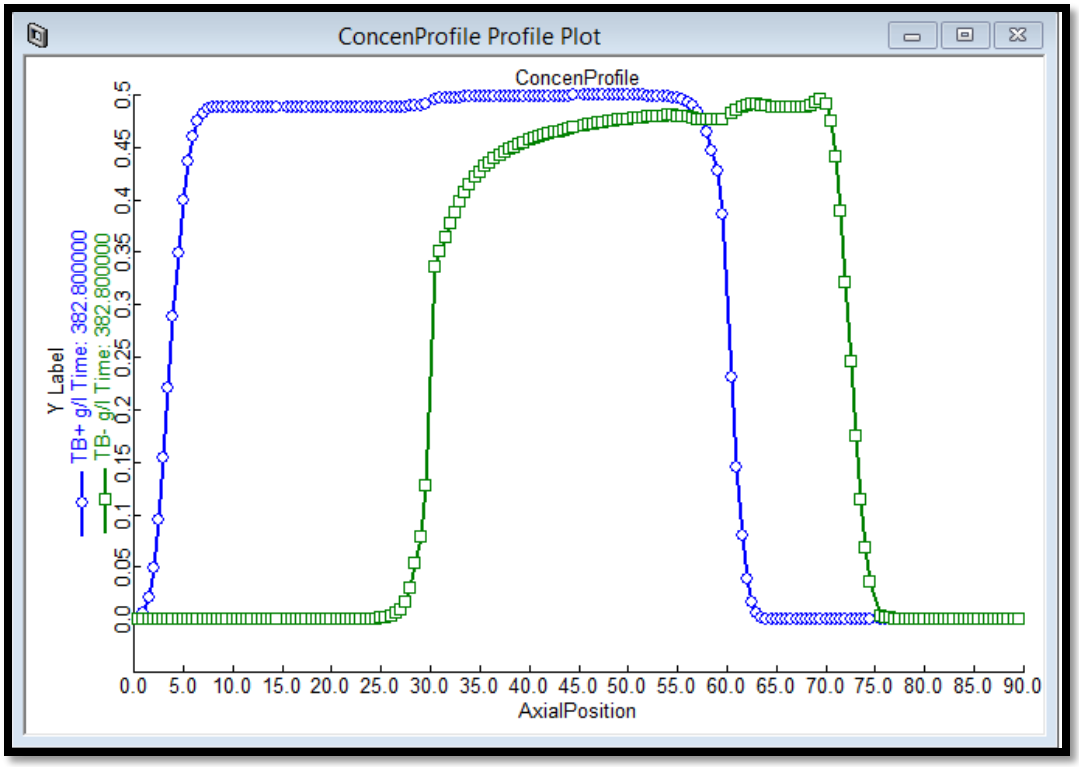

FIGURE 6.34.THE RESULTING CONCENTRATION PROFILE WITHIN THE SMB COLUMN.

ConcenProfile Profile Table

Time	Profile Name											
Minutes												
	TB-	g/l	-4.01208e-007	-4.47781e-007	-4.1059e-007	-3.2356e-007	-2.00016e-007	-2.8853e-008	1.98827e-007	4.54703e-007	6.67971e-007
381.6	AxialPosition	cm	0.5	1.0	1.5	2.0	2.5	3.0	3.5	4.0	4.5
	TB+	g/l	0.0546953	0.108054	0.177287	0.253037	0.324923	0.384881	0.429102	0.457987	0.47466
	TB-	g/l	-3.14451e-007	-4.26019e-007	-4.35787e-007	-3.77868e-007	-2.77376e-007	-1.35389e-007	6.07079e-008	3.04745e-007	5.48476e-007
381.72	AxialPosition	cm	0.5	1.0	1.5	2.0	2.5	3.0	3.5	4.0	4.5
	TB+	g/l	0.0423571	0.0890838	0.153323	0.227223	0.300721	0.364929	0.414574	0.448638	0.46936
	TB-	g/l	-1.85152e-007	-3.67226e-007	-4.34325e-007	-4.15031e-007	-3.40329e-007	-2.24326e-007	-6.00642e-008	1.5887e-007	4.08006e-007
381.84	AxialPosition	cm	0.5	1.0	1.5	2.0	2.5	3.0	3.5	4.0	4.5
	TB+	g/l	0.0321422	0.07231	0.130951	0.201921	0.275868	0.343463	0.398175	0.43754	0.46272
	TB-	g/l	-1.37244e-008	-2.6784e-007	-4.00241e-007	-4.29979e-007	-3.87645e-007	-2.97215e-007	-1.62366e-007	2.57531e-008	2.61288e-007
381.96	AxialPosition	cm	0.5	1.0	1.5	2.0	2.5	3.0	3.5	4.0	4.5
	TB+	g/l	0.0238637	0.0577334	0.110391	0.177503	0.250757	0.320765	0.380012	0.424638	0.454591
	TB-	g/l	1.96648e-007	-1.26521e-007	-3.28741e-007	-4.16926e-007	-4.15948e-007	-3.54372e-007	-2.46975e-007	-9.02619e-008	1.20018e-007
382.08	AxialPosition	cm	0.5	1.0	1.5	2.0	2.5	3.0	3.5	4.0	4.5
	TB+	g/l	0.0173063	0.0452908	0.0917886	0.154293	0.225775	0.297158	0.360252	0.409932	0.444857
	TB-	g/l	4.39639e-007	5.54933e-008	-2.16872e-007	-3.70437e-007	-4.20385e-007	-3.94197e-007	-3.1479e-007	-1.8799e-007	-8.1288e-009
382.2	AxialPosition	cm	0.5	1.0	1.5	2.0	2.5	3.0	3.5	4.0	4.5
	TB+	g/l	0.0122399	0.034866	0.0752228	0.132554	0.201291	0.272989	0.339116	0.393478	0.433438
	TB-	g/l	7.05386e-007	2.7405e-007	-6.40071e-008	-2.86315e-007	-3.95598e-007	-4.13264e-007	-3.65576e-007	-2.67771e-007	-1.19238e-007
382.32	AxialPosition	cm	0.5	1.0	1.5	2.0	2.5	3.0	3.5	4.0	4.5
	TB+	g/l	0.00843165	0.0263021	0.060706	0.112492	0.177642	0.248618	0.316874	0.375388	0.4203
	TB-	g/l	9.80157e-007	5.2172e-007	1.27765e-007	-1.62288e-007	-3.36703e-007	-4.06951e-007	-3.9743e-007	-3.29948e-007	-2.12052e-007
382.44	AxialPosition	cm	0.5	1.0	1.5	2.0	2.5	3.0	3.5	4.0	4.5
	TB+	g/l	0.00565601	0.0194132	0.0481941	0.0942461	0.155119	0.224396	0.293825	0.355832	0.405459
	TB-	g/l	1.24616e-006	7.87441e-007	3.53294e-007	1.48798e-009	-2.40154e-007	-3.70333e-007	-4.06909e-007	-3.73824e-007	-2.86529e-007
382.56	AxialPosition	cm	0.5	1.0	1.5	2.0	2.5	3.0	3.5	4.0	4.5
	TB+	g/l	0.00370306	0.013996	0.0375945	0.0778953	0.133967	0.20066	0.270292	0.335024	0.388982
	TB-	g/l	1.48168e-006	1.05626e-006	6.04022e-007	2.02016e-007	-1.04421e-007	-2.9911e-007	-3.89638e-007	-3.97255e-007	-3.42537e-007
382.68	AxialPosition	cm	0.5	1.0	1.5	2.0	2.5	3.0	3.5	4.0	4.5
	TB+	g/l	0.00238437	0.00984071	0.0287764	0.0634618	0.114374	0.177714	0.246603	0.313218	0.370989
	TB-	g/l	1.66163e-006	1.30925e-006	8.6768e-007	4.33109e-007	6.94944e-008	-1.90432e-007	-3.41148e-007	-3.96823e-007	-3.78997e-007
382.8	AxialPosition	cm	0.5	1.0	1.5	2.0	2.5	3.0	3.5	4.0	4.5
	TB+	g/l	0.00145762	0.00642619	0.0208218	0.0495604	0.0945068	0.153395	0.220444	0.288147	0.349431
	TB-	g/l	1.76134e-006	1.53523e-006	1.14385e-006	7.01306e-007	2.91737e-007	-3.30576e-008	-2.51258e-007	-3.65575e-007	-3.93644e-007

FIGURE 6.35.THE RESULTING CONCENTRATION PROFILE TABLE WITHIN THE SMB COLUMN.

6.2. *Workshop 2: Apply Varicol to the 4-Zone SMB Model*

As mentioned in section 4.1, the Varicol operation applies an asynchronous shift of the inlet/outlet ports upon the SMB column, where the zone lengths are varied in time. In the Varicol model, the asynchronous shifting ratio (AS) for each inlet or outlet port is a fraction of the switching time t_{sw} at which it moves to its next port position. Specifically, AS_D, AS_E, AS_F and AS_R represent, respectively, the asynchronous shifting ratios for the desorbent-in port, extract-out port, feed-in port and raffinate-out port. Their values are all between 0 and 1. For the Varicol modeling, all the process and operating conditions are the same as the basic SMB, except for the new asynchronous port switching. In this workshop, we demonstrate how to apply the Varicol operation to the current 4-zone SMB model developed in the workshop one.

Step 1: Open the "4-zone Basic SMB model", and save it as "4-zone Varicol model".

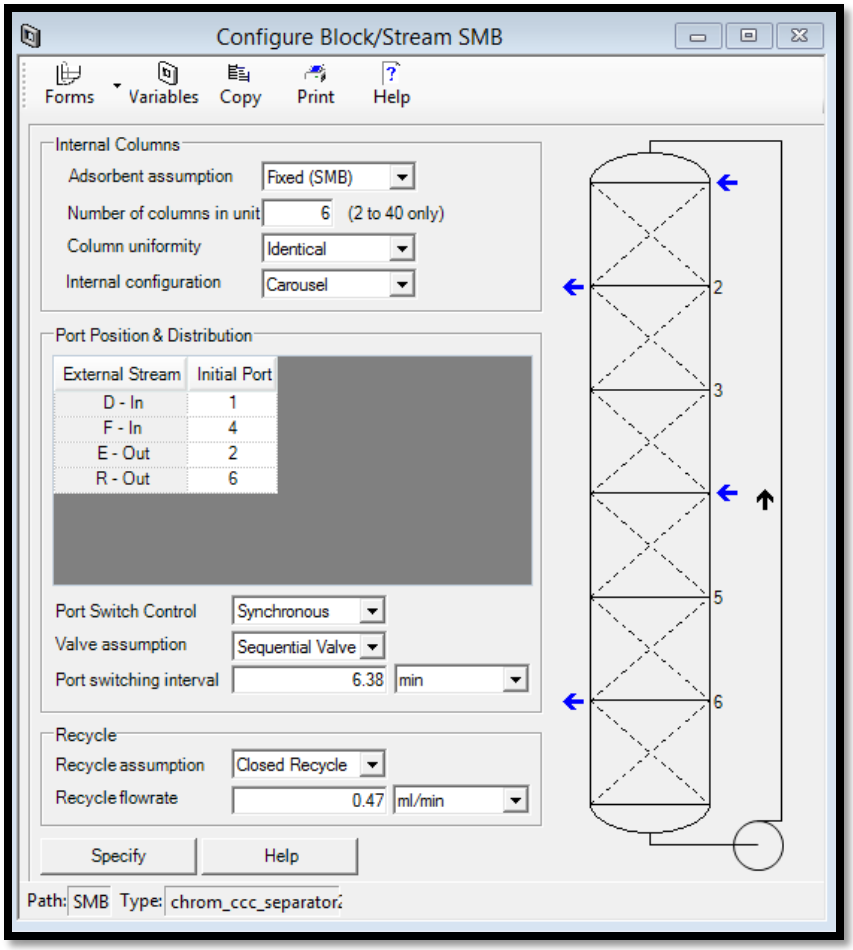

FIGURE 6.36. THE COLUMN CONFIGURATION BLOCK IN THE SMB MODEL.

Step 2: Port Switch Control ->Asynchronous.

We use the Port Switch Control box to specify whether the ports are shifted synchronously or asynchronously. In the SMB model, it is synchronously port switching, where all ports shift together; in the Varicol model, all ports shift independently within a master switching interval.

When we choose the asynchronous switching for Varicol in Figure 6.37, we need to specify additional information for each external stream with respect to the switching sub-interval used. This is entered in the Async Shift column of the port distribution table.

The sub-interval, or shift period, is defined as the fraction with a value between 0 to 1 into the current switching interval at which the port is switched. Assuming a 6-column Varicol system, during a dynamic simulation, we can modify the asynchronous shift through the port table. Here, we give an example of $AS_D = 1$, $AS_E = 1$, $AS_F = 0.6$ and $AS_R = 0.9$.

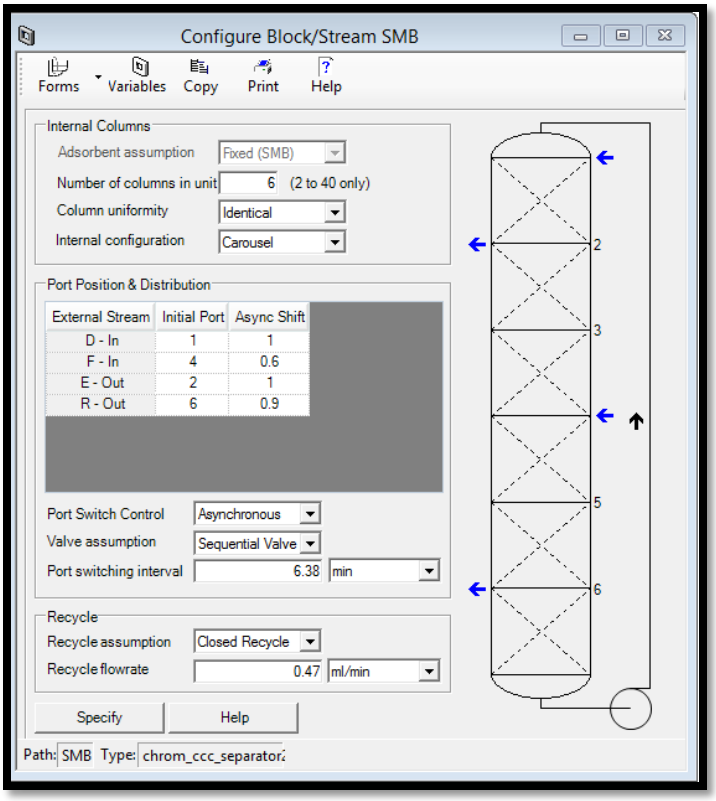

FIGURE 6.37. THE COLUMN CONFIGURATION BLOCK IN THE VARICOL MODEL.

Step 3: Configure Block -> Initialize.

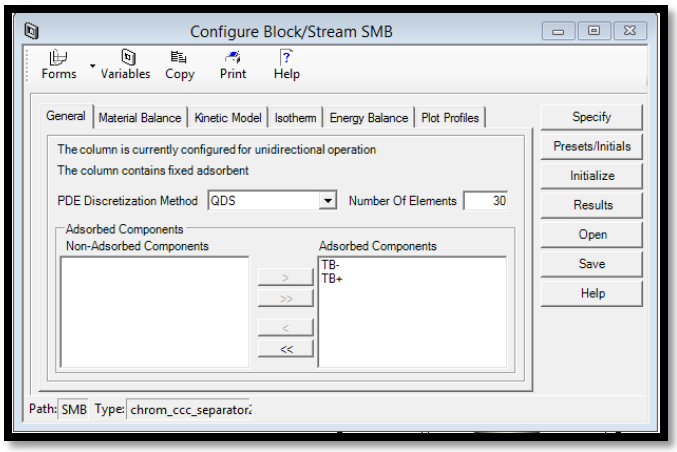

FIGURE 6.38. THE INITIALIZATION OF THE VARICOL COLUMN.

Step 4: Run Options->Initialization.

The model is ready to initialize.

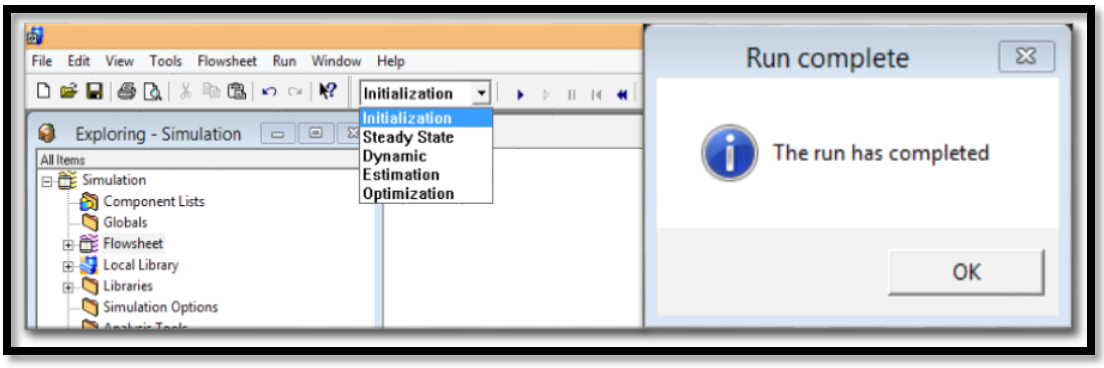

FIGURE 6.39.THE INITIALIZATION OF THE VARICOL MODEL.

Step 5: Run Options->Dynamic.

The model is ready for the dynamic run after reaching the pause time (382.8 min) we set.

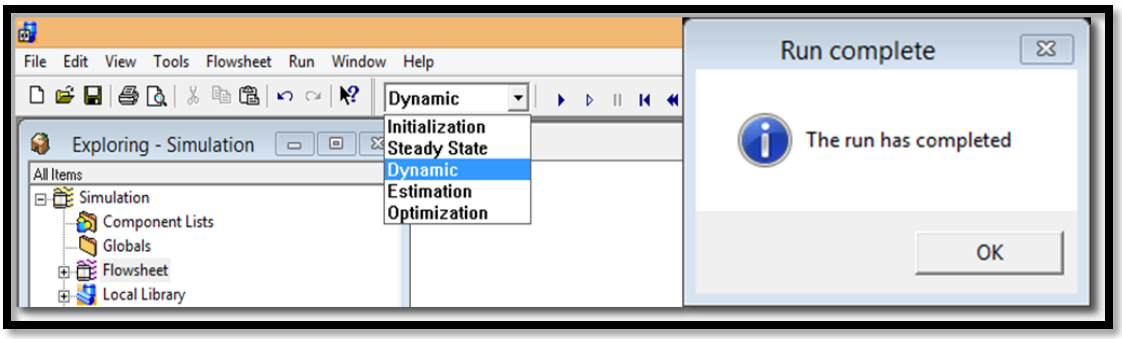

FIGURE 6.40.THE DYNAMIC RUN OF THE VARICOL MODEL.

Step 6: Results->Plots.

This step presents the extract concentration plot, raffinate concentration plot and the column concentration profile.

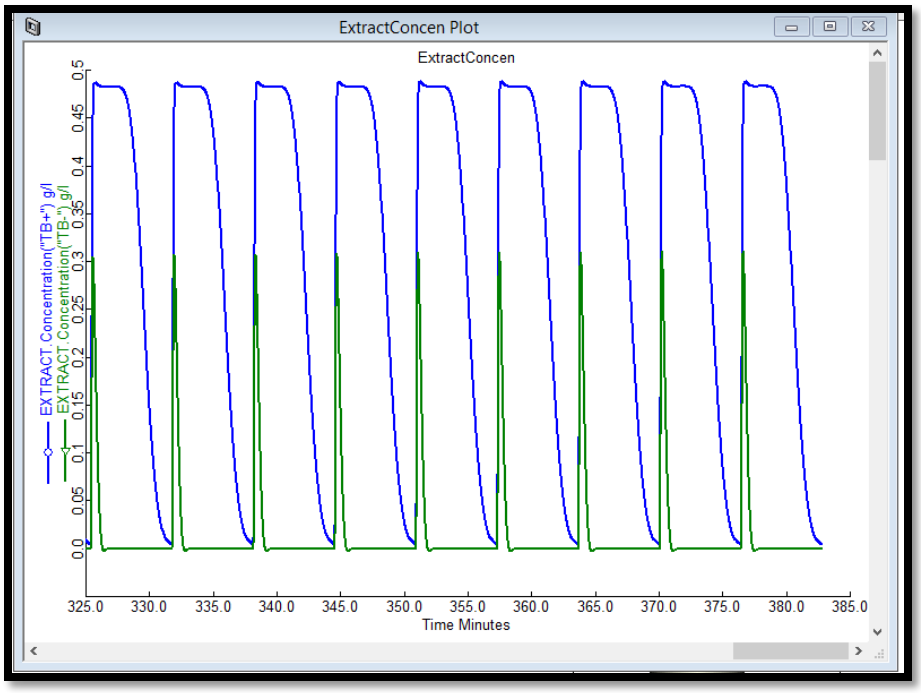

FIGURE 6.41.THE RESULTING EXTRACT CONCENTRATION RESULTS FOR BOTH COMPONENTS IN VARICOL.

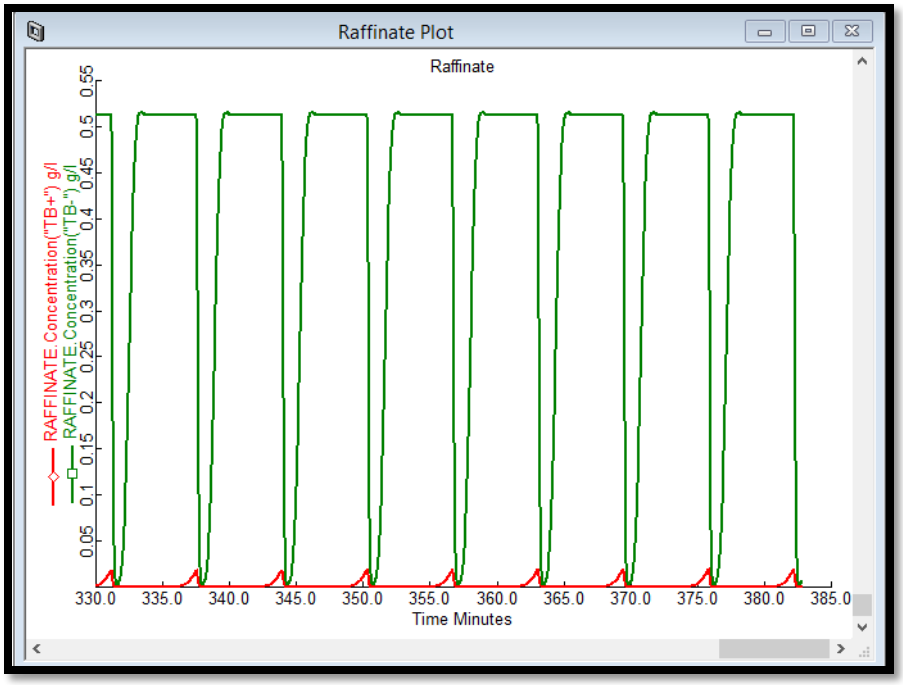

FIGURE 6.42.THE RESULTING RAFFINATE CONCENTRATION RESULTS FOR BOTH COMPONENTS IN VARICOL.

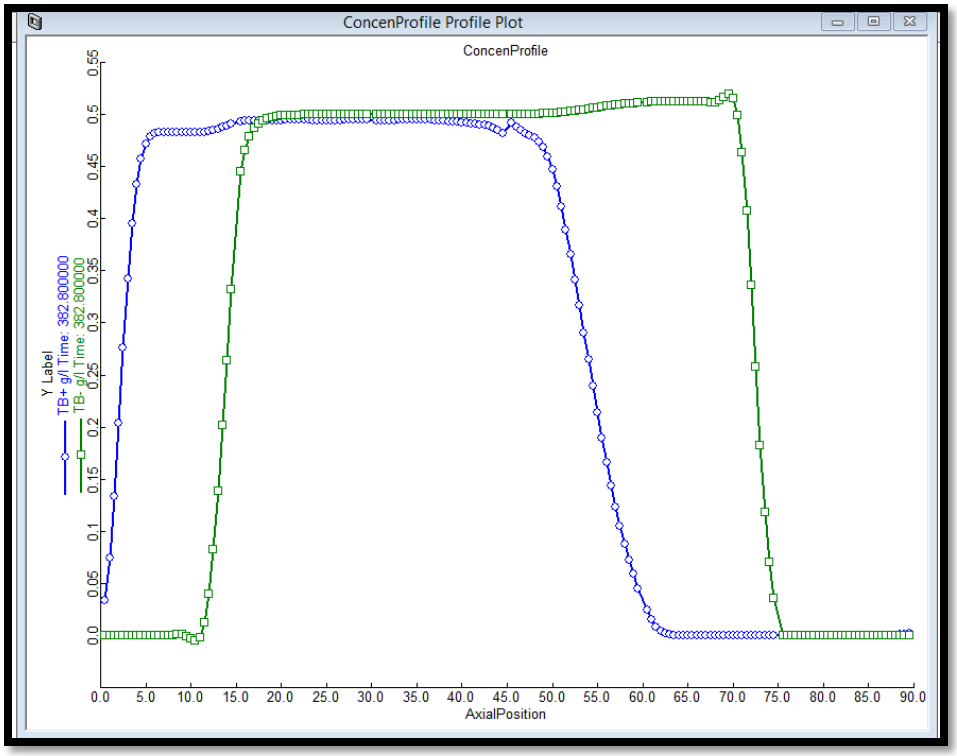

FIGURE 6.43.THE RESULTING CONCENTRATION PROFILE WITHIN THE VARICOL COLUMN.

6.3. Workshop 3: Apply PowerFeed to the 4-Zone SMB Model

In this workshop, we demonstrate how to create a PowerFeed model based on the basic SMB model. Since PowerFeed adjusts both the feed and recycle flow rates within the switching subintervals, we need to introduce the concept of the cycle organizer in Aspen Chromatography to define the cyclic operations.

Many adsorption processes operate in a cyclic manner. Each cycle is described by a series of one or more sequential steps or discrete events. When simulating a cyclic process, you must be able to specify when certain events are going to occur.

The Cycle Organizer lets us rapidly create the steps that define a cyclic process. Use it to:

- Create any number of steps
- Define the step termination event
- Manipulate flowsheet variables for a given step
- Generate a cyclic task based on the Task Language
- Distribute cycle information to other flowsheet blocks through global variables
- Store multiple cycle definitions
- Control variable recording and automated snapshots
- Execute VB (Visual Basic) scripts for additional calculations and control

Here is some more information about the Cycle Organizer:

- The main Configure form gives the status of the system, as well as the active state of the cyclic task.
- All entered data are stored in the block on the flowsheet. This allows the data to be saved with the flowsheet input file.
- Only one instance of the Cycle Organizer is allowed on the flowsheet.
- When we configure the flowsheet for cyclic operation, it is advisable to configure it as if it is about to execute the first step of the cycle.
- On addition of a new step, we are asked two questions:

- Is the new step to be placed before or after the currently selected step?
- Is the information to be copied from the currently selected step into the newly created one (to act as a template)

We give more details on how to create a cycle organizer in the PowerFeed model in the following steps.

Step 1: Open the "4-zone Basic SMB model", and save it as "4-zone PowerFeed model".

In this workshop, we apply the PowerFeed with a partial feeding. In Figure 6.44, we display the feed flow rate policies of the PowerFeed with two switching subintervals, at t= 0~t_1, F =$F_1 = 0$; at $t = t_1$~t_2, F =F_2.

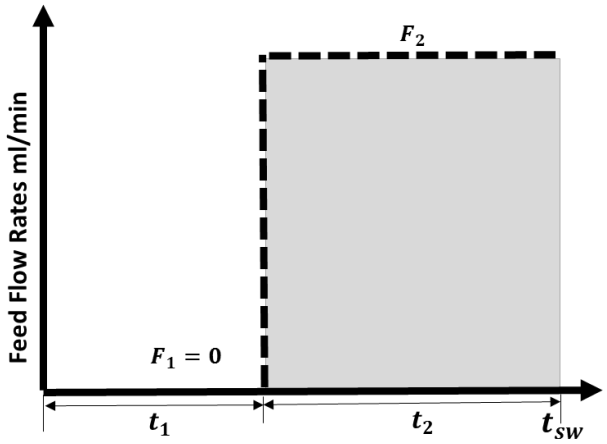

FIGURE 6.44. THE FEED FLOW RATE POLICIES IN THE POWERFEED WITH TWO SUBINTERVALS.

Step 2: Add the pressure drop constraints.

In PowerFeed, if we only change the feed flow rates, it may cause the system to exceed the maximum pressure drop. For example, eq 6.18 reveals the relationship between the zone flow rates and zone pressure drop:

$$\Delta P_j = \frac{-150\mu(1-\varepsilon)^2}{(2r_p\psi)^2\varepsilon^3}\frac{L * Q_j}{S} \tag{6.24}$$

In the equations, ΔP_j =pressure drop in each zone; L=length of each zone; S = cross-sectional area of the bed; ε = overall bed voidage; μ = fluid viscosity; r_p = particle radius; $and\ \psi$ = particle shape factor.

If we only increase the subinterval feed flow rate Q_F, then Q_3 ($Q_3 = Q_2 + Q_F$) could be very high, and ΔP_3 would exceed the maximum pressure drop of the system in that subinterval. In this workshop, we adjust the recycle flow rate to satisfy the pressure drop constraint.

In this step, we write a program to define and record the pressure drop through the whole column, and make sure that the total pressure drop is below the maximum pressure drop (40 bar). We define PreDrop as the total pressure drop variable for all the six beds in the column. Figure 6.45 shows the resulting value for the total pressure drop after each simulation run.

```
PreDrop as Pressure_Change;
  PreDrop=SMB.Column_(1).Pdrop+SMB.Column_(2).Pdrop+SMB.Column_(3).Pdrop+
        SMB.Column_(4).Pdrop+SMB.Column_(5).Pdrop+SMB.Column_(6).Pdrop;
```

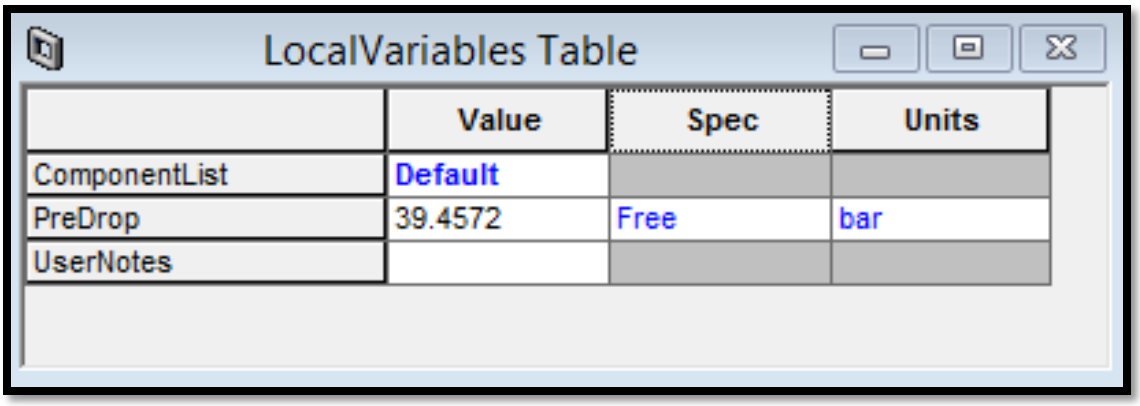

FIGURE 6.45. THE RESULTING VALUE FOR THE TOTAL PRESSURE DROP AFTER EACH SIMULATION RUN.

Step 3: Tool-> Cycle Organizer.

To access the Cycle Organizer, we click the Cycle Organizer from the Tools menu, as shown in Figure 6.46. If a Cycle Organizer block does not exist on the flowsheet, one is automatically placed on the flowsheet and the Cycle Organizer window appears. Figure 6.46 shows the block "Cycle_Organizer". Once a Cycle Organizer block is present on the flowsheet, you can open it either using the Tools menu, or by double-clicking on the flowsheet block. The Cycle Organizer toolbar gives access to the various fields and controls our specifications of a cyclic task.

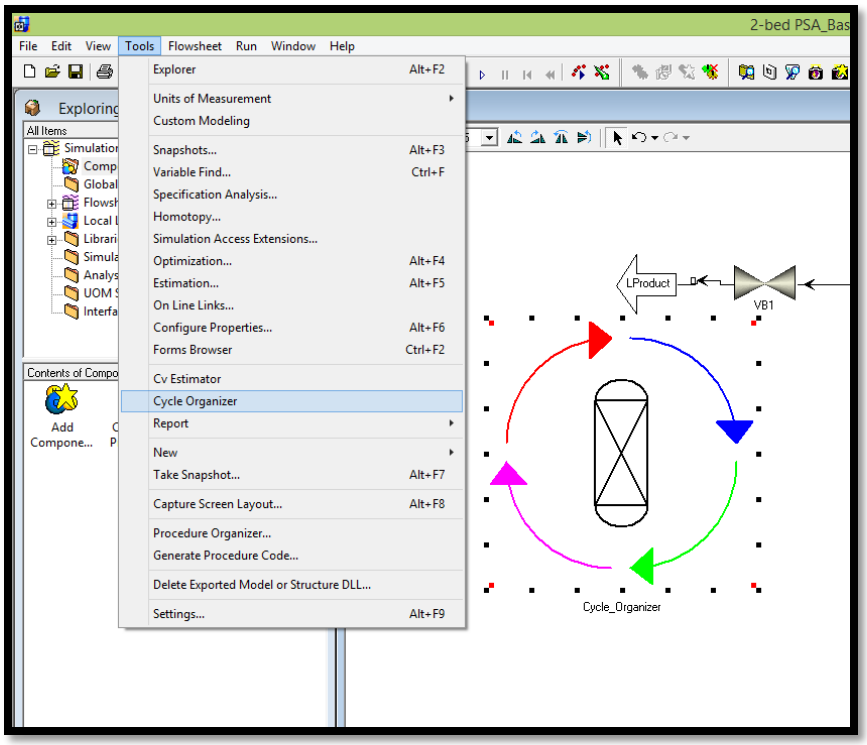

FIGURE 6.46. THE CYCLE ORGANIZER BLOCK IN THE POWERFEED MODEL.

Step 4: Cycle Organizer-> Cycle Options.

Table 6.4 lists the "Cycle" button on the toolbar, its purpose, and the options available on the drop-down menu. Figure 6.47 displays the cycle settings for the process in PowerFeed operation. We set the maximum cycle numbers as 100.

TABLE 6.4. THE "CYCLE" BUTTON ON THE TOOLBAR IN THE CYCLE ORGANIZER.

Toolbar Button	Purpose	Options
Cycle	Cycle controls, such as creating and activating cycles	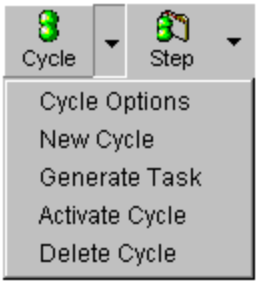

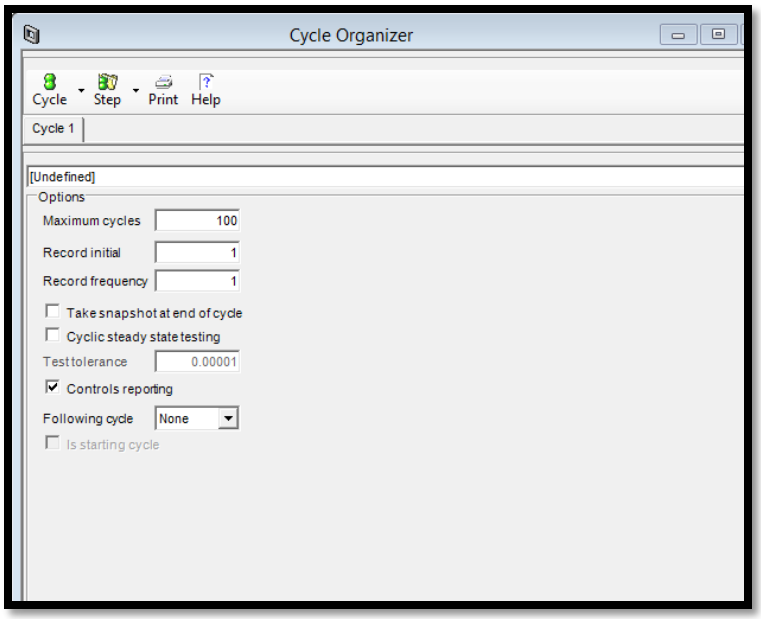

FIGURE 6.47. THE CYCLE OPTIONS IN THE CYCLE ORGANIZER OF THE POWERFEED MODEL.

Step 5: Cycle Organizer-> Step Control->Step 1: the first sub-switching interval.

Table 6.5 lists the "Step" button on the toolbar, its purpose, and the options available on the drop-down menu.

TABLE 6.5. THE "STEP" BUTTON ON THE TOOLBAR IN THE CYCLE ORGANIZER.

Toolbar Button	Purpose	Options
Step	Step controls, such as modifying and inserting steps	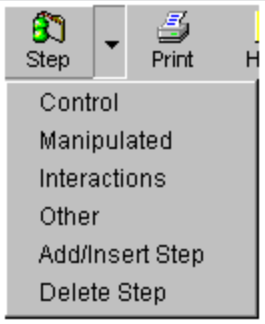

TABLE 6.6. THE CYCLE ORGANIZER CONDITIONS FOR THE POWERFEED MODEL.

	Step 1	Step 2
Subinterval switching time	4.27 min	2.11 min
Subinterval feed flow rates	0	1.149 mL/min
Subinterval recycle flow rates	0.344 mL/min	0.727 mL/min

Table 6.6 lists the cycle organizer settings for the subinterval switching times, feed and recycle flow rates in the PowerFeed model. We get all these optimized subinterval conditions from our simulation and evaluation strategy in the section 5.1.2. We show the detailed calculations for the values of Table 6.6 as follow:

From looking at the effect of the second subinterval feed flow rate on the B purity in Figure 5.6, we achieve the best performance when F_1= 0 and F_2= 0.149 ml/min in the PowerFeed operation with two subintervals.

$$\text{Since:} \quad F_{SMB} * t_{sw} = F_1 * t_1 + F_2 * t_2 \tag{6.25}$$

In this case, $F_{SMB} = 0.38 \frac{ml}{min}$; $t_1 + t_2 = t_{sw} = 6.38\ min$,

Then, $t_1 = 4.27\ \text{min}\ and\ t_2 = 2.11\ min$

For the calculation of the recycle flow rates, if we combine the following equations:

$$m_j = \frac{Q_j t_{sw} - V_{bed}\varepsilon - V_j^D}{V_{bed}(1-\varepsilon)} \tag{6.26}$$

$$t_{sw} = \frac{\phi L^2}{\Delta P_{max}} \sum_{j=1}^{j=4} n_j (m_j(1-\varepsilon) + \varepsilon) \quad \textbf{(6.27)}$$

$$Q_4 = Q_{\text{recycle}} \quad (6.28)$$

$$Q_3 = Q_2 + Q_F \quad (6.29)$$

$$Q_2 = Q_1 - (Q_F + Q_D - Q_R) \quad (6.30)$$

$$Q_1 = Q_4 + Q_D \quad (6.31)$$

We get eq. 6.26:

$$Q_{\text{recycle}} = \frac{V_{bed}\Delta\text{Pmax} - L^2\phi(n_1 Q_D - n_2 Q_F + (n_2+n_3)Q_R)}{L^2\phi(n_1+n_2+n_3+n_4)} \quad (6.32)$$

Since: $V_{bed} = 2.493\ cm^3$; $\Delta\text{Pmax} = 40$ bar; $L = 15\ cm$; $\phi = 0.1, n_1 = 1$; $n_2 = 2$; $n_3 = 2$; $n_4 = 1$; $Q_D = 0.65\frac{ml}{min}$; $Q_R = 0.43\frac{ml}{min}$

Then we get the final recycle flow rate equation based on the feed flow rate:

$$Q_{\text{recycle}} = 0.344 + 0.333 Q_F \quad (6.33)$$

Since: $Q_{F1} = 0\frac{ml}{min}$; $Q_{F2} = 0.149\frac{ml}{min}$

We get: $Q_{recy1} = 0.344\frac{ml}{min}$; $Q_{recy2} = 0.727\frac{ml}{min}$

Then, press the step control and follow Figures 6.48 to 6.51 to edit steps 1 and 2. In this case, we choose the time-driven method, which is the most common step control method. Here, the step control is a fixed elapsed time; for example, the step is set to terminate after 4.27 minutes. The step time remains constant from cycle to cycle.

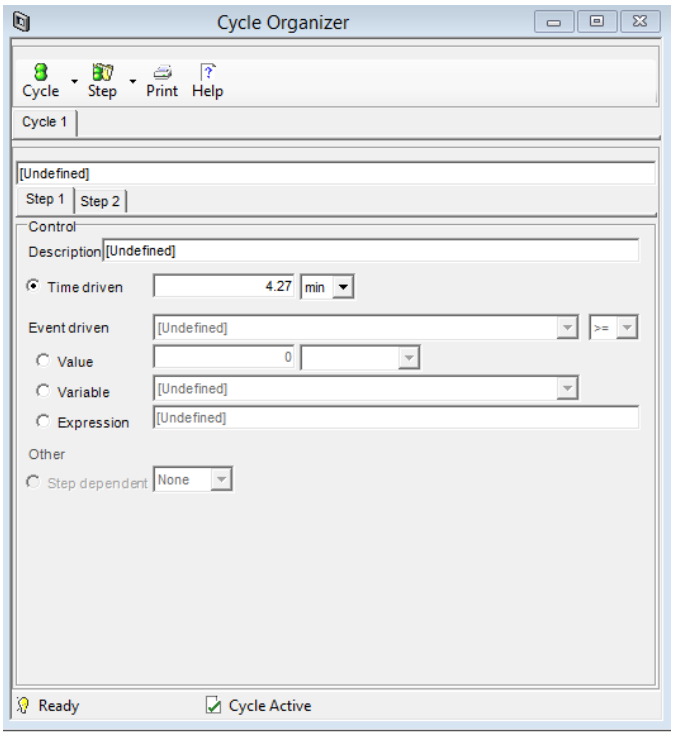

FIGURE 6.48. THE STEP CONTROL SETTING FOR STEP ONE IN THE POWERFEED MODEL.

Step 6: Cycle Organizer-> Step Control->Step 2: second subswitching interval.

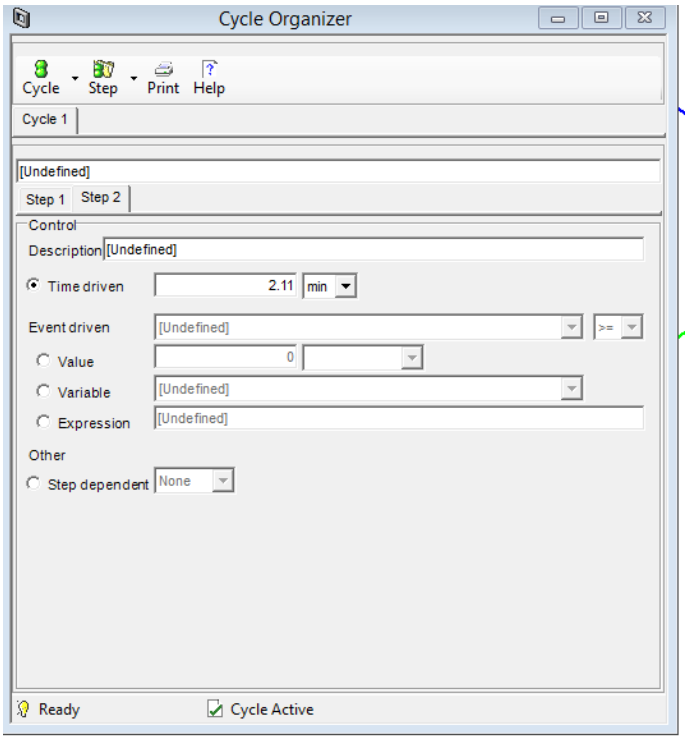

FIGURE 6.49. THE STEP CONTROL SETTING FOR STEP TWO IN THE POWERFEED MODEL.

Step 7: Cycle Organizer-> Step Manipulated->Step 1: first subswitching interval.

Table 6.6 lists the main buttons on the toolbar, their purposes, and the options available on their drop-down menus of the Variables. Within each step of a cycle, we may modify different variables. These variables may control, for example:

- Feed condition
- Valve opening
- Heater duty

To access the list of manipulated variables: From the Step button's drop-down list, click Manipulated. In our case, we mainly adjust the feed and recycle flow rates during different sub-switching intervals.

TABLE 6.7. THE "VARIABLE" BUTTON ON THE TOOLBAR IN THE CYCLE ORGANIZER.

Toolbar Button	Purpose	Options
Variable (available only if you selected Manipulated from the Step menu)	Adding or Deleting variables	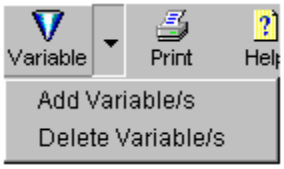

To add a new manipulated step variable:

1. Click the Variable button on the toolbar; or from its drop-down list, click Add Variable/s.

   The Variable Selector dialog box appears, which lists the available fixed and initial variables that have not already been selected in the current step.

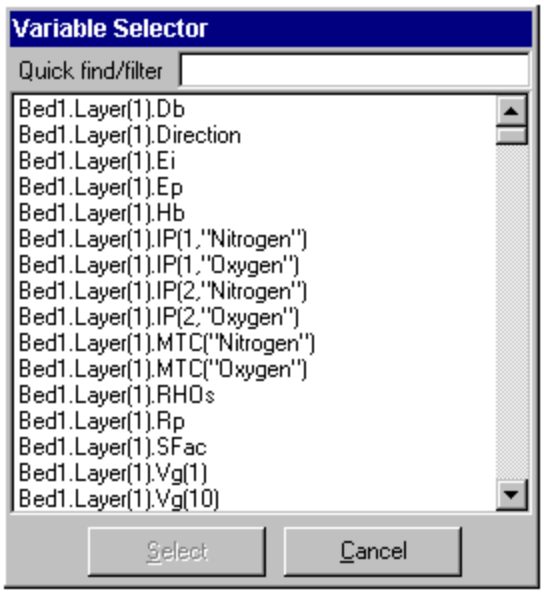

FIGURE 6.50. THE VARIABLE SELECTOR WINDOW FOR VARIABLE FINDING IN THE CYCLE ORGANIZER.

2. Select a variable using one of these actions:

    - Double-click on the variable in the list.
    - Type the name of the variable in the text box at the top of the dialog box (a dynamic search will take place during typing).
    - Select multiple variables, using either the SHIFT or CTRL key.
    - Use wildcards in the text box to reduce the list size and then select.

Figure 6.51 is the final look of step 1 and shows the subinterval conditions in step one:

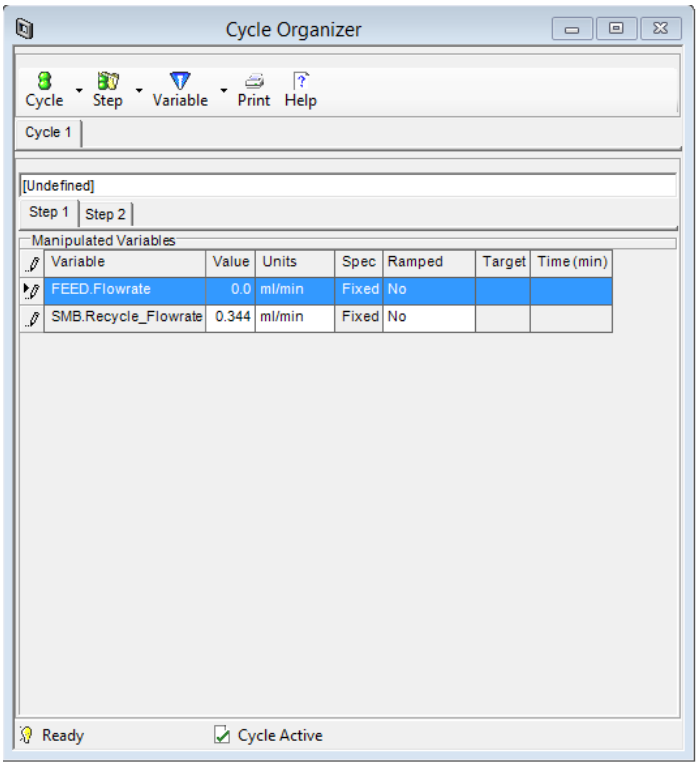

FIGURE 6.51. THE MANIPULATED VARIABLES FOR STEP ONE IN THE POWERFEED MODEL.

Step 8: Cycle Organizer-> Step Manipulated ->Step 2: second subswitching interval.

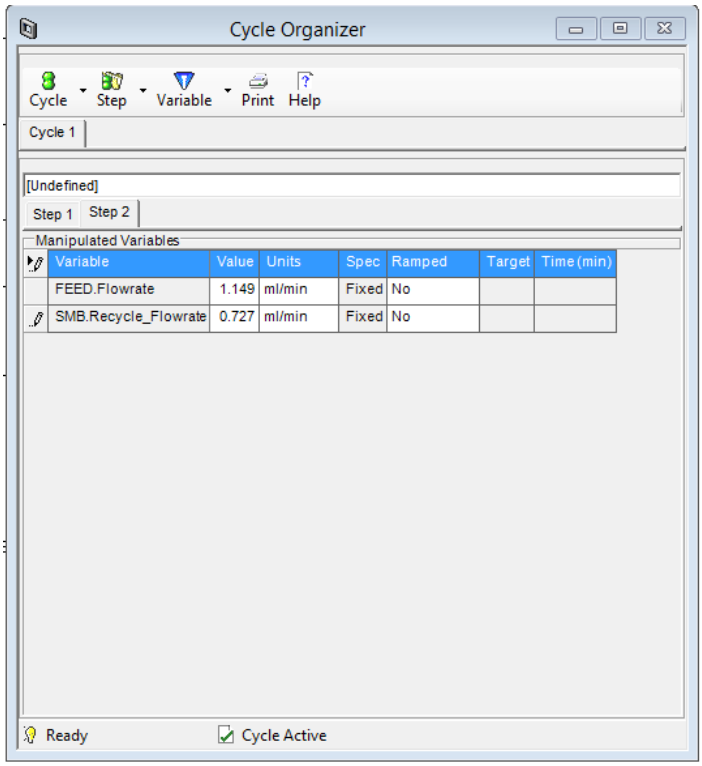

FIGURE 6.52. THE MANIPULATED VARIABLES FOR STEP TWO IN THE POWERFEED MODEL.

Step 9: Cycle Options->Generate Task.

Once a new cycle has been defined, or changes made to an existing definition, you must generate the cyclic task before the simulation can be run. To generate the cyclic task:

- On the Cycle button's drop-down menu, click Generate Task, as shown in Figure 6.53.

View the Cycle Organizer status bar to see how the generation is progressing:

- You see 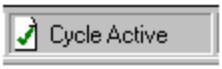

when the cyclic task has been successfully generated (errors are noted in the simulation messages window).

- You see 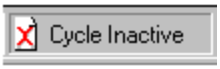

when there is another activated cycle.

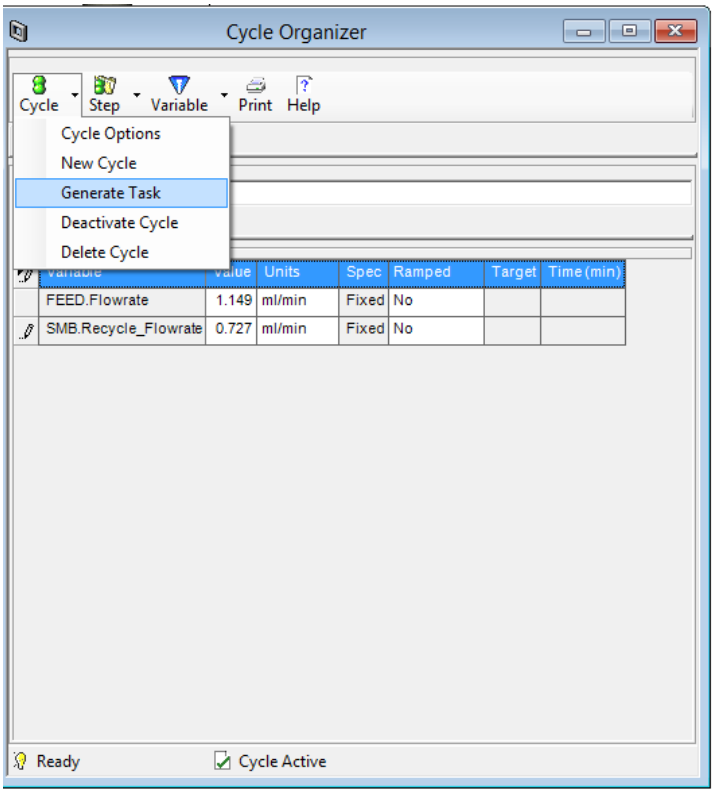

FIGURE 6.53. THE GENERATION PROGRESSING IN THE CYCLE ORGANIZER OF THE POWERFEED MODEL.

Step 10: Configure Block -> Initialize.

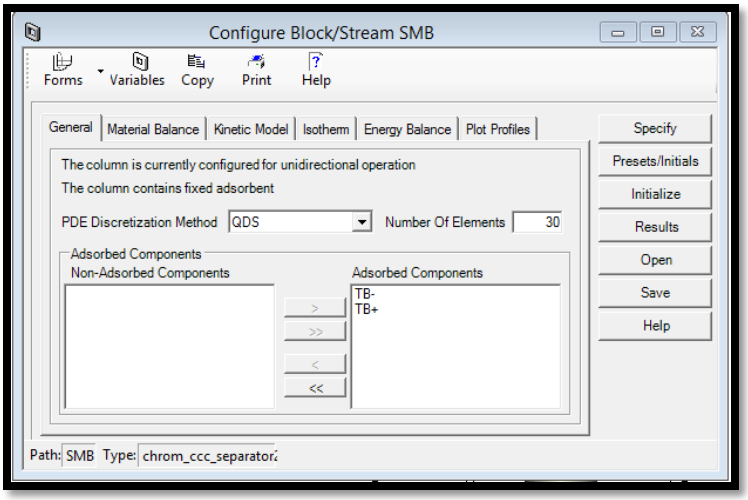

FIGURE 6.54. THE INITIALIZATION OF THE POWERFEED COLUMN.

Step 11: Run Options->Initialization.

The model is ready to initialize.

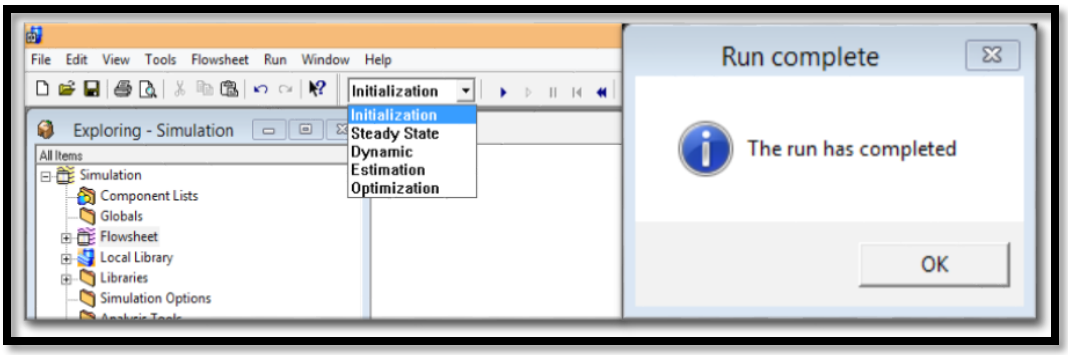

FIGURE 6.55.THE INITIALIZATION OF THE POWERFEED MODEL.

Step 12: Run Options->Dynamic.

The model is ready for the dynamic run after reaching the pause time (382.8 min) we set.

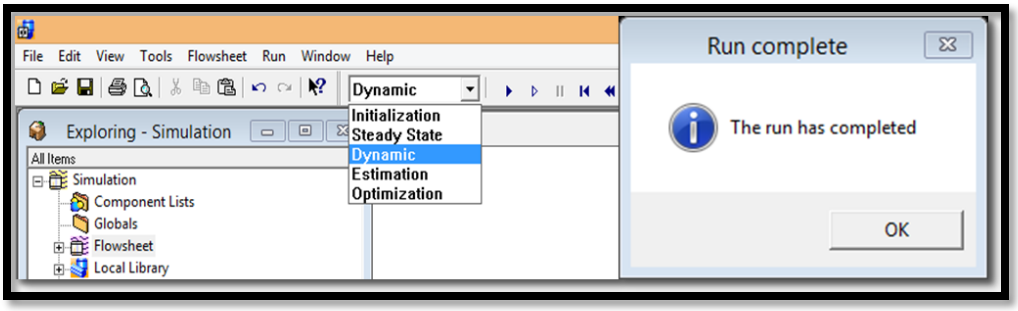

FIGURE 6.56.THE DYNAMIC RUN OF THE POWERFEED MODEL.

Step 13: Results->Plots.

This step presents the extract concentration plot, raffinate concentration plot and the column concentration profile.

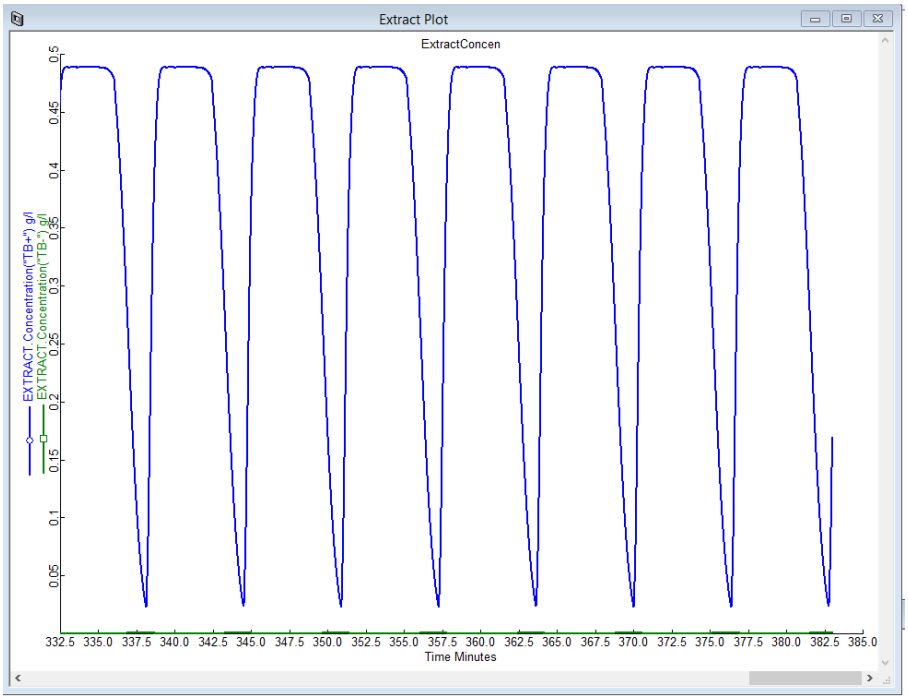

FIGURE 6.57.THE RESULTING EXTRACT CONCENTRATION RESULTS FOR BOTH COMPONENTS IN POWERFEED.

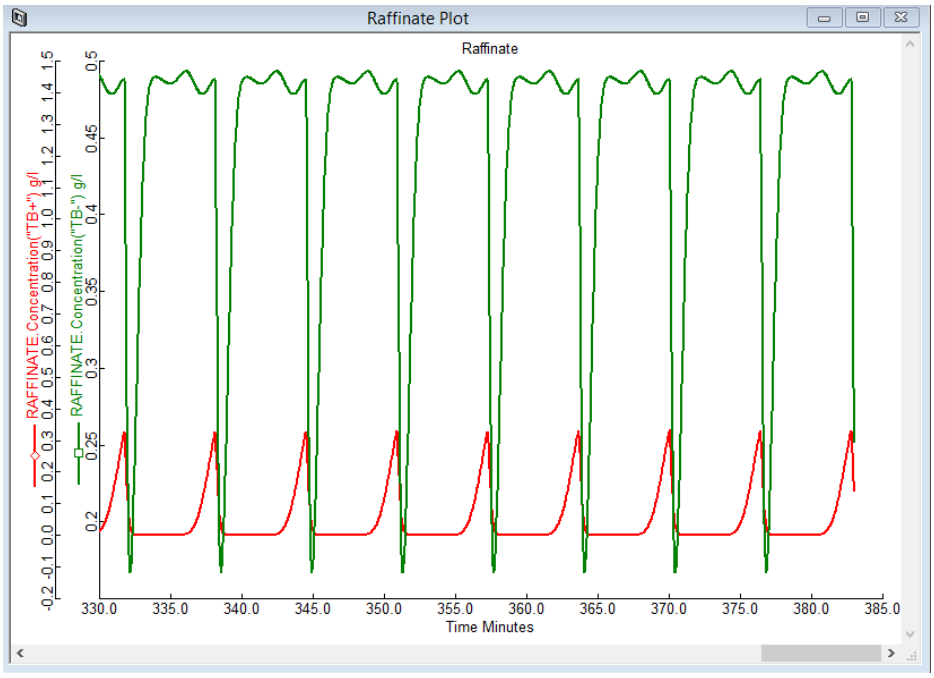

FIGURE 6.58.THE RESULTING RAFFINATE CONCENTRATION RESULTS FOR BOTH COMPONENTS IN POWERFEED.

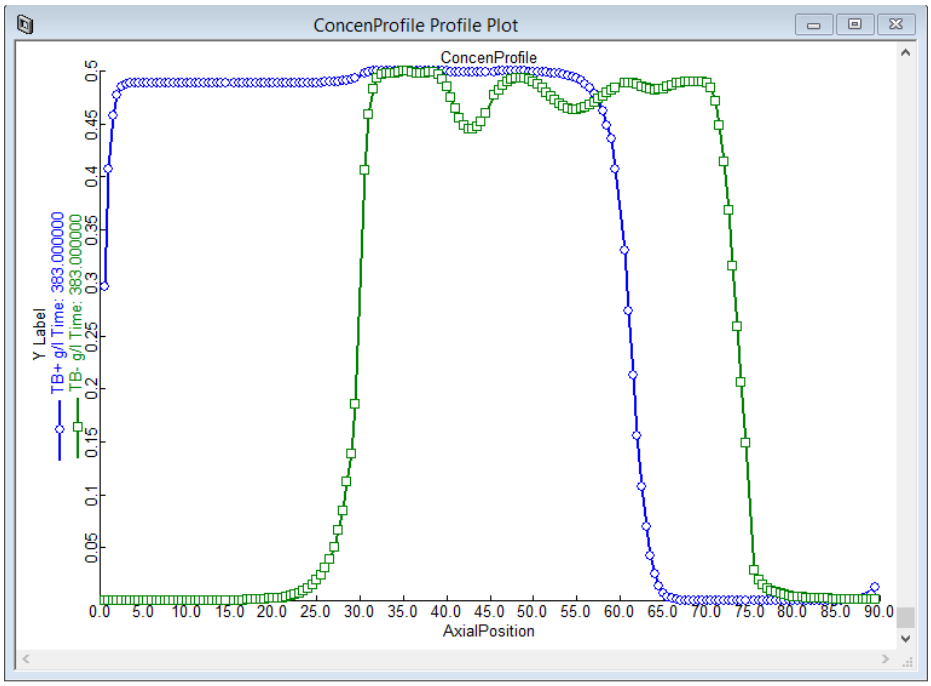

FIGURE 6.59.THE RESULTING CONCENTRATION PROFILE WITHIN THE POWERFEED COLUMN.

6.4. Workshop 4: Apply ModiCon to the 4-Zone SMB Model

In this workshop, we demonstrate how to create a ModiCon model from the basic 4-zone SMB model. ModiCon adjusts the feed concentration, instead of feed flow rates, within the switching subintervals, we still need to add a Cycle Organizer in the ModiCon model to control the change of the cyclic feed concentrations. We keep the feed flow rate and the column configuration the same as the basic SMB model. Basically, we follow the pretty similar steps as we did for the PowerFeed to build a ModiCon model.

Step 1: Open the "4-zone Basic SMB model", and save it as "4-zone ModiCon model".

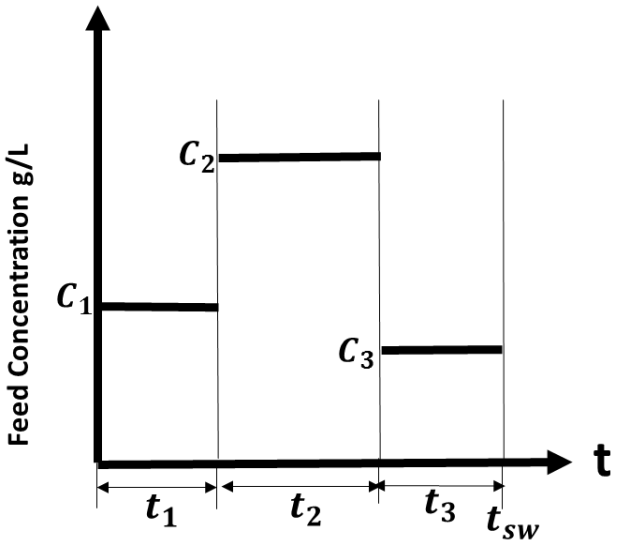

FIGURE 6.60. THE FEED FLOW RATE POLICIES IN THE MODICON WITH THREE SUBINTERVALS.

Step 2: Tool-> Cycle Organizer. We add a new Cycle Organizer block into the ModiCon model.
Step 3: Cycle Organizer-> Cycle Options.

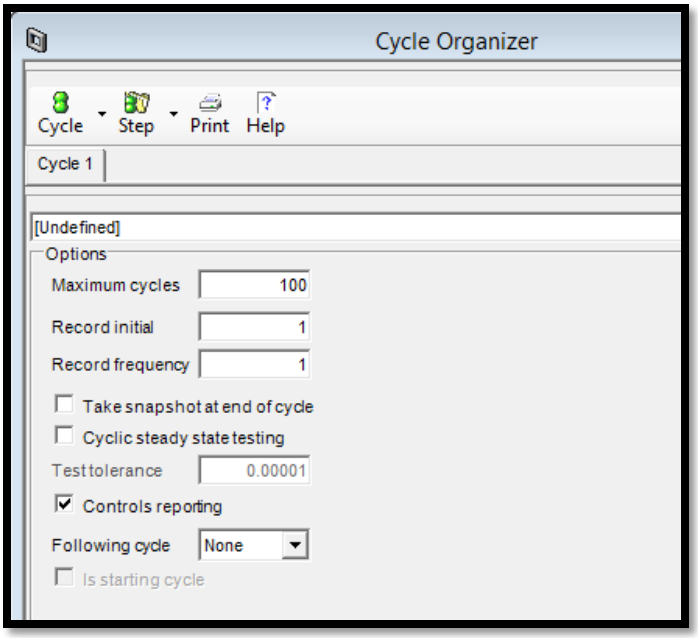

FIGURE 6.61. THE CYCLE OPTIONS IN THE CYCLE ORGANIZER OF THE MODICON MODEL.

Step 4: Cycle Organizer-> Step Control->Step 1: first subswitching interval.

TABLE 6.8. THE CYCLE ORGANIZER CONDITIONS FOR THE MODICON MODEL.

	Step 1	Step 2	Step 3
Subinterval switching time	1.3 min	3.78 min	1.3 min
Subinterval feed concentrations	0.166 g/L	1.6 g/L	0.166 g/L

Table 6.8 lists the cycle organizer settings for the subinterval switching times, feed concentrations in the ModiCon model with three subintervals. We get all these optimized subinterval conditions from our simulation and evaluation strategy in the section 5.1.3. We show the detailed calculations for the values of Table 6.8 as follow.

From looking at the effect of the second subinterval feed concentration on the B purity and A recovery in Figure 5.9, we achieve the best performance when $C_1 = C_3 = 0.166$ g/L and $C_2 = 1.6$ g/L in the ModiCon operation with three subintervals.

$$\text{Since:} \quad C_{SMB} * t_{sw} = C_1 * t_1 + C_2 * t_2 + C_3 * t_3 \tag{6.34}$$

In this case, $C_{SMB} = 1\ g/L;\ t_1 + t_2 + t_3 = t_{sw} = 6.38\ min,$

Then, $t_1 = 1.3\,\text{min}\ and\ t_2 = 3.78\ min\ ;\ t_3 = 1.3\ min$ We follow the Figures 6.62 to 6.67 to edit the steps one to three step by step.

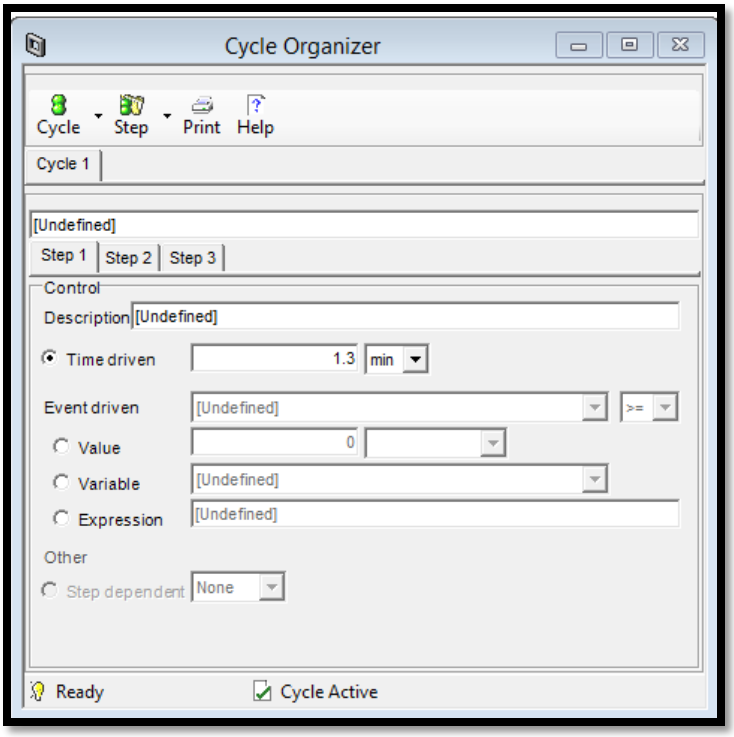

FIGURE 6.62. THE STEP CONTROL SETTING FOR STEP ONE IN THE MODICON MODEL.

Step 5: Cycle Organizer-> Step Control->Step 2: second subswitching interval.

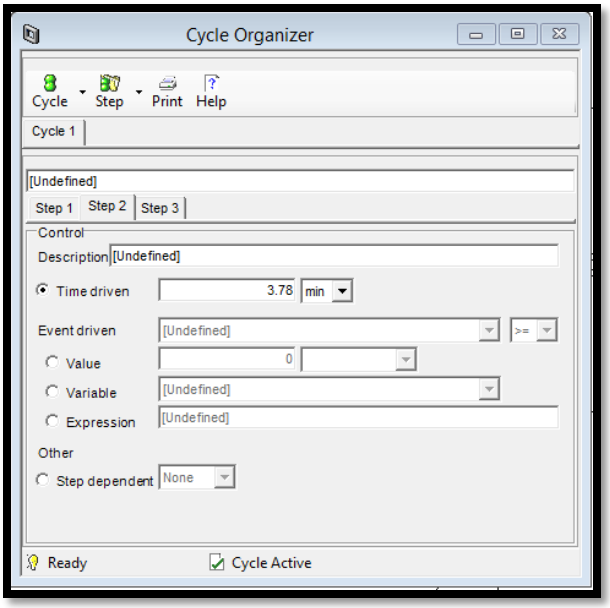

FIGURE 6.63. THE STEP CONTROL SETTING FOR STEP TWO IN THE MODICON MODEL.

Step 6: Cycle Organizer-> Step Control->Step 3: third subswitching interval.

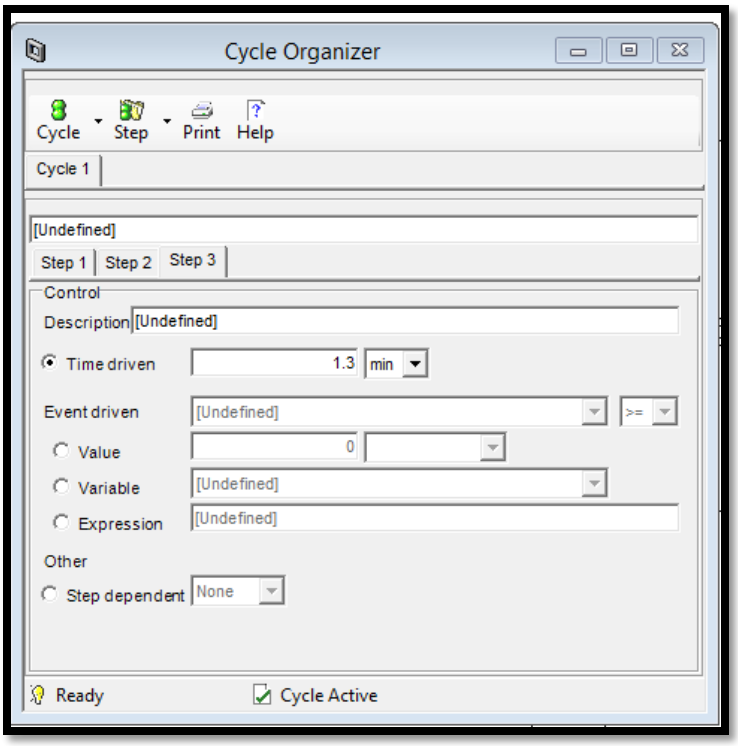

FIGURE 6.64. THE STEP CONTROL SETTING FOR STEP THREE IN THE MODICON MODEL.

Step 7: Cycle Organizer-> Step Manipulated -> Step 1: first subswitching interval.

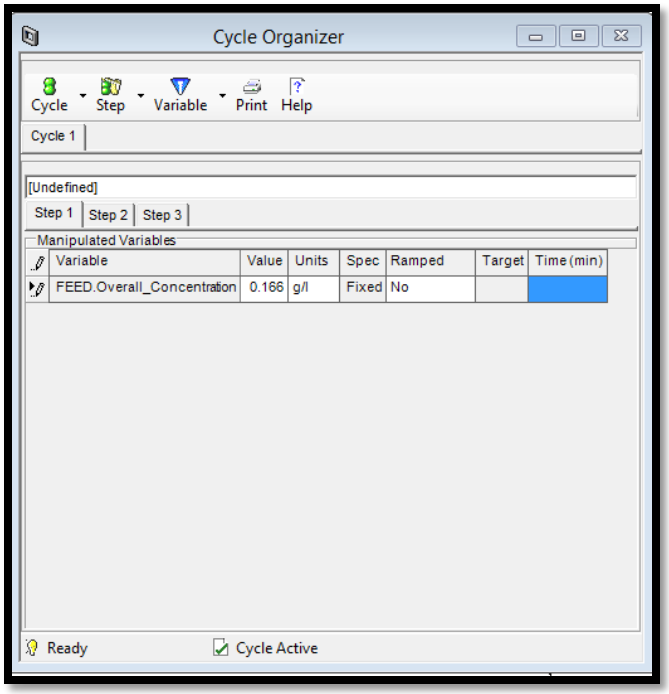

FIGURE 6.65. THE MANIPULATED VARIABLES FOR STEP ONE IN THE MODICON MODEL.

Step 8: Cycle Organizer-> Step Manipulated -> Step 2: second subswitching interval.

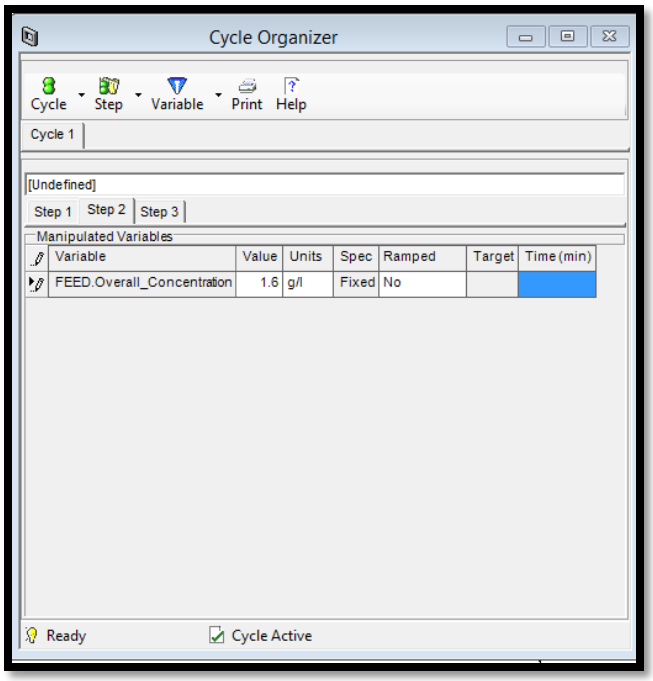

FIGURE 6.66. THE MANIPULATED VARIABLES FOR STEP TWO IN THE MODICON MODEL.

Step 9: Cycle Organizer-> Step Manipulated -> Step 3: third subswitching interval.

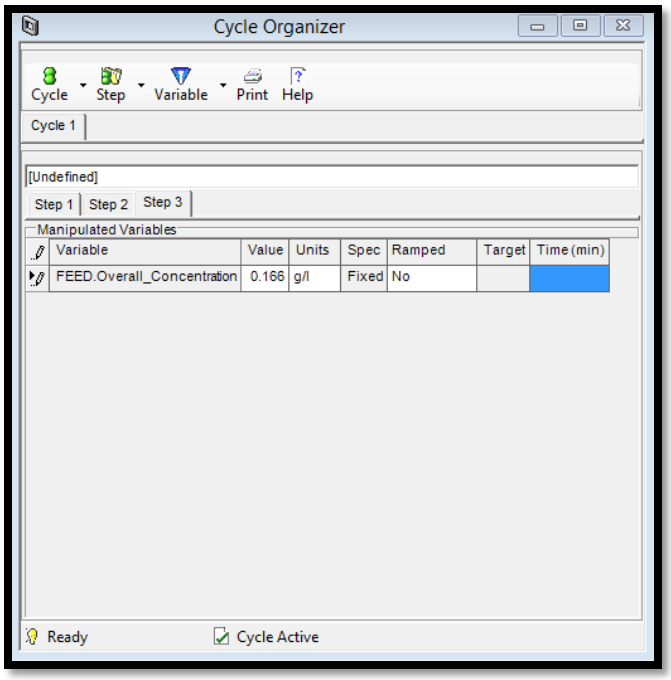

FIGURE 6.67. THE MANIPULATED VARIABLES FOR STEP THREE IN THE MODICON MODEL.

Step 10: Cycle Options->Generate Task.

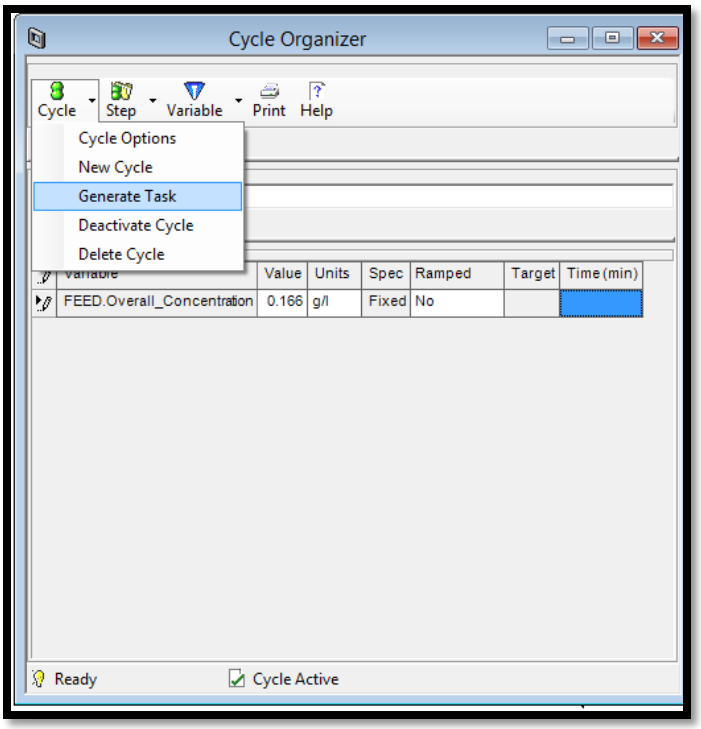

FIGURE 6.68. THE GENERATION PROGRESSING IN THE CYCLE ORGANIZER OF THE MODICON MODEL.

Step 11: Configure Block -> Initialize.

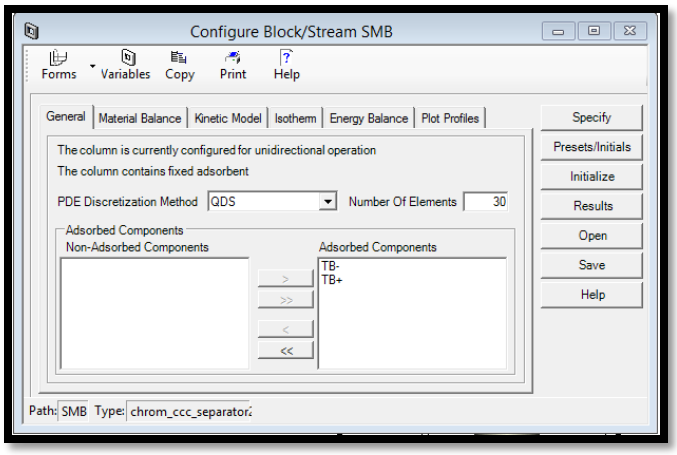

FIGURE 6.69. THE INITIALIZATION OF THE MODICON COLUMN.

Step 12: Run Options->Initialization.

The model is ready to initialize.

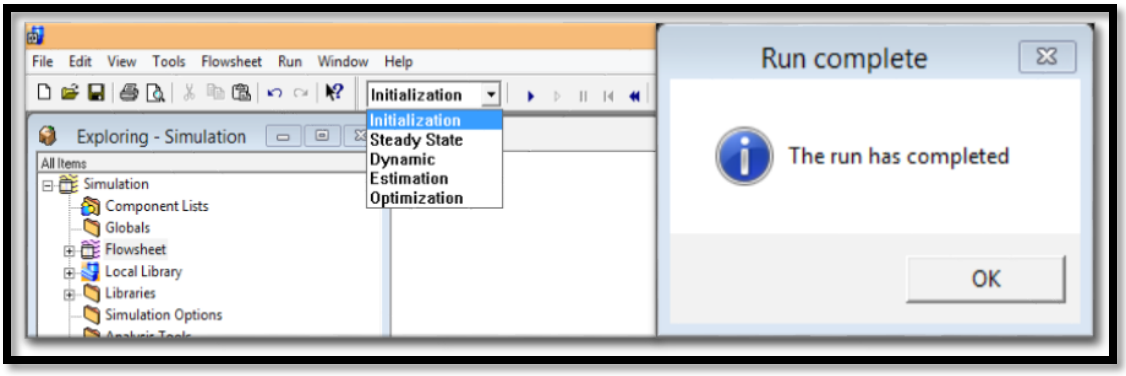

FIGURE 6.70.THE INITIALIZATION OF THE MODICON MODEL.

Step 13: Run Options->Dynamic.

The model is ready for the dynamic run after reaching the pause time (382.8 min) we set.

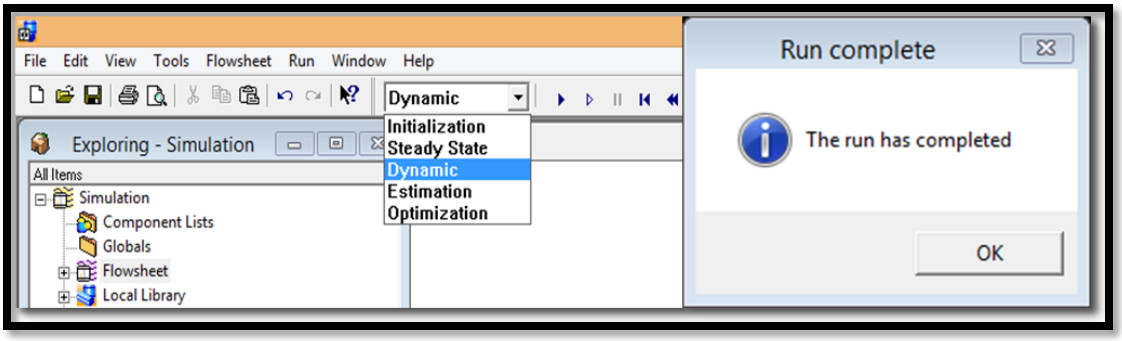

FIGURE 6.71.THE DYNAMIC RUN OF THE MODICON MODEL.

Step 14: Results->Plots.

This step presents the extract concentration plot, raffinate concentration plot and the column concentration profile.

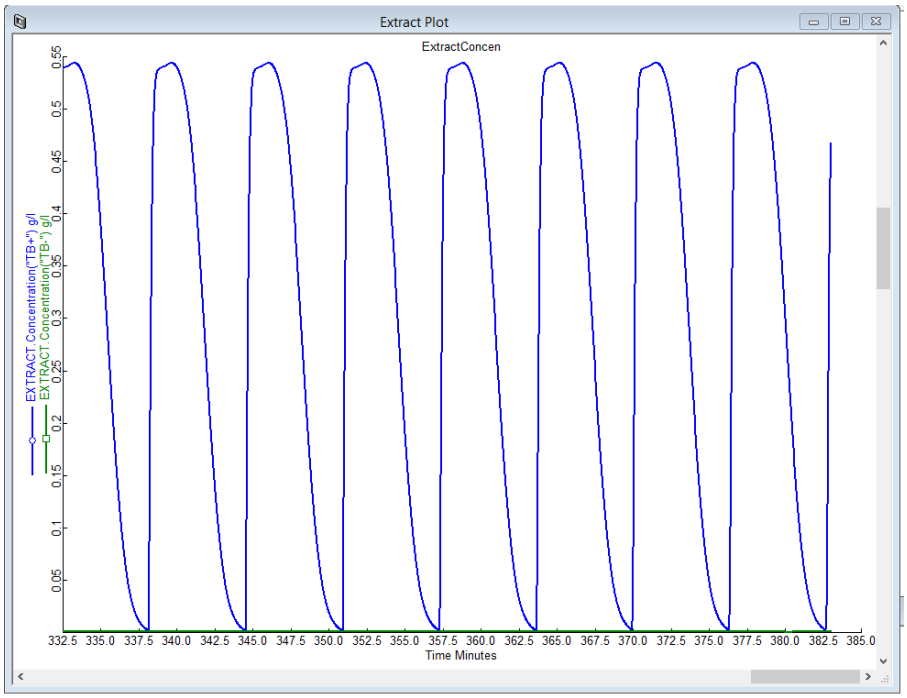

FIGURE 6.72. THE RESULTING EXTRACT CONCENTRATION RESULTS FOR BOTH COMPONENTS IN MODICON.

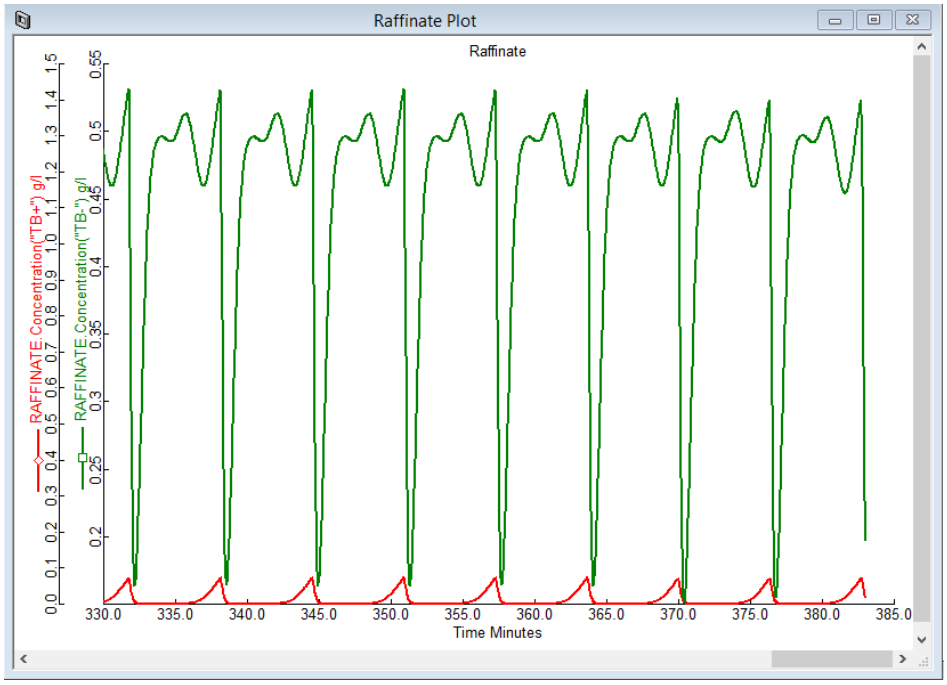

FIGURE 6.73. THE RESULTING RAFFINATE CONCENTRATION RESULTS FOR BOTH COMPONENTS IN MODICON.

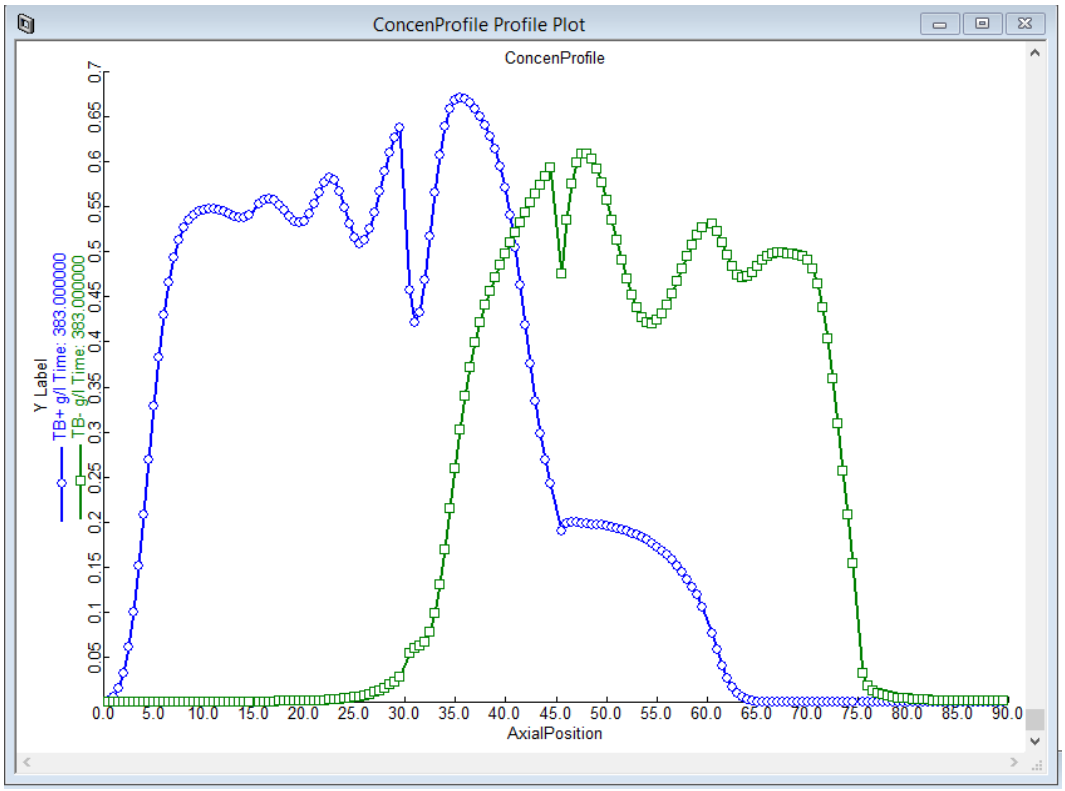

FIGURE 6.74.THE RESULTING CONCENTRATION PROFILE WITHIN THE MODICON COLUMN.

6.5. *Workshop 5: Apply Combined Operations to the 4-Zone SMB Model*

In this workshop, we combine two operational modes as a new combined operational mode to see if the integrated system will perform better than either one individually. We consider the combination of two operational modes, PowerFeed and ModiCon, and refer to it as PF&MC. We vary the feed flow rates, recycle flow rates and feed concentrations within three switching subintervals, as shown in Figure 6.75 and Table 6.9.

Step 1: Open the "4-zone Basic SMB model", and save it as "4-zone PF&MC model". Figure 6.75 shows the feed inlet policies in the PF&MC model with three subintervals.

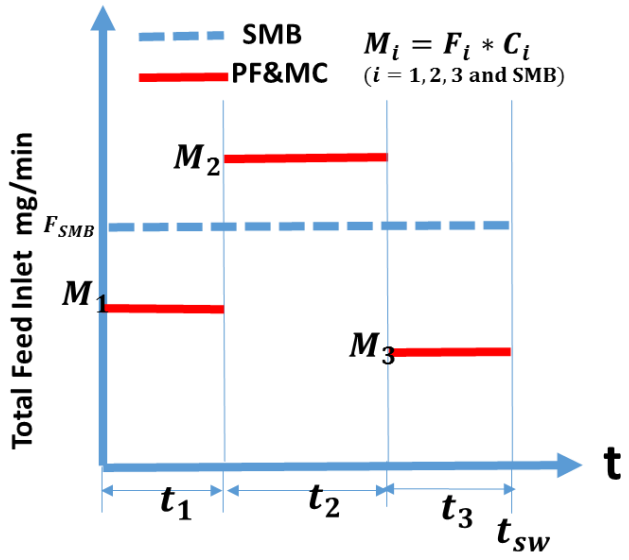

FIGURE 6.75. THE FEED INLET POLICIES IN THE PF&MC MODEL WITH THREE SUBINTERVALS.

Step 2: Tool-> Cycle Organizer. Similarly, we add a cycle organizer into the basic SMB model, and edit the cycle based on the following conditions in Table 6.9.

TABLE 6.9. THE CYCLE ORGANIZER CONDITIONS FOR THE COMBINED PF&MC MODEL.

	Step 1	Step 2	Step 3
Subinterval switching time	1.117 min	4.147 min	1.117 min
Subinterval feed concentrations	0.1 g/L	1.751 g/L	0.1 g/L
Subinterval feed flow rates	0.494 mL/min	0.319 mL/min	0.494 mL/min
Subinterval recycle flow rates	0.508 mL/min	0.45 mL/min	0.508 mL/min

Table 6.9 lists the cycle organizer settings for the subinterval switching times, feed concentrations, feed and recycle flow rates in the PF&MC model. We get all these optimized subinterval conditions from our simulation and evaluation strategy in the section 5.1.4. We show the detailed calculations for the values of Table 6.9 as follow:

From evaluation of the PF&MC operation on the product purity and recovery, we achieve the best performance when $C_1 = C_3 = 0.1$ g/L and $C_2 = 1.751$ g/L, and $F_1 = F_3 = 0.494$ ml/min and $F_2 = 0.319$ ml/min in the PowerFeed operation with two subintervals.

Since: $C_{SMB} * F_{SMB} * t_{sw} = C_1 * F_1 * t_1 + C_2 * F_2 * t_2 + C_3 * F_3 * t_3$ (6.35)

In this case, $F_{SMB} = 0.38 \frac{ml}{min}$; $C_{SMB} = 1\ g/L$; $t_1 + t_2 + t_3 = t_{sw} = 6.38\ min$,

Then, $t_1 = 1.117 \min\ and\ t_2 = 4.147\ min$; $t_3 = 1.117\ min$

For the calculation of the recycle flow rates, we use the same equation:

$$Q_{\text{recycle}} = 0.344 + 0.333 Q_F \quad (6.36)$$

Since: $Q_{F1} = 0.494 \frac{ml}{min}$; $Q_{F2} = 0.319 \frac{ml}{min}$; $Q_{F3} = 0.494 \frac{ml}{min}$

We get: $Q_{recy1} = 0.508 \frac{ml}{min}$; $Q_{recy2} = 0.45 \frac{ml}{min}$; $Q_{recy3} = 0.508 \frac{ml}{min}$

Step 3: Cycle Organizer-> Cycle Options. We still choose 100 as the maximum cycle number.

Step 4: Cycle Organizer-> Step Control->Step 1: first sub-switching interval.

We follow Figures 6.76 to 6.81 to edit the steps one to three for the PF&MC.

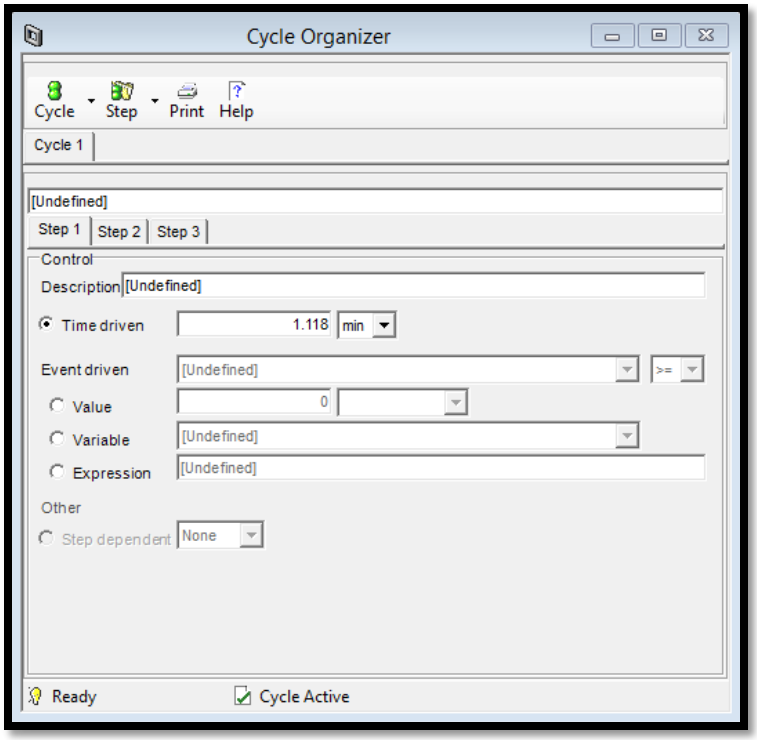

FIGURE 6.76. THE STEP CONTROL SETTING FOR STEP ONE IN THE PF&MC MODEL.

Step 5: Cycle Organizer-> Step Control->Step 2: second subswitching interval.

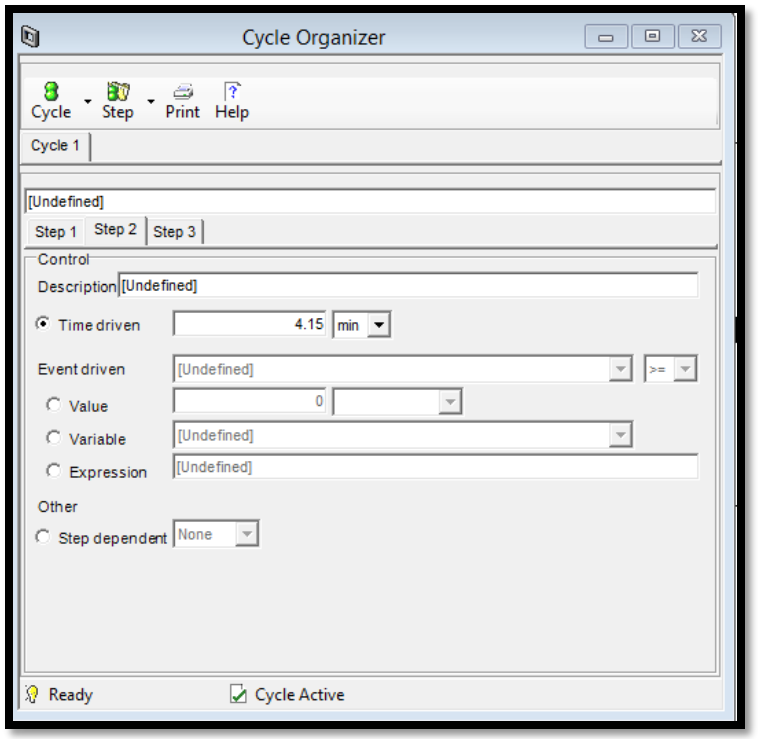

FIGURE 6.77. THE STEP CONTROL SETTING FOR STEP TWO IN THE PF&MC MODEL.

Step 6: Step 5: Cycle Organizer-> Step Control->Step 3: third subswitching interval.

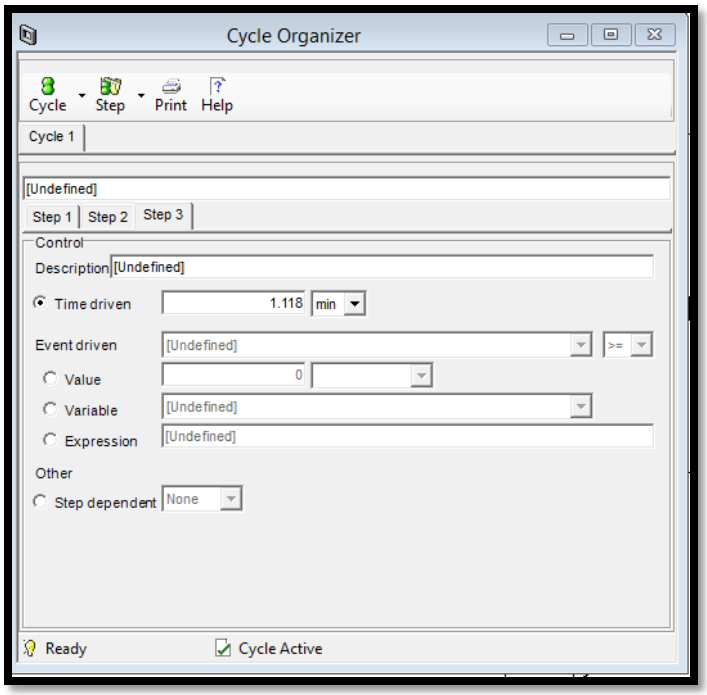

FIGURE 6.78. THE STEP CONTROL SETTING FOR STEP THREE IN THE PF&MC MODEL.

Step 7: Cycle Organizer-> Step Manipulated -> Step 1: first subswitching interval.

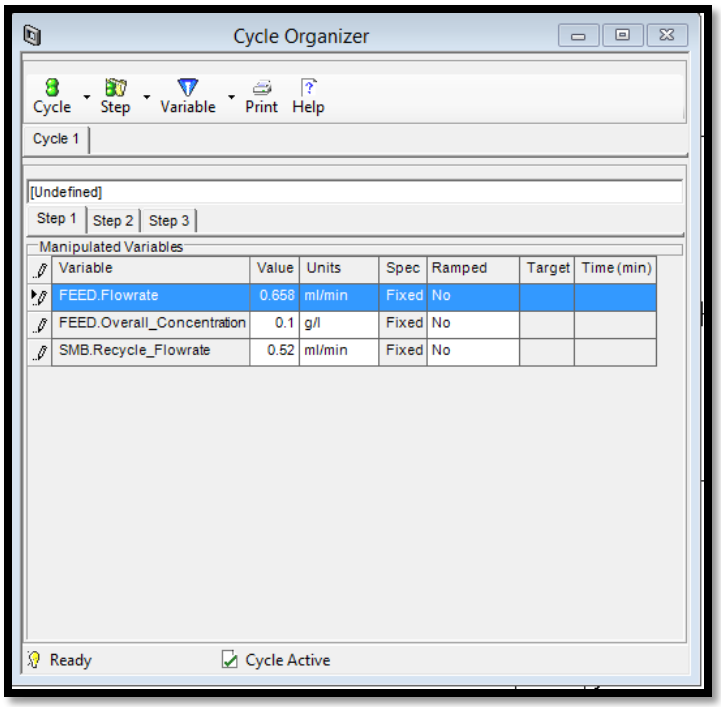

FIGURE 6.79. THE MANIPULATED VARIABLES FOR STEP ONE IN THE PF&MC MODEL.

Step 8: Cycle Organizer-> Step Manipulated -> Step 2: second subswitching interval.

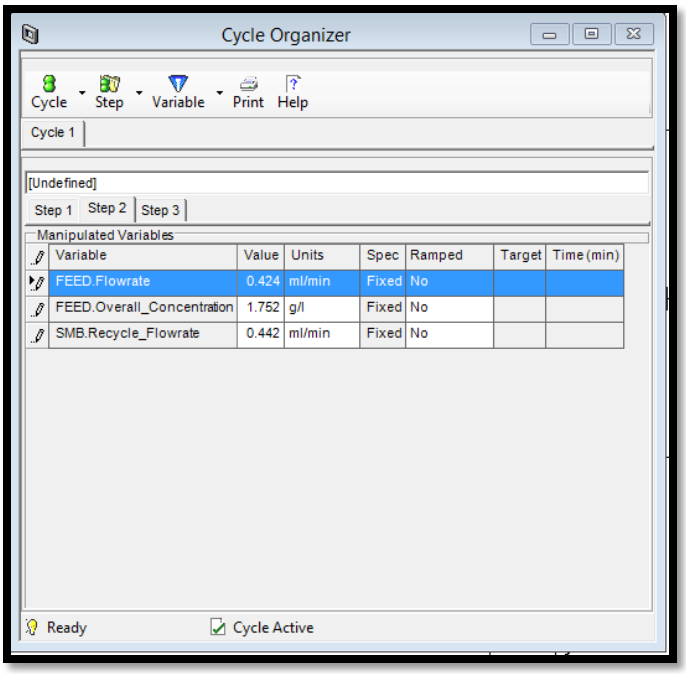

FIGURE 6.80. THE MANIPULATED VARIABLES FOR STEP TWO IN THE PF&MC MODEL.

Step 9: Cycle Organizer-> Step Manipulated -> Step 3: third subswitching interval.

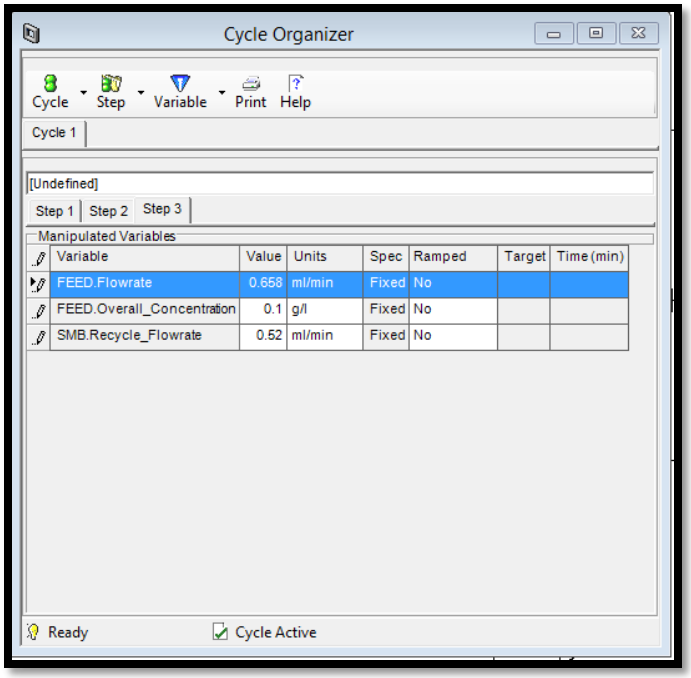

FIGURE 6.81. THE MANIPULATED VARIABLES FOR STEP THREE IN THE PF&MC MODEL.

Step 10: Cycle Options->Generate Task.

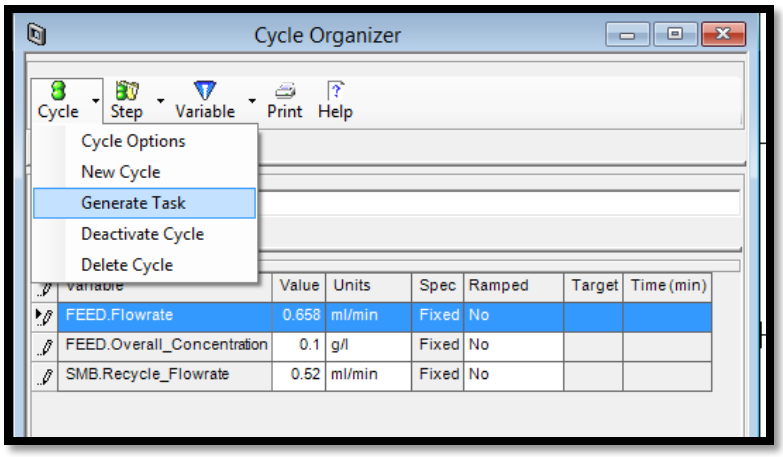

FIGURE 6.82. THE GENERATION PROGRESSING IN THE CYCLE ORGANIZER OF THE PF&MC MODEL.

Step 11: Configure Block -> Initialize.

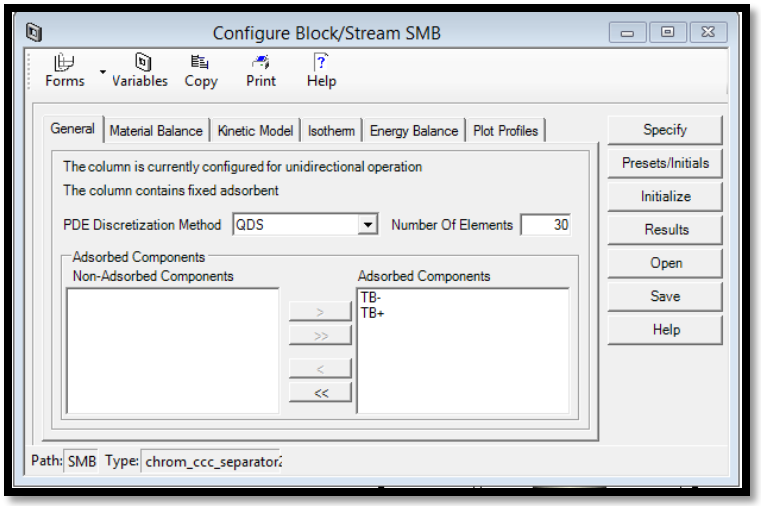

FIGURE 6.83. THE INITIALIZATION OF THE PF&MC COLUMN.

Step 12: Run Options->Initialization.

The model is ready to initialize.

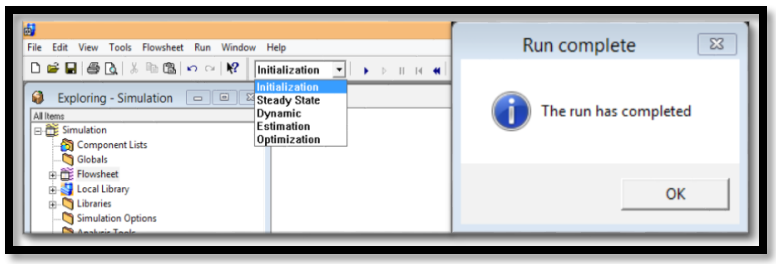

FIGURE 6.84.THE INITIALIZATION OF THE PF&MC MODEL.

Step 13: Run Options->Dynamic.

The model is ready for the dynamic run until reaching the pause time (382.8 min) we set.

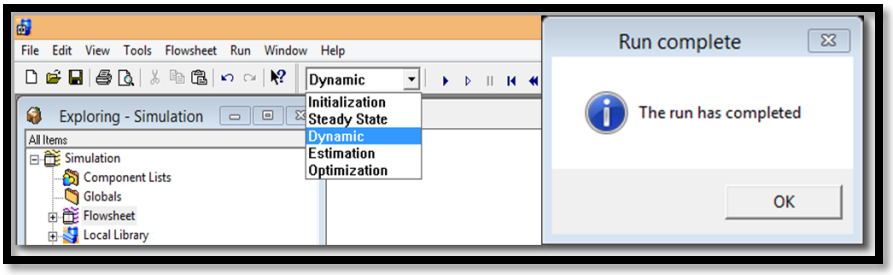

FIGURE 6.85.THE DYNAMIC RUN OF THE PF&MC MODEL.

Step 14: Results->Plots.

This step presents the extract concentration plot, raffinate concentration plot and the column concentration profile.

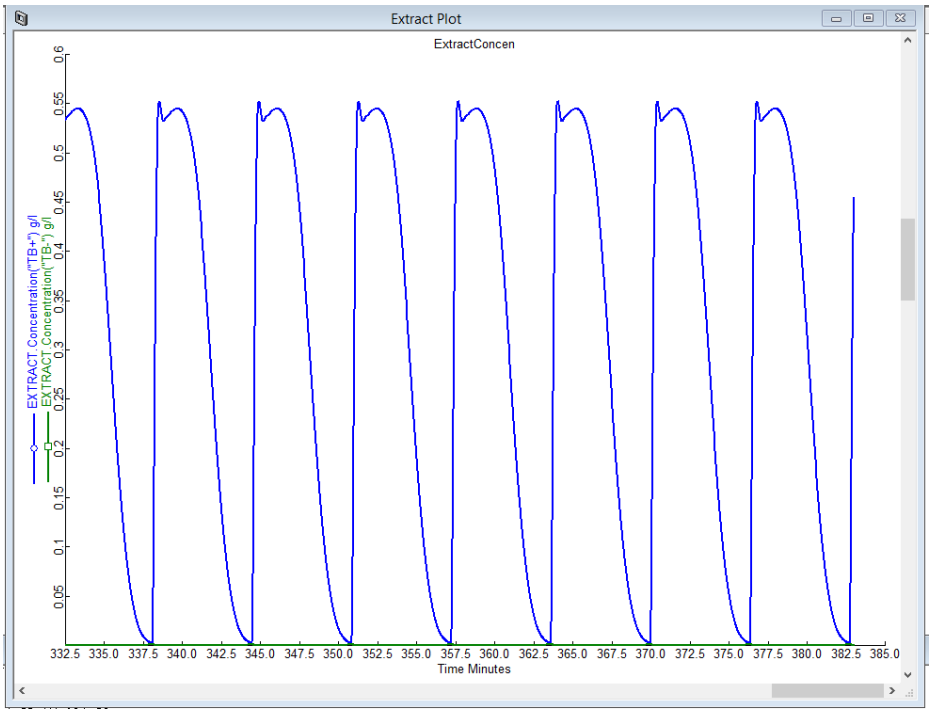

FIGURE 6.86.THE RESULTING EXTRACT CONCENTRATION RESULTS FOR BOTH COMPONENTS IN PF&MC.

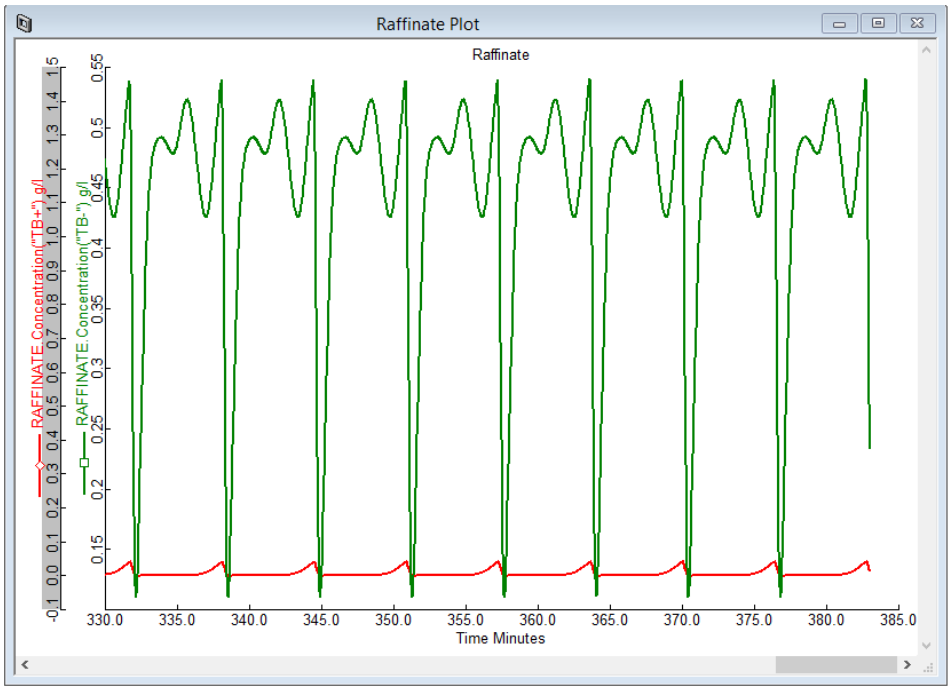

FIGURE 6.87.THE RESULTING RAFFINATE CONCENTRATION RESULTS FOR BOTH COMPONENTS IN PF&MC.

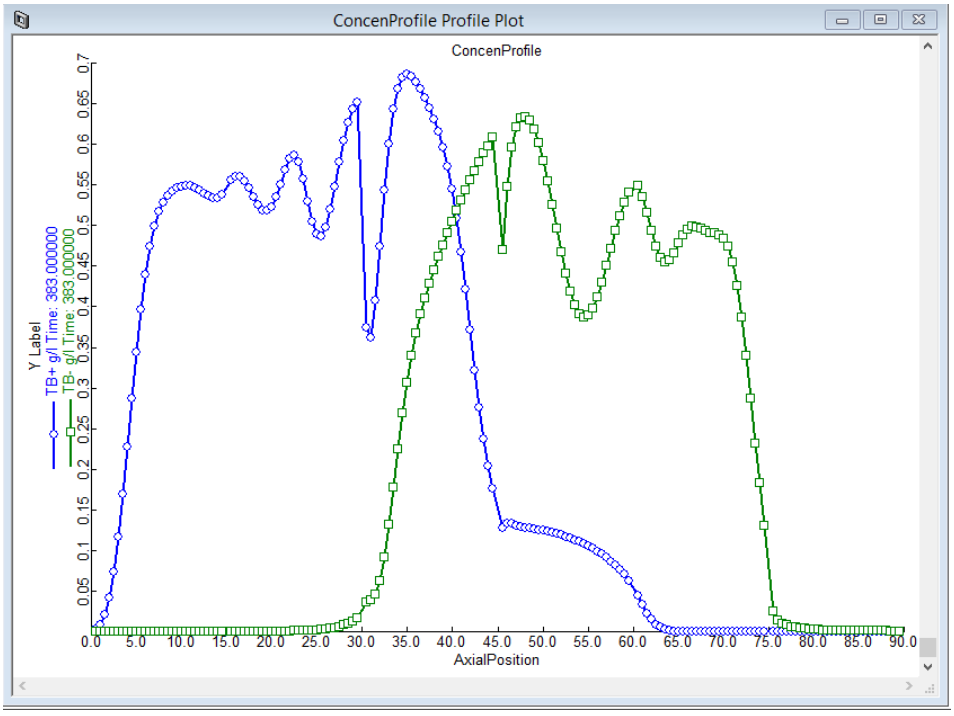

FIGURE 6.88.THE RESULTING CONCENTRATION PROFILE WITHIN THE PF&MC COLUMN.

Part II. Simulation and Demonstration of Gas-phase Adsorptive Separation

7. The Gas-Phase Adsorption Technologies

7.1. Introduction to Gas-Phase Adsorption Technologies

Gas adsorption represents the sticking of molecules of gases to the surface of a solid material. The adsorptive separation processes always involve two steps: (1) adsorption step, during which the adsorbent selectively uptakes the adsorbed species from the feed; and (2) regeneration or desorption step, during which the adsorbent releases these species, thus regenerating the adsorbent for use in the next cycle.

There are two main types of gas adsorption technologies according to different regeneration ways: by changing the pressure called pressure swing adsorption (PSA), and by varying the temperature called temperature swing adsorption (TSA).

Pressure swing adsorption (PSA) is a very versatile technology for separation and purification of gas mixtures. In a PSA process, we accomplish the regeneration step by reducing the pressure at essentially constant temperature and then by purging the bed at low pressure.

Figure 7.1 shows the basic schematic isotherms in a PSA operation for an adsorption process. The blue curve represents the gas isotherm for the strongly adsorbed gas component. The working capacity of the adsorbent loading is between the isotherm point at P_{low} and the isotherm point at P_{High} in the figure. The uptake and release directions show how the adsorption and regeneration steps operation on this isotherm curve.

Some of the key industrial applications include: (a) air separation and air drying[84], (b) hydrogen purification[85] (c) Nitrogen production from air[86] (d) separation of carbon dioxide and methane[87]. Our research focuses on the modeling and demonstration for air separation system by Pressure Swing Adsorption technology using Aspen Adsorption. Many literature talks about the dynamic models for air separation systems by pressure swing adsorption technology[93-100]. All these

dynamic models are mathematical models, and use the Skarstrom[93] cycles which is displayed in Figure 7.2.

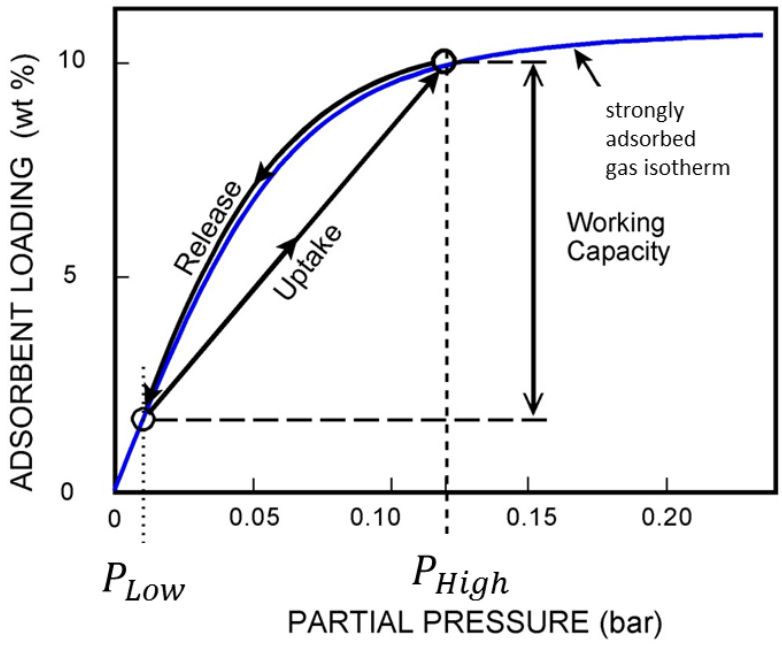

FIGURE 7.1. THE BASIC SCHEMATIC ISOTHERMS IN A PSA OPERATION FOR AN ADSORPTION PROCESS.

The basic Skarstrom[93-95] cycle utilizes two packed adsorbent beds, as shown schematically in Figure 7.2. The cycle consists of four steps: pressurization, adsorption, countercurrent blowdown and countercurrent purge. In step 1, feed flows into bed 2, and the more strongly adsorbed component is retained in the bed 2 and the gas outlet stream is enriched in the less strongly adsorbed component. At the same time, bed 1 is blown down to the atmospheric pressure in the opposite direction, as shown in the left graph of Figure 7.2. There is a fraction of the effluent stream from bed 2 withdrawn as product and the rest is used to purge bed 1 at the low operating pressure. The right graph of Figure 7.2 follow the same principle as the left graph, but with the beds interchanged.

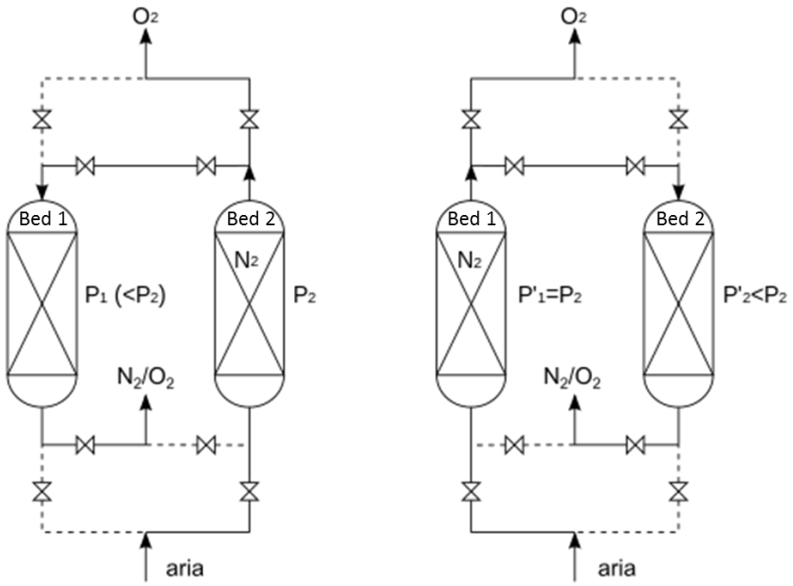

FIGURE 7.2. THE BASIC PRINCIPLE OF THE SKARSTROM CYCLE IN THE PSA PROCESS.

The temperature swing adsorption[88] (TSA) periodically varies the temperature of the adsorbent bed for regenerating the adsorbent. Heating by a stream of hot gas is the primary method. At the higher temperature for desorption step, solid adsorbent releases the adsorbed species from the bed into the fluid stream.

Figure 7.3 shows the basic schematic isotherms in a TSA operation for an adsorption process. The key difference between PSA isotherms and TSA isotherms is that TSA moves the operations between two isotherm curves at two different temperatures. The blue curve in Figure 7.2 represents the gas isotherm for the strongly adsorbed gas component at low temperature, and the red curve refers to the gas isotherm at high temperature. The working capacity of the adsorbent loading is between the highest loading at T_{low} and the lowest loading at T_{High} in the figure. The uptake and release arrows show the heating and cooling cycle, or the adsorption and regeneration cycle during the TSA operations.

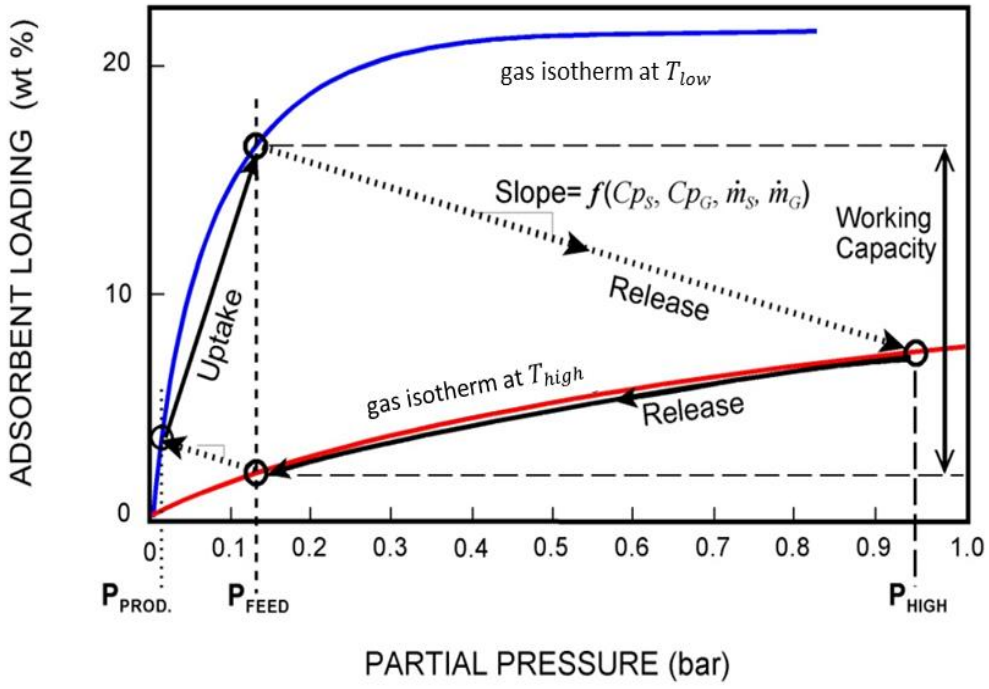

FIGURE 7.3. THE BASIC SCHEMATIC ISOTHERMS IN A TSA OPERATION FOR AN ADSORPTION PROCESS.

Based on the literature[89], we find the general features and disadvantages for PSA and TSA.

PSA commonly uses zeolites in two adsorption columns to separate molecules. It allows two or more columns to operate continuously for the adsorptive processes. We find that there are more academic research and industrial applications of PSA than the TSA. A major advantage of PSA, relative to TSA, is that we could change the pressure more rapidly than the temperature. Thus, it is possible to operate a PSA process on a much faster cycle, thereby increasing the throughout per unit of adsorbent bed volume. However, PSA does not work well for those components that are not too strongly adsorbed. But TSA is a good and preferred option for those very strongly adsorbed components. Each heating-cooling cycle usually requires a few hours to over a day. Thus, considering the time requirement, we use TSA exclusively for purification purposes, in which the amounts of adsorptive gases are small. Considering the large number of adsorption columns and the longer cycle time in TSA, it will definitely cost much more in operating the system.

In our study, we demonstrate two workshops of modeling a PSA process in chapter 8 and a TSA process in chapter 9. The PSA workshop focuses on how to make a PSA model in Aspen Adsorption for a specific air separation system for oxygen recovery[84, 90]. The TSA workshop refers to the TSA modeling using Aspen Adsorption for a CO_2 capture process[91, 92].

7.2. Introduction to Aspen Adsorption

Aspen Adsorption is a comprehensive flowsheet simulator for the optimal design, simulation, optimization, and analysis of industrial gas and liquid adsorption processes. This software simulates gas processes with adsorption only, or adsorptive reaction gas processes where both reaction and adsorption occur simultaneously.

For gas processes, the bed model makes the following assumptions:

- Isothermal or non-isothermal conditions apply.
- Plug flow or plug flow with axial dispersion occurs.
- The system is fully mixed in the radial direction.
- The gas phase is ideal or non-ideal.
- Gas phase pressure is either constant, or the pressure varies according to a laminar or turbulent flow momentum balance.
- Mass transfer is described using a lumped overall resistance, or by a model that accounts separately for micro- and macrospore effects. The driving force is based on a liquid or solid film, and is either linear, quadratic, or user-specified. Mass transfer coefficients are either constant, or vary with local conditions.
- Adsorption isotherms are either applicable for single or multi-component adsorption.

8. PSA Workshop: Aspen Adsorption Modeling for Air Separation

After briefly introducing the concept of PSA for gas-phase separation in chapter 7, we detail the basic principle of the cycle PSA operation and give an example of the modeling for air separation by PSA technology using Aspen Adsorption in this worshop[101-104]. In a PSA process, at a relatively high pressure (P_{High}), solid adsorbent selectively uptakes certain components of a gas mixture by contacting the gas with the solid in a packed column. In this way, the system produces a gas stream enriched in the less strongly adsorbed components of the feed gas. In the next step, by lowering their gas-phase partial pressure inside the column, it releases the adsorbed components from the solid, and we can reuse the solid adsorbent. The desorbed gases are enriched in the more strongly adsorbed components of the feed gas.

The early PSA patent of Skarstrom[93-96] described air separation to produce oxygen as one of the important PSA applications. It has been commercialized at scales ranging from a few liters per minutes for small-scale units to tens of tons per day for industrial systems. The processes normal use a zeolite adsorbent[105], generally 5A or 13X. Most small-scale units use a 2-bed system, operated on a Skarstrom cycle[93], sometimes with the addition of pressure equalization steps. The case study we choose is a binary air separation system of 79% N_2 and 21% O_2 using a 5A zeolite as the adsorbent[85]. In this PSA system, it adsorbs O_2 at higher pressure in the adsorption step, and releases O_2 when lowering the pressure during the regeneration step. We collect all the column and operating data from literatures[85], and will show the development of the PSA model step by step.

Figure 8.1 shows a cyclic PSA unit with two beds for a binary separation[89]. Both beds could switch their functions between adsorption and desorption. While Bed 1 is in the adsorption stage, Bed 2 is in the desorption stage. During the adsorption stage, at a relatively high pressure, solid adsorbent in the bed selectively adsorbs components of a binary gas mixture by contacting the gas with the solid. In this way, the system produces a gas stream named light product (LP) enriched in the less strongly adsorbed component. In the following desorption step, by lowering the gas-phase partial pressure inside the bed, it releases the adsorbed components from the solid, producing a gas stream called heavy product (HP) enriched in the more strongly adsorbed

components. We can reuse the solid adsorbent after regenerating it by changing the pressure through the beds.

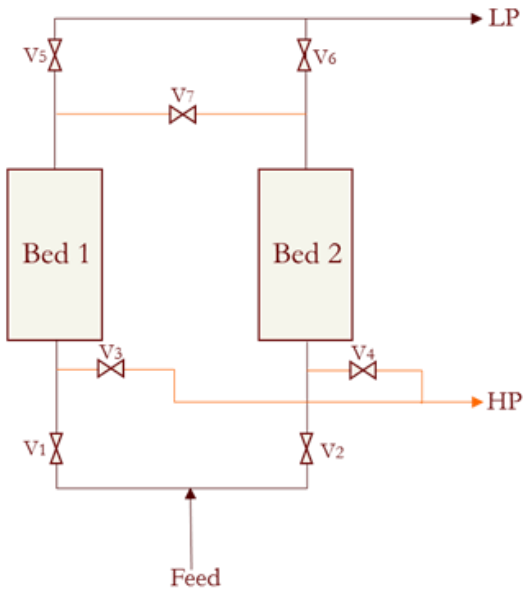

FIGURE 8.1. DIAGRAMATIC THEORY OF PRESSURE SWING ADSORPTION CYCLE.

Figure 8.2 displays the detailed four steps for both beds[106]. Each PSA cycle includes four steps: feeding, countercurrent depressurization, light reflux and light product pressurization. Step 1 represents high-pressure adsorption, where feed continuously enters the bed and solid adsorbent adsorbs the strongly adsorbed components at a relatively high pressure. Step 2 is countercurrent depressurization or blow down to a low pressure, which makes the regeneration occur and produce a heavy product stream containing most of the strongly adsorbed components. Step 3 is the desorption step at low pressure with light product purge. This step can improve the heavy product purity and recovery, but increases the energy cost. Step 4 is the pressurization with light product prior to feeding, which increases the gas partial pressure in the bed and prepares for the next adsorption step.

We design seven valves in total in this process shown in Figure 8.1. Each step works by controlling all of these valves. Table 8.1 shows how we operate each valve for each step.

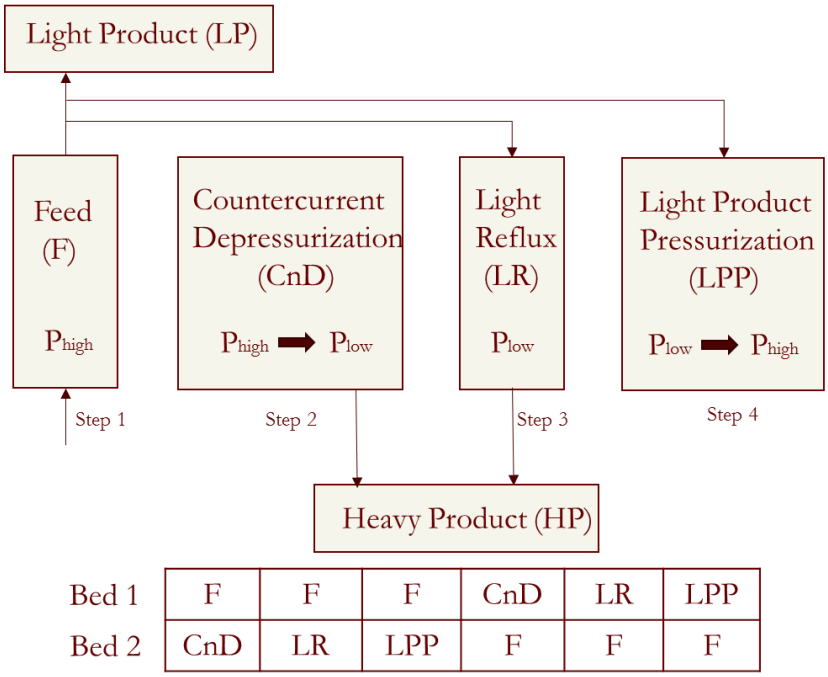

FIGURE 8.2. PRESSURE SWING ADSORPTION WITH 2 BEDS AND 4 STEPS.

TABLE 8.1. THE VALVE PLACEMENT IN EACH STEP.

Step Name	Function	V1	V2	V3	V4	V5	V6	V7
F (Step1)	Feeding and adsorption at P_{high} in Bed 1	√				√		
CnD (Step2)	Countercurrent blow down to P_{low} and desorption occurs in Bed 2	√			√	√		
LR (Step3)	Countercurrent desorption with LP purge in Bed 2	√			√	√		√
LPP (Step4)	Pressurization with LP prior to feeding to Bed 2	√				√		√
F (Step1)	Feeding and adsorption at P_{high} in Bed 2		√				√	
CnD (Step2)	Countercurrent blow down to P_{low} and desorption occurs in Bed 1		√	√			√	
LR (Step3)	Countercurrent desorption with LP purge in Bed 1		√	√			√	√
LPP (Step4)	Pressurization with LP prior to feeding to Bed 1		√				√	√

Step 1: Start a new blank file in Aspen Adsorption.

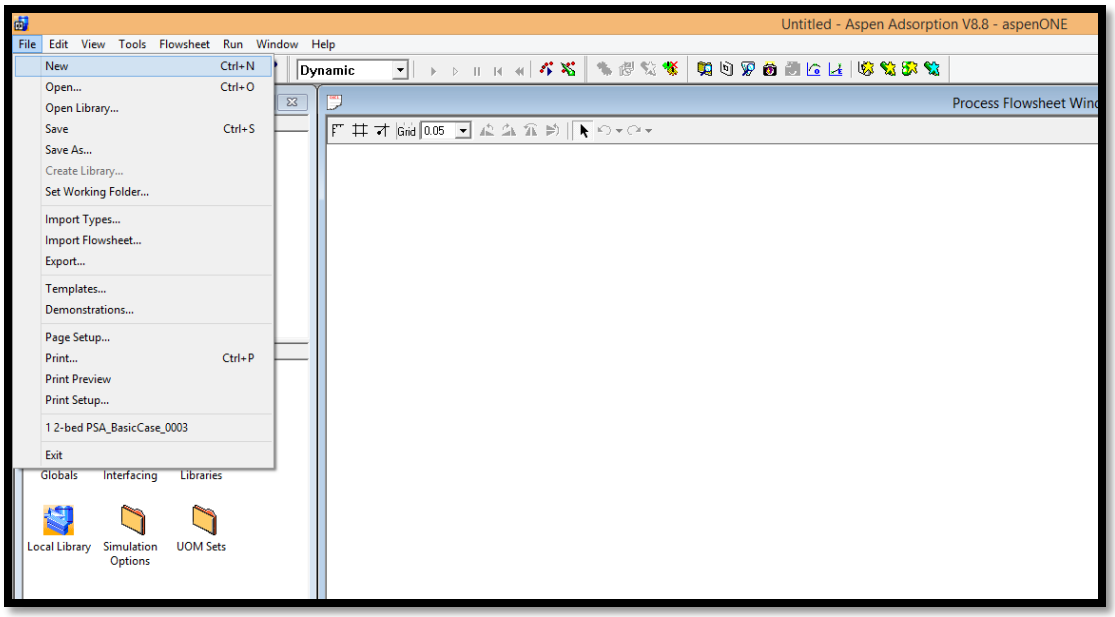

FIGURE 8.3. A NEW FILE IN ASPEN ADSORPTION.

Step 2: Save the new file as "PSA process with 4 steps for air separation".

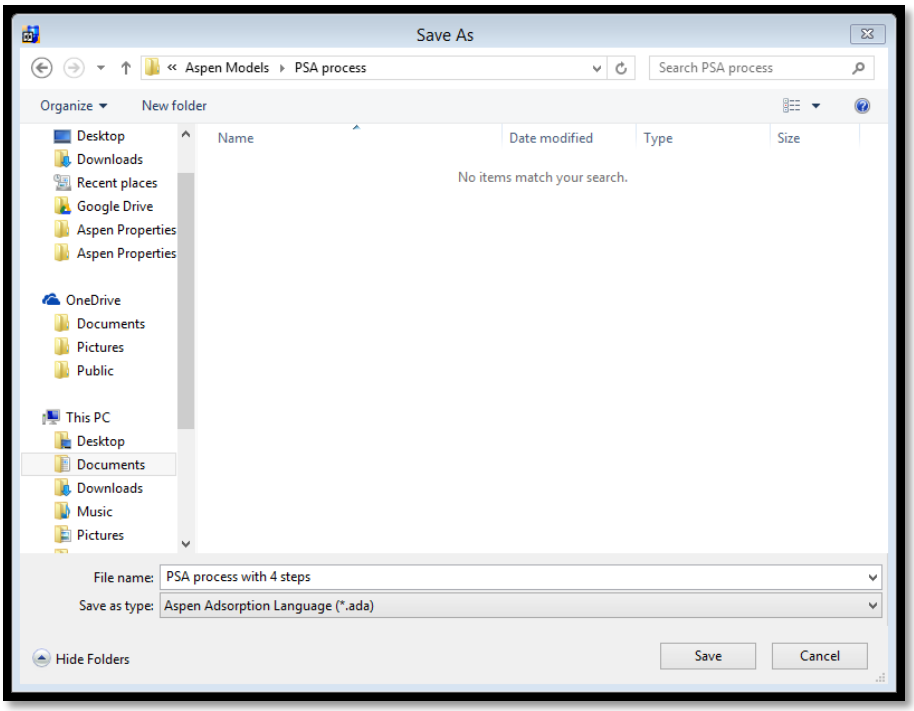

FIGURE 8.4. THE PSA PROCESS WITH 4 STEPS FOR AIR SEPARATION.

Step 3: Create a flowsheet using a single bed approach.

In this 2-bed PSA model, we apply a single bed approach, which is one way of modeling adsorption systems that comprise multiple adsorbent bed. It would simplify the multi-bed modeling with fewer equations and less data to be calculated. We could use this method because in our case study, each adsorbent bed is identical and both of them operate the same steps in a given cycle. And also this approach retains the accuracy of the final results with the same average purity and recovery results, as well as the same number of cycles to achieve a cyclic steady state.

Go to "Model Library", then choose the blocks in Figure 8.5, and create the flowsheet for the PSA model. Select "Gas:Dynamic" ->"gas_bed" for the adsorber column Bed 1; select "Gas:Dynamic" ->"gas_tank_void" for the tank blocks TBa and TBb; select "Gas:Dynamic" ->" gas_interaction" for the D1 block; select "Gas:Dynamic" ->" gas_valve" for the VF1, VW1, VP1 VD1 and VB1 valves; select "Gas:Dynamic" ->" gas_feed" for the Feed block; select "Gas:Dynamic" ->" gas_product" for the LProduct and HProduct blocks.

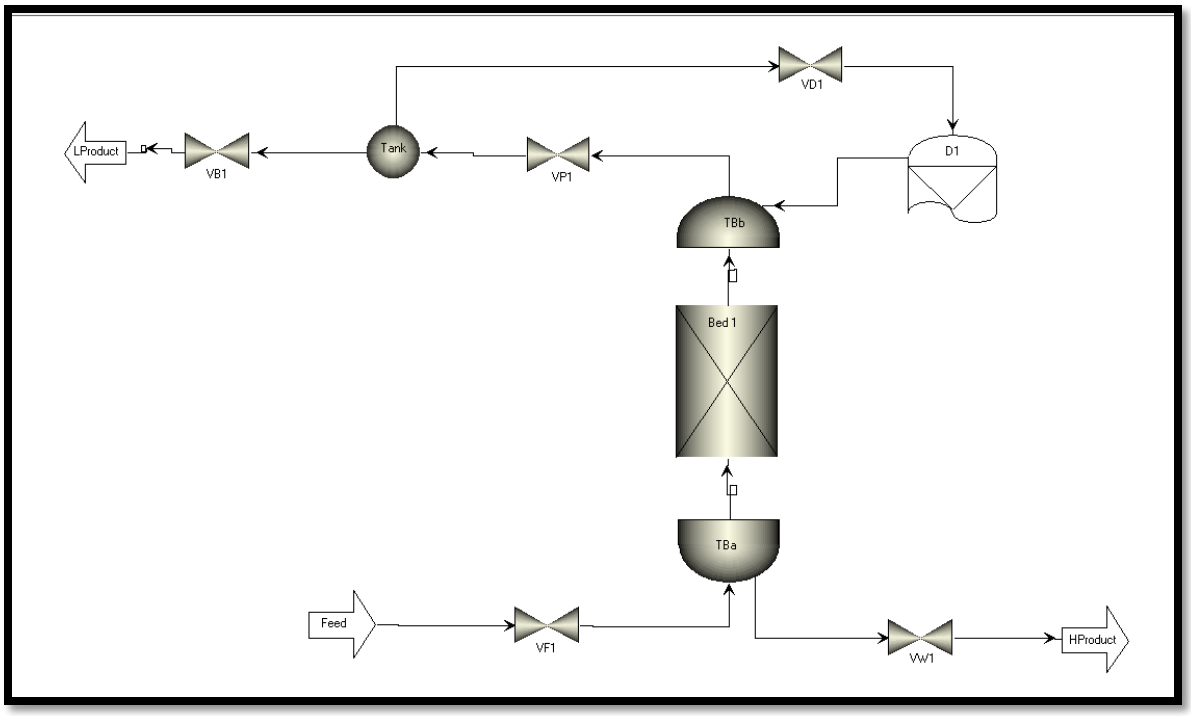

FIGURE 8.5. A PSA FLOWSHEET USING A SINGLE BED.

Step 4: Add components: Component Lists -> Configure Properties->Edit using Aspen Properties.

There are two methods of adding components into the model: component list and component set.

A component list contains:

- A list of component names.
- A list of options associated with these components. Typically we use it to store options for calculating physical properties for mixtures of these components.

A component set is a simplified version of a component list that does not include a list of physical property options.

In general, we use a full component list when using a physical property package such as Aspen Properties, and a component set when you are not using a physical property package. In the SMB workshops, we use the component set as the example, and we apply the component list using Aspen Properties in this workshop.

When we use Aspen Properties for Physical Properties, we can invoke the Aspen Properties user interface directly if we have it installed. In order to edit physical property options, we need to follow the steps in Figure 8.6:

1. In the Simulation Explorer, click "Component Lists".
2. In the Explorer of the Component Lists folder, double-click the "Configure Properties" node.
3. In the Physical Properties Configuration dialog box, choose "Use Aspen propertiey system" option, and then click "Edit using Aspen Properties" button to launch the user interface.

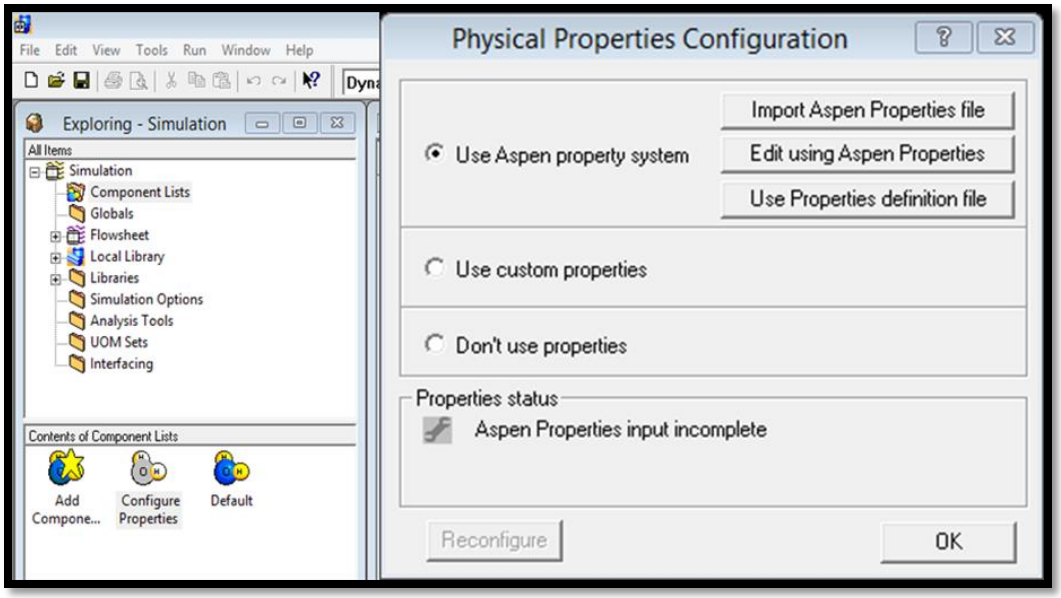

FIGURE 8.6. THE PHYSICAL PROPERTIES CONFIGURATION PANE.

Step 5: Add component names in Aspen Properties.

After we click "Edit using Aspen Properties" in the Physical Properties Configuration pane, it automatically opens the Aspen Properties for us to add component names and edit their physical and chemical properties. Figure 8.7 displays that we are trying to separate nitrogen from the nitrogen and oxygen mixture.

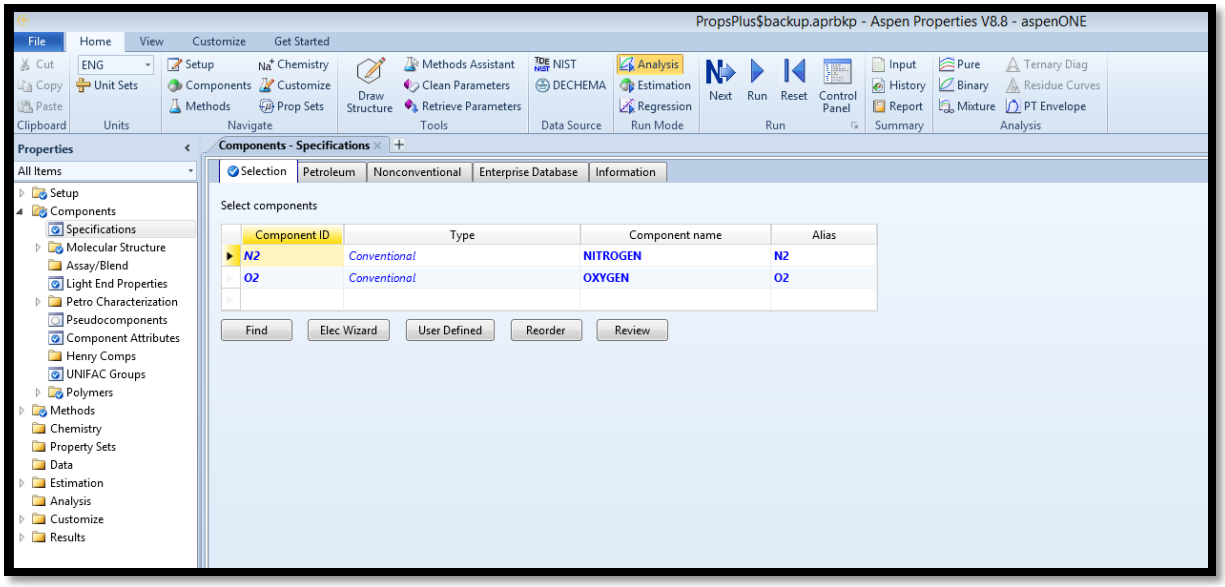

FIGURE 8.7. THE ASPEN PROPERTIES INTERFACE.

Step 6: Choose the property method, Run it and then save the results.

To edit components' physical properties in Aspen Properties, we follow the steps in Figure 8.8:

1. In the "All Items" pane of the "Properties", click "Specification" in the "Methods" folder.
2. Select "PENG-ROB" as the base method.
3. In the pane of "Home", click "Run" button.
4. Save the file until the run is completed in the Control Panel, as shown in Figure 8.9

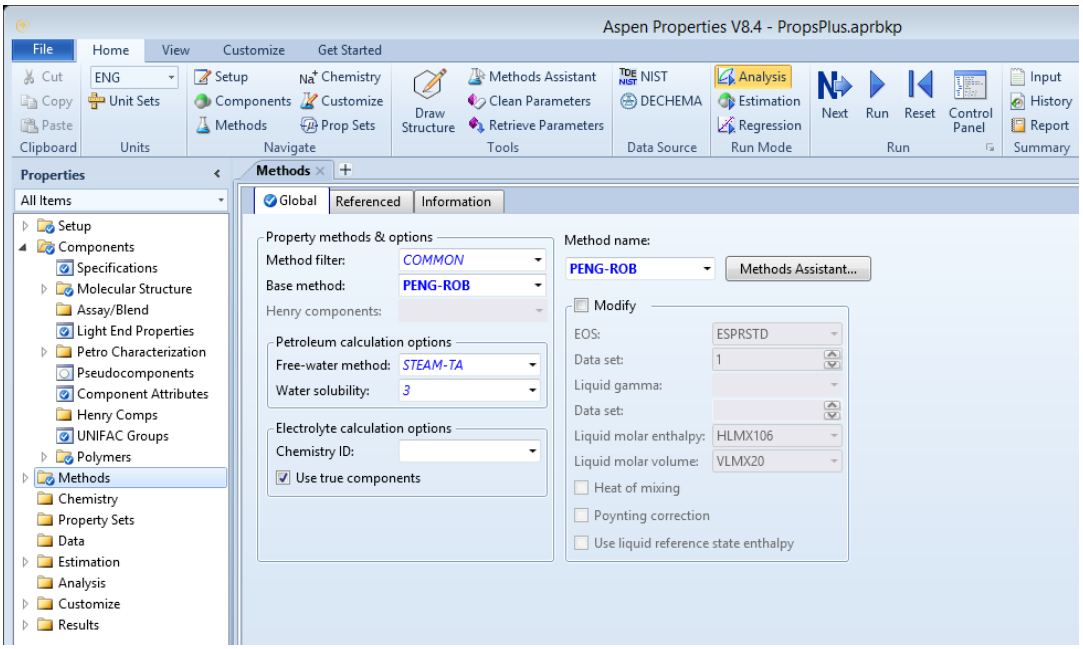

FIGURE 8.8. THE SPECIFICATION OF THE COMPONENTS IN ASPEN PROPERTIES.

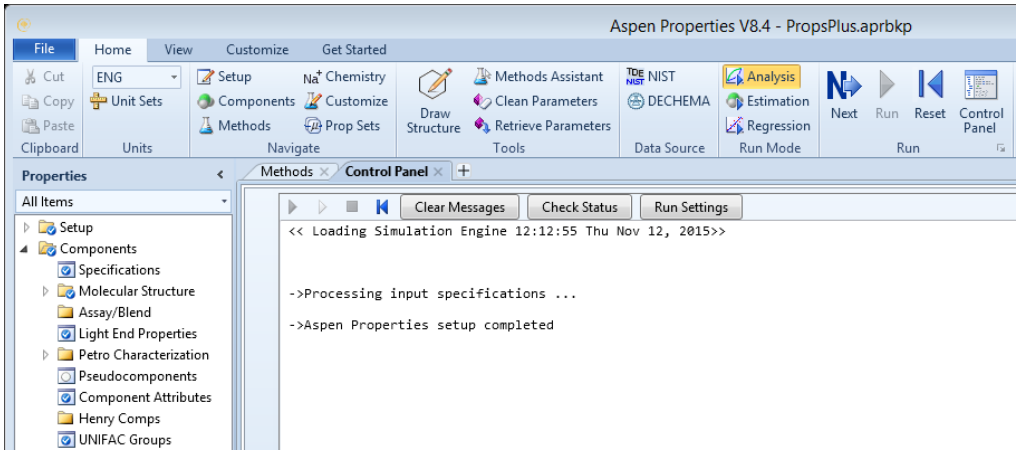

FIGURE 8.9. THE COMPLETION IN CONTROL PANEL IN ASPEN PROPERTIES.

Step 7: Configured using embedded Aspen Properties

Once we have done the import in Aspen Properties, the Aspen Properties input will be included in the file when we save the simulation file. Then go back to the Physical Properties Configuration panel, and the Properties status should become green, and shows "Configured using Embedded Aspen Properties".

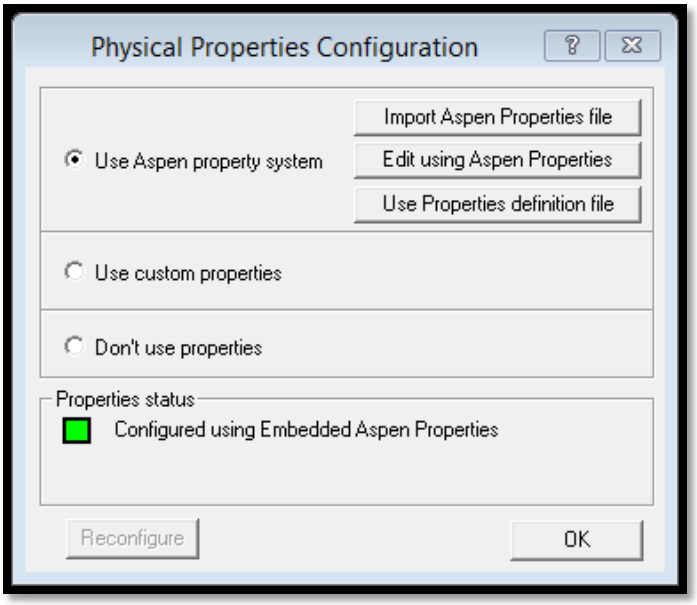

FIGURE 8.10. THE COMPLETION OF THE PHYSICAL PROPERTIES CONFIGURATION.

Step 8: Choose some or all the available components in the separation system.

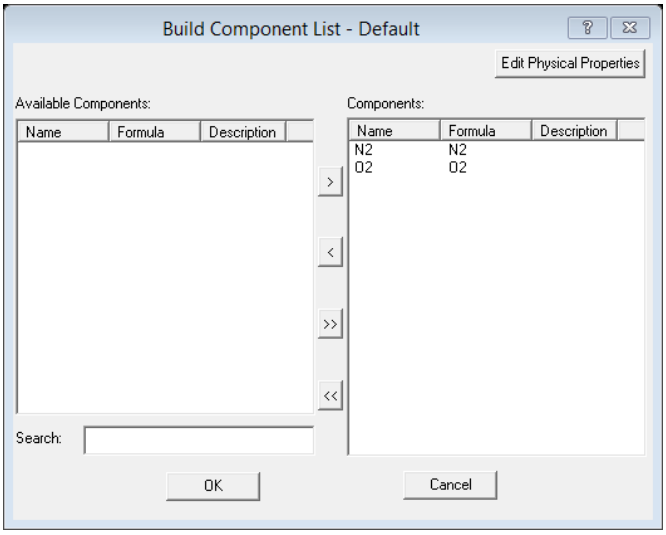

FIGURE 8.11. BUILD THE COMPONENT LIST IN THE PSA MODEL.

Step 9: Double-click Bed 1 to edit the column configuration.

Figure 8.12 shows the specification of the column in the PSA model. It has only one vertical independent adsorbent layer within the bed with the same packed adsorbent molecular sieve 5A. We choose 1-D as the spatial dimensions. There is no heat exchanger within the adsorbent layer.

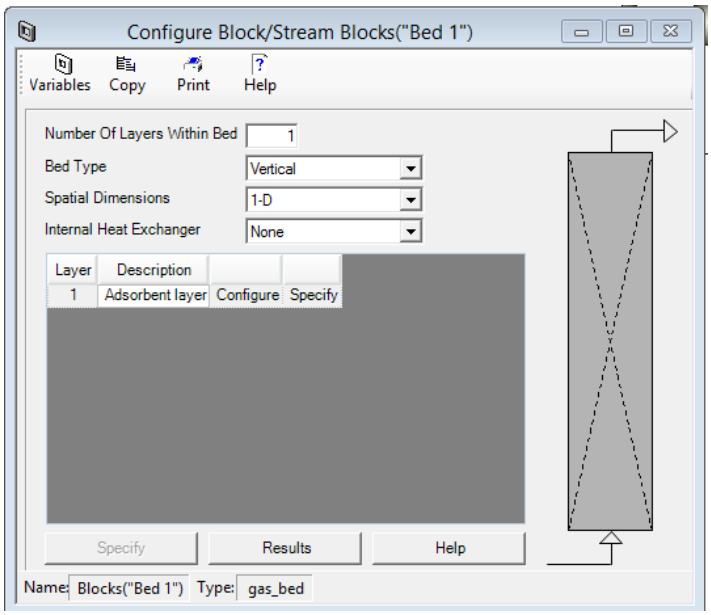

FIGURE 8.12. THE COLUMN CONFIGURATION SPECIFICATION.

Step 10: General->Discretization method to be used.

We use the General tab in Figure 8.13 to specify the numerical options for solving the partial differential equations, and to select the gas model assumption.

Basically, Aspen Adsorption uses a set of partial differential equations (PDEs), ordinary differential equations (ODEs) and algebraic equations, together with the appropriate initial and boundary conditions, to fully describe the adsorption column.

The upwind Differencing Scheme 1 (UDS1) is the preferred option in most cases. We prefer to use UDS1 for this dynamic PSA model because it saves the simulation time and the results are reasonably accurate. Therefore, we use the USD1 with 60 nodes.

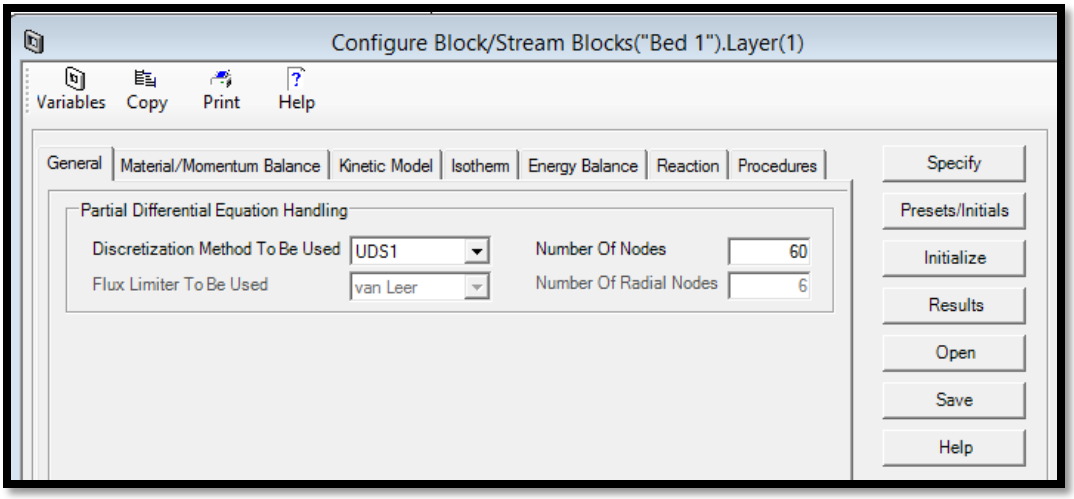

FIGURE 8.13. THE DISCRETIZATION METHOD IN THE PSA MODEL.

Step 11: Material/Momentum Balance->Assumptions.

We use the Material/Momentum Balance tab in Figure 8.14 to specify the material and momentum balances, and the dispersive properties. For simplicify, we choose convection only as the mass balance assumption. The Convection Only option drops the dispersion term from the material balance in eq. 8.1, so the model represents the plug flow with a zero dispersion coefficient. Local equilibrium is achieved instantaneously between the adsorbent and adsorbates at each axial location.

We use the Momentum Balance Assumption box to specify how the adsorption bed layer model treats gas velocity and pressure. For the calculation of the pressure drops in the PSA system, we use Ergun equation, which is valid for both laminar and turbulent flows and is the most popular option. It combines the description of pressure drop by the Carman-Kozeny equation for laminar flow and the Burke-Plummer equation for turbulent flow, as shown in eq. 8.2.

$$\frac{\partial C_i}{\partial t} + \frac{(1-\varepsilon)}{\varepsilon}\frac{\partial q_i}{\partial t} + u\frac{\partial C_i}{\partial z} = D_L\frac{\partial^2 C_i}{\partial z^2} = 0 \quad \textbf{(8.1)}$$

$$\frac{\partial \mathrm{P}}{\partial \mathrm{z}} = -\left(\frac{1.5 * 10^{-3}\mu(1-\varepsilon)^2}{\left(2r_p\psi\right)^2\varepsilon^3}u + 1.75 * 10^{-5}\rho\frac{(1-\varepsilon)}{2r_p\psi\varepsilon^3}u^2\right) \quad \textbf{(8.2)}$$

In the equations, C_i is the concentration for component i in the gas phase, q_i is the concentration for component i in the solid phase, and ε represents the overall bed voidage, z is the axial

distance through the column and D_L is the axial dispersion coefficient. P is the pressure drop within the column; u is the superficial velocity of the gas flow; μ = fluid viscosity; r_p = particle radius; ψ = particle shape factor.

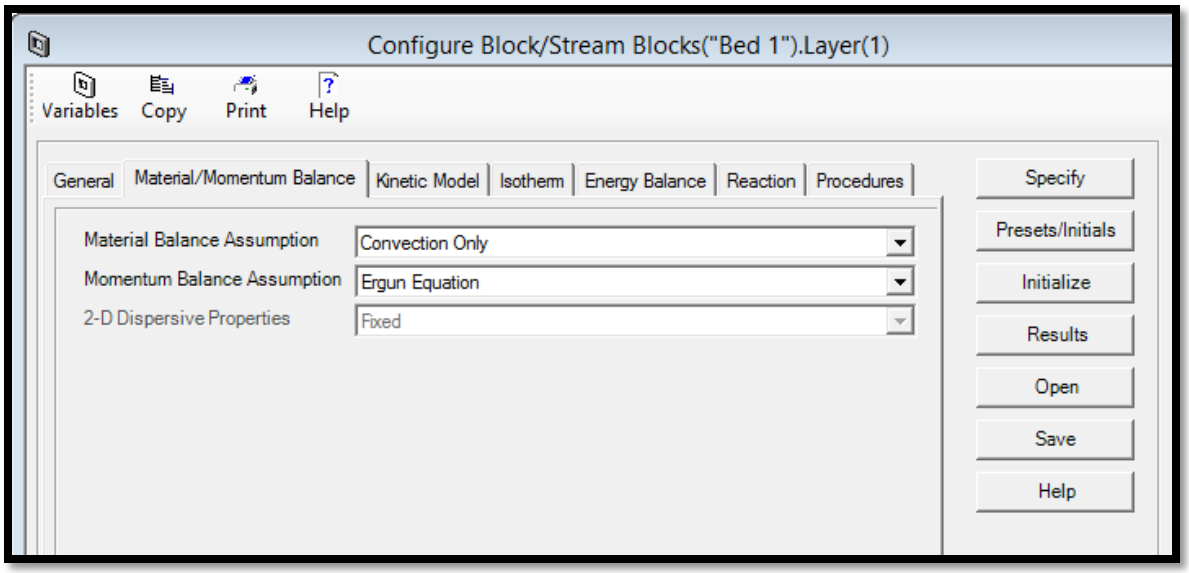

FIGURE 8.14. THE MATERIAL BALANCE ASSUMPTION IN THE PSA MODEL.

Step 12: Kinetic Model->Film Model Assumption & Mass Transfer Coefficients.

We use the Kinetic Model tab in Figure 8.15 to specify the model kinetics, such as resistances, diffusivities and mass transfer coefficients.

In the Film Model Assumption box, we choose the solid form, where the mass transfer driving force is expressed as a function of the solid-phase loading.

Typically, several mass transfer resistances occur in the gas-phase adsorption processes:

- Mass transfer resistance between the bulk gas phase and the gas-solid interface.
- Mass transfer resistance due to the porous structure of the adsorbent.

In our case, we consider the mass transfer resistance as a lumped and linear resistance in the Kinetic Model Assumption box. It means that we lump these mass transfer resistances as a single overall factor, or one resistance dominates all others. The mass transfer coefficient for

each component is constant throughout the bed. The mass transfer driving force for component i is a linear function of the solid phase loading (solid film) as shown in eq. 8.3.

$$\frac{\partial q_i}{\partial t} = k_i(q_i^* - q_i) \tag{8.3}$$

where k_i is the linear lumped mass transfer coefficient, q_i is solute concentrations of the solid phase, and q_i^* represents the adsorbed phase concentration at equilibrium with the gas phase.

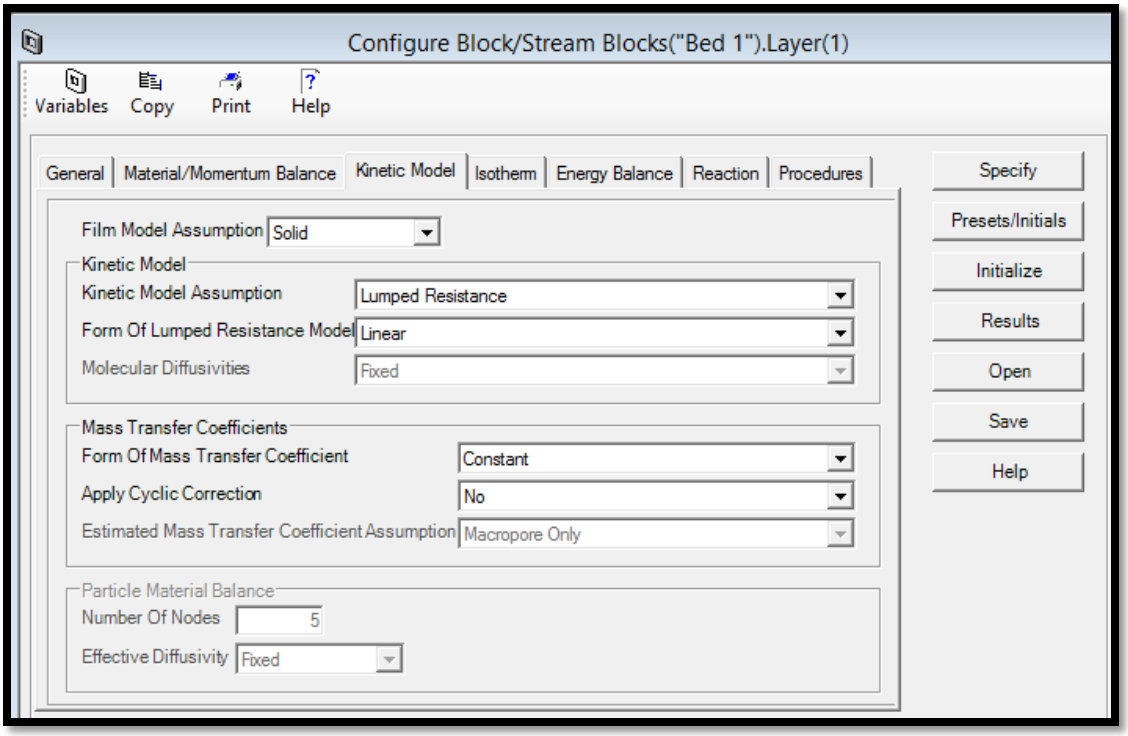

FIGURE 8.15. THE KINETIC METHOD IN THE PSA MODEL.

Step 13: Isotherm->Extended Langmuir Assumption.

We use the Isotherm tab in Figure 8.16 to define the adsorption isotherms to be used in your gas adsorption process.

In an adsorber design, we are usually interested in the adsorption equilibria of mixtures, rather than those of pure components. This is because adsorbed gas components interact on the solid surface, so individual gas components adsorb differently when mixed with other components.

Mixture adsorption equilibrium data are not readily available. Although measurements can be made, they are tedious and time-consuming to perform, so it is a common practice to predict mixture isotherms from pure component isotherms. We use the extended Langmuir isotherm as the isotherm model, which is a function of partial pressure in the system. In this approach, we can predict mixture isotherms from pure component data[107]. The extended Langmuir adsorption isotherm is:

$$q_i^* = \frac{q_{i,1} K_i P_i}{1 + \sum K_i P_i} \quad (i = N_2, O_2) \tag{8.4}$$

In the equation, q_i^* is the adsorbed phase concentration of component i in equilibrium with the mobile phase. $q_{i,1}$is the bi-Langmuir isotherm parameters for component i. $K_i$is the equilibrium constant for component I; $P_i$is the partial pressure for component i.

In Aspen Adsorption, the expression of the extended Langmuir isotherm is:

$$q_i^* = \frac{IP_{1i} P_i}{1 + \sum IP_{2i} P_i} \quad (i = N_2, O_2) \tag{8.5}$$

Comparing eqs. 8.4 and 8.5, in conjunction with Table 8.2, we get:

$IP_{1,N2} = q_{N2,1} K_{N2} = 0.023496;$

$IP_{1,O2} = q_{O2,1} K_{O2} = 0.02442;$

$IP_{2,N2} = K_{N2} = 8.9;$

$IP_{2,O2} = K_{O2} = 9.25;$

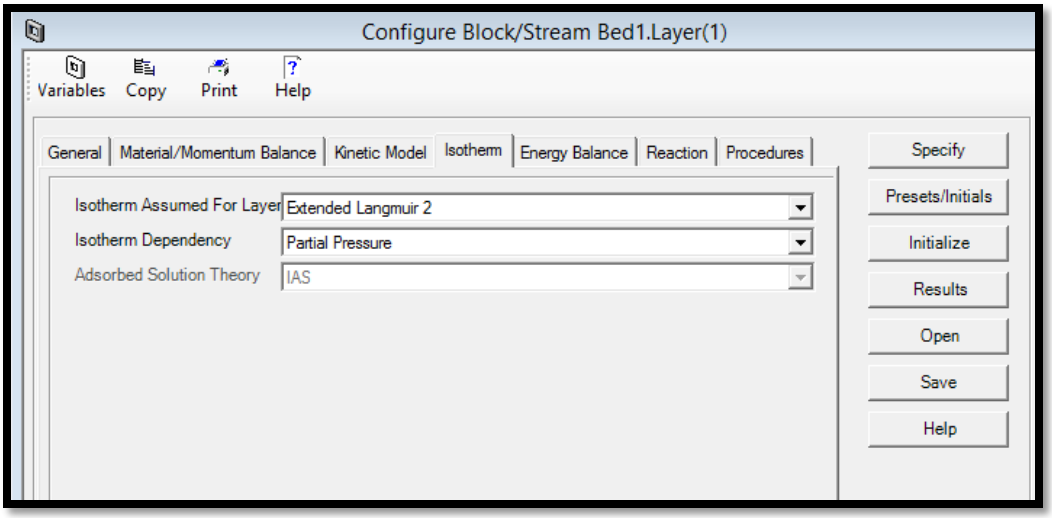

FIGURE 8.16. THE ENERGY METHOD IN THE PSA MODEL.

Step 14: Energy Balance->Non-Isothermal with No Conduction Assumption.

We use the Energy Balance tab in Figure 8.17 to specify how the energy balance is incorporated into the model for this gas adsorption process. We use the non-isothermal with no conduction as the energy assumption. The heat transfer to environment is adiabatic.

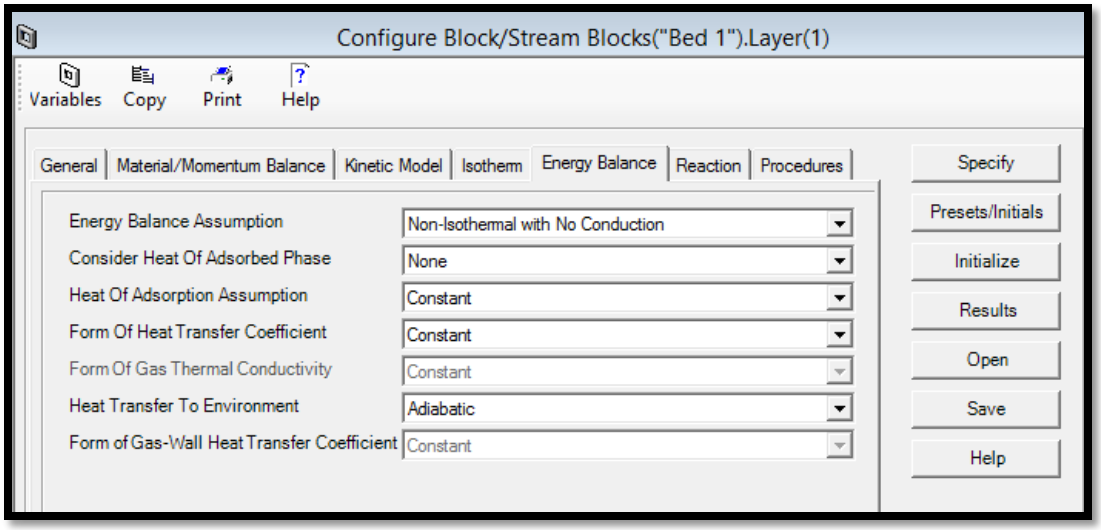

FIGURE 8.17. THE ISOTHERM METHOD IN THE PSA MODEL.

Step 15: Reaction->No reaction.

There is no reaction in this PSA system.

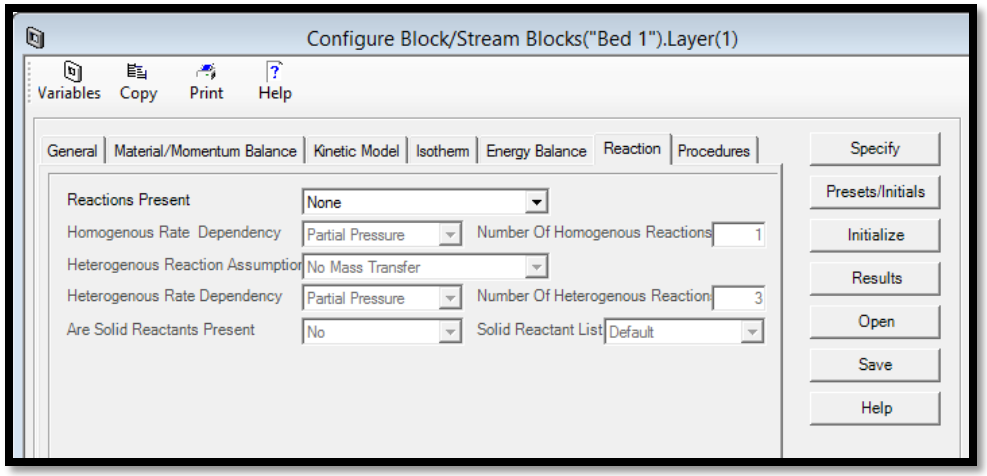

FIGURE 8.18. THE REACTION METHOD IN THE PSA MODEL.

Step 16: Procedures-> Available procedures in FORTRAN program.

We can use the Procedures tab in Figure 8.18 to view a list of user procedures within the current adsorption layer model.

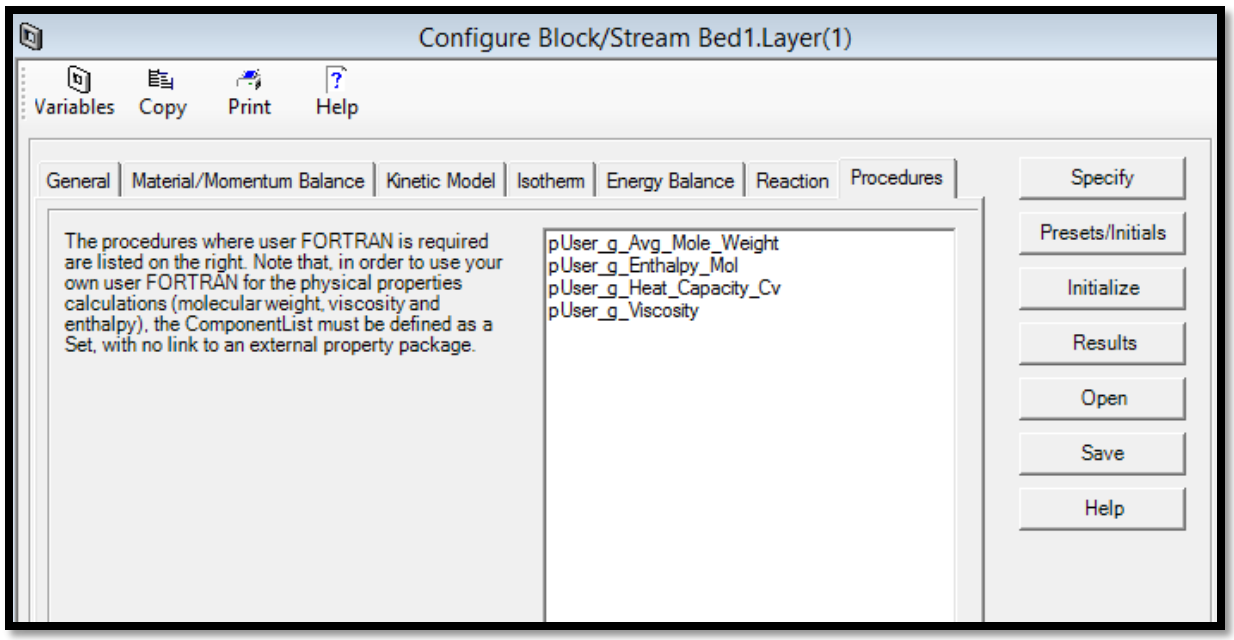

FIGURE 8.19. THE AVAILABLE PROCEDURES IN THE PSA MODEL.

Step 17: Specify->Input all the variable values for all the assumptions we made.

After defining all assumptions for the layer, we click the Specify button in the Configuration form to open the data table. We follow Table 8.2 to enter the required data for the layer Specify Form in Figure 8.20.

TABLE 8.2. THE SPECIFICATION OF THE ADSORBENT LAYER.

Column (Adsorbent layer) Height (m)		3
Internal diameter of the column (m)		0.5
Inter-particle voidage (m3 void/m3 bed)		0.4
Intra-particle voidage (m3 void/m3 bead)		1.E-7
Solid density of the adsorbent (kg/m3)		1200
Adsorbent particle radius (mm)		1.7
	Nitrogen (N_2)	Oxygen (O_2)
Mass transfer coefficient (1/s)	0.00009	0.024
Equilibrium constant K_i	8.9	9.25
Saturation constant $q_{i,1}$ (mol/cm^3)	2.64×10^{-3}	2.64×10^{-3}
Heat of adsorption constant KJ/mol	-20.34	-14

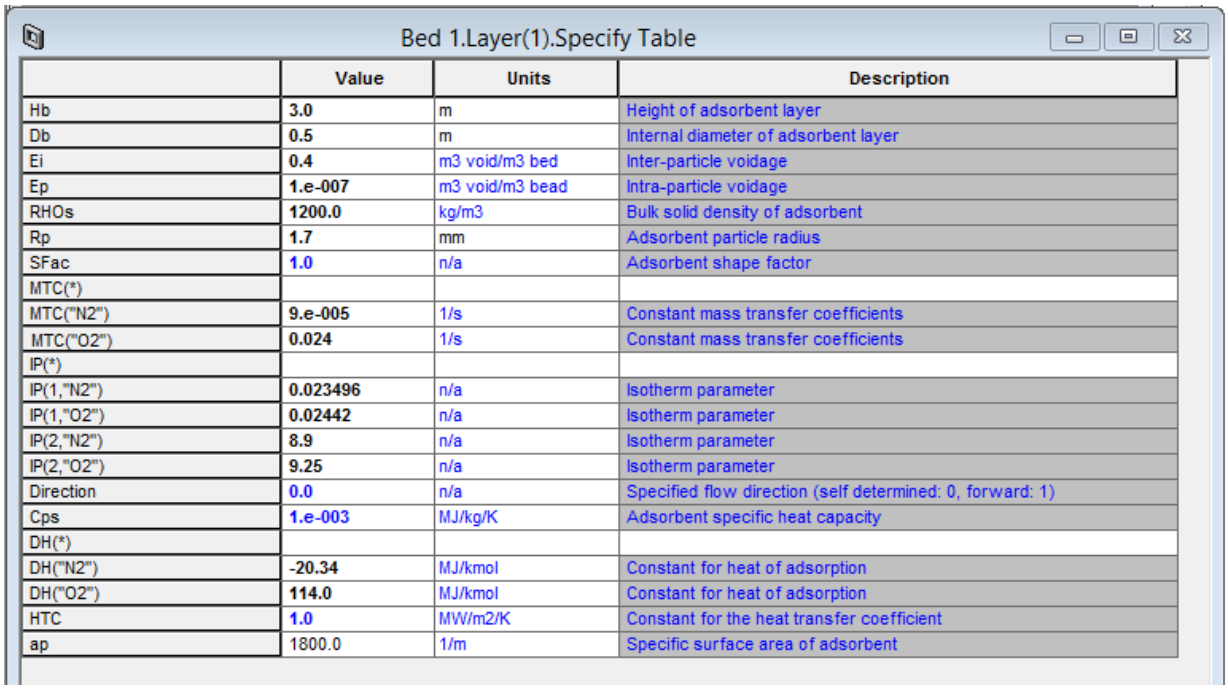

Bed 1.Layer(1).Specify Table

	Value	Units	Description
Hb	3.0	m	Height of adsorbent layer
Db	0.5	m	Internal diameter of adsorbent layer
Ei	0.4	m3 void/m3 bed	Inter-particle voidage
Ep	1.e-007	m3 void/m3 bead	Intra-particle voidage
RHOs	1200.0	kg/m3	Bulk solid density of adsorbent
Rp	1.7	mm	Adsorbent particle radius
SFac	1.0	n/a	Adsorbent shape factor
MTC(*)			
MTC("N2")	9.e-005	1/s	Constant mass transfer coefficients
MTC("O2")	0.024	1/s	Constant mass transfer coefficients
IP(*)			
IP(1,"N2")	0.023496	n/a	Isotherm parameter
IP(1,"O2")	0.02442	n/a	Isotherm parameter
IP(2,"N2")	8.9	n/a	Isotherm parameter
IP(2,"O2")	9.25	n/a	Isotherm parameter
Direction	0.0	n/a	Specified flow direction (self determined: 0, forward: 1)
Cps	1.e-003	MJ/kg/K	Adsorbent specific heat capacity
DH(*)			
DH("N2")	-20.34	MJ/kmol	Constant for heat of adsorption
DH("O2")	114.0	MJ/kmol	Constant for heat of adsorption
HTC	1.0	MW/m2/K	Constant for the heat transfer coefficient
ap	1800.0	1/m	Specific surface area of adsorbent

FIGURE 8.20. THE SPECIFY FORM OF THE ADSORBENT LAYER IN THE PSA MODEL.

Step 18: Presets/Initials-> initialization form of the adsorbent layer.

Input all the initial values in Figure 8.21 for the model, and then press the "Initial" button. The mole fraction within first element for nitrogen is 0.79, for oxygen is 0.21. The temperature for both gas and solid phases is 25 °C.

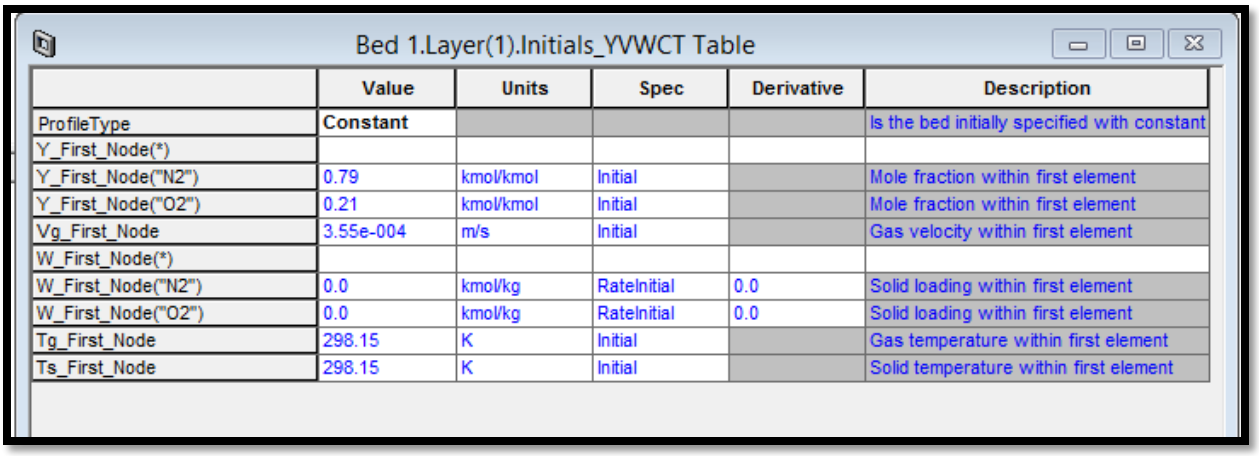

Bed 1.Layer(1).Initials_YVWCT Table

	Value	Units	Spec	Derivative	Description
ProfileType	Constant				Is the bed initially specified with constant
Y_First_Node(*)					
Y_First_Node("N2")	0.79	kmol/kmol	Initial		Mole fraction within first element
Y_First_Node("O2")	0.21	kmol/kmol	Initial		Mole fraction within first element
Vg_First_Node	3.55e-004	m/s	Initial		Gas velocity within first element
W_First_Node(*)					
W_First_Node("N2")	0.0	kmol/kg	RateInitial	0.0	Solid loading within first element
W_First_Node("O2")	0.0	kmol/kg	RateInitial	0.0	Solid loading within first element
Tg_First_Node	298.15	K	Initial		Gas temperature within first element
Ts_First_Node	298.15	K	Initial		Solid temperature within first element

FIGURE 8.21. THE INITIALIZATION FORM OF THE ADSORBENT LAYER IN THE PSA MODEL.

Step 19: Feed block->Feed Specification.

In this PSA model, we set the feed-in flow rate in the "Feed" block as free, because we control the feed flow in the Cycle Organizer through the VF1 valve. The feed composition is fixed with 0.79 mole fraction nitrogen and 0.21 mole fraction oxygen. The temperature and pressure in the feed are both fixed, with 25 °C and 8.5 bar, respectively.

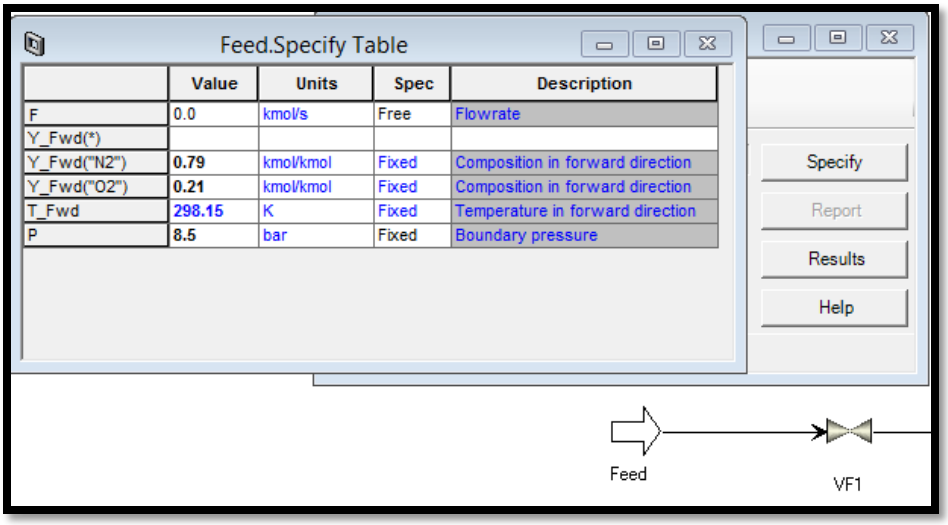

FIGURE 8.22. THE FEED SPECIFICATION IN THE PSA MODEL.

Step 20: HProduct block->Heavy Product Specification.

In the "HProduct" block, we set the flow rate as free, and control it in the Cycle Organizer through the VW1 valve. The reversed direction of the composition is fixed with 0.79 mole fraction nitrogen and 0.21 mole fraction oxygen. The reversed direction of the temperature is still fixed with 25 °C, and the pressure in the HProduct block is fixed with 1 bar.

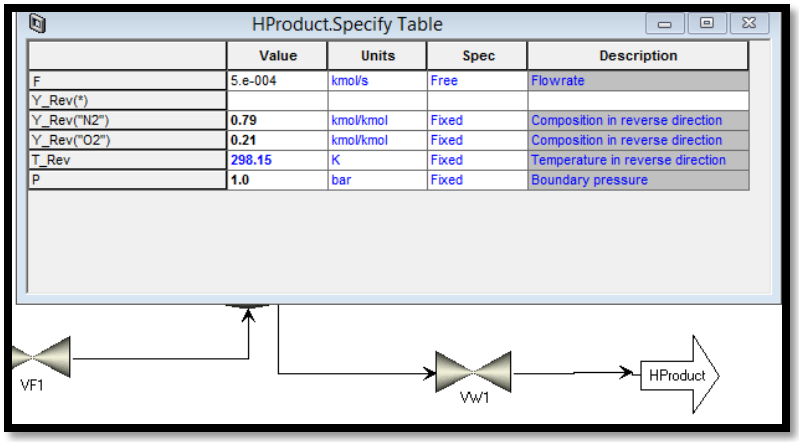

FIGURE 8.23. THE HEAVY PRODUCT SPECIFICATION IN THE PSA MODEL.

Step 21: LProduct block->Light Product Specification.

In the "LProduct" block, we also set the flow rate as free, and control it in the Cycle Organizer through the VB1 valve. The reversed direction of the composition is fixed with 0.79 mole fraction nitrogen and 0.21 mole fraction oxygen. The reversed direction of the temperature is still fixed with 25 °C, and the pressure in the LProduct block is fixed with 1 bar.

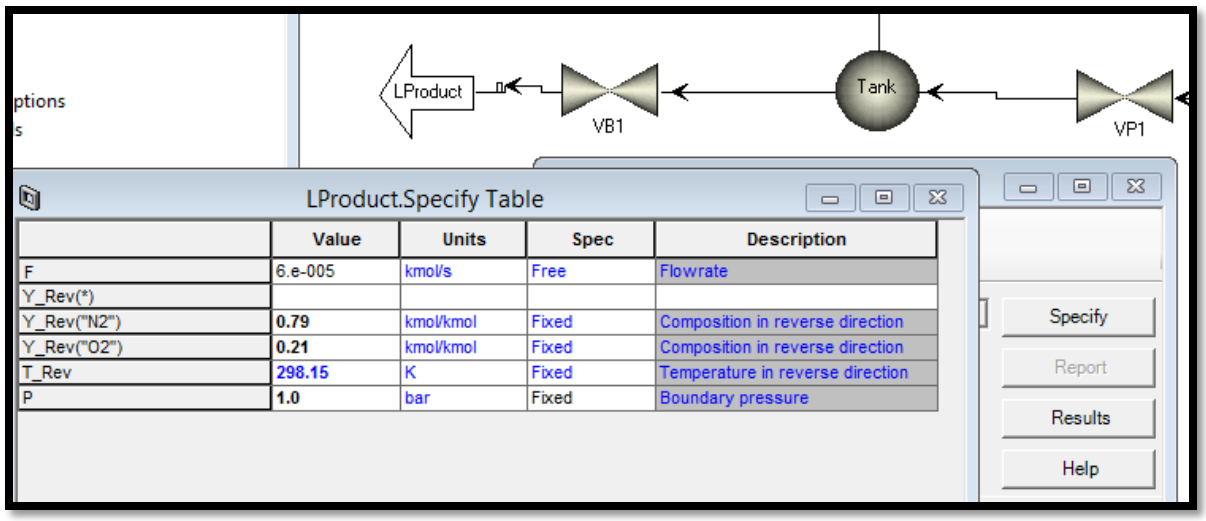

FIGURE 8.24. THE LIGHT PRODUCT SPECIFICATION IN THE PSA MODEL.

Step 22: TBa Tank block-> Specification.

We set the total volume of this bottom tank TBa as 10 cm^3.

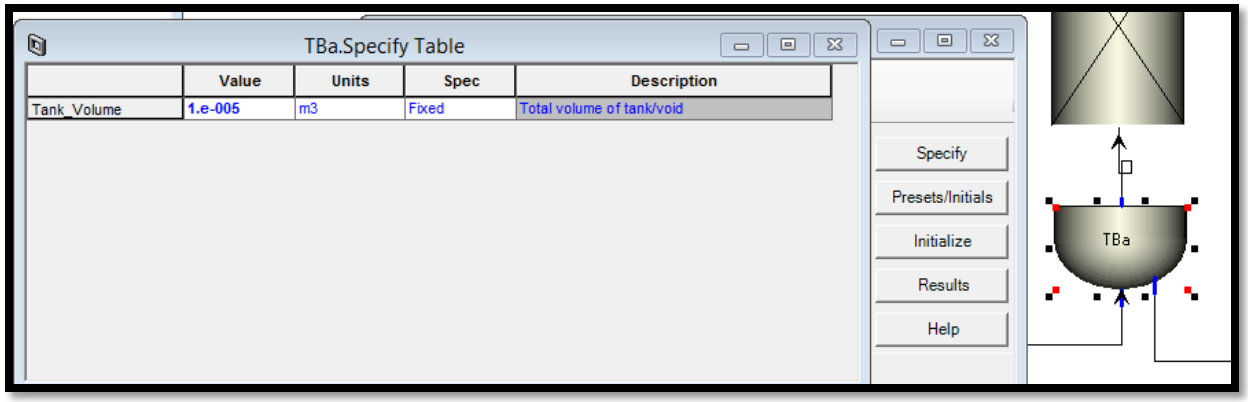

FIGURE 8.25. THE TBA TANK VOLUME IN THE PSA MODEL.

Step 23: TBa Tank block-> Presets/Initials.

We set the initial mole fractions of nitrogen and oxygen randomly similar but not exactly identical, as shown in Figure 8.26. The initial temperature of this TBa tank is still 25 °C, and we set the initial pressure as 8 bar, which is lower than the feed in pressure (10 bar).

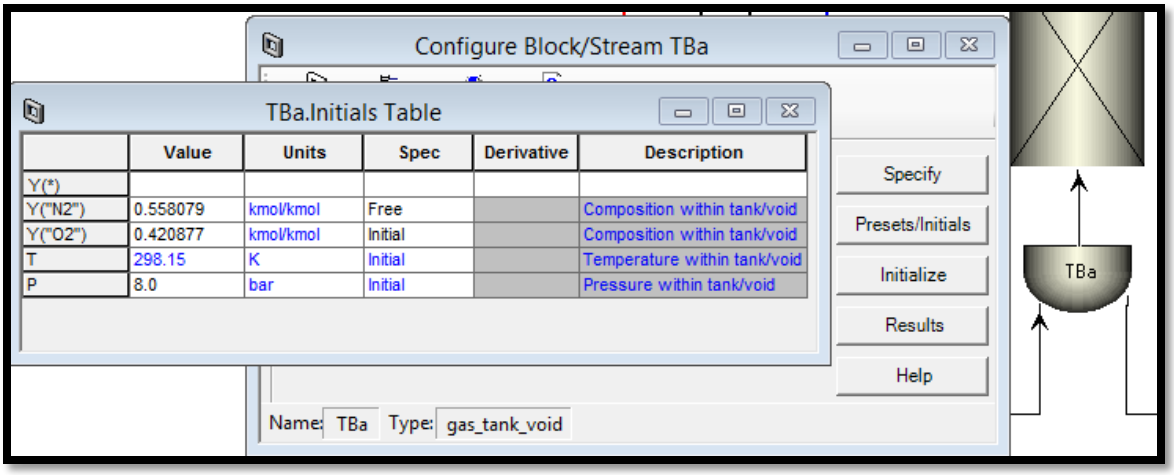

FIGURE 8.26. THE TBA TANK INITIAL CONDITIONS IN THE PSA MODEL.

Step 24: TBb Tank block-> Specification.

We also set the total volume of this top tank TBb as 10 cm^3.

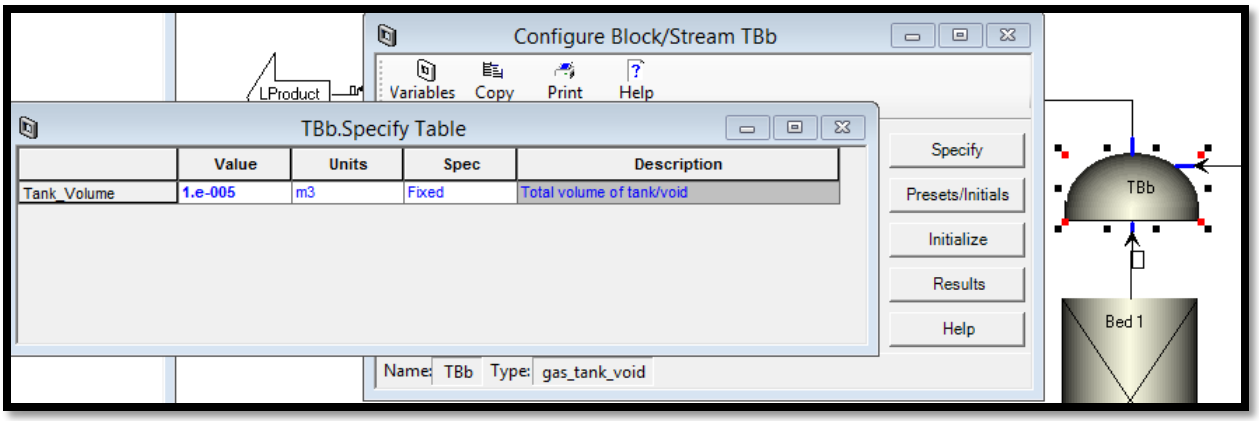

FIGURE 8.27. THE TBB TANK VOLUME IN THE PSA MODEL.

Step 25: TBb Tank block-> Presets/Initials.

We set the initial mole fractions of nitrogen and oxygen randomly similar but not exactly identical, as shown in Figure 8.28. The initial temperature of this TBb tank is still 25 °C, and we set the initial pressure as 8 bar (or a little bit lower than 8 bar), the same as that in TBa.

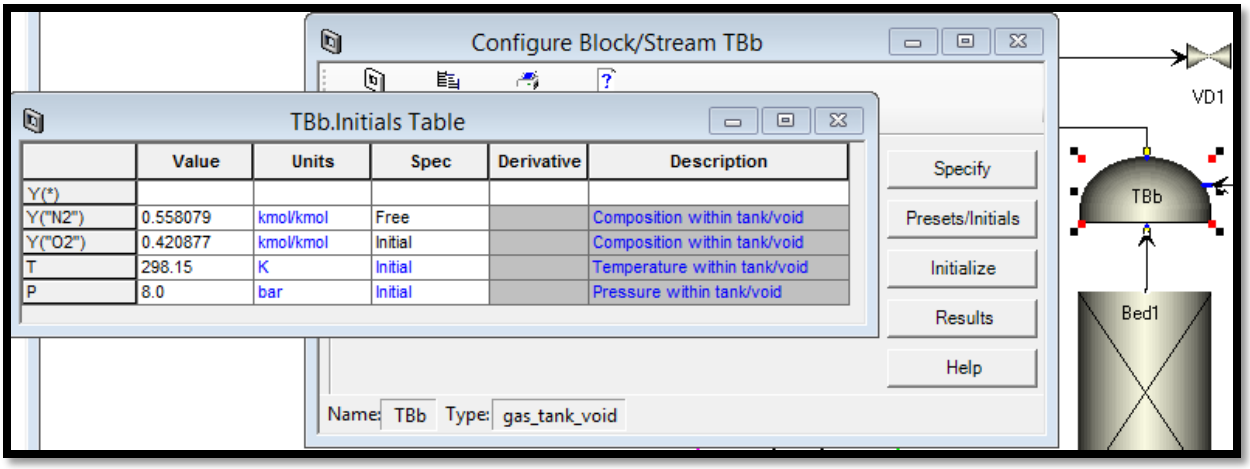

FIGURE 8.28. THE TBB TANK INITIAL CONDITIONS IN THE PSA MODEL.

Step 26: Tank block-> Specification.

We consider this tank as a story tank, so we set the total volume of this tank much 3 m^3.

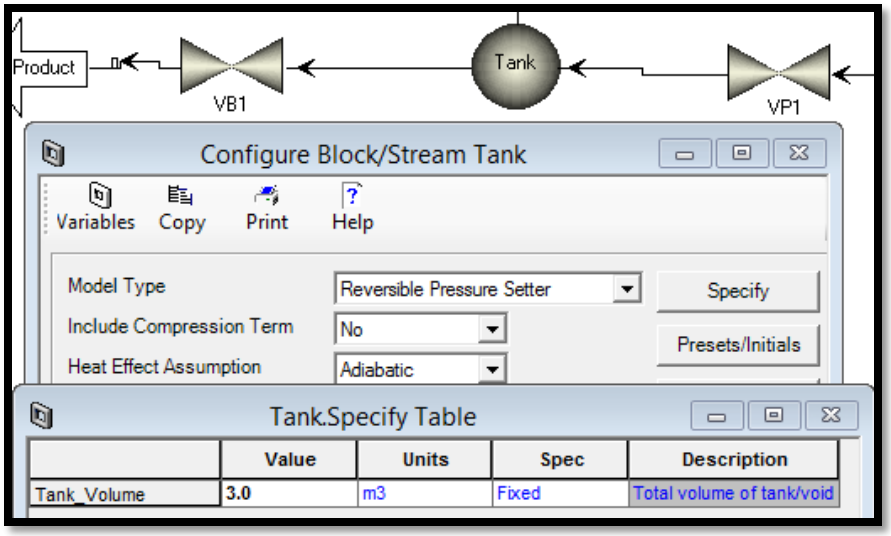

FIGURE 8.29. THE STORE TANK VOLUME IN THE PSA MODEL.

Step 27: Tank block-> Presets/Initials.

We set the initial mole fractions of nitrogen and oxygen randomly but not exactly identical, as shown in Figure 8.30. The initial temperature of this tank is still 25 °C, and we set the initial pressure as 5 bar, which is lower than the TBb pressure (8 bar).

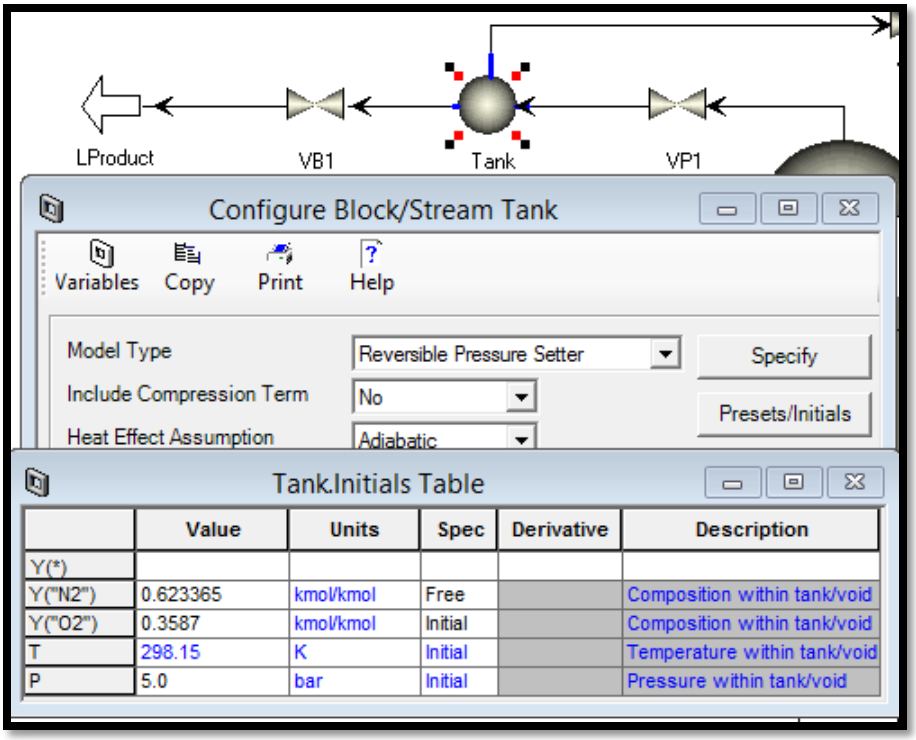

FIGURE 8.30. THE STORE TANK INITIAL CONDITIONS IN THE PSA MODEL.

Step 28: D1 block-> Specification.

We use the gas_interaction block D1 in Figure 8.31 as part of the single bed modeling approach, to act like another bed by recording the profile of material received.

Figure 8.31 shows the initial variables in the table we need to specify, and they are the same as the initial conditions as we set in the PSA bed. The estimated effective volume of the real bed is 0.353 m^3, which is the bed volume we set $V_{bed} = \pi {r_{bed}}^2 * bed\ height = \pi 0.25^2 * 3 = 0.353$ m^3. We set the initial pressure of the interaction unit the same as the pressure of the outlet stream 1bar. The initial molar flow rate for reversed interaction is zero. We randomly set the average composition of returned material during a reverse interaction as 0.5. The initial temperature and

pressure for reversed interaction are 25 °C and 3.5 bar. All these variables are used in the first cycle by the following expression:

$$XFac\frac{\partial P}{\partial t} * V_{bed} = \frac{\partial n}{\partial t}\mathrm{RT}$$

In the equation, XFac is a volume correction factor with a value close to 1. After the first cycle, a real material profile is available by receiving from the bed results and is used for the subsequent cycles.

D1.Specify Table

	Value	Units	Description
Notional_Volume	**0.353**	m3	Notional bed volume for use in pressure estimation
P_Stage_Start	1.0	bar	Estimated sink pressure
XFac	**10.0**	n/a	Notional bed volume correction factor
F_Initial_Reverse	**0.0**	kmol/s	Initial molar flowrate for reversed interaction
Y_Initial_Reverse(*)			
Y_initial_reverse("N2")	**0.79**	kmol/kmol	Initial mole fraction for reversed interaction
Y_initial_reverse("O2")	**0.21**	kmol/kmol	Initial mole fraction for reversed interaction
T_Initial_Reverse	**298.15**	K	Initial temperature for reversed interaction
P_Initial_Reverse	**1.0**	bar	Initial pressure for reversed interaction
P	3.5	bar	Actual pressure of the sink

FIGURE 8.31. THE INTERACTION BLOCK SPECIFICATION IN THE PSA MODEL.

Step 29: Tool-> Cycle Organizer.

The most important part of a PSA process is the arrangement of the cycle operations. The choice of a suitable operating cycle is in fact critical, and there are a wide range of different cycles proposed to optimize different aspects of the overall process. The PSA processes differ from one another in the sequence of the elementary steps in the cycle operations. The most common elementary steps includes:

1. Adsorption: The solid adsorbent adsorbs the components at high pressure based on their different selectivities to the solid. The product end in the gas phase is enriched of the less selectively adsorbed species.
2. Blowdown (cocurrent or countercurrent to the feed):

Countercurrent blowdown to a low pressure is used when only raffinate product is required at high purity. It can prevent contamination of the product end with more strongly adsorbed species. The cocurrent blowdown happens prior to countercurrent blowdown, and only blowdown to an intermediate pressure. It is used when extract product is also required in high purity, and can improve extract product purity and may also increase raffinate recovery.

3. Purge: The bed is purged with the preferentially adsorbed species after the high-pressure adsorption.
4. Repressurization: It increases the pressure of the column, and prepares for the high-pressure adsorption step.

In the workshop, we provide an example of the basic cycle operation of PSA in Figure 8.32. This is a 2-bed PSA Process with four steps including adsorption, blowdown, purge and repressurization steps.

Figure 8.33 displays how to generate a Cycle Organizer in Aspen Adsorption. It is very similar as we did in Aspen Chromatography. To access the Cycle Organizer, we click the Cycle Organizer from the Tools menu. Once a Cycle Organizer block is present on the flowsheet, we can open it either using the Tools menu, or by double-clicking on the flowsheet block.

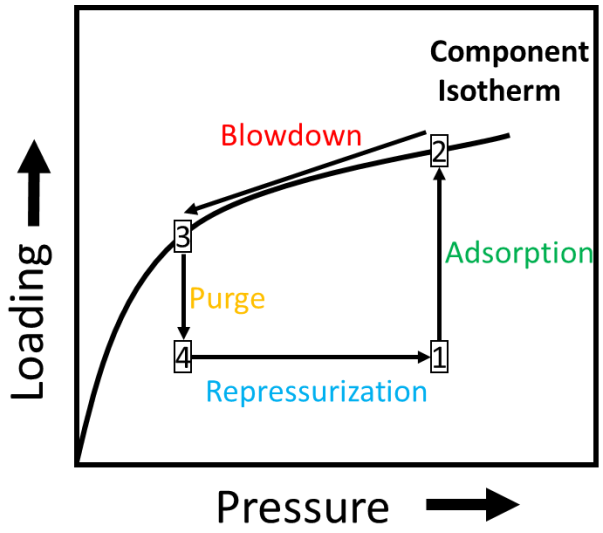

Bed 1	Adsorption			Blowdown	Purge	Repressurization
Bed 2	Blowdown	Purge	Repressurization	Adsorption		

FIGURE 8.32. 2-BED 4-STEP PSA PROCESS ISOTHERM CYCLE AND STEP CHART.

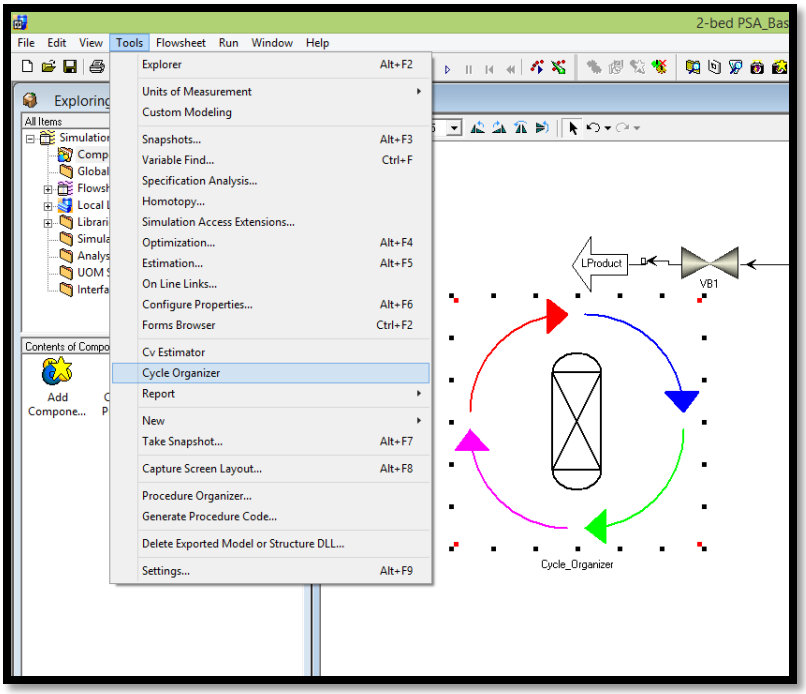

FIGURE 8.33. THE GENERATION OF A CYCLE ORGANIZER IN THE PSA MODEL.

Step 30: Cycle Organizer-> Cycle Options.

Figure 8.34 displays the cycle settings for the process in the PSA model. We set the maximum cycle numbers as 100.

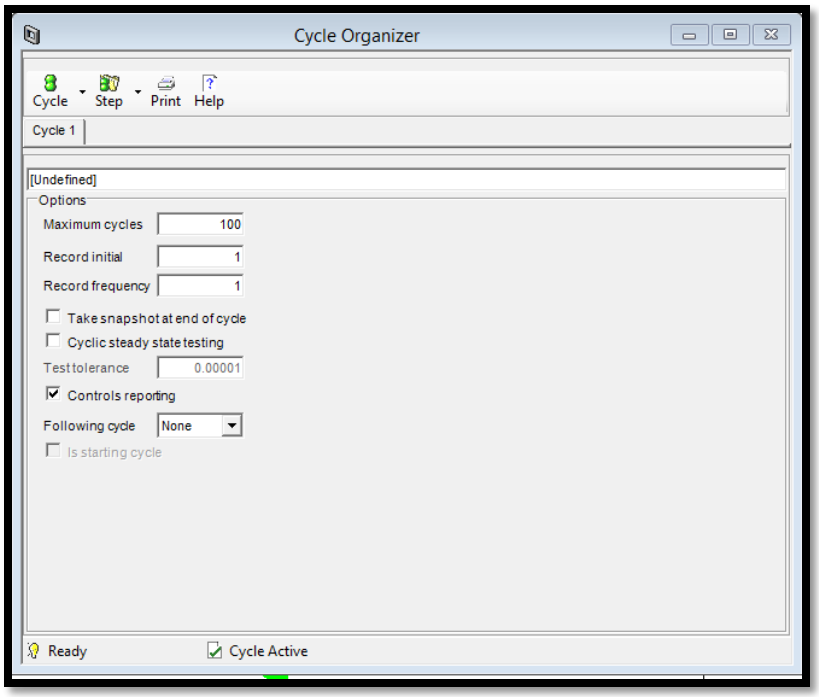

FIGURE 8.34. THE CYCLE OPTIONS OF THE CYCLE ORGANIZER IN THE PSA MODEL.

Step 31: Cycle Organizer-> Step Control->Step 1: Adsorption.

Table 8.4 lists the step time for each step in the PSA cycle. We make sure that the time of adsorption step equals to the sum of the times for blowdown, purge and repressurization steps. Then, we set the step time for each step in the following steps 31 to 34.

Table 8.4. Time for each step in the PSA cycle.

Step 1: Adsorption	60 s
Step 2: Blowdown	20 s
Step 3: Purge	20 s
Step 4: Repressurization	20 s

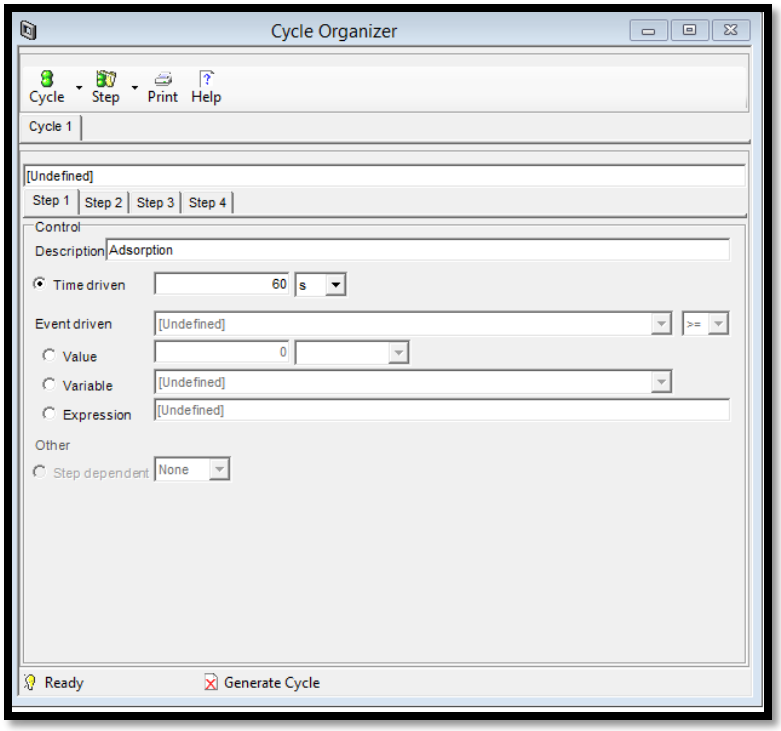

FIGURE 8.35. THE ADSORPTION STEP TIME IN CYCLE ORGANIZER IN THE PSA MODEL.

Step 32: Cycle Organizer-> Step Control->Step 2: Blowdown.

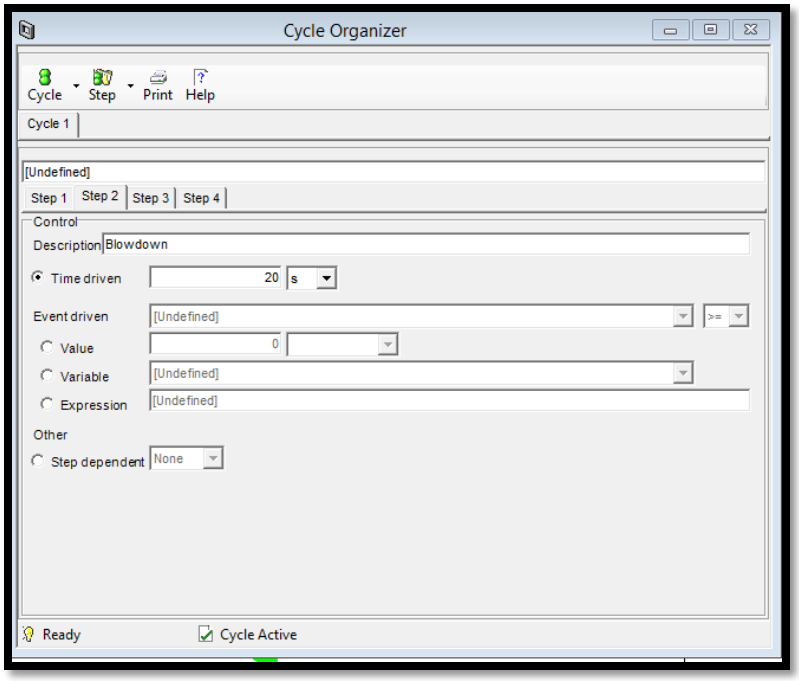

FIGURE 8.36. THE BLOWDOWN STEP TIME IN CYCLE ORGANIZER IN THE PSA MODEL.

Step 33: Cycle Organizer-> Step Control->Step 3: Purge.

Since the represssurization step depends on the step 2, it has same step time as step 2, then the purge step time is controlled by step 1. Basiclly, $T_{step3} = T_{step1} - T_{step2} - T_{step4}$.

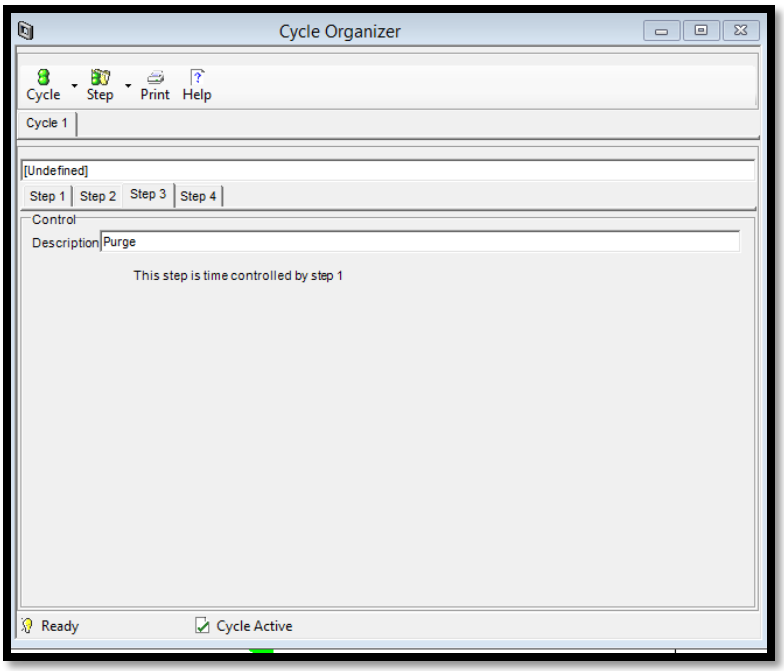

FIGURE 8.37. THE PURGE STEP TIME IN CYCLE ORGANIZER IN THE PSA MODEL.

Step 34: Cycle Organizer-> Step Control->Step 4: Repressurization.

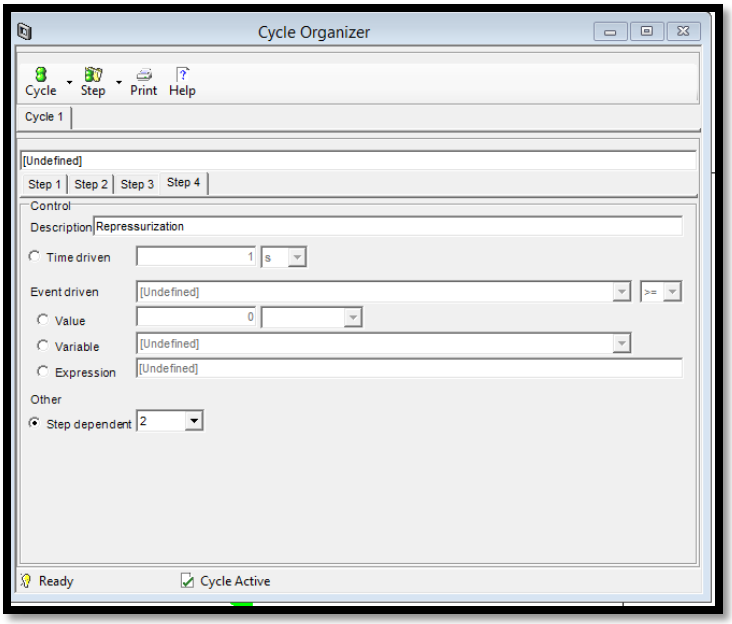

FIGURE 8.38. THE REPRESSURIZATION STEP TIME IN CYCLE ORGANIZER IN THE PSA MODEL.

Step 35: Cycle Organizer-> Step Manipulated->Step 1: Adsorption.

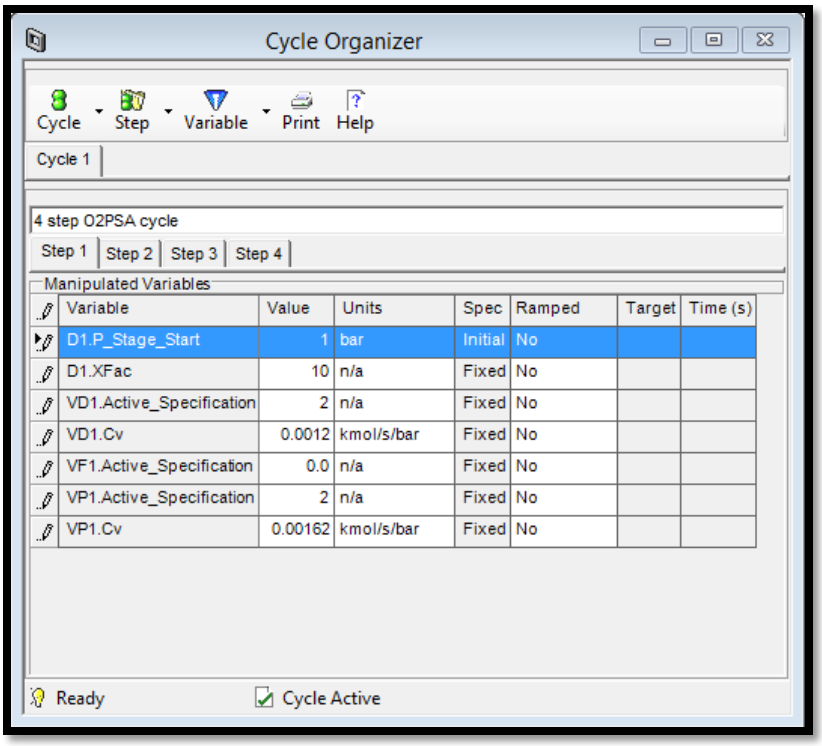

FIGURE 8.39. THE ADSORPTION STEP CONDITIONS IN CYCLE ORGANIZER IN THE PSA MODEL.

Step 36: Cycle Organizer-> Step Manipulated ->Step 2: Blowdown.

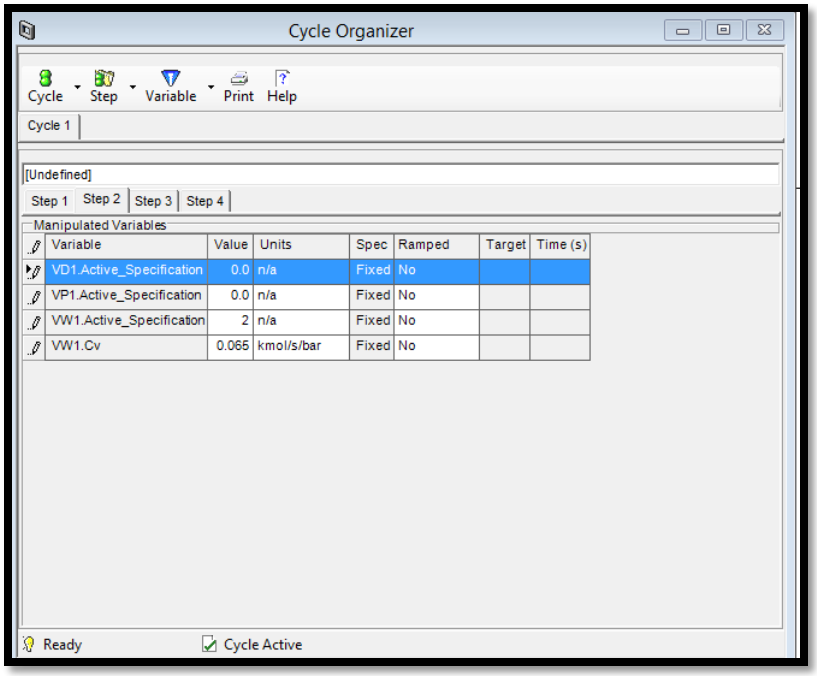

FIGURE 8.40. THE BLOWDOWN STEP CONDITIONS IN CYCLE ORGANIZER IN THE PSA MODEL.

Step 37: Cycle Organizer-> Step Manipulated ->Step 3: Purge.

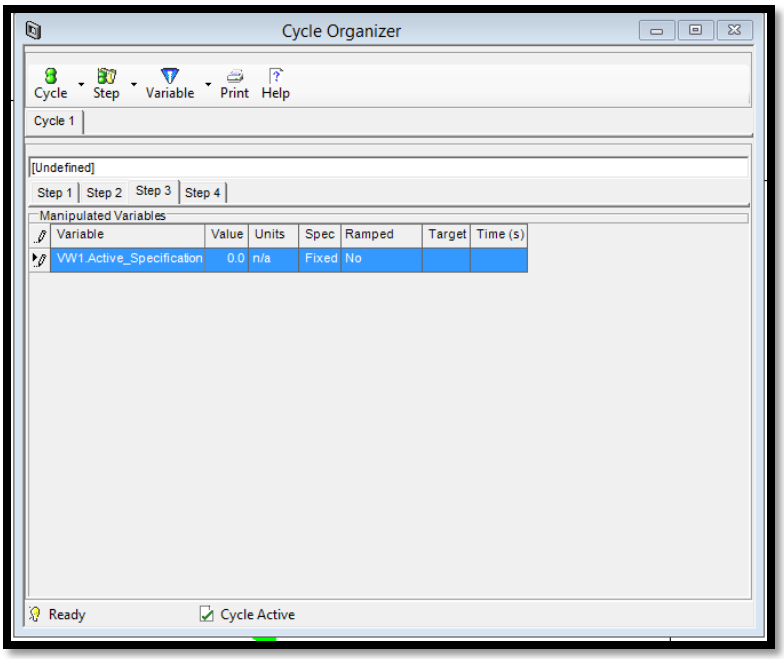

FIGURE 8.41. THE PURGE STEP CONDITIONS IN CYCLE ORGANIZER IN THE PSA MODEL.

Step 38: Cycle Organizer-> Step Manipulated ->Step 4: Repressurization.

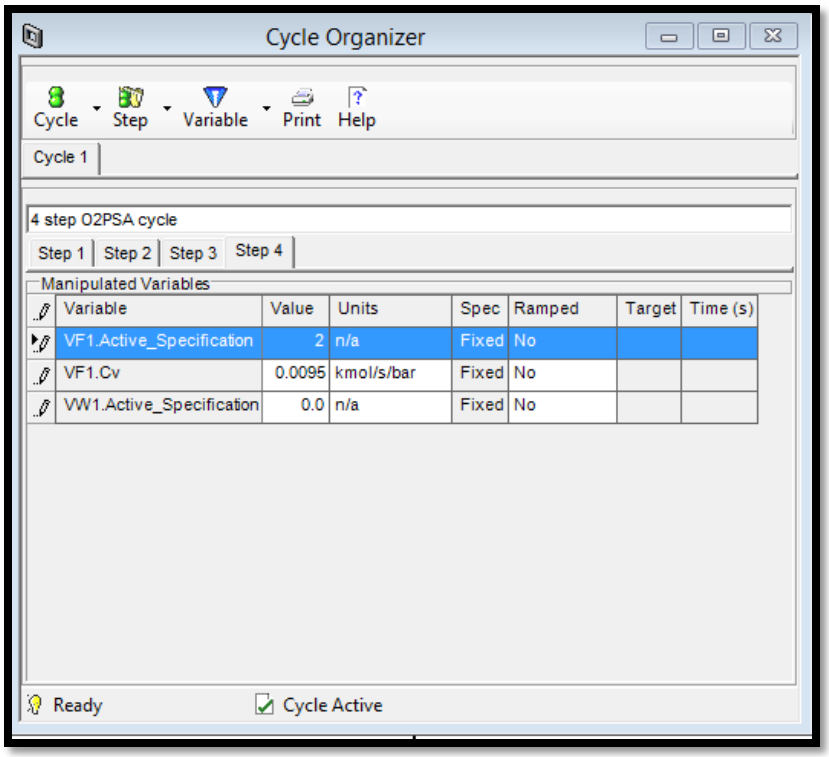

FIGURE 8.42. THE REPRESSURIZATION STEP CONDITIONS IN CYCLE ORGANIZER IN THE PSA MODEL.

Step 39: Run Options->Pause at 6000 seconds. We set the model run 50 cycles, then the simulation time would be (50*120) = 6000 seconds.

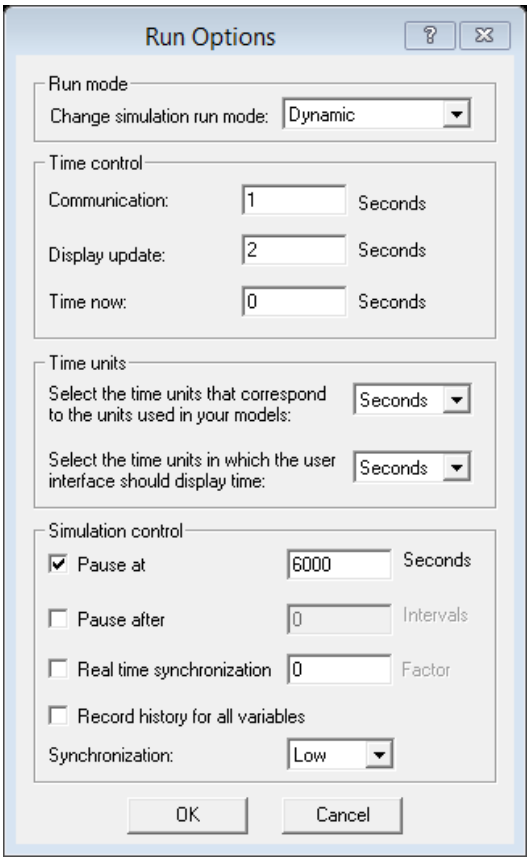

FIGURE 8.43. THE SIMULATION TIME SETTINGS IN THE PSA MODEL.

Step 40: Add Form-> Plot->BedPressure.

First, we want to see the pressure change within the bed over time, and make the bed pressure plot in steps 40 and 41.

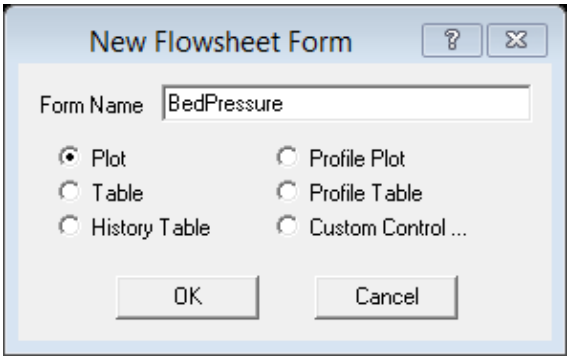

FIGURE 8.44. THE GENERATION OF A BED PRESSURE PLOT OVER TIME.

Step 41: Variables finding for the BedPressure plot.

Figure 8.45 displays the pressure changes for the D1 interaction block, TBa and TBb tanks, and the store tank over the simulation time.

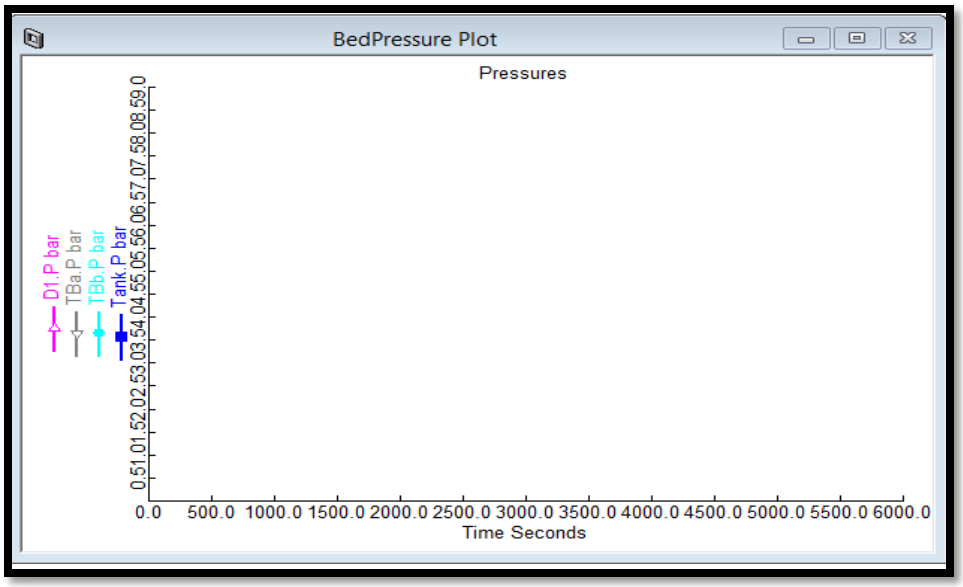

FIGURE 8.45. THE BED PRESSURE PLOT OVER TIME IN THE PSA MODEL.

Step 42: Add Form-> Plot->LProduct-> Variables finding for the LightProduct plot.

We also make a plot to record the composition in the light product stream over time.

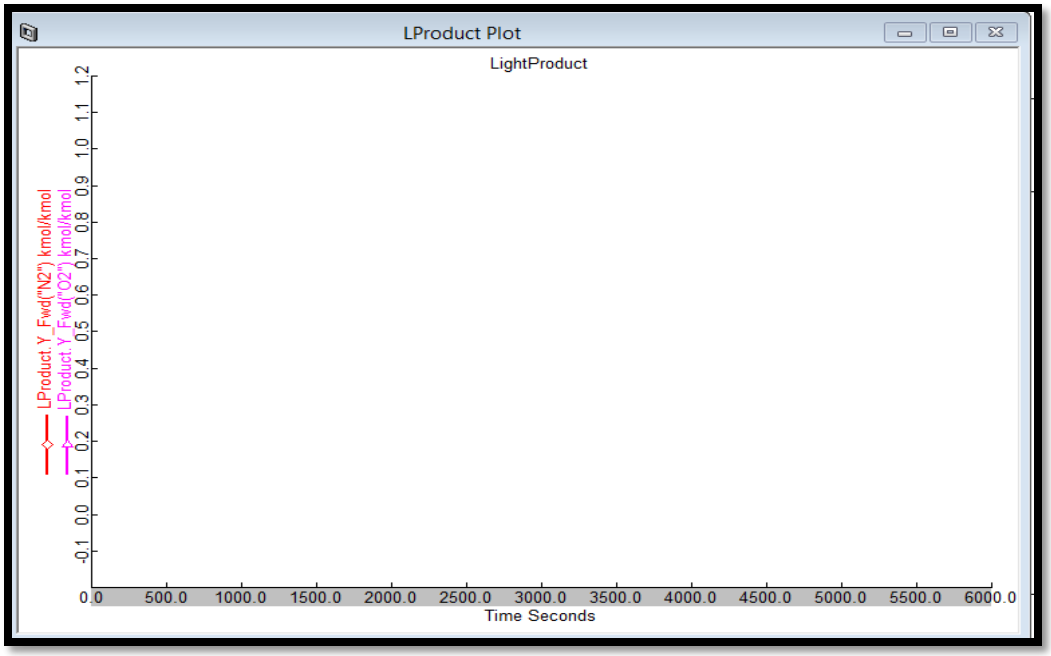

FIGURE 8.46. THE COMPOSITION PLOT IN THE LIGHT PRODUCT STREAM OVER TIME IN THE PSA MODEL.

Step 43: Add Form-> Plot->HProduct-> Variables finding for the HeavyProduct plot.

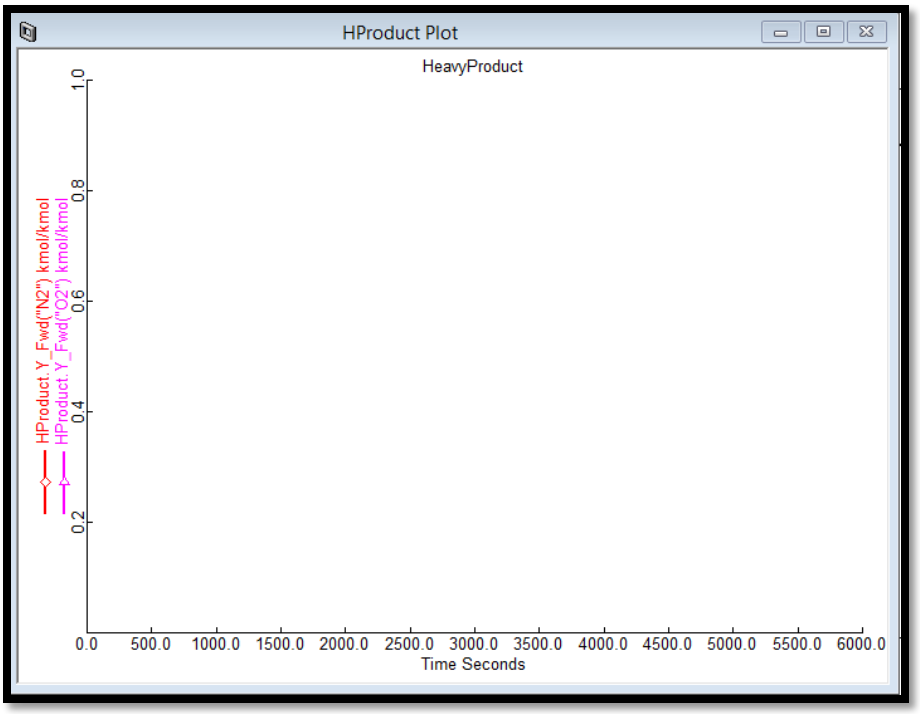

FIGURE 8.47. THE COMPOSITION PLOT IN THE HEAVY PRODUCT STREAM OVER TIME IN THE PSA MODEL.

Step 44: Add Form->Profile Plot->Axial_Composition.

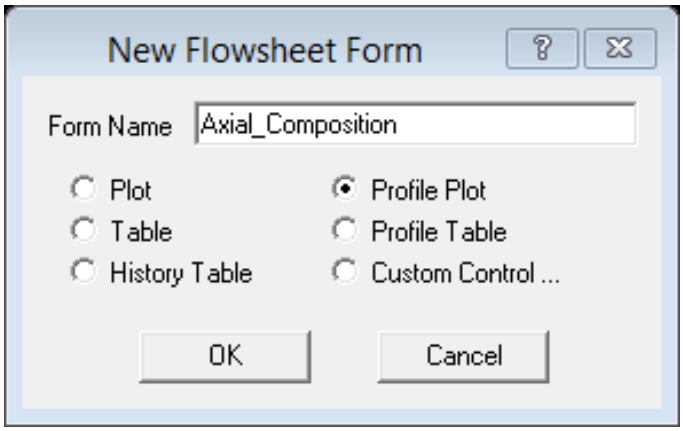

FIGURE 8.48. THE GENERATION OF A CONCENTRATION PROFILE WITHIN THE COLUMN.

Step 45: Profile Editor for the Axial_Composition profile plot.

Position: Bed 1. Layer(*).Axial_Distance(*)

N2 Partial Pressure: Bed 1. Layer(*).Y (*,"N2")

N2 Partial Pressure: Bed 1. Layer(*).Y (*,"N2")

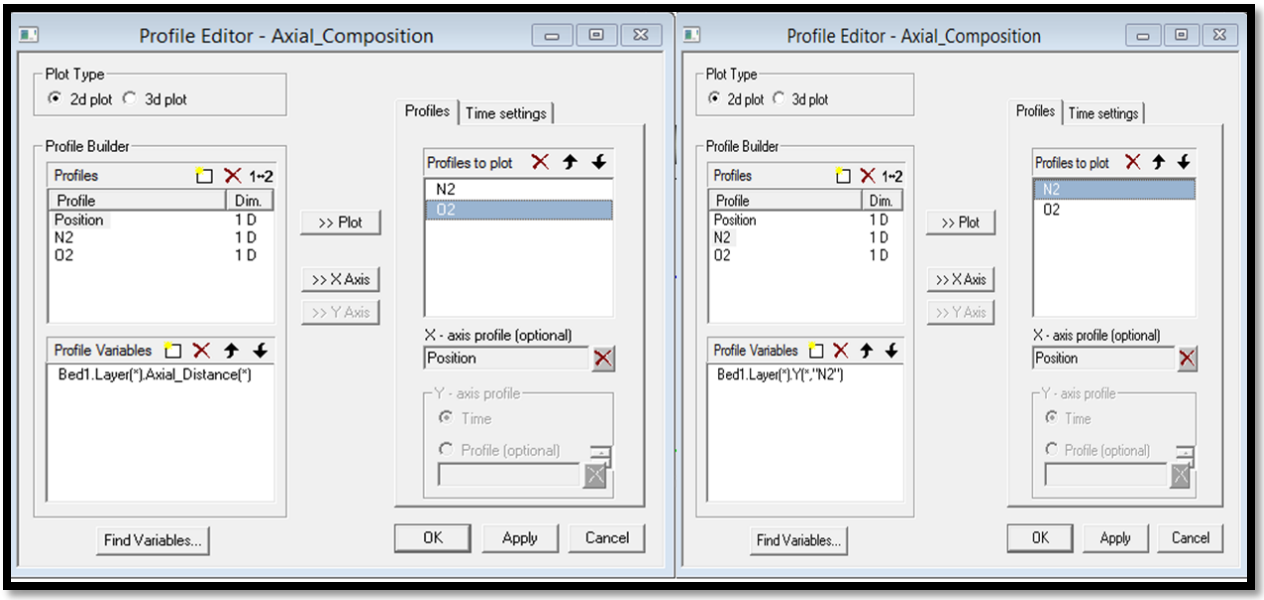

FIGURE 8.49. THE AXIAL COMPOSITION PROFILE PLOT IN THE PSA MODEL.

Step 46: Run Options->Initialization.

The model is ready to initialize.

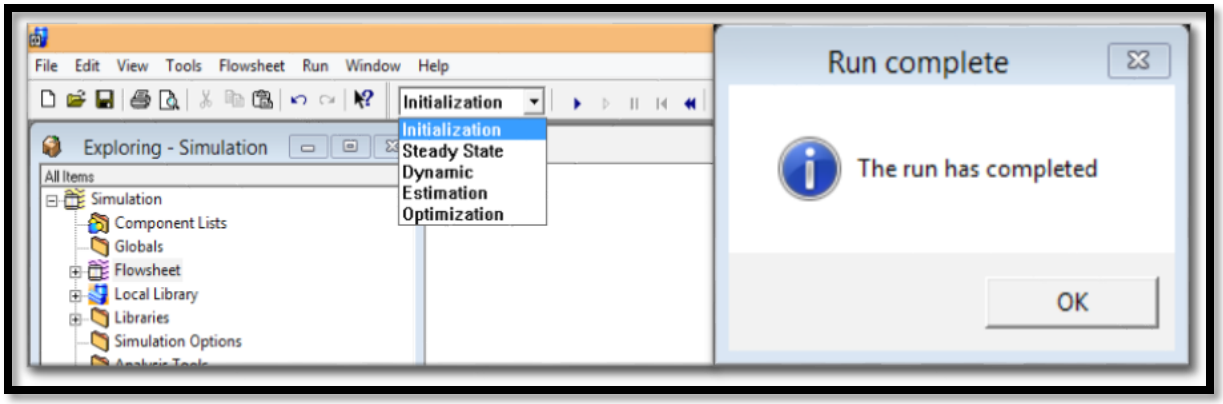

FIGURE 8.50.THE INITIALIZATION OF THE PSA MODEL.

Step 47: Run Options->Dynamic.

The model is ready for the dynamic run after reaching the pause time (382.8 min) we set.

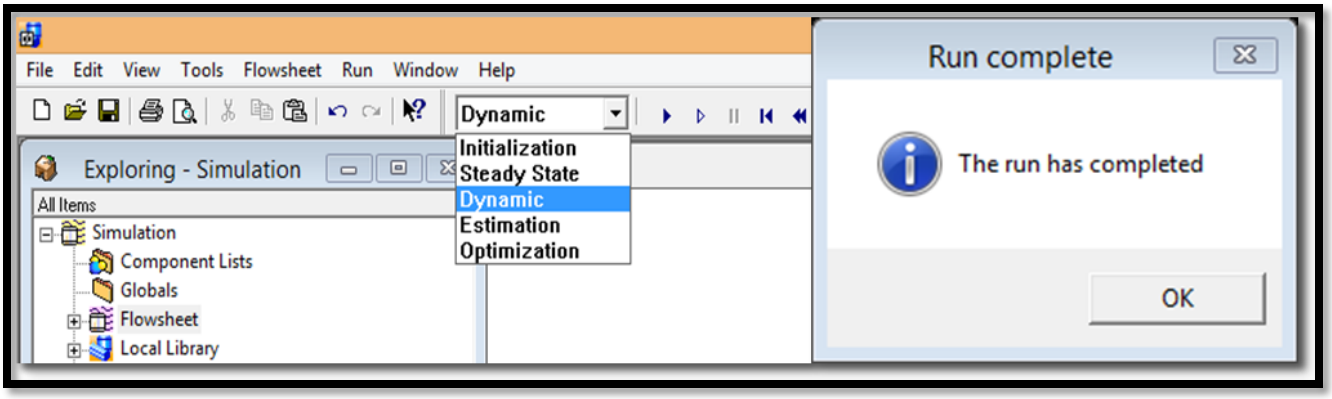

FIGURE 8.51.THE DYNAMIC RUN OF THE PSA MODEL.

Step 48: Results->Plots.

We display all the plots made in steps 41 to 45. In this workshop, we developed a two-bed PSA model for a binary separation of an O2/N2 mixture. Figure 8.52 reveals the changing of pressure between the adsorption and regeneration steps within the bed and tanks. Figure 8.53 shows the resulting light product mole fraction in the LProduct stream with high O_2 mole fraction. The resulting heavy product plot in Figure 8.54 shows the high concentration of O2 in the HProduct stream. Figure 8.55 illustrates the axial composition profile plot within the bed in the PSA model, which shows a good separation between the component N_2 and O_2.

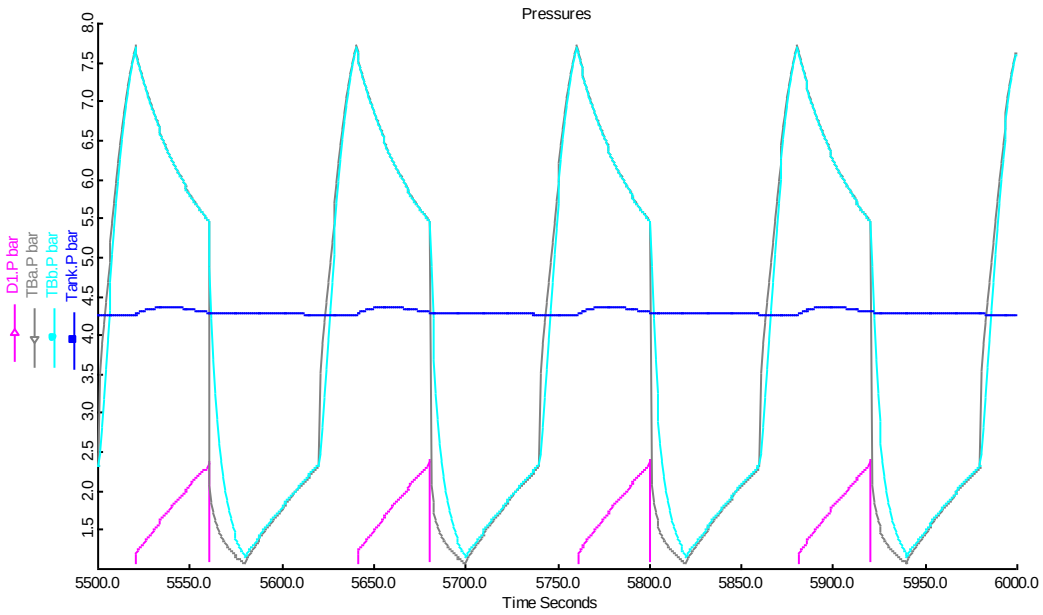

FIGURE 8.52. THE RESULTING BED PRESSURE PLOT IN THE PSA MODEL.

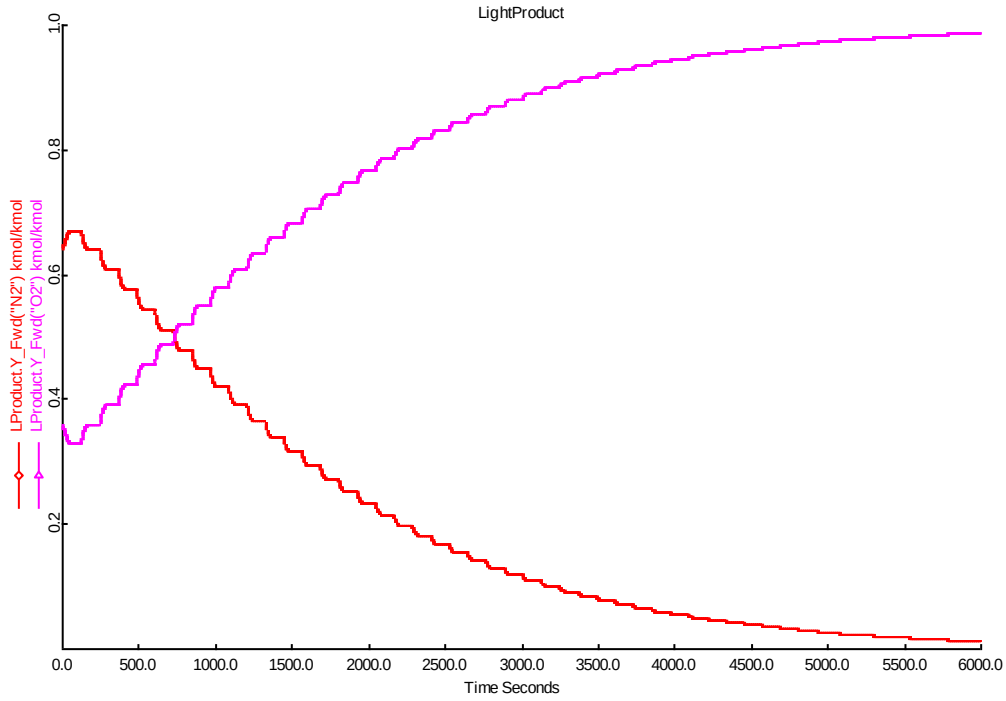

FIGURE 8.53. THE RESULTING LIGHT PRODUCT PLOT IN THE PSA MODEL.

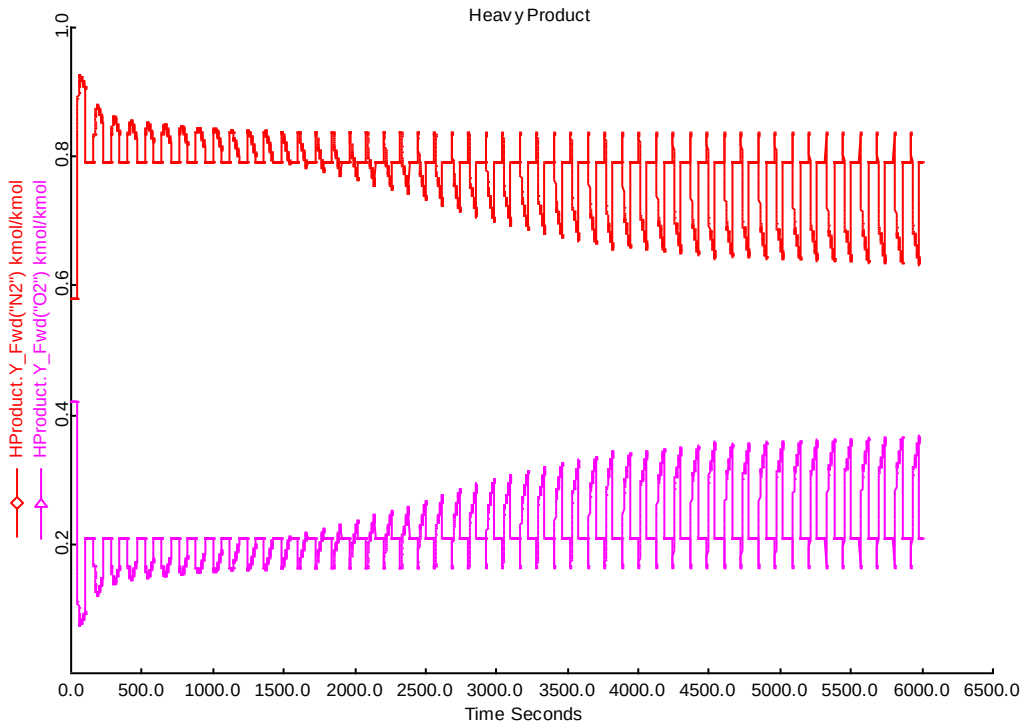

FIGURE 8.54. THE RESULTING HEAVY PRODUCT PLOT IN THE PSA MODEL.

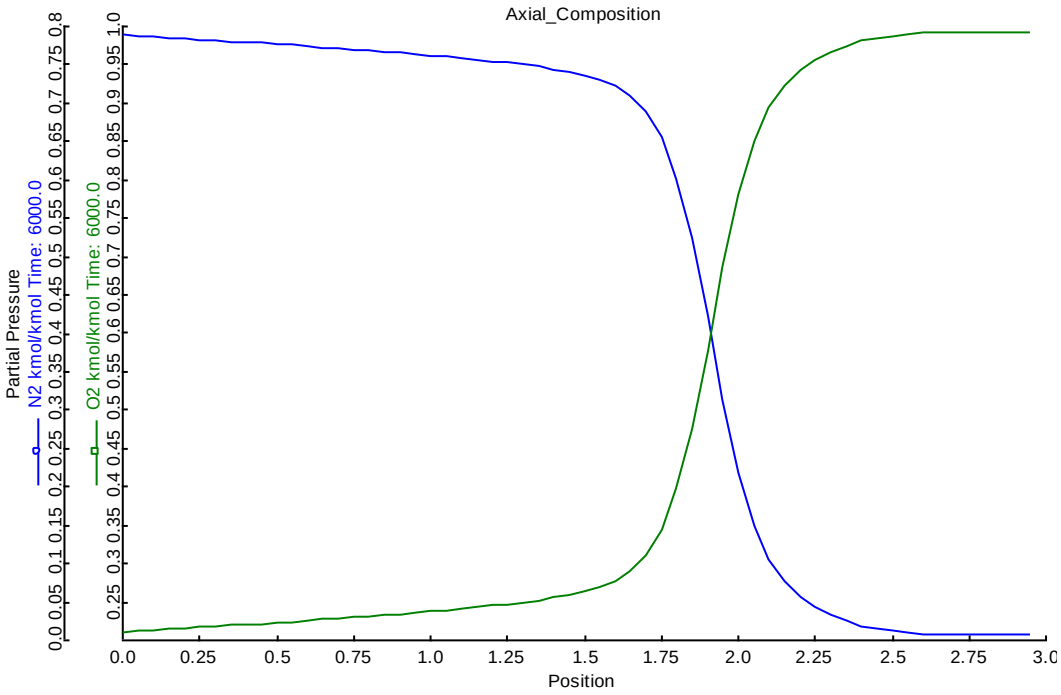

FIGURE 8.55.THE AXIAL COMPOSITION PROFILE PLOT WITHIN THE BED OF THE PSA MODEL.

9. TSA Workshop: Aspen Adsorption Modeling for CO2 Capture

The environmental impact of rising carbon dioxide emissions continues to attract the researchers and engineers' attentions[108, 109]. The coal-fired power plants contribute more than 40% to annual global CO_2 emissions[108]. As we mentioned in chapter 7, the regeneration of an solid adsorbent is usually accomplished via pressure swing adsorption (PSA), temperature swing adsorption (TSA), or a combination of these processes[110]. Among these methods, TSA is particularly promising for post-combustion CO_2 capture, owing to difficulties with compressing or applying a vacuum to a large volume of a low-pressure gas stream, as well as to the potential availability of low-grade heat in a power plant as a source of energy for regeneration[111-115]. Thus, the energy requirement for CO_2 capture utilizing TSA may be reduced over the corresponding PSA processes.

In order to improve the adsorptive performance for CO_2 capture processes, researchers have developed a variety of TSA technology in the literature[111-115]. Merel et al[111] use a TSA process with indirect heating and cooling by means of an internal heat exchanger and 13X and 5A zeolites for post-combustion CO_2 capture. In this case, an indirect heating system reduces the energy consumption. Bonjour et al[112] invents a rapid adsorber to reduce the time of the regeneration step and adsorbent inventory.

Our case study is a study of adsorptive separation for CO_2 capture on carbon molecular sieves from a CO_2/N_2 mixture[116,117]. Figure 9.1 illustrates the principle of the temperature swing adsorption process. This TSA process involves adsorbing CO_2 from flue gas at low temperature to obtain the pure nitrogen in the outlet stream, and heating the saturated adsorbent to desorb the captured CO_2 and regenerate the solid adsorbent in the bed.

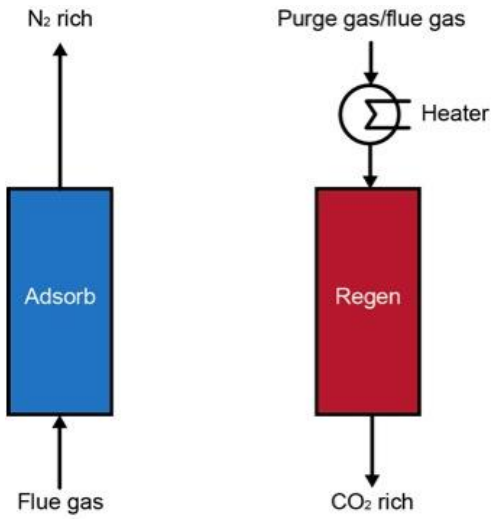

FIGURE 9.1. THE TEMPERATURE SWING ADSORPTION OPERATION.

We demonstrate the modeling of a separation process of capturing CO_2 by applying the temperature swing adsorption (TSA) technology step by step using Aspen Adsorption in this workshop[116-118]. In our separation system, the adsorption step includes CO_2/N_2 feeding (13% CO_2) until complete saturation. In the following generation step, the bed is heated by the hot feeding at 150 ^oC to desorb the CO_2.

Step 1: Start a new case in Aspen Adsorption.

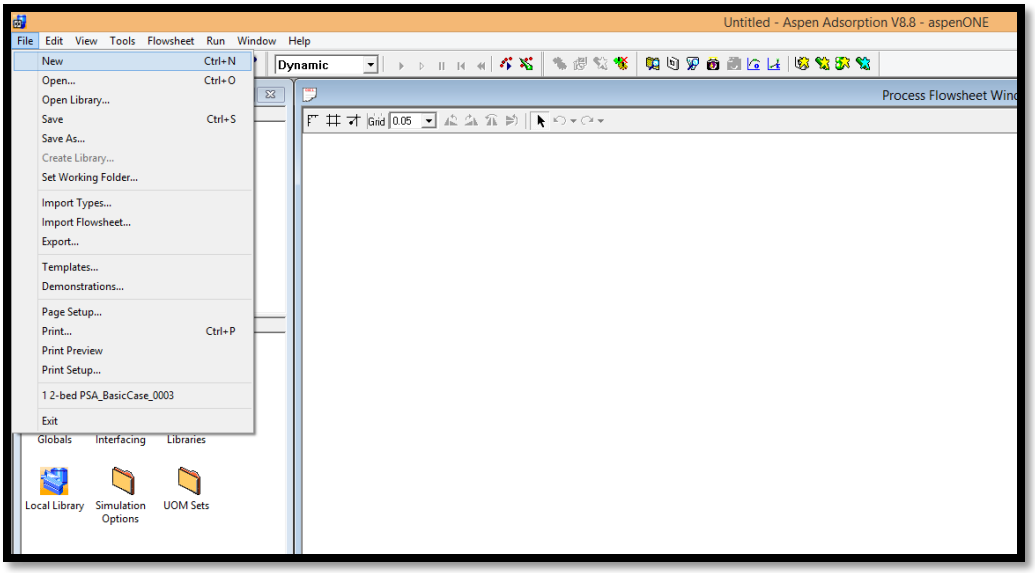

FIGURE 9.2. A NEW FILE IN ASPEN ADSORPTION FOR THE TSA MODEL.

Step 2: Save the new file as “TSA Process for CO2 Capture”.

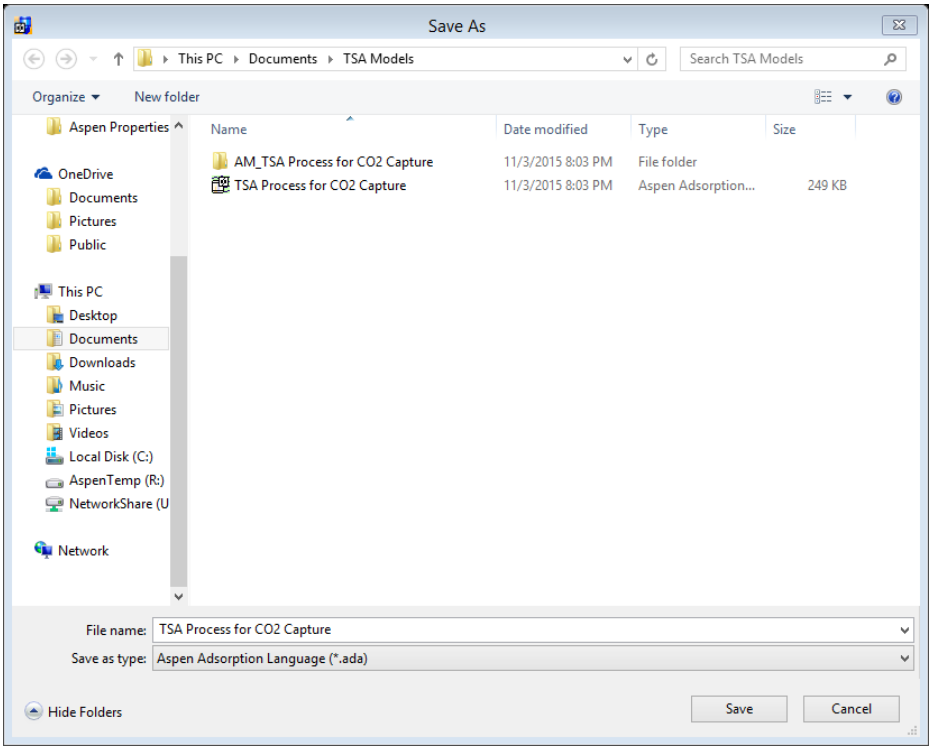

FIGURE 9.3. THE TSA PROCESS FOR CO2 CAPTURE.

Step 3: Choose the blocks in the Library Model, and create the flowsheet for the TSA model.

The general design of an adsorption carbon capture process involves a large, packed bed of solid adsorbents, as shown in Figures 9.4 and 9.5. Figure 9.4 is a simple diagram for a single TSA bed with two inlet streams and two outlet streams. Figure 9.5 is an Aspen flowsheet for this single TSA bed model.

To make the Aspen flowsheet for a typical TSA process in Figure 9.6, go to “Model Library” in Aspen Adsorption, choose each block in Figure 9.6, and connect them using “gas_Material_Connection” to create the flowsheet for the TSA model.

Choose “Gas:Dynamic” ->”gas_bed” for the TSA bed; select “Gas:Dynamic” ->”gas_tank_void” for the tank blocks TD1 and TD2; choose “Gas:Dynamic” ->” gas_valve” for the VF1, VW1, VP1 and VF2 valves; select “Gas:Dynamic” ->” gas_feed” for the Feed blocks F1 and F2; choose “Gas:Dynamic” ->” gas_product” for the product block P1 and the waste block W1.

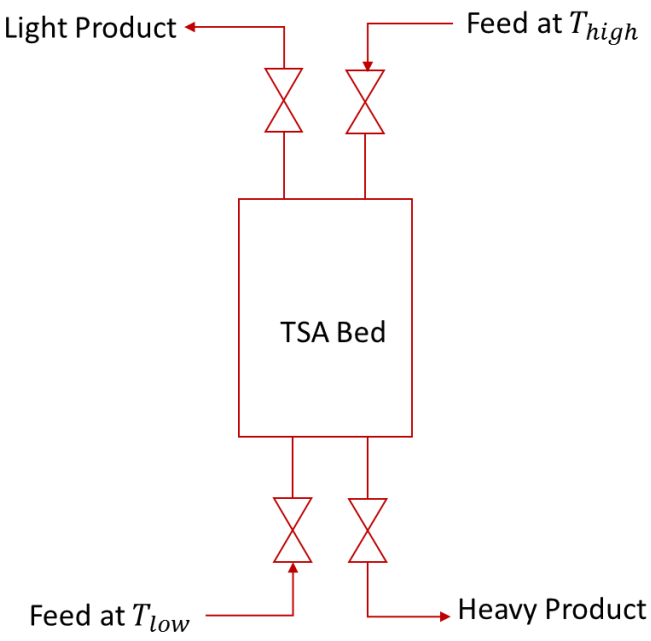

FIGURE 9.4. A TEMPERATURE SWING ADSORPTION BED.

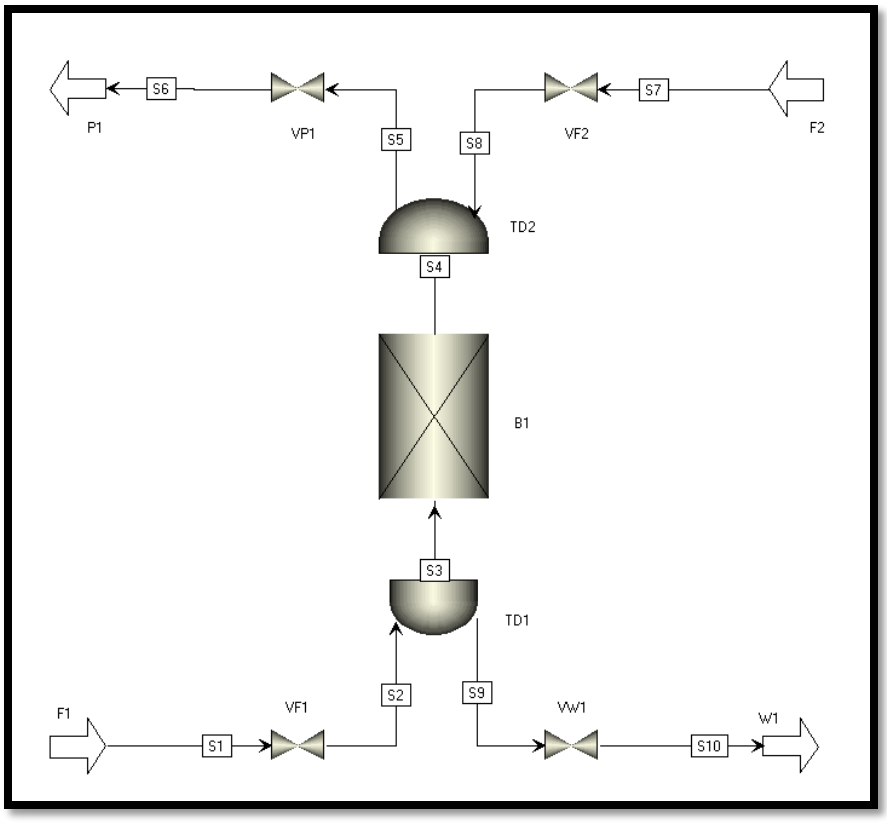

FIGURE 9.5. THE ASPEN ADSORPTION MODEL OF THE TEMPERATURE SWING ADSORPTION PROCESS.

Step 4: Add components: Component Lists -> Configure Properties.

Like the PSA workshop, we add and edit a component list using Aspen Properties. We invoke the Aspen Properties user interface by the following steps, as shown in Figure 9.6:

1. In the Simulation Explorer, click "Component Lists".

2. In the Explorer of the Component Lists folder, double-click the "Configure Properties" node.

3. In the Physical Properties Configuration dialog box, choose "Use Aspen properties system" option, and then click "Edit using Aspen Properties" button to launch the user interface.

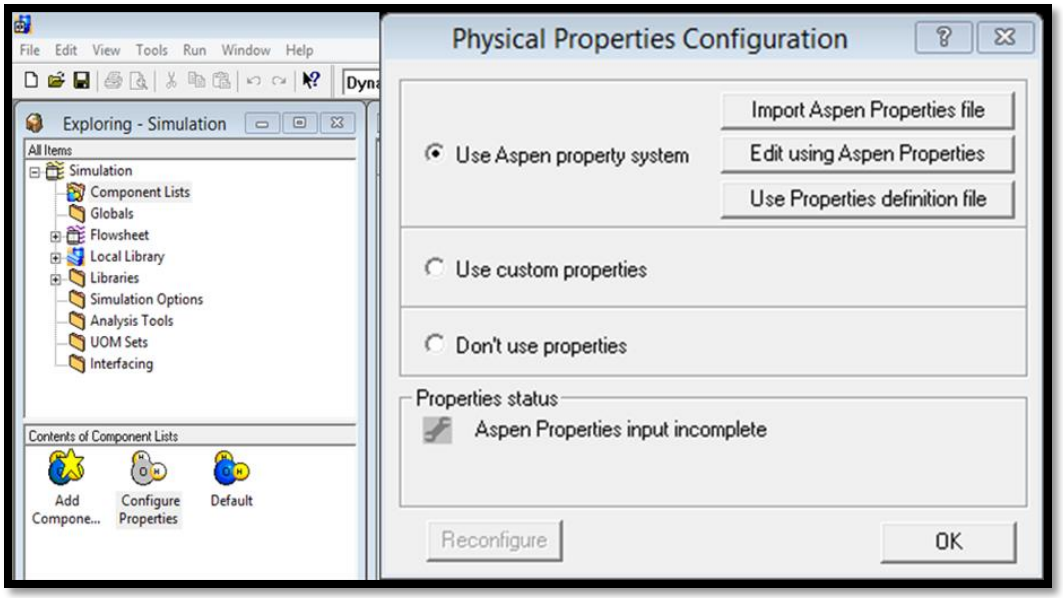

FIGURE 9.6. THE PHYSICAL PROPERTIES CONFIGURATION PANE.

Step 5: Edit using Aspen Properties.

After we click "Edit using Aspen Properties" in the Physical Properties Configuration pane, it automatically opens the Aspen Properties to add component names and edit their physical and chemical properties. Figure 9.7 displays the binary mixture of nitrogen and carbon dioxide.

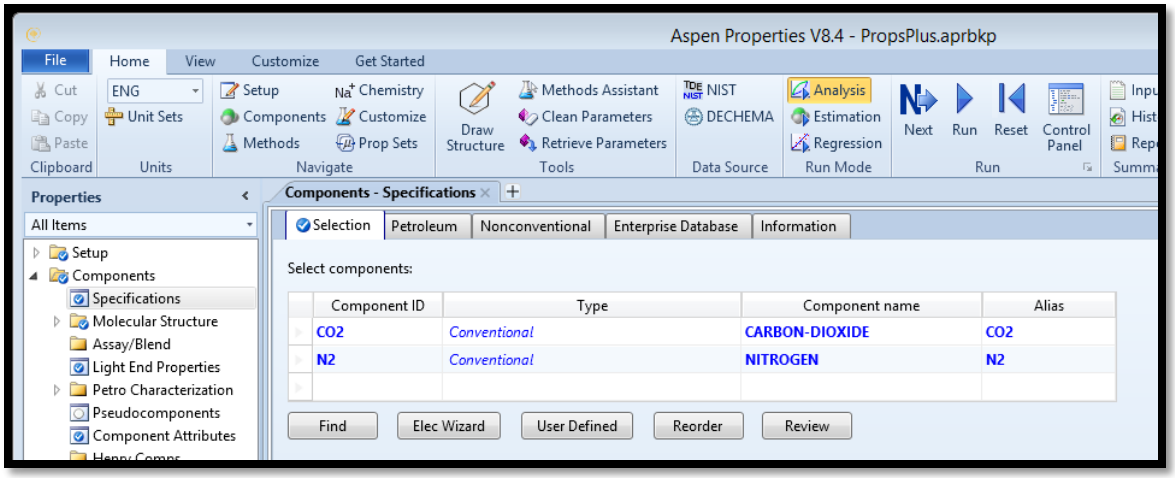

FIGURE 9.7. THE ASPEN PROPERTIES INTERFACE.

Step 6: Choose the property method, run it and save the results.

To edit components' physical properties in Aspen Properties, we follow the steps in Figure 9.8:

1. In the "All Items" pane of the "Properties", click "Specification" in the "Methods" folder.
2. Select "PENG-ROB" as the base method.
3. In the pane of "Home", click "Run" button.
4. Save the file until the run is completed in the Control Panel, as shown in Figure 9.9

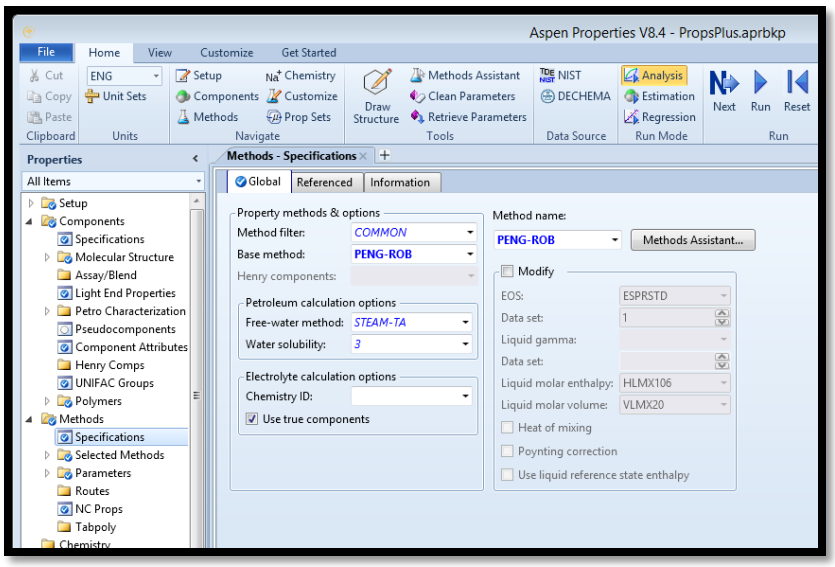

FIGURE 9.8. THE SPECIFICATION OF THE COMPONENTS IN ASPEN PROPERTIES.

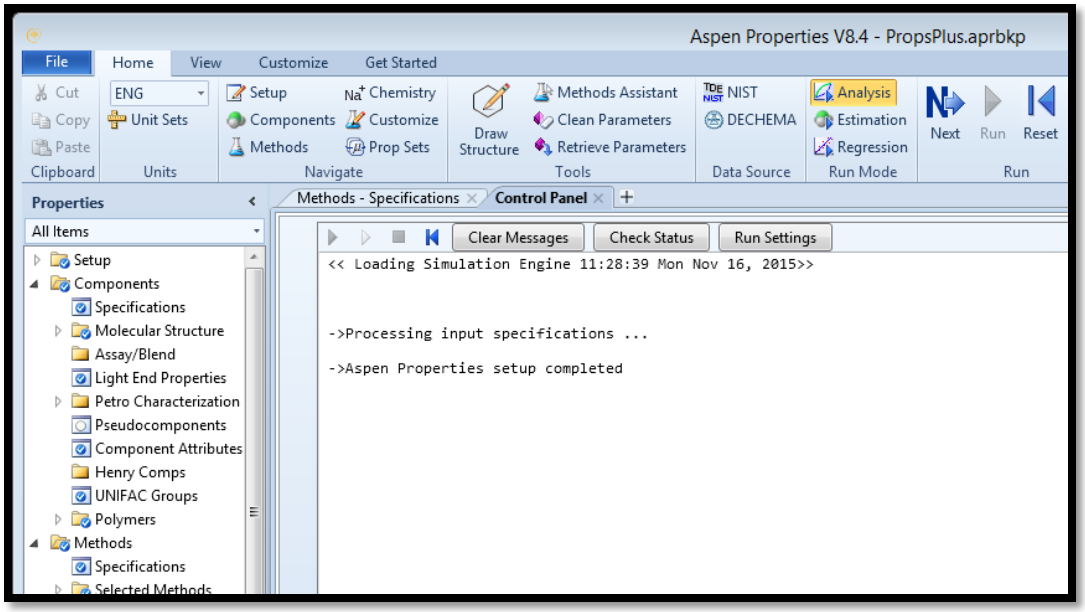

FIGURE 9.9. THE COMPLETION IN CONTROL PANEL IN ASPEN PROPERTIES.

Step 7: Configured using embedded Aspen Properties

Once we have done the import in Aspen Properties, the Aspen Properties input will be included in the file when we save the simulation file. Then go back to the Physical Properties Configuration panel, and the Properties status should become green, and shows "Configured using Embedded Aspen Properties".

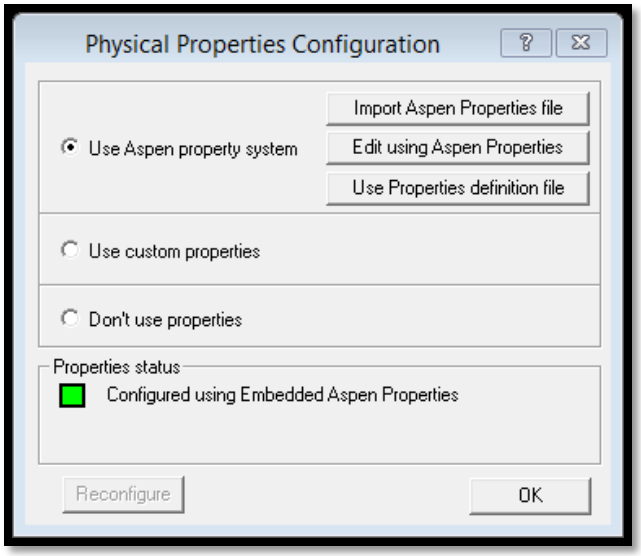

FIGURE 9.10. THE COMPLETION OF THE PHYSICAL PROPERTIES CONFIGURATION.

Step 8: Choose some or all the available components in the separation system.

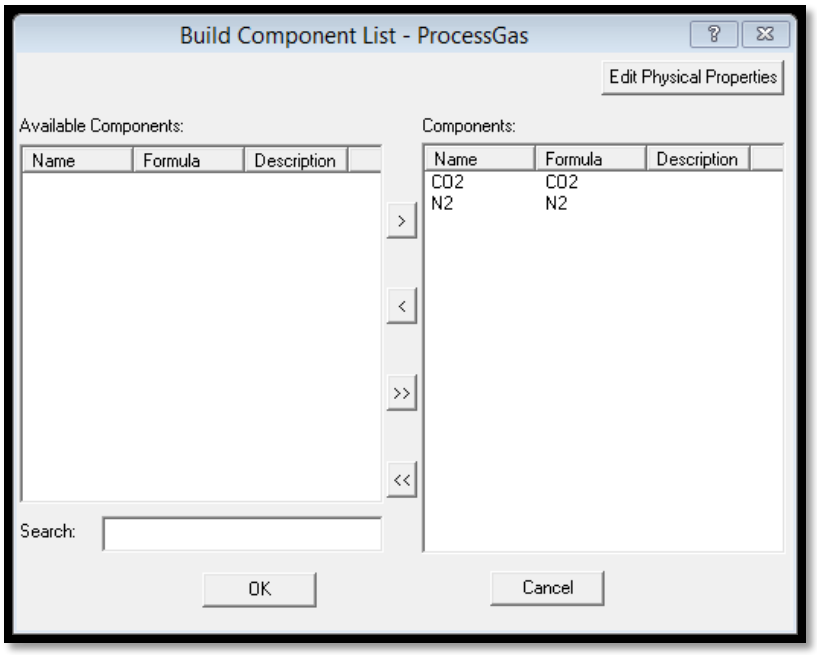

FIGURE 9.11. BUILD THE COMPONENT LIST IN THE TSA MODEL.

Step 9: Double-click the bed to edit the column configuration.

Figure 9.8 shows the specification of the column in the TSA model. It has only one vertical independent adsorbent layer within the bed. We choose 1-D as the spatial dimensions. There is no heat exchanger within the adsorbent layer.

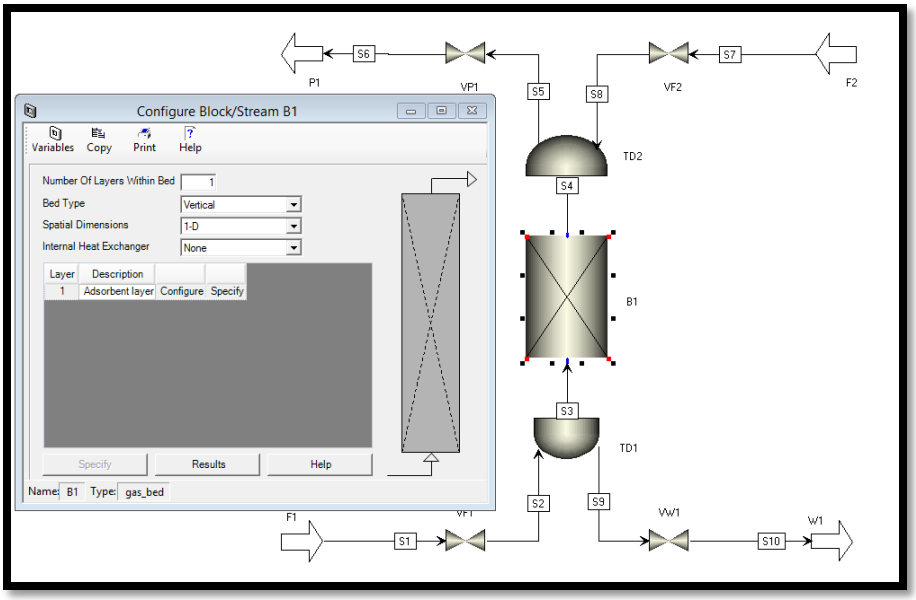

FIGURE 9.12. THE COLUMN CONFIGURATION SPECIFICATION IN THE TSA MODEL.

Step 10: General->Discretization method to be used.

We use the General tab in Figure 9.13 to specify the numerical options for solving the partial differential equations, and to select the gas model assumption.

The upwind Differencing Scheme 1 (UDS1) is the preferred option in most gas adsorption cases, because it saves the simulation time and the results are reasonably accurate. Therefore, we use the USD1 with 60 nodes in the General tab in Figure 9.13.

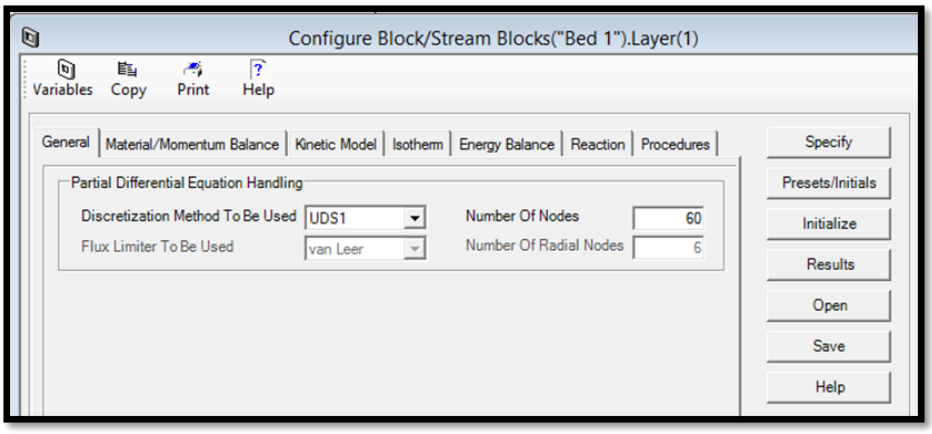

FIGURE 9.13. THE DISCRETIZATION METHOD IN THE TSA MODEL.

Step 11: Material/Momentum Balance->Assumptions.

We use the Material/Momentum Balance tab in Figure 9.14 to specify the material and momentum balances, and the dispersive properties. Like the PSA model, we choose convection only as the mass balance assumption. The Convection Only option drops the dispersion term from the material balance in eq. 9.1, so the model represents the plug flow with a zero dispersion coefficient.

We use the Momentum Balance Assumption box to specify how the adsorption bed layer model treats gas velocity and pressure. For the calculation of the pressure drops in the TSA system, we use Ergun equation, which is valid for both laminar and turbulent flows and is the most popular option. It combines the description of pressure drop by the Carman-Kozeny equation for laminar flow and the Burke-Plummer equation for turbulent flow, as shown in eq. 9.2.

$$\frac{\partial C_i}{\partial t} + \frac{(1-\varepsilon)}{\varepsilon}\frac{\partial q_i}{\partial t} + u\frac{\partial C_i}{\partial z} = D_L\frac{\partial^2 C_i}{\partial z^2} = 0 \quad \textbf{(9.1)}$$

$$\frac{\partial \mathrm{P}}{\partial \mathrm{z}} = -\left(\frac{1.5 * 10^{-3}\mu(1-\varepsilon)^2}{\left(2r_p\psi\right)^2\varepsilon^3}u + 1.75 * 10^{-5}\rho\frac{(1-\varepsilon)}{2r_p\psi\varepsilon^3}u^2\right) \quad \textbf{(9.2)}$$

In the equations, C_i is the concentration for component i in the gas phase, q_i is the concentration for component i in the solid phase, and ε represents the overall bed voidage, z is the axial distance through the column and D_L is the axial dispersion coefficient. P is the pressure drop within the column; u is the superficial velocity of the gas flow; μ = fluid viscosity; r_p = particle radius; ψ = particle shape factor.

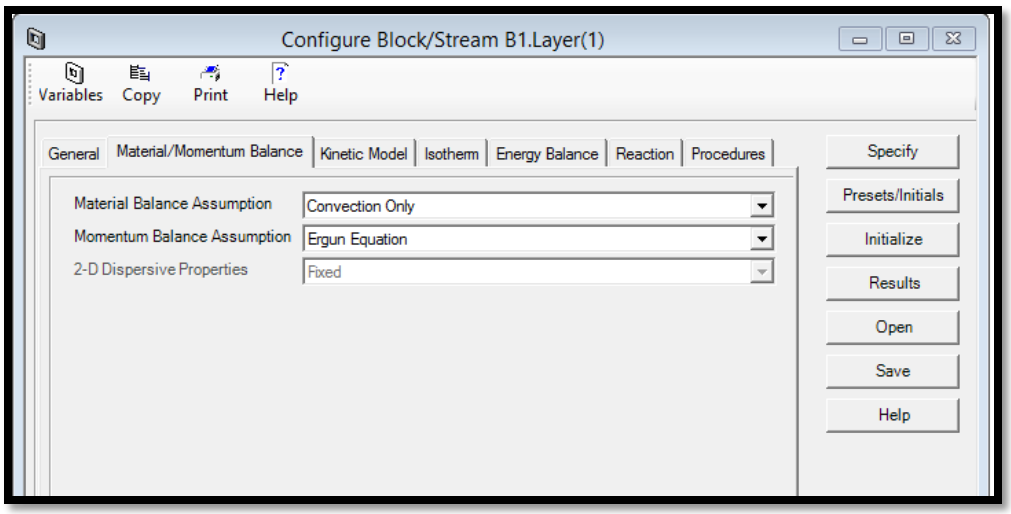

FIGURE 9.14. THE MATERIAL BALANCE ASSUMPTION IN THE TSA MODEL.

Step 12: Kinetic Model->Film Model Assumption and Mass Transfer Coefficients.

We use the Kinetic Model tab in Figure 9.15 to specify the model kinetics. In the Film Model Assumption box, we choose the solid form, where the mass transfer driving force is expressed as a function of the solid phase loading.

We consider the mass transfer resistance as a lumped and linear resistance in the Kinetic Model Assumption box. This method lumps the mass transfer resistance between the bulk gas phase and the gas-solid interface, and the mass transfer resistance due to the porous structure of the adsorbent, as a single overall factor. The mass transfer coefficient for each component is constant

throughout the bed. The mass transfer driving force for component i is a linear function of the solid-phase loading (solid film) as shown in eq. 9.3.

$$\frac{\partial q_i}{\partial t} = k_i(q_i^* - q_i) \tag{9.3}$$

where k_i is the linear lumped mass transfer coefficient, q_i is solute concentrations of the solid phase, and q_i^* represents the adsorbed phase concentration at equilibrium with the gas phase.

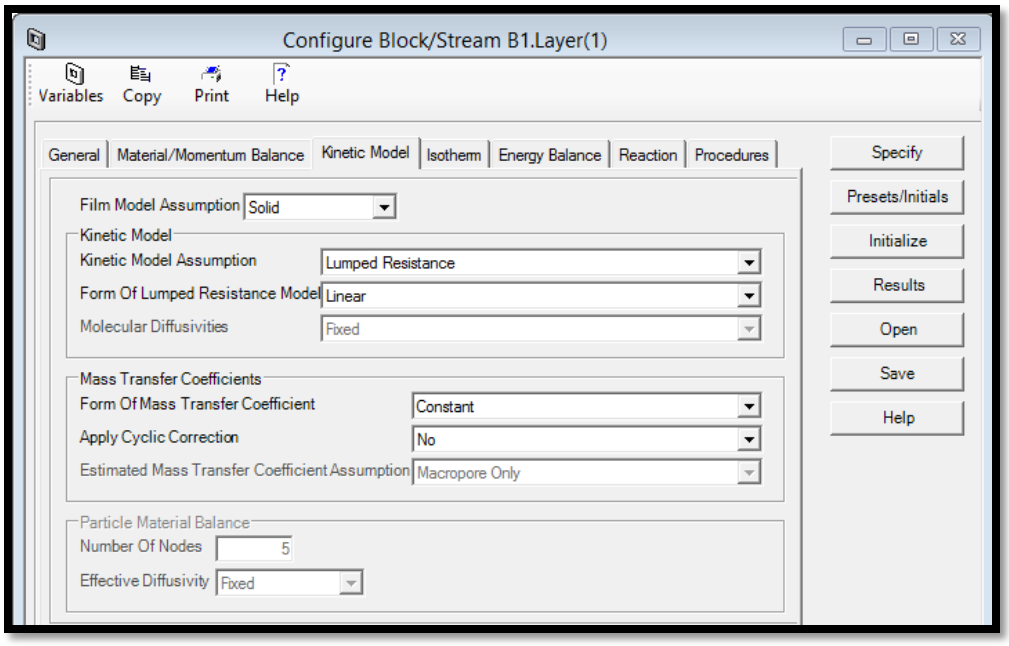

FIGURE 9.15. THE KINETIC METHOD IN THE TSA MODEL.

Step 13: Isotherm-> Langmuir Assumption.

We use the Isotherm tab in Figure 9.16 to define the adsorption isotherms in the TSA process. We use the Langmuir isotherm as the isotherm model, which is a function of partial pressure in the system. In this approach, we can predict mixture isotherms from pure component data. The Langmuir adsorption isotherm is:

$$q_i^* = \frac{q_{i,1} K_i P_i}{1 + \sum K_i P_i} \qquad (i = N_2, CO_2) \tag{9.4}$$

In the equation, q_i^* is the adsorbed phase concentration of component i in equilibrium with the mobile phase. $q_{i,1}$is the bi-Langmuir isotherm parameters for component i. $K_i$is the equilibrium constant for component I; $P_i$is the partial pressure for component i.

In Aspen Adsorption, the expression of the Langmuir isotherm is:

$$q_i^* = \frac{IP_{1i}P_i}{1 + \sum IP_{2i}P_i} \quad (i = N_2, CO_2) \tag{9.5}$$

Comparing eqs. 9.4 and 9.5[117], in conjunction with Table 9.2, we get:

$IP_{1,N2} = q_{N2,1}K_{N2} = 29.676 * 1.79e^{-5} = 0.00053;$

$IP_{1,CO2} = q_{CO2,1}K_{CO2} = 17.901 * 1.4e^{-8} = 2.506e^{-7};$

$IP_{2,N2} = K_{N2} = 1.79e^{-5};$

$IP_{2,CO2} = K_{CO2} = 1.4e^{-8}$

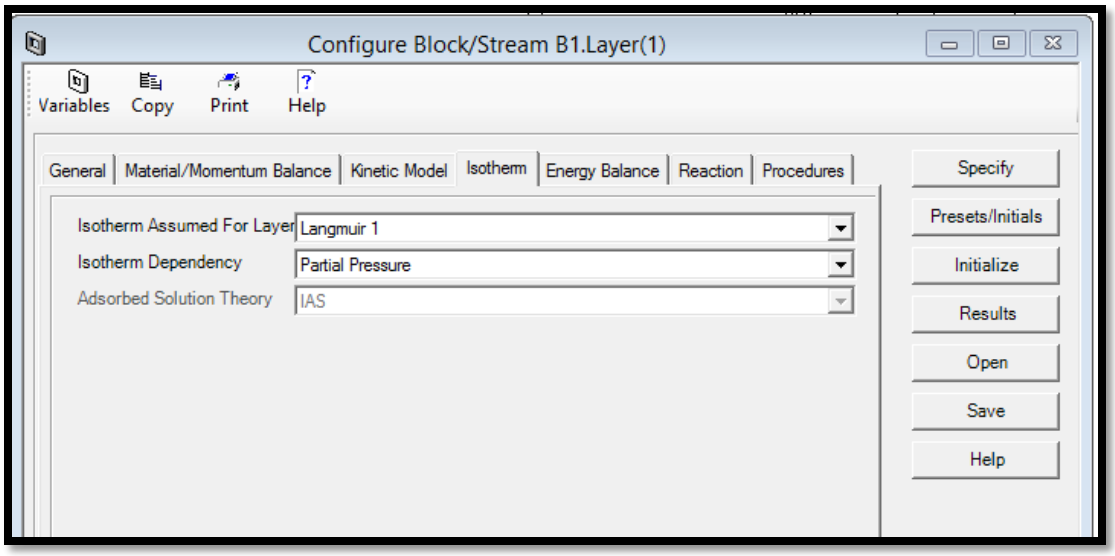

FIGURE 9.16. THE ISOTHERM METHOD IN THE TSA MODEL.

Step 14: Energy Balance->Non-Isothermal with No Conduction Assumption.

We use the Energy Balance tab in Figure 9.17 to specify how the energy balance is incorporated into the model for this gas adsorption process. We use the non-isothermal with no conduction as the energy assumption. The heat transfer to environment is adiabatic.

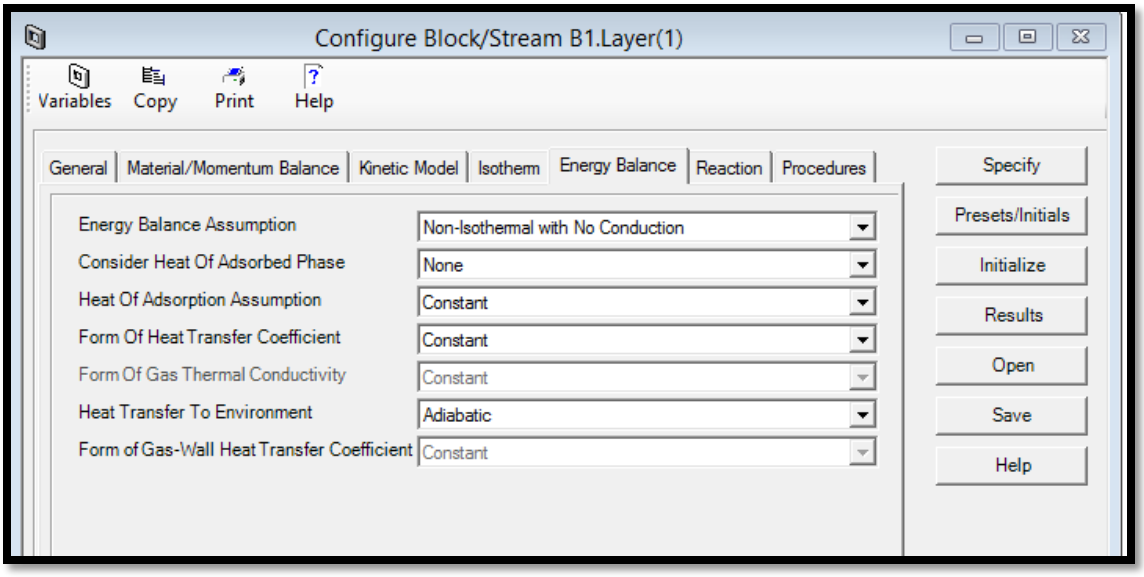

FIGURE 9.17. THE ENERGY METHOD IN THE TSA MODEL.

Step 15: Reaction->No reaction.

There is no reaction in this TSA system.

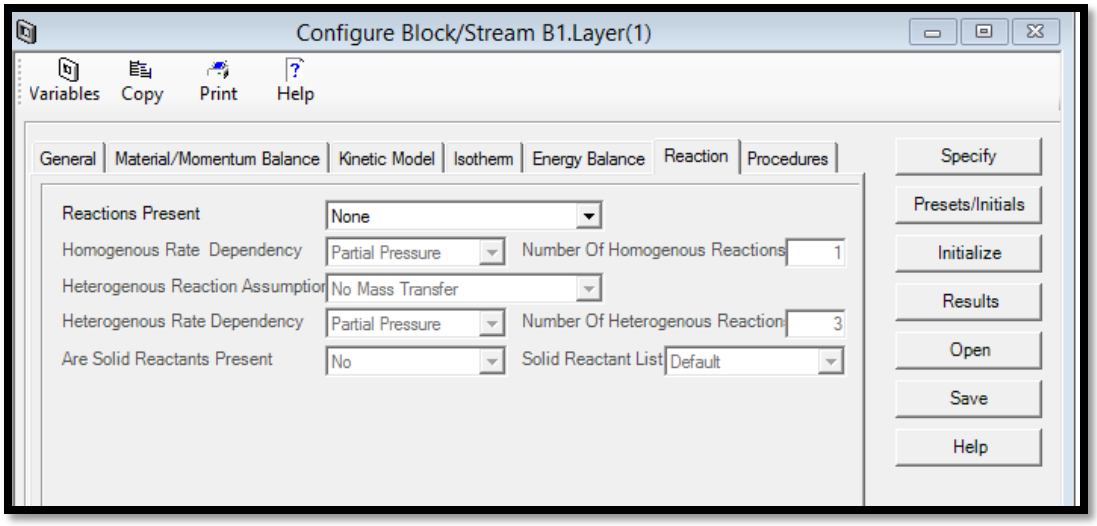

FIGURE 9.18. THE REACTION METHOD IN THE TSA MODEL.

Step 16: Procedures-> Available procedures in FORTRAN program.

We can use the Procedures tab in Figure 9.19 to view a list of user procedures, which automatically produced by Aspen Adsorption within the current adsorption layer model.

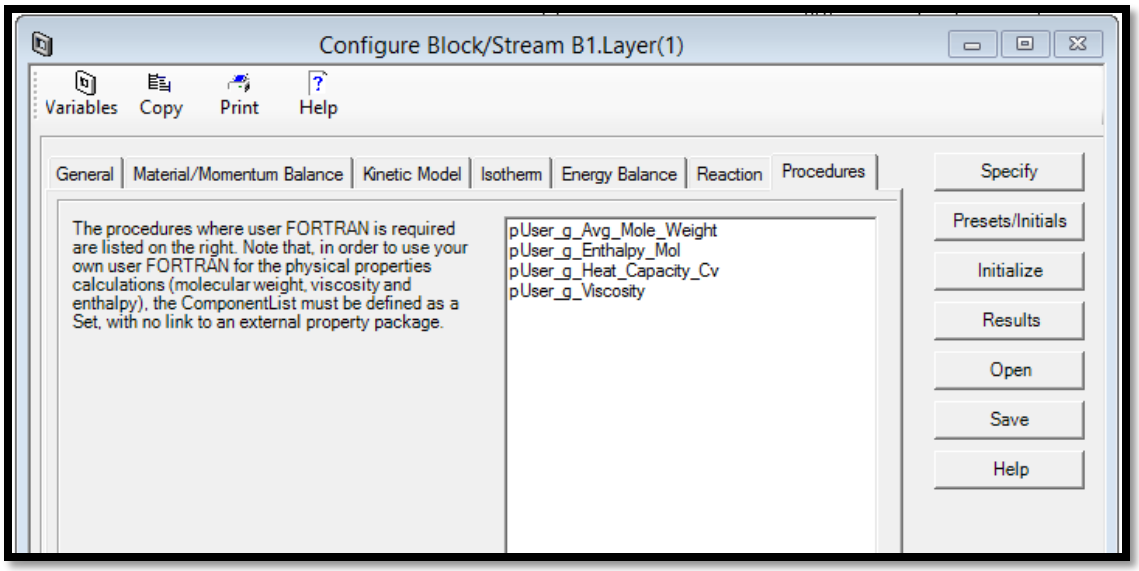

FIGURE 9.19. THE AVAILABLE PROCEDURES IN THE TSA MODEL.

Step 17: Specify->Input all the variable values for all the assumptions we made.

After defining all assumptions for the layer[116,117], we follow Table 9.1 to enter the required data for the layer Specify Form in Figure 9.20. Click the Specify button in the Configuration form to open the data table.

TABLE 9.1. THE SPECIFICATION OF THE ADSORBENT LAYER IN THE TSA MODEL.

Column (Adsorbent layer) Height (m)	1
Internal diameter of the column (m)	0.27
Inter-particle voidage (m^3 void/m^3 bed)	0.33
Intra-particle voidage (m^3 void/m^3 bead)	1.E-10
Solid density of the adsorbent (kg/m3)	630

Adsorbent particle radius (m)		0.0105
	Nitrogen (N_2)[117]	Carbon Dioxide (CO_2)[117]
Mass transfer coefficient (1/s)	0.5	0.11
Equilibrium constant K_i [bar^{-1}]	$1.79E^{-5}$	$1.4E^{-8}$
Saturation constant $q_{i,1}$ (mol/kg)	29.676	17.901
Heat of adsorption constant KJ/mol	-15.716	-54.729

B1.Layer(1).Specify Table

	Value	Units	Description
Hb	1.0	m	Height of adsorbent layer
Db	0.27	m	Internal diameter of adsorbent layer
Ei	0.33	m3 void/m3 bed	Inter-particle voidage
Ep	1.e-010	m3 void/m3 bead	Intra-particle voidage
RHOs	630.0	kg/m3	Bulk solid density of adsorbent
Rp	0.0105	m	Adsorbent particle radius
SFac	1.0	n/a	Adsorbent shape factor
MTC(*)			
MTC("CO2")	0.11	1/s	Constant mass transfer coefficients
MTC("N2")	0.5	1/s	Constant mass transfer coefficients
IP(*)			
IP(1,"CO2")	2.5e-007	n/a	Isotherm parameter
IP(1,"N2")	5.3e-004	n/a	Isotherm parameter
IP(2,"CO2")	1.4e-008	n/a	Isotherm parameter
IP(2,"N2")	1.79e-005	n/a	Isotherm parameter
Direction	0.0	n/a	Specified flow direction (self determined: 0, forward: 1)
Cps	1.e-003	MJ/kg/K	Adsorbent specific heat capacity
DH(*)			
DH("CO2")	-54.729	MJ/kmol	Constant for heat of adsorption
DH("N2")	-15.716	MJ/kmol	Constant for heat of adsorption
HTC	1.0	MW/m2/K	Constant for the heat transfer coefficient
ap	191.429	1/m	Specific surface area of adsorbent

FIGURE 9.20. THE SPECIFY FORM OF THE ADSORBENT LAYER IN THE TSA MODEL.

Step 18: Presets/Initials-> initialization form of the adsorbent layer.

Input all the initial values in Figure 9.21 for the model, and then press the "Initial" button. The mole fraction within first element for nitrogen is 0.87, for carbon dioxide is 0.13. The temperature for both gas and solid phases is 15 °C.

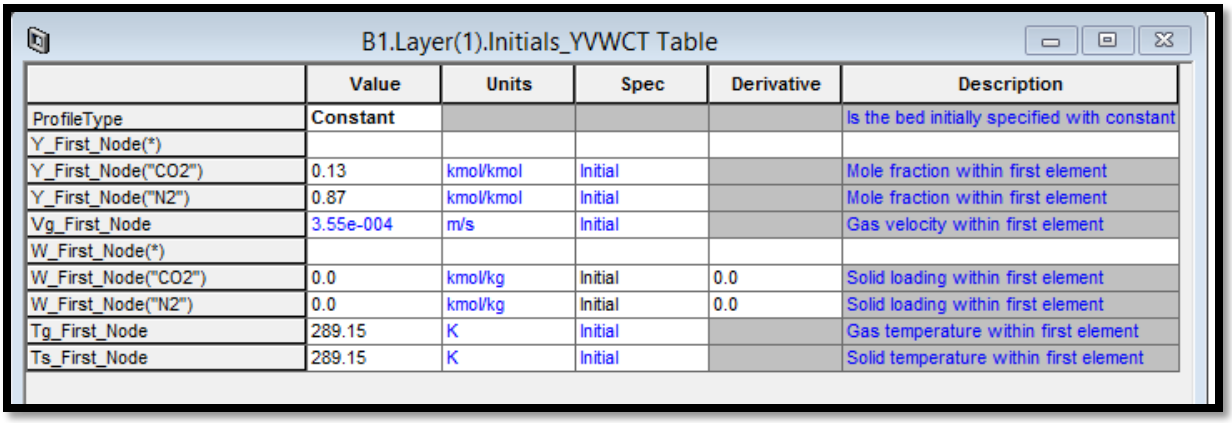

B1.Layer(1).Initials_YVWCT Table

	Value	Units	Spec	Derivative	Description
ProfileType	Constant				Is the bed initially specified with constant
Y_First_Node(*)					
Y_First_Node("CO2")	0.13	kmol/kmol	Initial		Mole fraction within first element
Y_First_Node("N2")	0.87	kmol/kmol	Initial		Mole fraction within first element
Vg_First_Node	3.55e-004	m/s	Initial		Gas velocity within first element
W_First_Node(*)					
W_First_Node("CO2")	0.0	kmol/kg	Initial	0.0	Solid loading within first element
W_First_Node("N2")	0.0	kmol/kg	Initial	0.0	Solid loading within first element
Tg_First_Node	289.15	K	Initial		Gas temperature within first element
Ts_First_Node	289.15	K	Initial		Solid temperature within first element

FIGURE 9.21. THE INITIALIZATION FORM OF THE ADSORBENT LAYER IN THE TSA MODEL.

Step 19: F1 block->Feed Specification.

In this TSA model, we set the cold feed-in flow rate in the "F1" block as free, because we control the feed flow in the Cycle Organizer through the VF1 valve. The feed composition is fixed with nitrogen mole fraction nitrogen of 0.87 and carbon dioxide mole fraction of 0.13. The temperature and pressure in the feed are both fixed, with 25 °C and 10 bar, respectively.

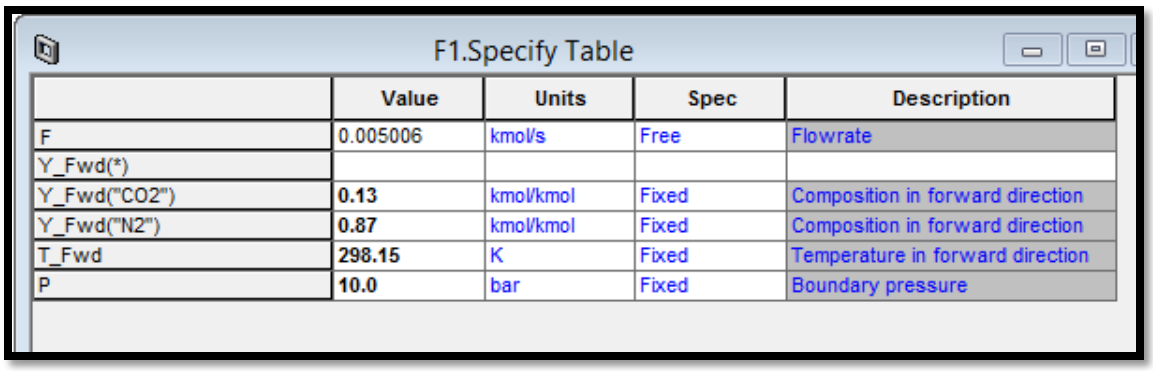

F1.Specify Table

	Value	Units	Spec	Description
F	0.005006	kmol/s	Free	Flowrate
Y_Fwd(*)				
Y_Fwd("CO2")	**0.13**	kmol/kmol	Fixed	Composition in forward direction
Y_Fwd("N2")	**0.87**	kmol/kmol	Fixed	Composition in forward direction
T_Fwd	**298.15**	K	Fixed	Temperature in forward direction
P	**10.0**	bar	Fixed	Boundary pressure

FIGURE 9.22. THE COLD FEED SPECIFICATION IN THE TSA MODEL.

Step 20: P1 block-> Product Specification.

In the "P1" block, we set the flow rate as free, and control it in the Cycle Organizer through the VP1 valve. The reversed direction of the composition is fixed with nitrogen mole fraction of 1.0. The reversed direction of the temperature is still fixed with 25 °C, and the pressure in the P1 block is fixed with 9.993 bar.

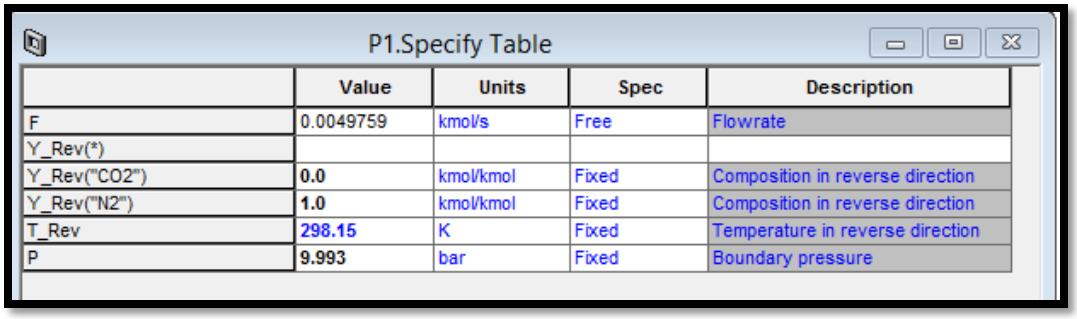

P1.Specify Table

	Value	Units	Spec	Description
F	0.0049759	kmol/s	Free	Flowrate
Y_Rev(*)				
Y_Rev("CO2")	0.0	kmol/kmol	Fixed	Composition in reverse direction
Y_Rev("N2")	1.0	kmol/kmol	Fixed	Composition in reverse direction
T_Rev	298.15	K	Fixed	Temperature in reverse direction
P	9.993	bar	Fixed	Boundary pressure

FIGURE 9.23. THE LIGHT PRODUCT SPECIFICATION IN THE TSA MODEL.

Step 21: F2 block->Hot feed Specification.

In this PSA model, we set the hot feed-in flow rate in the "F2" block as free, because we control the feed flow in the Cycle Organizer through the VF2 valve. The feed composition is fixed with nitrogen mole fraction of 1.0, and with 140 °C temperature and 1.2 bar pressure.

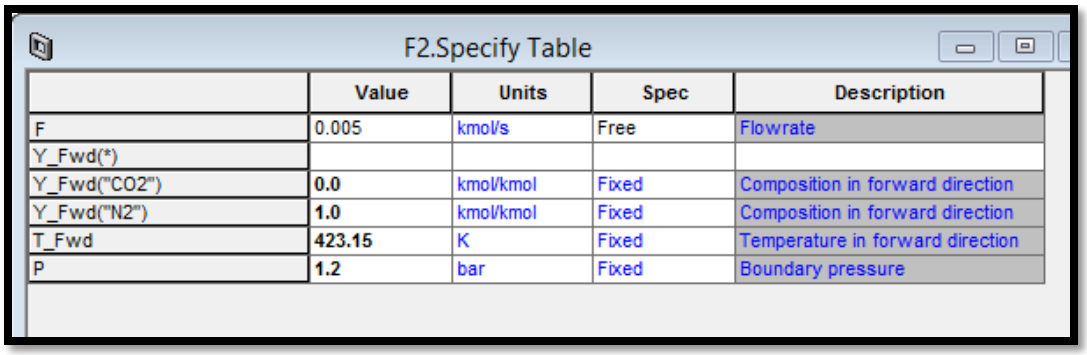

F2.Specify Table

	Value	Units	Spec	Description
F	0.005	kmol/s	Free	Flowrate
Y_Fwd(*)				
Y_Fwd("CO2")	0.0	kmol/kmol	Fixed	Composition in forward direction
Y_Fwd("N2")	1.0	kmol/kmol	Fixed	Composition in forward direction
T_Fwd	423.15	K	Fixed	Temperature in forward direction
P	1.2	bar	Fixed	Boundary pressure

FIGURE 9.24. THE HOT FEED SPECIFICATION IN THE TSA MODEL.

Step 22: W1 block-> waste Specification.

In the "W1" block, we also set the flow rate as free, and control it in the Cycle Organizer through the VW1 valve. The reversed direction of the composition is fixed with nitrogen mole fraction of 1, and with 25 °C and 1.013 bar.

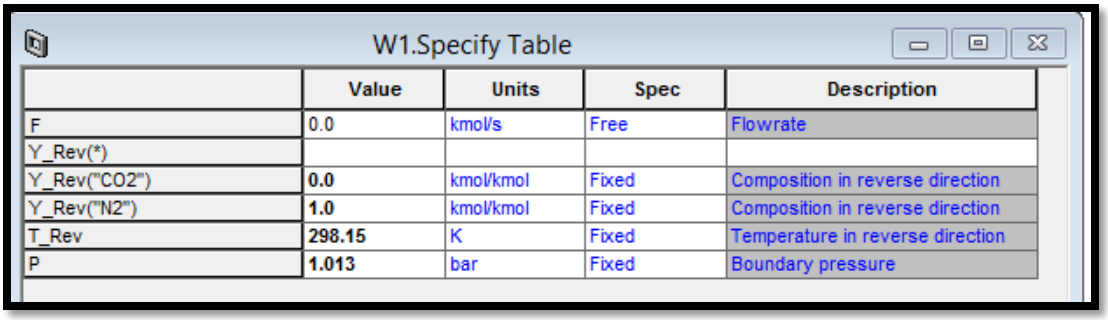

W1.Specify Table

	Value	Units	Spec	Description
F	0.0	kmol/s	Free	Flowrate
Y_Rev(*)				
Y_Rev("CO2")	0.0	kmol/kmol	Fixed	Composition in reverse direction
Y_Rev("N2")	1.0	kmol/kmol	Fixed	Composition in reverse direction
T_Rev	298.15	K	Fixed	Temperature in reverse direction
P	1.013	bar	Fixed	Boundary pressure

FIGURE 9.25. THE HEAVY PRODUCT SPECIFICATION IN THE TSA MODEL.

Step 23: TD1 Tank block-> Specification.

We set the total volume of this bottom tank TD1 as 250 cm^3.

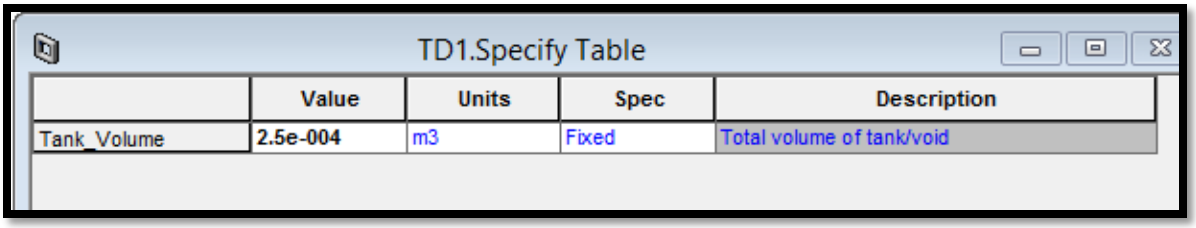

	Value	Units	Spec	Description
Tank_Volume	2.5e-004	m3	Fixed	Total volume of tank/void

FIGURE 9.26. THE TD1 TANK VOLUME IN THE TSA MODEL.

Step 24: TD1 Tank block-> Presets/Initials.

We set the initial mole fractions of nitrogen and carbon dioxide the same as the cold feed, as shown in Figure 9.27. The initial temperature of this TD1 tank is still 25 °C, and we set the initial pressure as 9.9999 bar. This initial pressure is a randomly set value, as long as it is a little bit lower than the feed in pressure.

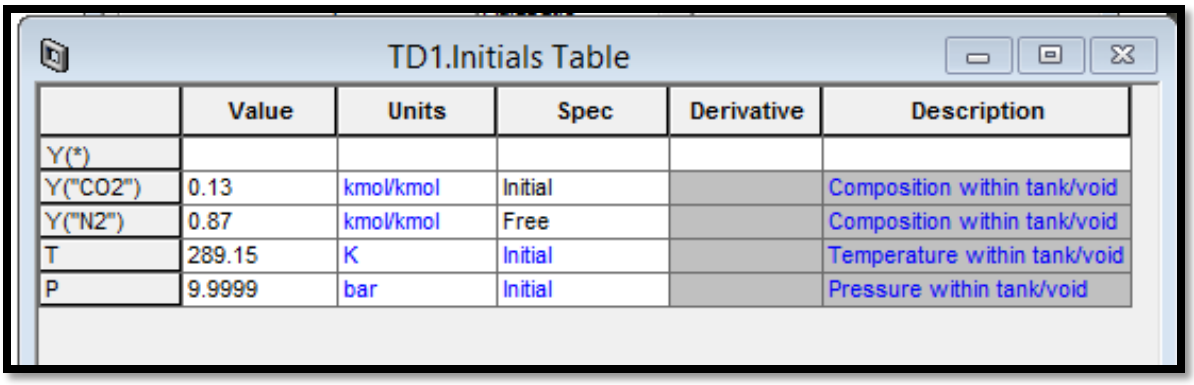

	Value	Units	Spec	Derivative	Description
Y(*)					
Y("CO2")	0.13	kmol/kmol	Initial		Composition within tank/void
Y("N2")	0.87	kmol/kmol	Free		Composition within tank/void
T	289.15	K	Initial		Temperature within tank/void
P	9.9999	bar	Initial		Pressure within tank/void

FIGURE 9.27. THE TD1 TANK INITIAL CONDITIONS IN THE TSA MODEL.

Step 25: TD2 Tank block-> Specification.

We set the total volume of this top tank TD2 as 250 cm^3.

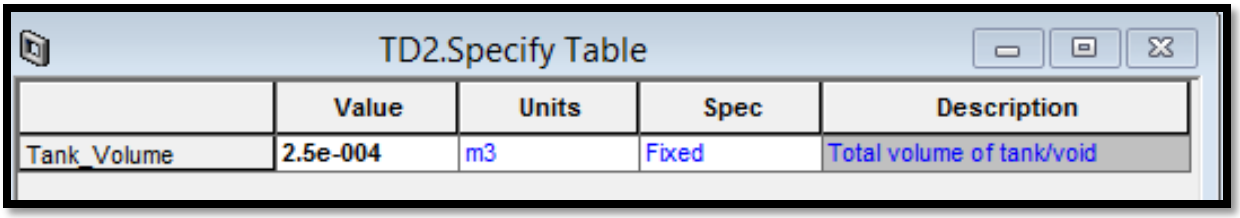

	Value	Units	Spec	Description
Tank_Volume	2.5e-004	m3	Fixed	Total volume of tank/void

FIGURE 9.28. THE TD2 TANK VOLUME IN THE TSA MODEL.

Step 26: TD2 Tank block-> Presets/Initials.

We set the initial mole fractions of nitrogen and carbon dioxide the same as the cold feed, as shown in Figure 9.29. The initial temperature of this TD1 tank is still 25 °C, and we set the initial pressure as 9.9964 bar, which is a little bit lower than the TD1 pressure (9.9999 bar).

TD2.Initials Table

	Value	Units	Spec	Derivative	Description
Y(*)					
Y("CO2")	0.13	kmol/kmol	Initial		Composition within tank/void
Y("N2")	0.87	kmol/kmol	Free		Composition within tank/void
T	289.15	K	Initial		Temperature within tank/void
P	9.9964	bar	Initial		Pressure within tank/void

FIGURE 9.29. THE TD2 TANK INITIAL CONDITIONS IN THE TSA MODEL.

Step 27: Tool-> Cycle Organizer.

This workshop involves a single-bed TSA Process with five steps, including adsorption, depressurization, heat, cool and repressurization.

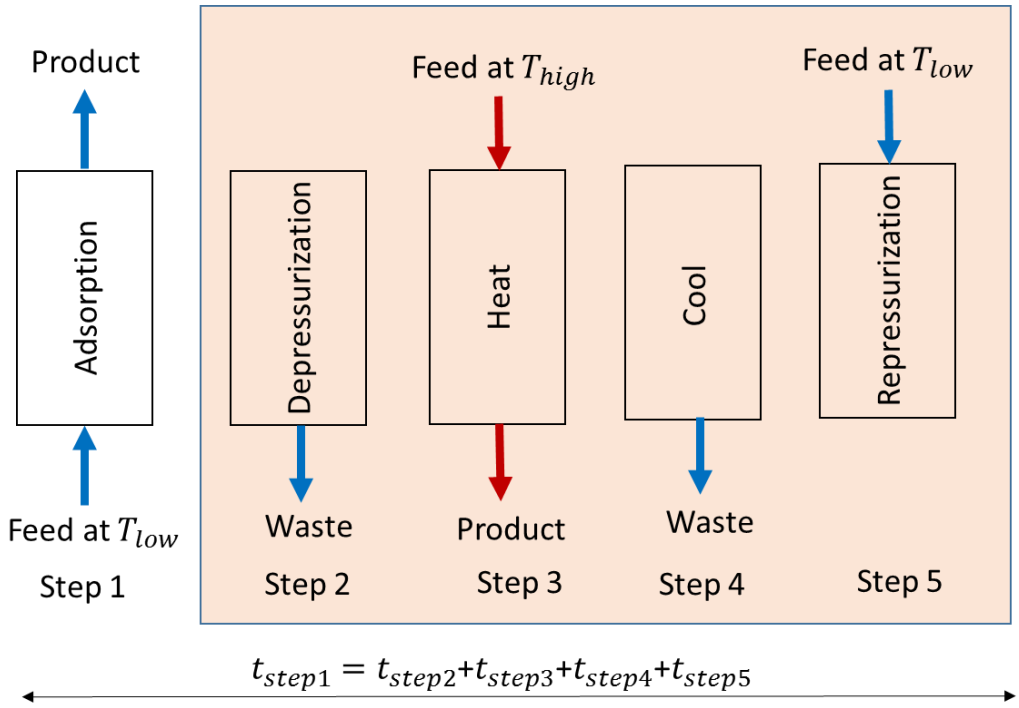

FIGURE 9.30. THE STEP CHART OF A SINGLE BED TSA PROCESS WITH FIVE STEPS.

Figure 9.30 illustrates the steps in a typical TSA process:

(1) Adsorption: The flue gas at low temperature is passed through the bed, where the CO_2 is adsorbed by the molecular sieve 5A. The exit stream is the product with significantly less CO_2.
(2) Depressurization: We only open the waste stream to reduce the column pressure.
(3) Heat: We heat the CO2 loaded bed to a critical temperature at which the captured CO2 is desorbed/released as a high purity stream of CO2, which is subsequently compressed for transportation and storage.
(4) Cool: We stop inputting the hot feed, and only open the waste stream to cool down the TSA bed.
(5) Repressurization: We use the feed at low temperature to re-pressurize the bed for the preparation of the adsorption step.

Figure 9.31 displays how to generate a Cycle Organizer in Aspen Adsorption, it is very similar as we did in Aspen Chromatography. To access the Cycle Organizer, we click the Cycle Organizer from the Tools menu. Once a Cycle Organizer block is present on the flowsheet, we can open it either using the Tools menu, or by double-clicking on the flowsheet block.

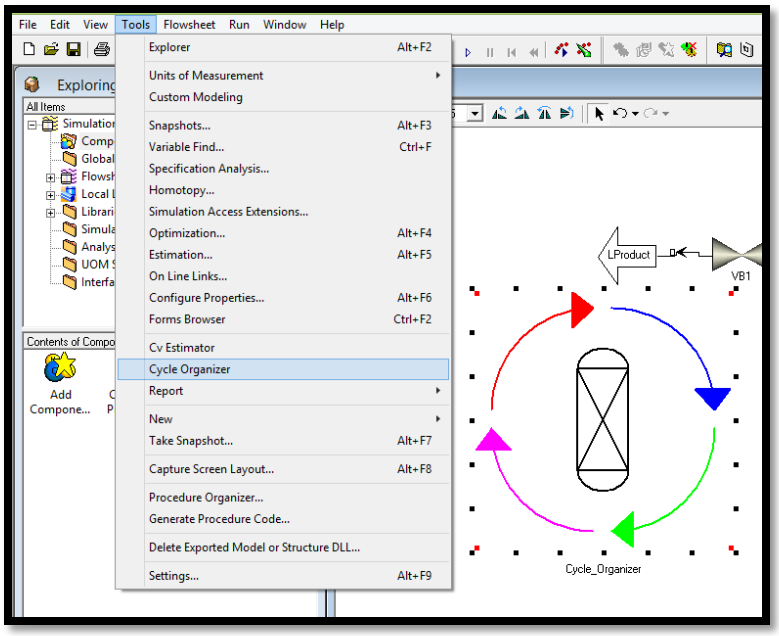

FIGURE 9.31. THE GENERATION OF A CYCLE ORGANIZER IN THE TSA MODEL.

Step 28: Cycle Organizer-> Cycle Options.

Figure 9.32 displays the cycle settings for the process in the PSA model. We set the maximum cycle numbers as 100.

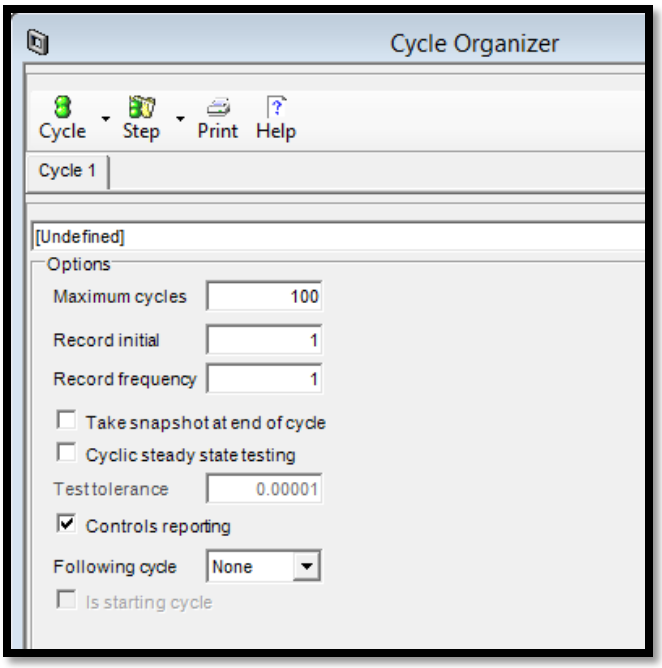

FIGURE 9.32. THE CYCLE OPTIONS OF THE CYCLE ORGANIZER IN THE TSA MODEL.

Step 29: Cycle Organizer-> Step time settings in the TSA cycle.

Table 9.1 lists the step time for each step in the TSA cycle[116]. We make sure that the time of adsorption step equals to the sum of the times for steps 2 to 4. Then, we set the step time for each step in the following steps 30 to 34.

TABLE 9.2. TIME FOR EACH STEP IN THE TSA CYCLE.

Step 1: Adsorption	49 min
Step 2: Depressurization	1 min
Step 3: Heat	16 min
Step 4: Cool	31 min
Step 5: Repressurization	1 min

Step 30: Cycle Organizer-> Step Control->Step 1: Adsorption.

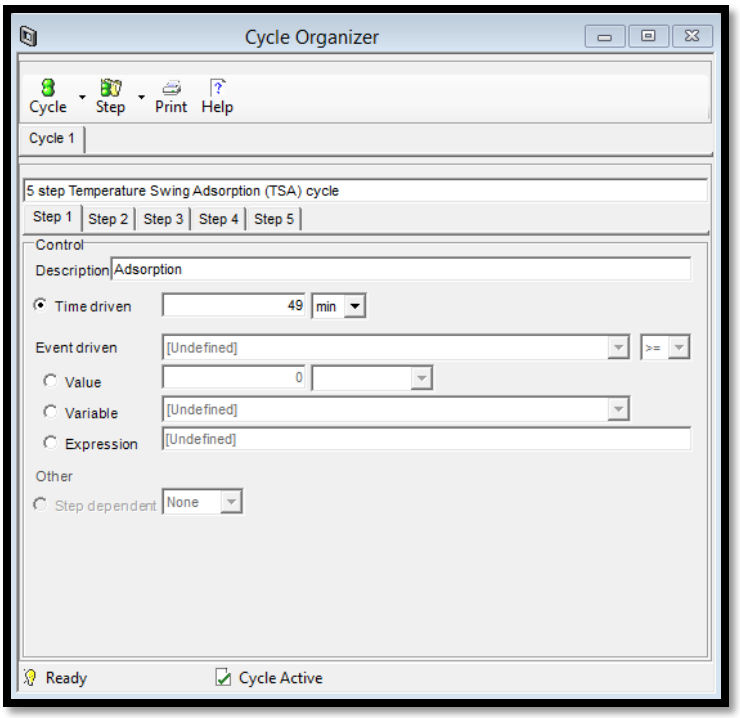

FIGURE 9.33. THE ADSORPTION STEP TIME IN CYCLE ORGANIZER IN THE TSA MODEL.

Step 31: Cycle Organizer-> Step Control->Step 2: Depressurize.

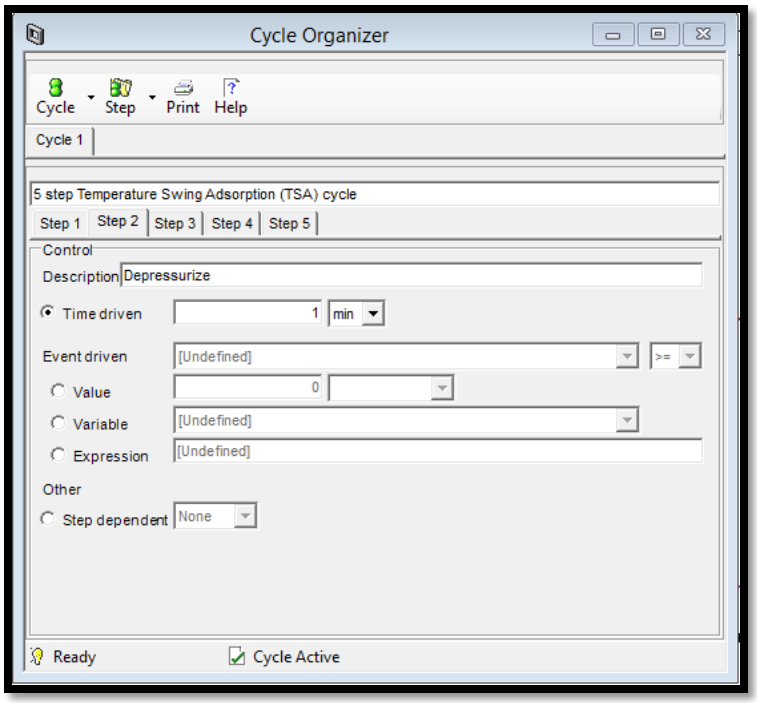

FIGURE 9.34. THE DEPRESSURIZATION STEP TIME IN CYCLE ORGANIZER IN THE TSA MODEL.

Step 32: Cycle Organizer-> Step Control->Step 3: Heat.

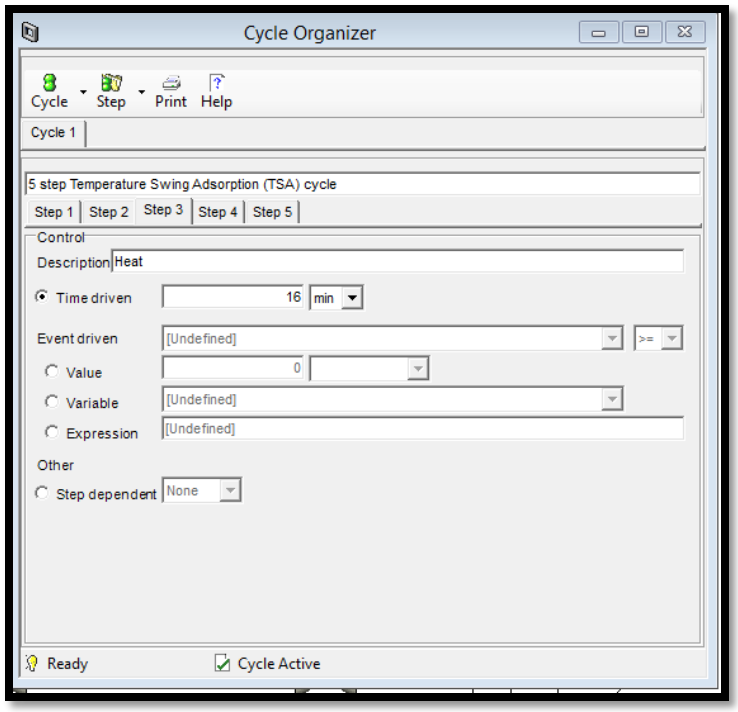

FIGURE 9.35. THE HEAT STEP TIME IN CYCLE ORGANIZER IN THE TSA MODEL.

Step 33: Cycle Organizer-> Step Control->Step 4: Cool.

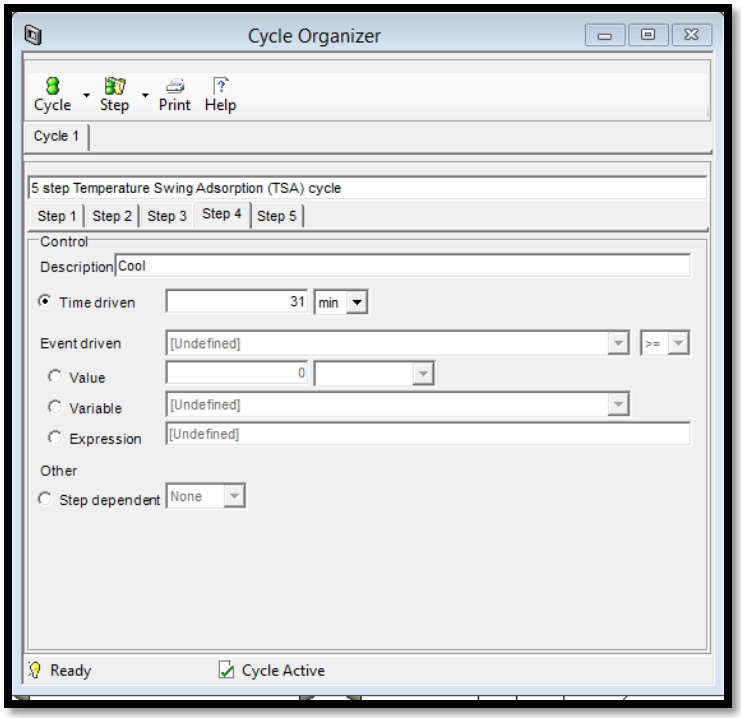

FIGURE 9.36. THE COOL STEP TIME IN CYCLE ORGANIZER IN THE TSA MODEL.

Step 34: Cycle Organizer-> Step Control->Step 5: Repressurization.

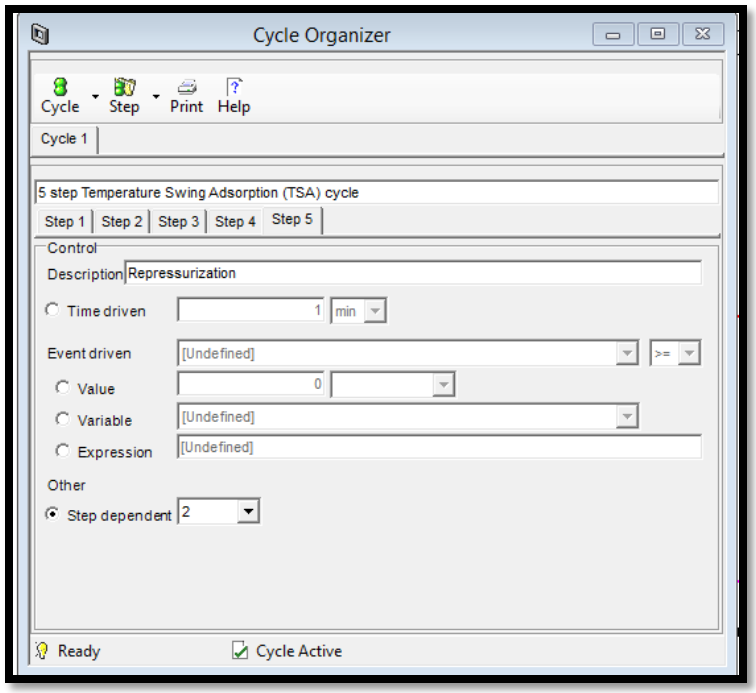

FIGURE 9.37. THE REPRESSURIZATION STEP TIME IN CYCLE ORGANIZER IN THE TSA MODEL.

Step 35: Cycle Organizer-> Step Manipulated->Step 1: Adsorption.

The following table shows the valve on/off conditions and the flow rates for inlet and outlet streams in the TSA model.

	Gas flow rate in each stream mol/s			
	Cold Feed	Hot Feed	Light product	Heavy product
Step 1	5	off	14.63	off
Step 2	off	off	off	0.1
Step 3	off	88.8	7.2e-7	off
Step 4	off	off	off	0.055
Step 5	off	0.6 (cold)	off	off

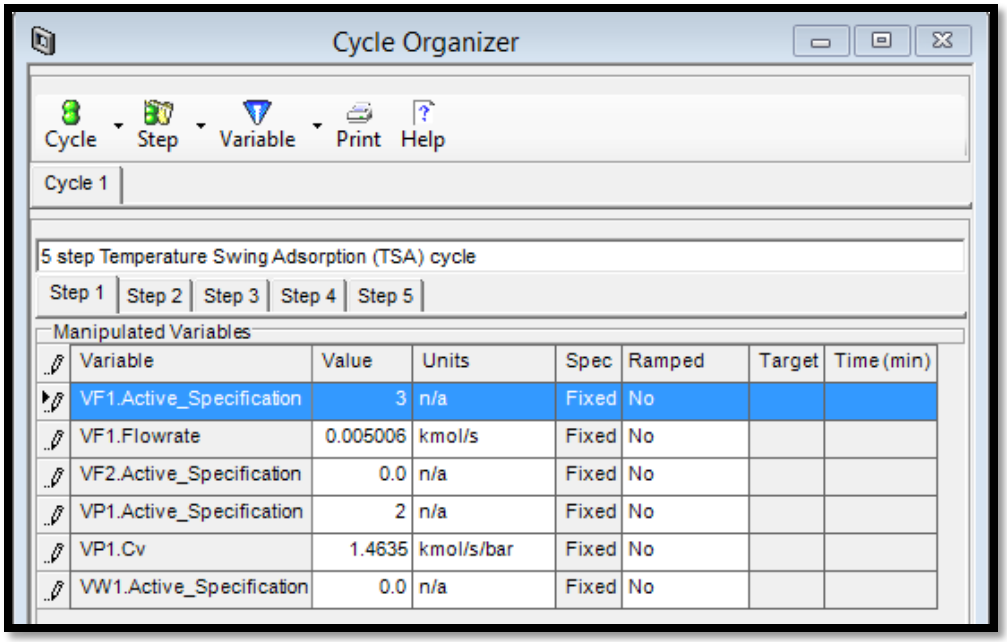

FIGURE 9.38. THE ADSORPTION STEP CONDITIONS IN CYCLE ORGANIZER IN THE TSA MODEL.

Step 36: Cycle Organizer-> Step Manipulated ->Step 2: Depressurize.

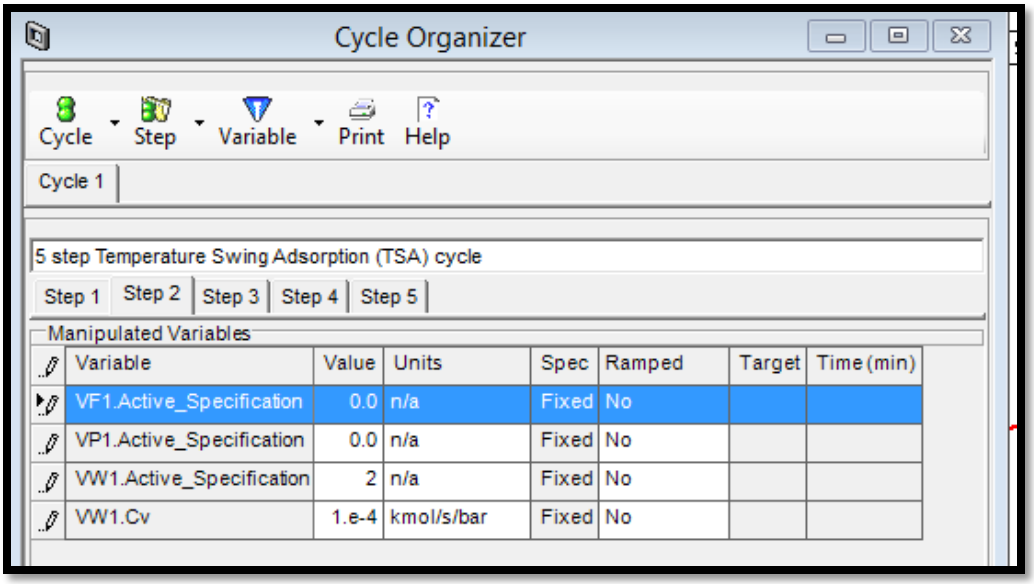

FIGURE 9.39. THE DEPRESSURIZATION STEP CONDITIONS IN CYCLE ORGANIZER IN THE TSA MODEL.

Step 37: Cycle Organizer-> Step Manipulated ->Step 3: Heat.

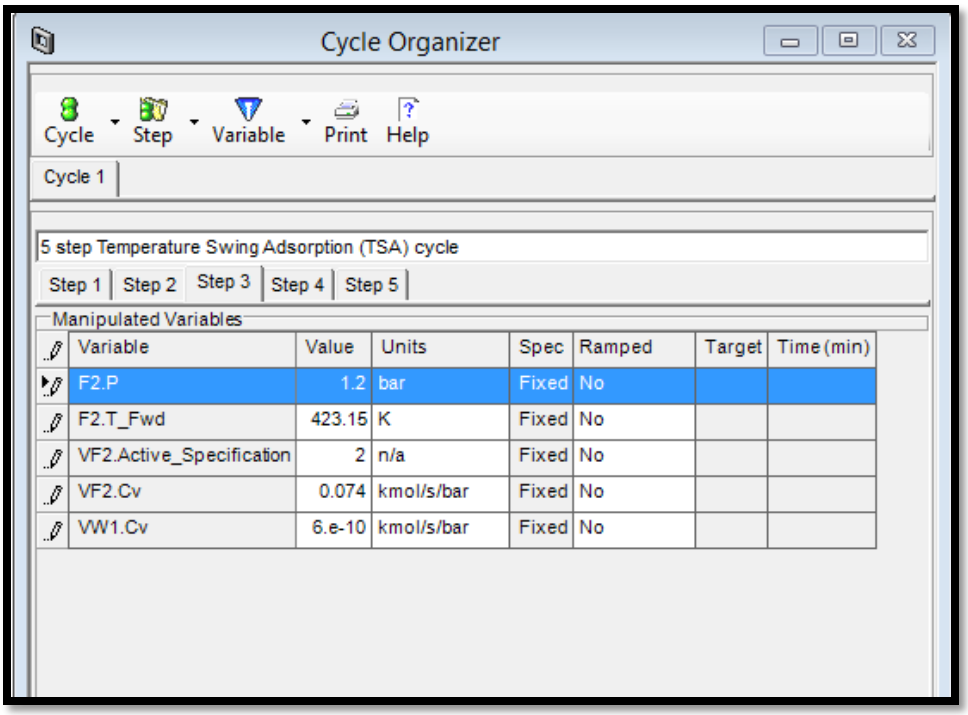

FIGURE 9.40. THE HEAT STEP CONDITIONS IN CYCLE ORGANIZER IN THE TSA MODEL.

Step 38: Cycle Organizer-> Step Manipulated ->Step 4: Cool.

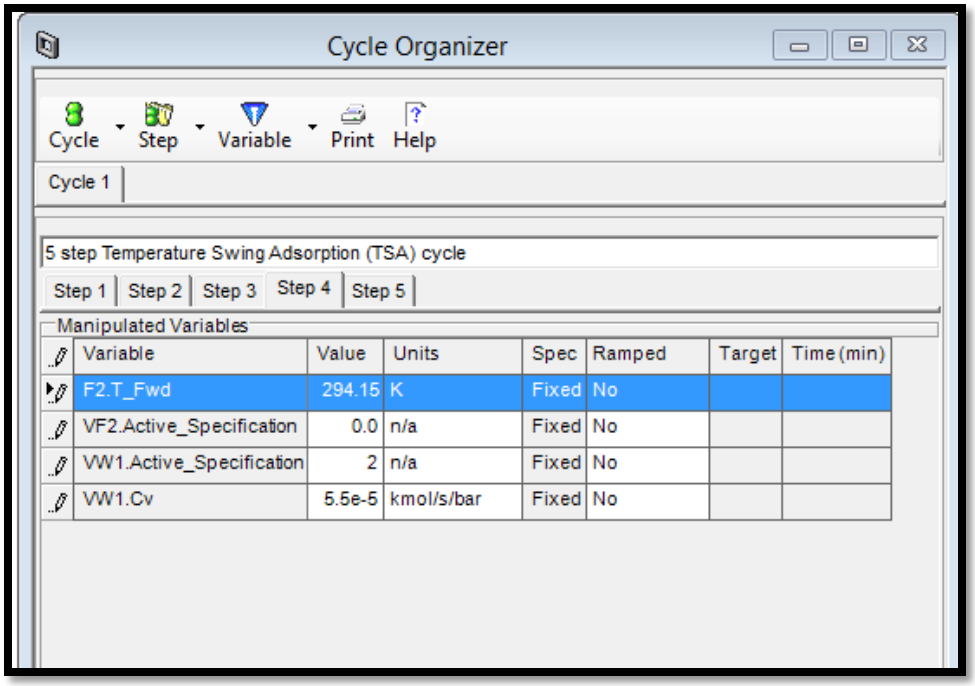

FIGURE 9.41. THE COOL STEP CONDITIONS IN CYCLE ORGANIZER IN THE TSA MODEL.

Step 39: Cycle Organizer-> Step Manipulated ->Step 5: Repressurization.

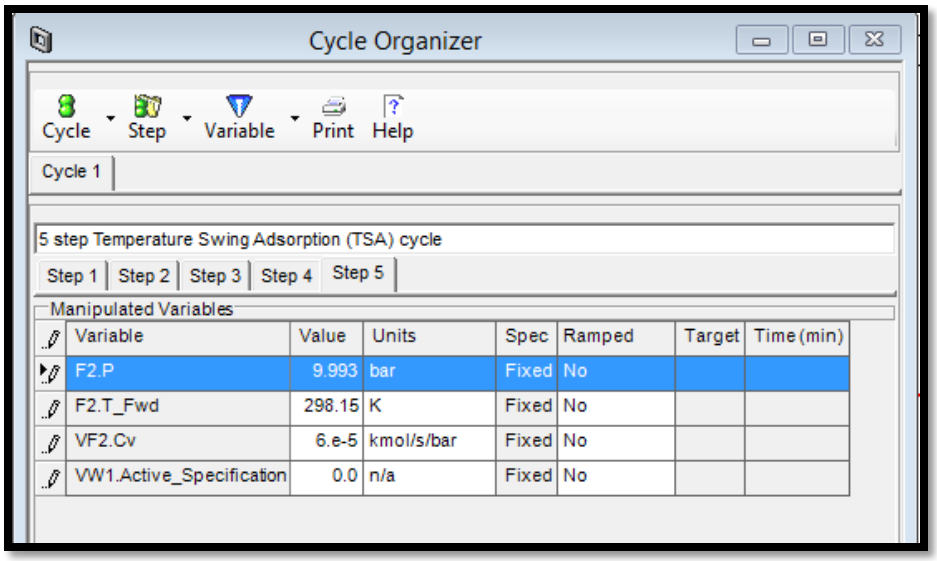

FIGURE 9.42. THE REPRESSURIZATION STEP CONDITIONS IN CYCLE ORGANIZER IN THE TSA MODEL.

Step 40: Run Options->Pause at 162600 seconds. We set the model run 10 cycles, then the simulation time would be (10*5880) = 58800 seconds.

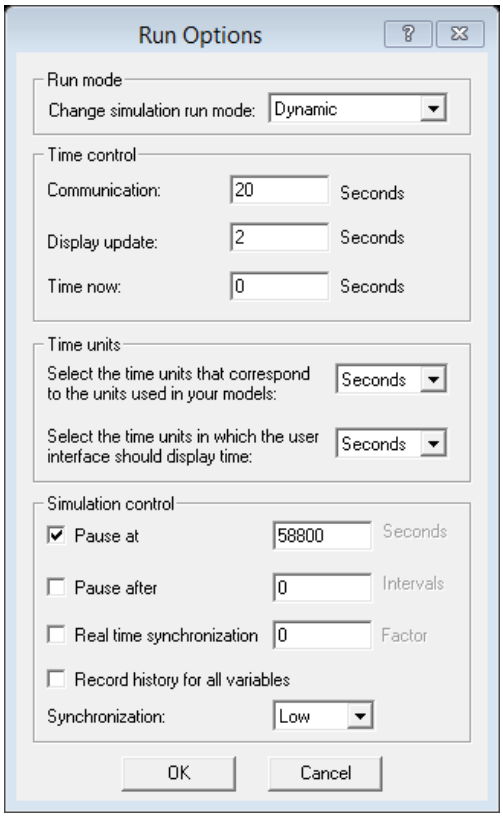

FIGURE 9.43. THE SIMULATION TIME SETTINGS IN THE TSA MODEL.

Step 41: Solver Options->Integrator.

We integrate the resulting ordinary differential equations using Gear method with a variable time step size (01 min initial step size, 0.1 to 0.5 min step size range and 0.5 step reduction factor) and the integration error tolerance set to the value of $5 * 10^{-4}$ in Aspen Adsorption, as shown in Figure 9.44.

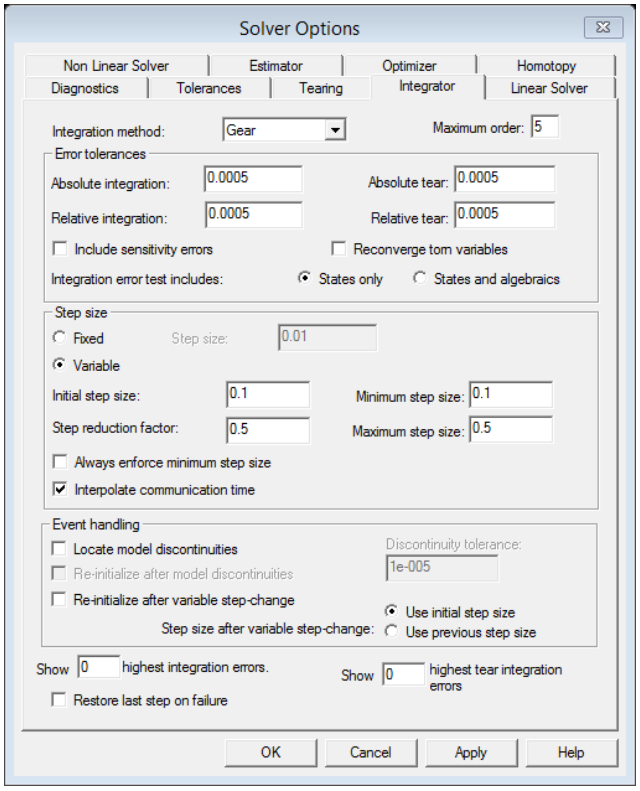

FIGURE 9.44. THE SOLVER OPTION SETTINGS IN THE TSA MODEL.

Step 42: Solver Options->Tolerance.

The Tolerances tab in Figure 9.45 enables us to change the options for controlling the absolute and relative variable tolerances.

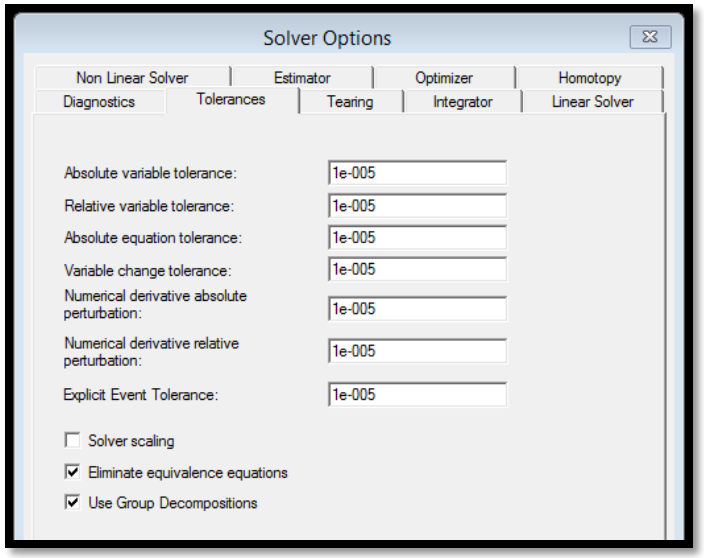

FIGURE 9.45. THE TOLERANCE SETTINGS IN THE TSA MODEL.

Step 43: Solver Options->Non Linear Solver.

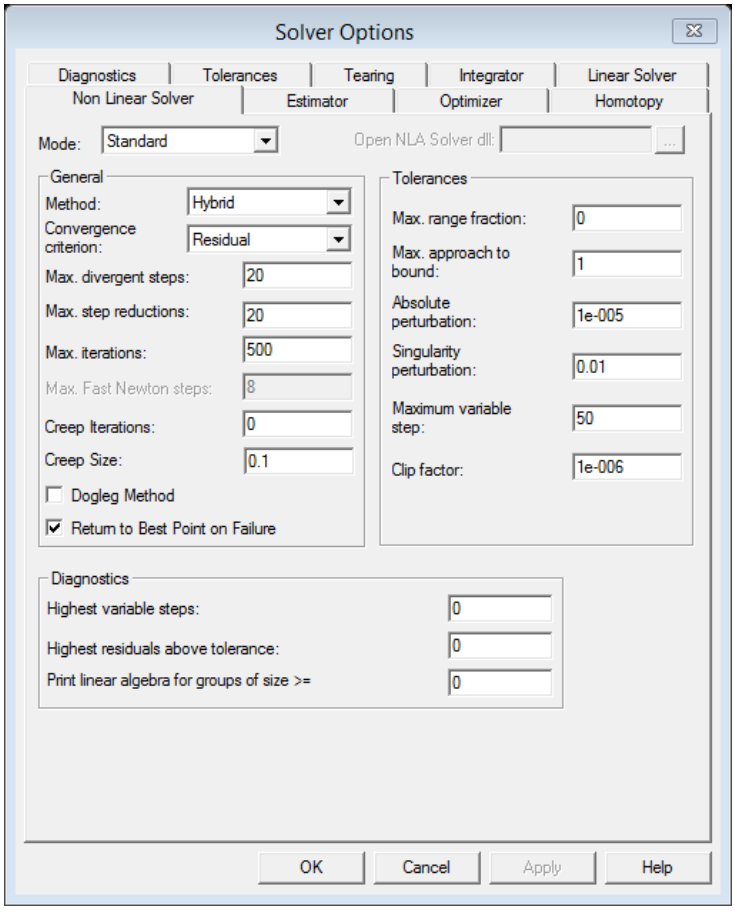

FIGURE 9.46. THE NON-LINEAR SOLVER SETTINGS IN THE TSA MODEL.

Step 44: Add Form-> Plot->Temperature.

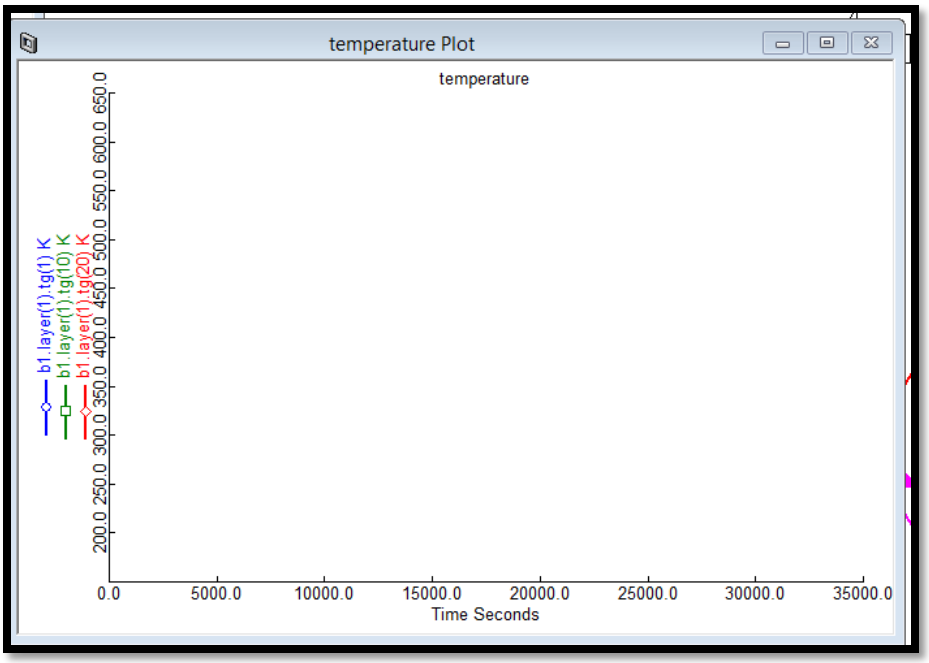

FIGURE 9.47. THE BED TEMPERATURE PLOT OVER TIME IN THE TSA MODEL.

Step 45: Add Form-> Plot->Product Composition.

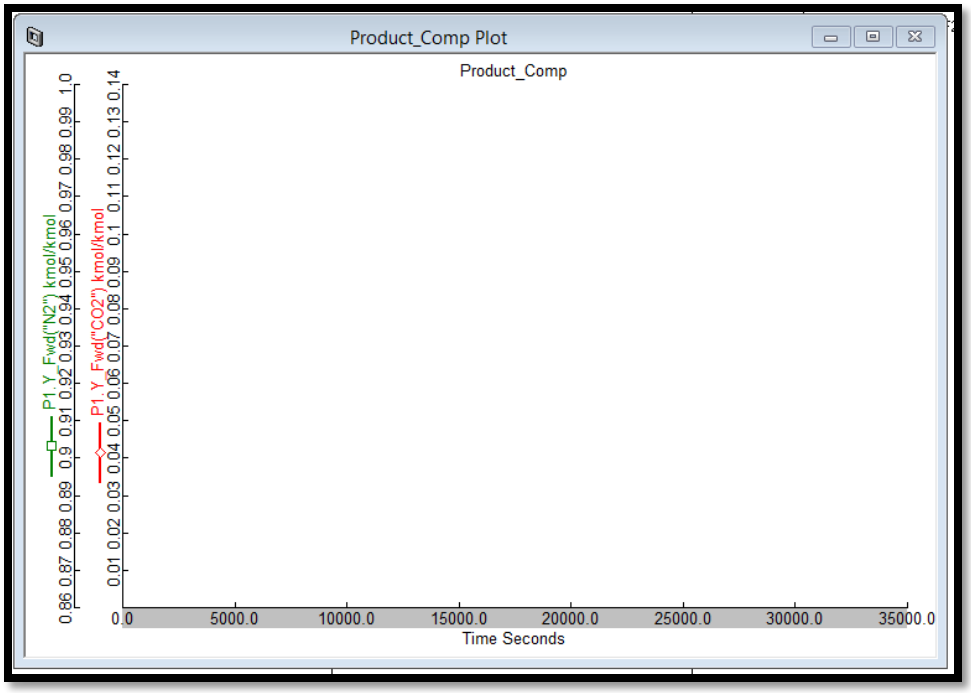

FIGURE 9.48. THE COMPOSITION PLOT IN THE LIGHT PRODUCT STREAM OVER TIME IN THE TSA MODEL.

Step 46: Add Form-> Plot-> Composition in the Column.

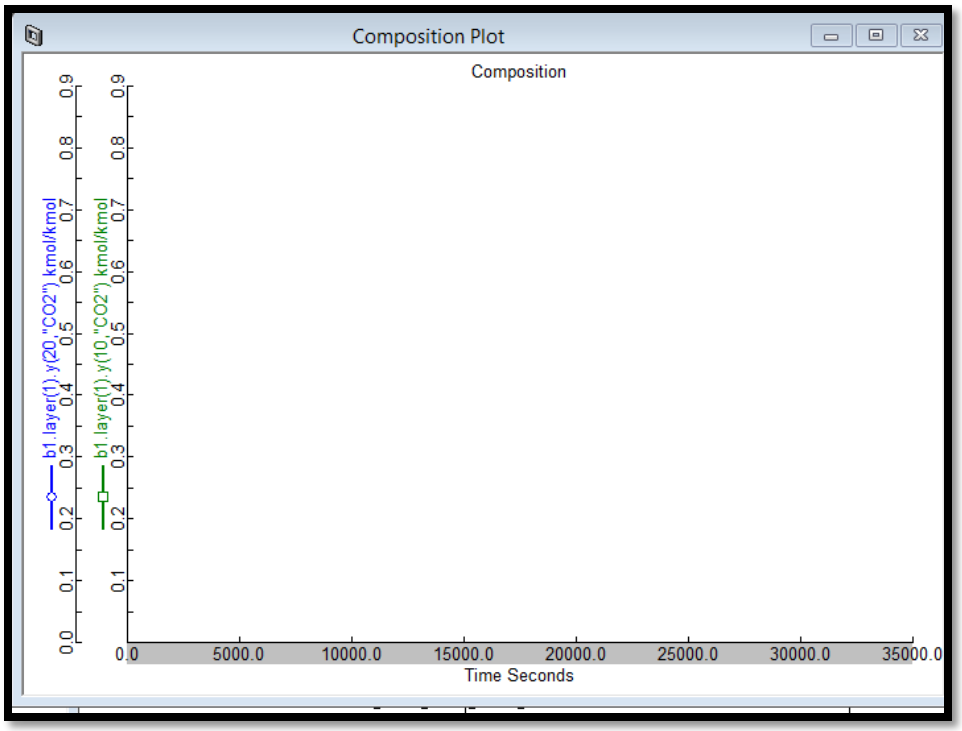

FIGURE 9.49. THE COMPOSITION PLOT WITHIN THE BED OVER TIME IN THE TSA MODEL.

Step 47: Add Form->Profile Plot->Axial_Composition.

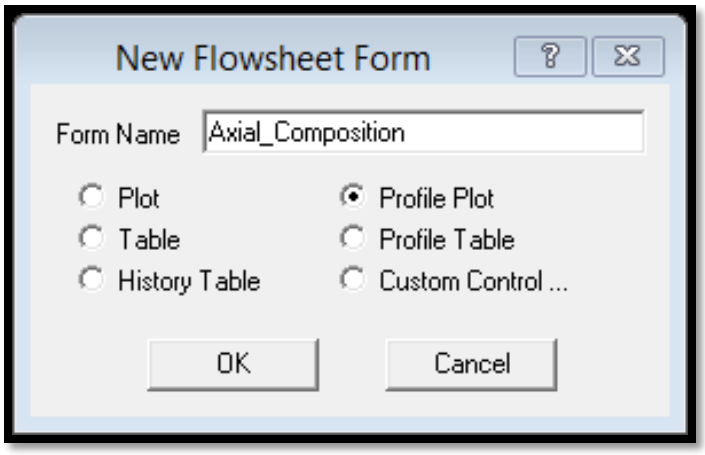

FIGURE 9.50. THE GENERATION OF A CONCENTRATION PROFILE WITHIN THE TSA BED.

Step 48: Profile Editor for the Axial_Composition profile plot.

Position: B1. Layer(*).Axial_Distance(*)

CO2 Partial Pressure: B1. Layer(*).Y (*,"CO2")

N2 Partial Pressure: B1. Layer(*).Y (*,"N2")

FIGURE 9.51. THE AXIAL COMPOSITION PROFILE PLOT IN THE TSA MODEL.

Step 49: Profile Editor for the Axial_Temperature profile plot.

Position: B1. Layer(*).Axial_Distance(*)

Gas Phase Temperature: B1.Layer(*).Tg(*)

Solid Phase Temperature: B1.Layer(*).Ts(*)

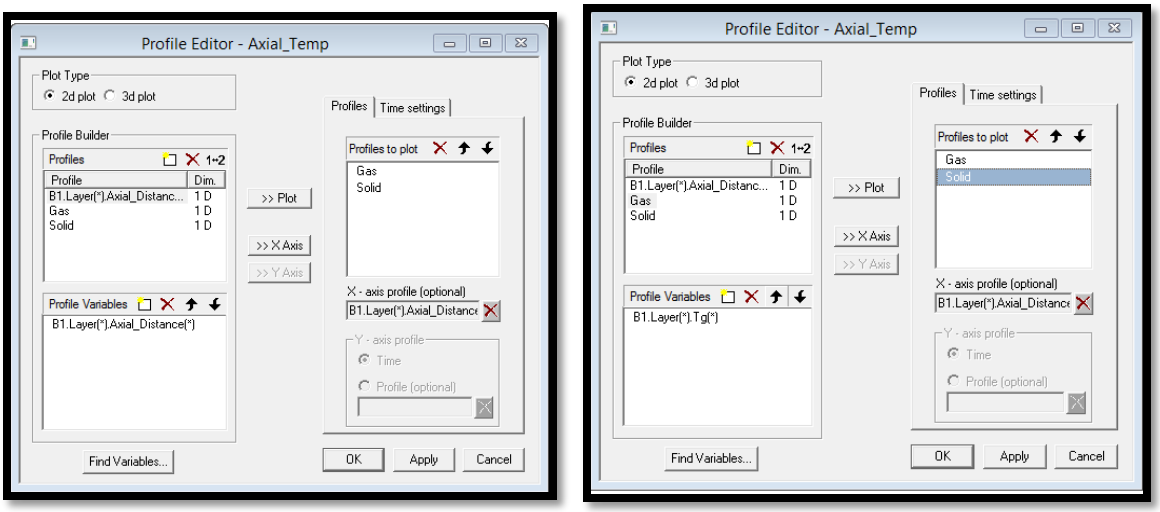

FIGURE 9.52. THE AXIAL TEMPERATURE PROFILE PLOT IN THE TSA MODEL.

Step 50: Run Options->Initialization.

The model is ready to initialize.

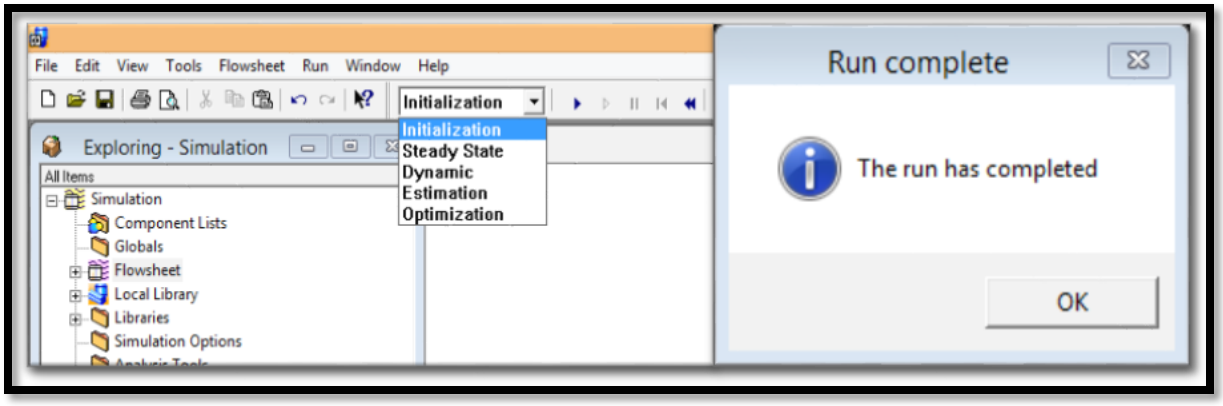

FIGURE 9.53.THE INITIALIZATION OF THE TSA MODEL.

Step 51: Run Options->Dynamic.

The model is ready for the dynamic run after reaching the pause time (382.8 min) we set.

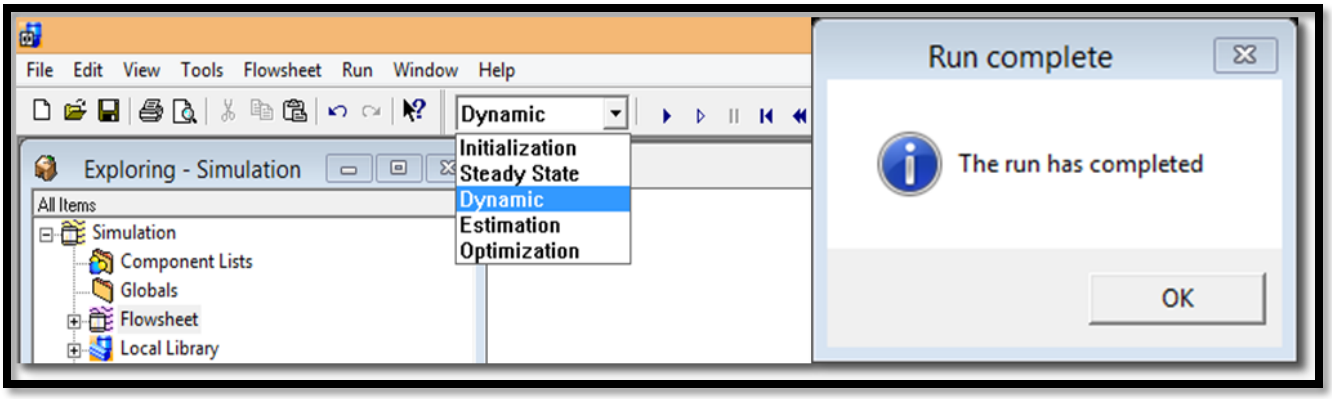

FIGURE 9.54.THE DYNAMIC RUN OF THE TSA MODEL.

Step 52: Results->Plots.

We display all the plots made in steps 40 to 45. A single-bed TSA model has been developed for a binary separation of capturing CO2 from a CO2/N2 mixture. Figure 9.55 reveals the changing of temperature between the adsorption and regeneration steps. Figure 9.56 shows the resulting light product mole fraction in the Product stream with 99.9% N_2 purity. The resulting bed composition plot in Figure 9.57 tells that 10% CO_2 has been adsorbed into the solid adsorbent bed during the adsorption step. Figure 9.58 illustrates the increasing of the CO_2 and decreasing

of the N2 within the TSA bed during the adsorption section. Figure 9.59 gives the information of the resulting axial temperature profile plot in the TSA model.

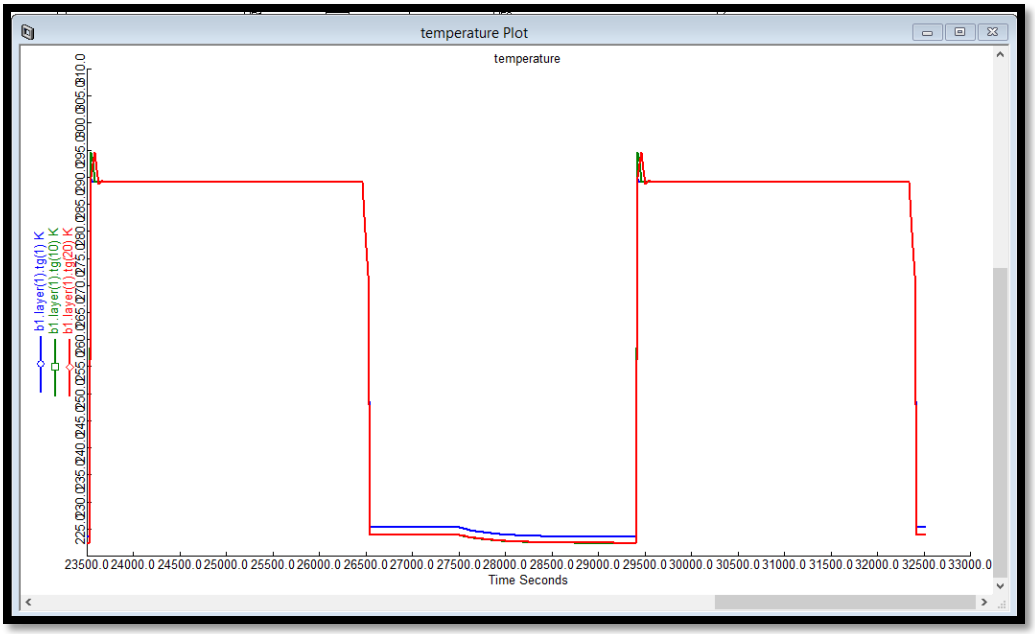

FIGURE 9.55. THE RESULTING BED TEMPERATURE PLOT IN THE TSA MODEL.

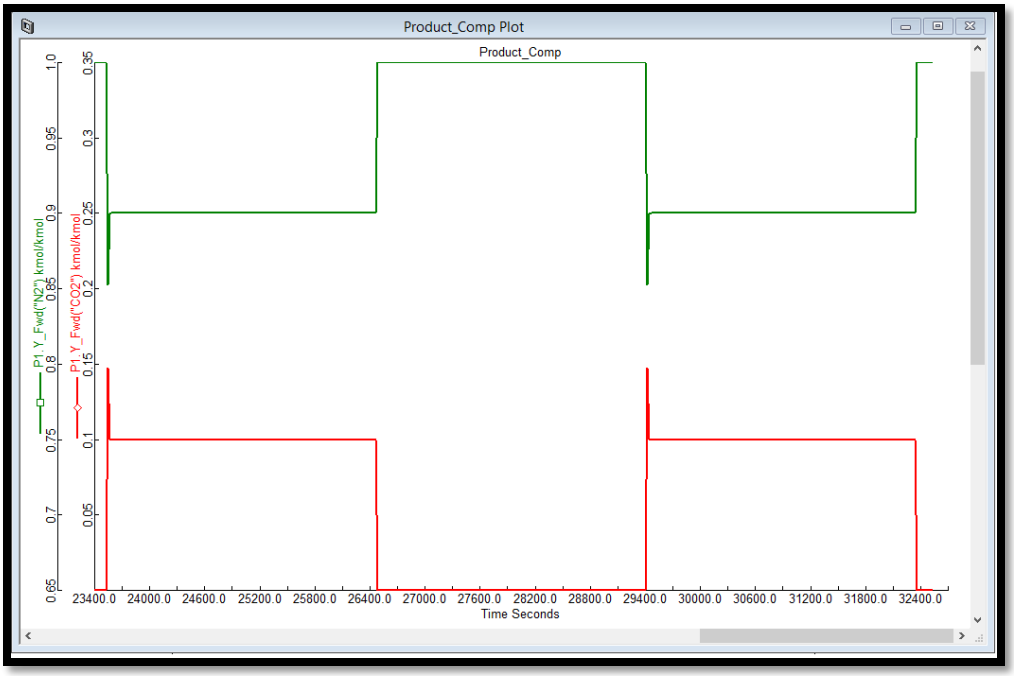

FIGURE 9.56. THE RESULTING LIGHT PRODUCT PLOT IN THE TSA MODEL.

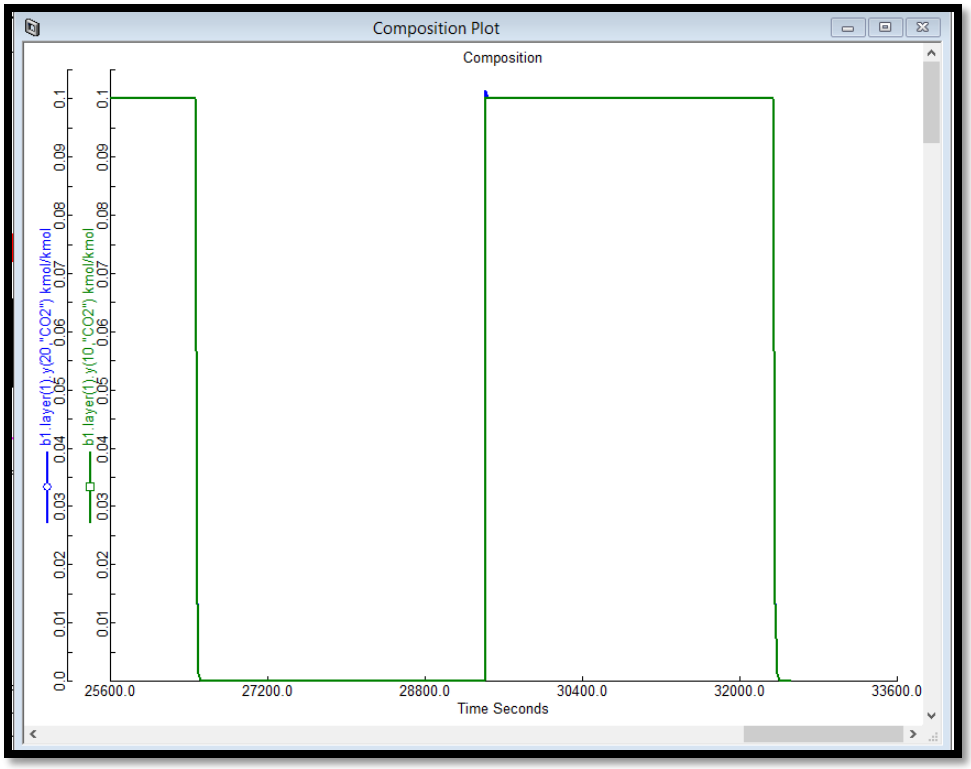

FIGURE 9.57. THE RESULTING BED COMPOSITION PLOT IN THE TSA MODEL.

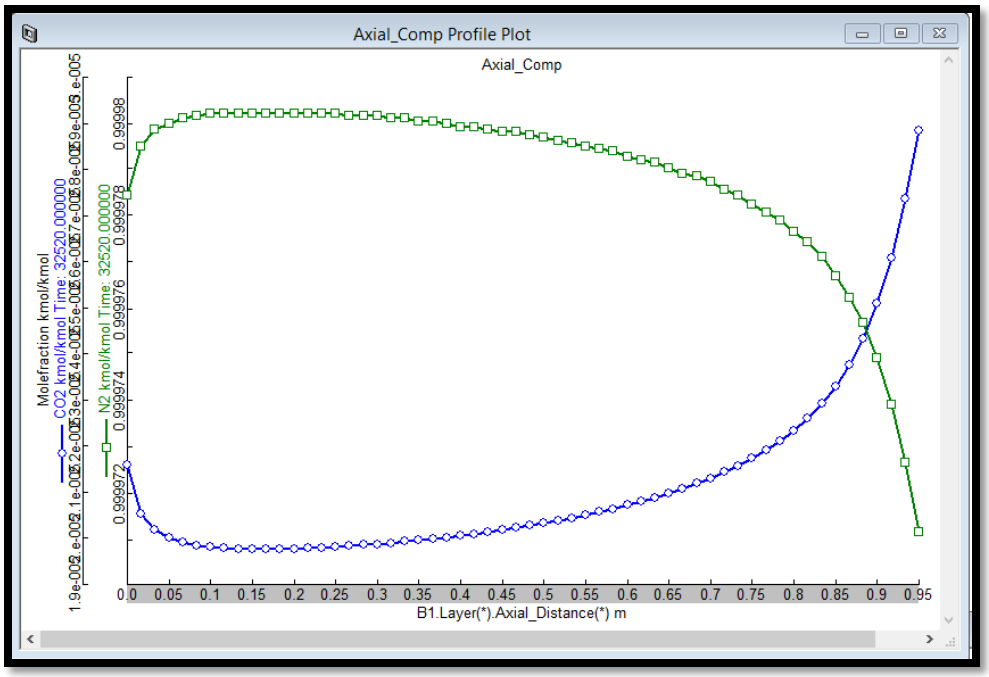

FIGURE 9.58. THE RESULTING AXIAL COMPOSITION PROFILE PLOT IN THE TSA MODEL.

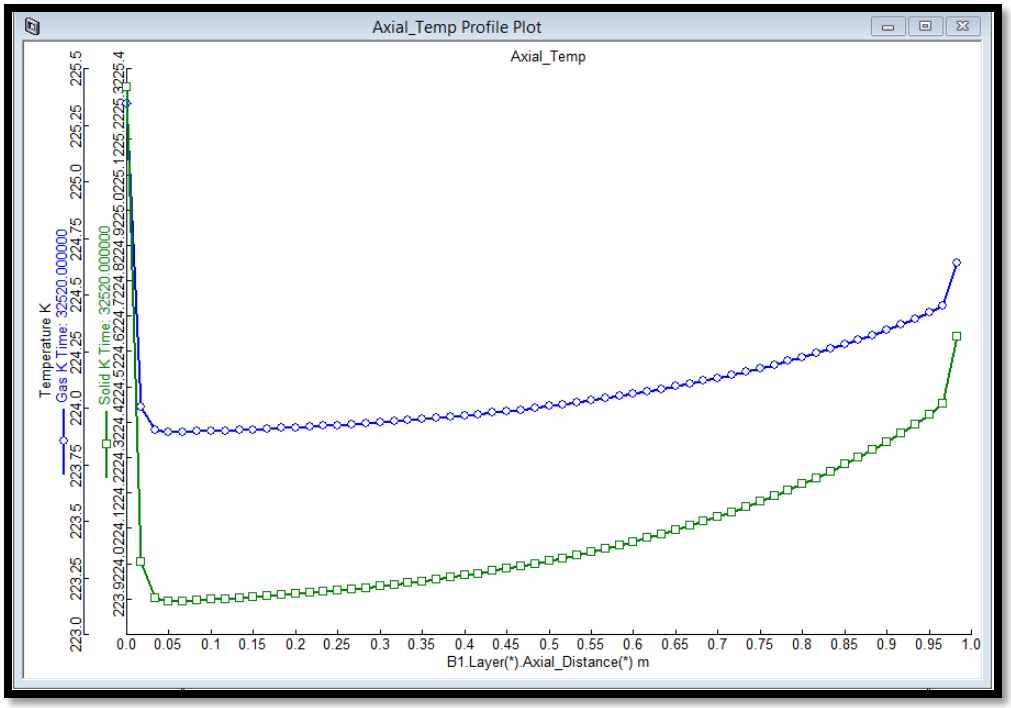

FIGURE 9.59. THE RESULTING AXIAL TEMPERATURE PROFILE PLOT IN THE TSA MODEL.

10. Conclusions and Recommendations for Future Research

This research contains two parts: liquid separation modeling by Aspen Chromatography, and gas separation modeling by Aspen Adsorption. In the first part, we focus on the modeling and optimization of the Simulated Moving Bed (SMB) units and its various operational modes for bioprocess separation systems. It demonstrates a methodology for the simulation and optimization of operational modes of SMB chromatography for the separation and purification in bioprocesses using Aspen Chromatography. After discussing briefly the basic SMB concepts, we introduce two bioprocesses, a binary chiral separation of Tröger's base enantiomers and a ternary separation of amino acids. We simulate the performance of the 4-zone SMB unit as well as several operational modes and their combinations in purifying and separating the binary and ternary mixtures. The specific operational modes include the asynchronous shift of inlet/outlet ports ("Varicol"), variable feed flow rates ("PowerFeed" and "Partial feeding") and variable feed concentrations ("ModiCon") within time interval of inlet/outlet port switching, and 5-zone SMB, together with their combinations. We compare the simulation results in terms of purity and recovery of extract and raffinate products, adsorbent consumption and other performance indices. We give physical insights of why a given operational mode performs better or worse

than the basic SMB. We provide quantitative guidelines for optimizing the performance of various operational modes, and present the optimum operating regions where certain purity and recovery thresholds are met for various operational modes. The second part focuses on the modeling demonstration of two gas adsorption separation processes by Pressure Swing Adsorption (PSA), and Temperature Swing Adsorption (TSA) using Aspen Adsorption.

We have done the simulation and optimization for above SMB operational modes for a binary and a ternary separation system. For the future research, we have the following recommendations to improve the study:

(1) In order to give a general guideline for the selection of operational modes across a variety of systems, it is necessary to evaluate several more separation systems, such as multi-components system, SMB column with more than 5 beds, etc.
(2) For the combined operational modes, it would be an interesting topic to do a complete process control analysis for practical purposes.
(3) Apply and compare varied operational modes for both pressure and temperature swing adsorption processes.

11.Nomenclature

Variables	Units	Description
AS_i	$[-]$	asynchronous switching ratios for inlet and outlet ports
$a_{i,1}$	$[-]$	bi-Langmuir isotherm parameter a_1 for component i
$a_{i,2}$	$[-]$	bi-Langmuir isotherm parameter a_2 for component i
$b_{i,1}$	$[\mathrm{L/g}]$	bi-Langmuir isotherm parameter b_1 for component i
$b_{i,2}$	$[\mathrm{L/g}]$	bi-Langmuir isotherm parameter b_2 for component i
$\bar{C}_{\mathrm{A}}^{\mathrm{E}}$	$[\mathrm{g/L}]$	average concentration of component A in the extract stream
$\bar{C}_{\mathrm{B}}^{\mathrm{R}}$	$[\mathrm{g/L}]$	average concentration of component B in the raffinate stream
C_A^F	$[\mathrm{g/L}]$	average concentration of component A in the feed
C_B^F	$[\mathrm{g/L}]$	average concentration of component B in the feed
C_{i}	$[\mathrm{g/L}]$	subinterval switching feed concentration
C_i^*	$[\mathrm{g/L}]$	equilibrium concentration for component i in the fluid phase
D	N/A	Desorbent stream
D_{L}	$[cm^2/\mathrm{min}]$	axial dispersion coefficient
Dia	$[\mathrm{cm}]$	column diameter
$\overline{DC}$	$[\mathrm{L/g}]$	desorbent consumption
E	N/A	Extract stream in 4-zone unit
E1	N/A	Extract1 stream in 5-zone unit
E2	N/A	Extract2 stream in 5-zone unit
F	N/A	Feed stream
F_{i}	$[\mathrm{mL/min}]$	subinterval switching feed flow rate
H_{i}	$[-]$	Henry's constant coefficient for component i
IP1	[--]	isotherm parameter 1 in Aspen
IP2	[--]	isotherm parameter 2 in Aspen
k_{i}	$[1/\mathrm{s}]$	mass transfer coefficient for component i
K_i	[--]	equilibrium constant for component i
L	$[\mathrm{m}]$	column length
l	$[\mathrm{m}]$	length of each bed in the column
m_{j}	$[-]$	net mass flow rate ratio in zone j

N_{i}	$[-]$	bed number in zone j
P	$[bar]$	bed pressure drop
P_i	$[bar]$	partial pressure drop for component i
Pe	$[-]$	particle Peclet number
$\overline{Pur}$	[%]	average product purity performance
$\overline{Rec}$	[%]	average product recovery performance
$\overline{Pro}$	$\left[\frac{\mathrm{g}}{\mathrm{L}}/\mathrm{hr}\right]$	productity of the product
q_{i}	[g/g]	solid loading for component i
q_i^*	[g/g]	equilibrium solid loading for component i
Q_{j}	[mL/min]	internal flow rate in zone j
Q_{D}	[mL/min]	desorbent flow rate
Q_{F}	[mL/min]	feed flow rate
Q_{E}	[mL/min]	extract flow rate in 4-zone unit
Q_{E1}	[mL/min]	extract1 flow rate in 5-zone unit
Q_{E2}	[mL/min]	extract2 flow rate in 5-zone unit
Q_{R}	[mL/min]	raffinate flow rate
Q_{recy}	[mL/min]	recycle flow rate
R	N/A	raffinate stream
$Recy_{\mathrm{i}}$	[mL/min]	subinterval switching recycle flow rate
r_{p}	[micron]	particle radius
S	$[\mathrm{cm}^2]$	cross-sectional area of the bed
t_{sw}	[min]	switching time
t_{i}	[min]	subinterval switching time
u	[m/s]	the superficial velocity of the gas flow
V_{bed}	$[\mathrm{cm}^3]$	bed volume per column
$V_{\mathrm{j}}^{\mathrm{D}}$	$[\mathrm{cm}^3]$	dead volume through the column
$XFac$	[--]	volume correction factor
z	[m]	axial distance through the column
Z_{j}	$[-]$	effective numbers of beds in zone j
χ	N/A	column configuration

ΔP_{j}	[bar]	pressure drop in zone j
$\Delta P_{\max}$	[bar]	maximum pressure drop through the column
ε	$\left[\frac{m^3\ void}{m^3}\right]$	overall bed voidage
ε_i	$\left[\frac{m^3\ void}{m^3}\right]$	inter-particle voidage
ε_p	$\left[\frac{m^3\ void}{m^3}\right]$	intra-particle voidage
μ	[cp]	liquid viscosity
ψ	$[-]$	particle shape factor
ϕ	$\left[\frac{\mathrm{bar}*\mathrm{min}}{\mathrm{cm}^2}\right]$	pressure drop coefficient

12.Literature Cited

(1) Rajendran, A.; Paredes, G.; Mazzotti, M. Simulated Moving Bed Chromatography for the Separation of Enantiomers. *J. Chromatogr. A.* **2009**, *1216*, 709.

(2) Gomes, P.S.; Minceva, M.; Rodrigues, A.E. Simulated Moving Bed Technology: Old and New. *Adsorption.* **2006**, *12*, 375.

(3) Juza, M.; Mazzotti, M.; Morbidelli, M. Simulated Moving-bed Chromatography and its Application to Chirotechnology. *Trends Biotechnol.* **2000**, *18*, 108.

(4) Aniceto, J.P.; Silva, C.M. Simulated Moving Bed Strategies and Designs: From Established Systems to the Latest Developments. *Separation & Purification Reviews*. Taylor & Francis. **2014,** *44*, pp: 41-73.

(5) Gomes, P.S.; Rodrigues, A.E. Simulated Moving Bed Chromatography: From Concept to Proof-of-Concept. *Chem. Eng. Technol.* **2012**, *35*, 17.

(6) Aboul-enein, H. Y.; Islam, R. M., Direct HPLC Separation of Thalidomide Enantiomers Using Cellulose Tris-4-Methylphenyl Benzoate Chiral Stationary Phase. *J. Liquid Chromatogr*. **1991**, 14, 667.

(7) Ruthven, D. M.; Farooq, S.; knaebel, K.S. Pressure Swing Adsorption; John Wiley and Sons: New York, **1994**.

(8) Kalbassi, M.A.; Allam, R.J.; Golden, T.C. Temperature Swing Adsorption, Patent US5846295 A, **1998**.

(9) International Strategic Directions, Los Angeles, USA.

(10) Ruthven, D.M. Principles of Adsorption and Adsorption Processes, John Wiley and Sons: New York, **1984.**

(11) Braithwaite, A.; Smith, F.J. Chromatographic Methods, **1985**.

(12) Scott, R.P.W. Techniques and Practice of Chromatography. Marcel Dekker: New York, **1995**.

(13) Heftmann, E. Chromatography Part A: Fundamentals and Techniques. Elsevier B.V., **2004**.

(14) Guiochon G.; Felinger, A.; Shirazi, D.G.; Katti, A.M. Fundamentals of Preparative and Nonlinear Chromatography. Elsevier Inc., **2006**.

(15) Broughton, D.B.; Gerhold, G.G. Continuous Sorption Process Employing Fixed Bed of Sorbent and Moving Inlets and Outlets. US patent 2985589, **1961**.

(16) Nishizawa, H.; Tahara, K. Miyamori, S.; Motegi, Y.; Shoji, T.; Abe, Y. True Moving Bed Chromatography: Solid-liquid Multi-stage Counter-current Extraction. *J. Chromatogr. A.* **1999**, *849*, 61.

(17) Ruthven, D. M.; Ching, C. B. Counter-current and Simulated Counter-current Adsorption Separation Process. *Chem. Eng. Sci.*, **1989**, 44, 1013-1038.

(18) Rodrigues, A.E.; Pereira, C.; Minceva, M.; Pais, L.S.; Ribeiro, A.M.; Ribeiro, A.; Silva, M.; Graca, N.; Santos, J.C. Simulated Moving Bed Technology: Principle, Design and Process Applications. Elsevier Inc., **2015**.

(19) Jo, S.-H.; Kim, J.K.; Yoo, C.G.; Kim, J.-I.; Koo, Y.-M.; Mun, S. Comparative Analysis of Single-Cascade Five-Zone and Two-Zone SMB System for the Separation of a Ternary Amino Acid Mixture. *Can. J. Chem. Eng.* **2007**, *85*, 874.

(20) Katsuo, S.; Langel, C.; Schanen, P.; Mazzotti, M. Extra-column Dead Volume in Simulated Moving Bed Separations: Theory and Experiments. *J. Chromatogr. A.* **2009,** *1216*, 1084.

(21) Mun, S.; Xie, Y.; Kim, J.-H.; Wang, N.-H.L. Optimal Design of a Size-Exclusion Tandem Simulated Moving Bed for Insulin Purification. *Ind. Eng. Chem. Res.* **2003**, *42*, 1977.

(22) Kim, J.K.; Zang, Y.; Wankat, P.C. Single-Cascade Simulated Moving Bed Systems for the Separation of Ternary Mixtures. *Ind. Eng. Chem. Res.* **2003**, *42*, 4849.

(23) Xie, Y.; Mun, S.; Kim, J.; Wang, N.-H. L. Standing Wave Design and Experimental Validation of a Tandem Simulated Moving Bed Process for Insulin Purification. *Biotechnol. Prog.* **2002**, *18*, 1332.

(24) Hur, J.S.; Wankat, P.C. Two-Zone SMB/Chromatography for Center-Cut Separation from Ternary Mixtures: Linear Isotherm Systems. *Ind. Eng. Chem. Res.* **2006**, *45*, 1426.

(25) Hur, J. S.; Wankat, P.C.; Kim, J.-I.; Kim, J.K.; Koo, Y.-M. Purification of L-Phenylalanine from a Ternary Amino Acid Mixture Using a Two-Zone SMB/Chromatography Hybrid System. *Sep. Sci. Technol.* **2007**, *42*, 911.

(26) Khan, H.; Younas, M. Theoretical Analysis and Simulation of Five-zone Simulating Moving Bed for Ternary Mixture Separation. *Can. J. Chem. Eng.* **2011**, *89*, 1480.

(27) Wooley, R.; Ma, Z.; Wang, N.-H. L. A Nine-Zone Simulating Moving Bed for the Recovery of Glucose and Xylose from Biomass Hydrolyzate. *Ind. Eng. Chem. Res.* **1998**, *37*, 3699.

(28) Mun, S. Improving Performance of a Five-zone Simulated Moving Bed Chromatography for Ternary Separation by Simultaneous Use of Partial-feeding and Partial-closing of the Product Port in Charge of Collecting the Intermediate-affinity Solute Molecules. *J. Chromatogr. A*. **2011**, *1218*, 8060.

(29) Wang, X.; Ching, C.B. Chiral Separation of β-blocker Drug (nadolol) by Five-zone Simulated Moving Bed Chromatography. *Chem. Eng. Sci.* **2005**, *60*, 1337.

(30) Broughton, D.B.; Carson, D.B. The Molex Process. *Pet.Refin*. **1959**, 38, 130.

(31) Minceva, M.; Rodrigues, A.E. UOP's Parex: Modeling, Simulation and Optimization.

(32) Barker, P.E.; Critcher, D. The Separation of Volatile Liquid Mixtures by Continuous Gas-liquid Chromatography. *Chem.Eng.Sci.* **1960**, 18, 82-89.

(33) Ching, C.B.; Ruthven, D.M. An Experimental Study of A Simulated Counter-current Adsorption System – 1. Isothermal Steady State Operation. *Chem.Eng.Sci.* **1985**, 40, 877-885.

(34) Azevedo, D.C.S.; Rodrigues, A.E. Fructose-glucose Separation in a SMB Pilot Unit: Modeling, Simulation, Design, and Operation. *AIChE J.* **2001**, 47, 2042.

(35) Ching, C.B.; Ruthven, D.M. An Experimental Study of A Simulated Counter-current Adsorption System – 2.Transient Response. *Chem.Eng.Sci.* **1985**, 40, 6, 887-891.

(36) Klatt, K.; Hanisch, F.; Dünnebier, G. Model-based Control of a Simulated Moving Bed Chromatographic Process for the Separation of Fructose and Glucose. *J. of Process Control.* **2002**, 12,203-219.

(37) Johnson, J.A.; Kabza, R.G. Sorbex: Industrial-scale Adsorptive Separation. *Advances in Separation Processes*. **1990**, Hemisphere Pub.

(38) Balannex, B.; Hotier, G. From Batch Elution to Simulated Countercurrent Chromatography. Preparative and Production Scale Chromatography. **1992**, CRC Press.

(39) Negawa, M.; Shoji, F. Optical Resolution by Simulated Moving-bed Adsorption Technology. *J. Chromatogr. A*., **1992**, 590, 113-117.

(40) Ching, C.B.; Lim, B.G.; Lee, E.J.D.; Ng, S.C. Preparative Resolution of Praziquantel Enantiomers by Simulated Counter-current Chromatography. *J. Chromatogr. A*., **1993**, 634, 215-219.

(41) Francotte, E. R. Enantioselective Chromatography as a Powerful Alternative for the Preparation of Drug Enantiomers. *J. Chromatogr. A*., **2001**, 906, 379-397.

(42) Schulte, M.; Strube, J. Preparative Enantioseparation by Simulated Moving Bed Chromatography. *J. Chromatogr. A.*, **2001**, 906, 399-416.

(43) Toumi, A.; Engell, S.; Ludemann-Hombourger, O.; Nicoud, R.; Bailly, M. Optimization of Simulated Moving Bed and Varicol Processes. *J. Chromatogr. A.*, **2003**, 1006, 15-31.

(44) Juza, M.; Mazzotti, M.; Morbidelli, M. Simulated Moving-bed Chromatography and Its Application to Chirotechnology. *Trends in Biotechnology*, 2000, 18, 108-118.

(45) Guiochon, G. Preparative Liquid Chromatography. *J. Chromatogr. A.*, **2002**, 965, 129-161.

(46) Schulte, M.; Strube, J. Preparative Enantioseparation by Simulated Moving Bed Chromatography. *J. Chromatogr. A.*, **2001,** 906, 1084-1093.

(47) McCoy, M. *Chem. Eng. News*, **2000**, 78, 17 (Chiral Business).

(48) Anon., *Chem. Eng. News*, **2003**, 81, 18.

(49) Nicoud, R.M.; Fuchs, G.; Adam, P.; Bailly, M.; Kusters, E.; Antia, F.D.; Reuille, R.; Schmid, E. Preparative scale enantioseparation of a chiral epoxide: Comparison of liquid chromatography and simulated moving bed adsorption technology. *Chirality*, **1993**, 5, 267.

(50) Abel, S.; Juza, M. Chiral Separation Techniques: A Practical Approach, Wiley–VCH, Germany, **2007**, 618.

(51) Zhang, Z.; Mazzotti, M.; Morbidelli, M. Continuous Chromatographic Processes with a Small Number of Columns: Comparison of Simulated Moving Bed with Varicol PowerFeed and ModiCon. *Korean J. Chem. Eng.* **2004**, *21*, 454.

(52) Ludemann-Hombourger, O.; Nicoud, R. M.; Bailly, M. The "VARICOL" Process: A New Multicolumn Continuous Chromatographic Process. *Sep. Sci. Technol.* **2000**, *35*, 1829.

(53) Ludemann-Hombourger, O.; Pigorini, G.; Nicoud, R.M.; Ross, D.S.; Terfloth, G. Application of the "VARICOL" Process to the Separation of the Isomers of the SB-553261 Racemate. *J. Chromatogr. A.* **2002**, *947*, 59.

(54) Pais, L.S.; Rodrigues, A.E. Design of Simulated Moving Bed and Varicol Processes for Preparative Separations with a Low Number of Columns. *J. Chromatogr. A.* **2003**, *1006*, 33.

(55) Toumi, A.; Engell, S.; Ludemann-Hombourger, O.; Nicoud, R. M.; Bailly, M. Optimization of Simulated Moving Bed and Varicol Processes. *J. Chromatogr. A.* **2003**, *1006*, 15.

(56) Zhang, Y.; Hidajat, K.; Ray, A. K. Multi-objective Optimization of Simulated Moving Bed and Varicol Processes for Enantio-separation of Racemic Pindolol. *Sep. Purif. Technol.* **2009**, *65*, 311.

(57) Silva Jr., A.C.; Salles Jr., A.G.; Perna, R.F.; Correia, C.R.D.; Santana, C.C. Chromatographic Separation and Purification of Mitotane Racemate in a Varicol Multicolumn Continuous Process. *Chem. Eng. Technol.* **2012**, *35*, 83.

(58) Zhang, Z.; Mazzotti, M.; Morbidelli, M. PowerFeed Operation of Simulated Moving Bed Units: Changing Flow-rates during the Switching Interval. *J. Chromatogr. A.* **2003**, *1006*, 87.

(59) Zhang, Z.; Morbidelli, M.; Mazzotti, M. Experimental Assessment of PowerFeed Chromatography. *AIChE J.* **2004**, *50*, 625.

(60) Kawajiri, Y.; Biegler, L.T. Optimization Strategies for Simulated Moving Bed and PowerFeed Processes. *AIChE J.* **2006**, *52*, 1343.

(61) Zang, Y.; Wankat, P.C. SMB Operation Strategy-Partial Feed. *Ind. Eng. Chem. Res.* **2002**, *41*, 2504.

(62) Zang, Y.; Wankat, P.C. Three-Zone Simulated Moving Bed with Partial Feed and Selective Withdrawal. *Ind. Eng. Chem. Res.* **2002**, *41*, 5283.

(63) Schramm, H.; Kaspereit, M.; Kienle, A.; Seidel-Morgenstern, A. Simulated Moving Bed Process with Cyclic Modulation of the Feed Concentration. *J. Chromatogr. A.* **2003**, *1006*, 77.

(64) Schramm, H.; Kienle, A.; Kaspereit, M.; Seidel-Morgenstern, A. Improved Operation of Simulated Moving Bed Processes through Cyclic Modulation of Feed Flow and Feed Concentration. *Chem. Eng. Sci.* **2003**, *58*, 5217.

(65) Zang, Y.; Wankat, P.C. Variable Flow Rate Operation for Simulated Moving Bed Separation Systems: Simulation and Optimization. *Ind. Eng. Chem. Res.* **2003**, *42*, 4840.

(66) Bae, Y.S.; Lee, C.H. Partial-discard Strategy for obtaining High Purity Products using Simulated Moving Bed Chromatography. *J. Chromatogr. A.*, **2006**, 1122, 161.

(67) Mun, S. Partial port-closing strategy for obtaining high throughput or high purities in a four-zone simulated moving bed chromatography for binary separation. *J. Chromatogr. A.*, **2010**, 1217, 6522.

(68) Gomes, P.S.; Rodrigues, A.E. Outlet Streams Swing (OSS) and MultiFeed Operation of Simulated Moving Beds. *Sep. Sci. and Technol.*, **2007**, 42, 223.

(69) Pedeferri, M.; Zenoni, G.; Mazzotti, M.; Morbidelli, M. Experimental Analysis of a Chiral Separation through Simulated Moving Bed Chromatography. *Chem. Eng. Sci.*, **1999**, 54, 3735-3748.

(70) Katsuo, S.; Mazzotti, M. Intermittent Simulated Moving Bed Chromatography: 1.Design Criteria and Cyclic Steady-state. *J. Chromatogr. A.* **2010**, *1217*, 1354.

(71) Katsuo, S.; Mazzotti, M. Intermittent Simulated Moving Bed Chromatography: 2. Separation of Tröger's Base Enantiomers. *J. Chromatogr. A.* **2010,** *1217*, 3067.

(72) Katsuo, S.; Langel, C.; Sandre, A.-L.; Mazzotti, M. Intermittent Simulated Moving Bed Chromatography: 3. Separation of Tröger's Base Enantiomers under Nonlinear Conditions. *J. Chromatogr. A.* **2011**, *1218*, 9345.

(73) Amanullah, M.; Mazzotti, M. Optimization of a Hybrid Chromatography-Crystallization Process for the Separation of Tröger's Base Enantiomers. *J. Chromatogr. A.* **2006**, *1107*, 36.

(74) Sreedhar, B. Kawajiri, Y. Multi-column Chromatographic Process Development using Simulated Moving Bed Superstructure and Simultaneous Optimization – Model Correction Framework. *Chem. Eng. Sci.* **2014**, *116*, 428.

(75) Wu, D.-J.; Xie, Y.; Ma, Z.; Wang, N.-H.L. Design of Simulated Moving Bed Chromatography for Amino Acid Separations. *Ind. Eng. Chem. Res.* **1998**, *37*, 4023.

(76) Chin, C. Y.; Wang, N.-H. L. Simulated Moving-Bed Technology for Biorefinery Applications. In *Separation and Purification Technologies in Biorefineries*; Ramaswamy, S., Huang, H.-J., Ramarao, B.V., Eds.; John Wiley & Sons, Ltd.: United Kingdom, **2013**; pp: 167-202.

(77) Storti, G.; Mazzotti, M.; Morbidelli, M.; Carrà, S.; Robust Design of Binary Countercurrent Adsorption Separation Processes. *AIChE J.* **1993**, *39*, 471.

(78) Mazzotti, M. Design of Simulated Moving Bed Separations: Generalized Langmuir Isotherm. *Ind. Eng. Chem. Res.* **2006**, *45*, 6311.

(79) Chung, S.F.; Wen, C.Y. Longitudinal Dispersion of Liquid Flowing Through Fixed and Fluidized Beds. *AIChE J.* **1968,** 14, 857.

(80) Kawajiri, Y.; Biegler, L. T. Nonlinear Programming Superstructure for Optimal Dynamic Operations of Simulated Moving Bed Processes. *Ind. Eng. Chem. Res.*, **2006**, 45, 8503.

(81) Agrawal, G.; Kawajiri, Y. Full Superstructure for Multiobjective Optimization of Multicolumn Chromatography for Ternary Separations. *Chem. Eng. Technol.* **2015**,38,1.

(82) Powell, M.J.D. An efficient Method for Finding the Minimum of a Function of Several Variables without Calculating Derivations. *Computer Journal*. **1964**, *7*, 155.

(83) Aspen Technology, Inc., Bedford, MA. Course ES289-Introduction to Aspen Chromatography, Support & Training.

(84) Farooq, S.; Ruthven, D.M.; Boniface, H.A. Air Separation by Pressure Swing Adsorption. *Chem. Eng. Sci.* **1990**, 44, 2809-2816.

(85) Doong, S.J.; Yang, R.T. Hydrogen Purification by the Multibed Pressure Swing Adsorption Process. *Reactive Polymers*, **1987**, 6, 7-13.

(86) Hassan, M.M.; Raghavan, N.S.; Ruthven, D.M. Pressure Swing Air Separation on a Carbon Molecular Sieve-II Investigation of a Modified Cycle with Pressure Equalization and No Purge. *Chem. Eng. Sci.* **1987**, 42, 2037-2043.

(87) Liu, Z.; Grande, C.A.; Li, P.; Yu, J.; Rodrigues, A.E. Multi-bed Vacuum Pressure Swing Adsorption for Carbon Dioxide Capture from Flue Gas. *Separation and Purification Technology*. **2011**, 81, 3, 307-317.

(88) Kalbassi, M.A.; Allam, R. J.; Golden, T.C. Temperature Swing Adsorption. Patent. **1997**, US5846295.

(89) Ruthven, D.M.; Farooq, S.; Knaebel, K.S. Pressure Swing Adsorption. WILEY-VCH, **1994**, Hoboken, NJ.

(90) Mendes, A.; Costa, C.; Rodrigues, A. Oxygen Separation from Air by PSA: Modeling and Experimental Results Part I: Isotherm Operation. *Separation and Purification Technology*, **2001**, 24, 173-188.

(91) Tlili, N.; Grevillot, G.; Vallieres, C. Carbon Dioxide Capture and Recovery by Means of TSA and/or VSA. *International Journal of Greenhouse Gas Control.* **2009**, 3, 519-527.

(92) Chue, K.T.; kim, J.N.; Yoo, Y.J.; Cho, S.H.; Yang, R.T. Comparison of Activated Carbon and Zeolite 13X for CO2 Recovery from Flue Gas by Pressure Swing Adsorption. *Ind. Eng.Chem. Res.* **1995**, 34, 591-598.

(93) Chihara, K.; Suzuki, M. Simulation of nonisothermal pressure swing adsorption. *J. Chem. Eng. Japan*. **1983**, 16, 53-61.

(94) Raghavan, N.S.; Ruthven, D.M. Pressure Swing Adsorption Part II: Numerical Simulation of a Kinetically Controlled Bulk Gas Separation. *AIChE J*. **1985**, 31, 2017-2025.

(95) Hassan, M.M.; Ruthven, D.M.; Raghavan, N.S. Air Separation by Pressure Swing Adsorption on a Carbon Molecular Sieve. *Chem. Eng. Sci.* **1986**, 41, 1333-1343.

(96) Raghavan, N.S.; Hassan, M.M.; Ruthven, D.M. Numerical Simulation of a PSA System Using a Pore Diffusion Model. *Chem. Eng. Sci.* **1986**, 41, 2787-2793.

(97) Shin, H.S.; Knaebel, K.S. Pressure Swing Adsorption: An Experimental Study of Diffusion-Induced Separation. *AIChE J.* **1988**, 34, 1409-1416.

(98) Farooq, S.; Ruthven, D.M.; Boniface, H.A. Air Separation by Pressure Swing Adsorption. *Chem. Eng. Sci.* **1990**, 44, 2809-2816.

(99) Ritter, J.A.; Yang, R.T. Pressure Swing Adsorption: Experimental and Theoretical Study on Air Purification and Vapor Recovery. *Ind. Eng.Chem. Res.* **1991**, 30, 1023-1032.

(100) Farooq, S.; Ruthven, D.M. Numerical Simulation of a Kinetically Controlled Pressure Swing Adsorption Bulk Separation Process Based on a Diffusion Model. *Chem. Eng. Sci.* **1991**, 46, 2213-2224.

(101) Leavitt, F.W. Air Separation Pressure Swing Adsorption Process. Patent. **1990**, US5074892A.

(102) Fernandez, G. F.; Kenney, C. N. Modeling of the Pressure Swing Air Separation Process. *Chem. Eng. Sci.* **1983**, 38, 827.

(103) Kent S. Kneabel, Frank B. Hill. Pressure Swing Adsorption: Development of an Equilibrium Theory for Gas Separations. *Chem. Eng. Sci.* **1985**, 40, 2351.

(104) Jee J-G; Kim M-B; Lee C-H. Pressure Swing Adsorption to Purify Oxygen Using a Carbon Molecular Sieve. *Chem. Eng. Sci.* **2005**, 60, 869.

(105) Jee, J. G.; Lee, S. J.; Lee, C. H. Comparison of the Adsorption Dynamics of Air on Zeolite 5A and Carbon Molecular Sieve Beds. *Korean J. Chem. Eng.* **2004**, 21, 1183.

(106) Kostroski, K. P.; Wankat, P. C. High Recovery Cycles for Gas Separations by Pressure Swing Adsorption. *Ind. Eng. Chem. Res.* **2006**, 45, 8117.

(107) Mendes, A. M. M.; Costa, C. A. V.; Rodrigues, A. E. Oxygen Separation from Air by PSA: Modelling and Experimental Results Part I: Isothermal Operation. *Sep. Purif. Technol.* **2001**, 24, 173.

(108) Yu, C.H., Huang, C.H.; Tan, C.S. A Review of CO2 Capture by Absorption and Adsorption. *Aerosol Air Qual. Res.* **2012**, 12, 745.

(109) Zaman, M.; Lee, J.H. Carbon capture from stationary power generation sources: A review of the current status of the technologies. *Korean J Chem Eng.* **2013**, 30, 1794.

(110) Mulgundmath, V.; Tezel, F. H. Optimization of Carbon Dioxide Recovery from Flue Gas in a TPSA System. *Adsorption.* **2010**, 16, 587.

(111) Merel, J.; Clausse, M.; Meunier, F. Carbon Dioxide Capture by Indirect Thermal Swing Adsorption Using 13X Zeolite. *Environ. Prog.* **2006**, 25, 327-333.

(112) Bonjour, J.; Chalfen, J.B.; Meunier, F. Temperature Swing Adsorption Process with Indirect Cooling and Heating. *Ind. Eng.Chem. Res.* **2002**, 41, 5802-5811.

(113) Clausse, M.; Bonjour, J.; Meunier, F. Adsorption of gas mixtures in TSA adsorbers under various heat removal conditions. *Chem. Eng. Sci.* **2004**; 59, 3657.

(114) Yang, M.; Chen, N.; Huang, C.; Shen, Y.; Yang, H.; Chou, C. Temperature Swing Adsorption Process for CO2 Capture using Polyaniline Solid Sorbent. *Energy Procedia.* **2014**, 63, 2351.

(115) Ling, J.; Ntiamoah, A.; Xiao, P.; Xu, D.; Webley, P. A.; Zhai, Y. Overview of CO2 Capture from Flue Gas Streams by Vacuum Pressure Swing Adsorption Technology. *Austin J. Chem. Eng.* **2014**, 1, 1009.

(116) Merel, J.; Clausse, M.; Meunier, F. Experimental Investigation on CO2 Post-Combustion Capture by Indirect Thermal Swing Adsorption Using 13X and 5A Zeolites. *Ind. Eng. Chem. Res.* **2008**, 47, 209.

(117) Gomes, V.G.; Yee, K.w.k. Pressure Swing Adsorption for Carbon Dioxide Sequestration from Exhaust Gases. *Sep. Puri. Technol.* **2002**, 28, 161.

(118) Grande, C.; Rodrigues, A.E. Pressure Swing Adsorption for Carbon Dioxide Sequestration. 2nd Mercosur Congress on Chemical Engineering, 4th Mercosur Congress on Process System Engineering, **2015**.